



Ph.D. Thesis

Stable water isotope variability as a proxy of past temperatures

Using polar ice cores as a climate archive

Christian Terkelsen Holme

Supervisor: Bo M. Vinther

Co-supervisor: Vasileios Gkinis

This thesis has been submitted to the PhD School of The Faculty of Science, University of Copenhagen

January 2, 2019

PREFACE

This dissertation represents the completion of my PhD in geophysics, which was conducted in the period November 1, 2015 to January 2, 2019 at the Centre for Ice and Climate, Niels Bohr Institute, University of Copenhagen. The work was carried out under supervision of Bo Møllesøe Vinther and Vasileios Gkinis.

University: University of Copenhagen

Institute: Niels Bohr Institute

Department: Centre for Ice and Climate

Author: Christian Terkelsen Holme

KU-username: xbj204

Email: christian.holme@nbi.ku.dk

Title: Stable water isotope variability as a proxy of past temperatures

Submitted: January 2, 2019

Signature

Date

ACKNOWLEDGEMENTS

The completion of this PhD would not have been possible without the support of my two supervisors, Bo M. Vinther and Vasileios Gkinis. I appreciate how you always encourage scientific curiosity and that you always are keen to engage in a discussion about everything from ice core science to the current world situation. This PhD dissertation is a product of your good balance between guidance and scientific freedom. For that, I am grateful, and I look forward to keep working with you in the future!

I also want to thank Eric Steig, Emma Kahle, Bradley Markle and Jessica Badgeley for their hospitality and great discussions during my three months stay at the University of Washington, Seattle. Seattle is an amazing city surrounded by beautiful mountains and welcoming people and I really enjoyed my time there. I would recommend such a stay abroad to anyone, and the second paper presented in this thesis is a product of my collaboration with Emma and Eric. Hopefully, I get to visit you in the future!

I want to thank the Centre for Ice and Climate for a great working environment both scientifically and personally. I am thankful for the opportunity to participate in the field activities on EastGRIP, Greenland during the summers of 2016 and 2017. It was a fun and insightful experience where I worked as a carpenter's assistant the first year and as an experimentalist doing CFA measurements of water isotopes the second year.

I also want to acknowledge my two office mates Marius and Nicholas together with my fellow PhD students Søren, Mads and Kasper. It has been great working with you guys for the past three years, and I am going to miss our celebrations of scientific achievements and failures.

Last but not least, I want to thank my family for their support. Especially my partner Elin who deserves a tremendous amount of credit for helping me improve this work. I want to think that my tendency to write very dynamically (sloppy) has decreased over the past three years. If that is true, you deserve all the credit!

ABSTRACT

The stable water isotope signal ($\delta^{18}\text{O}$ and δD) of polar ice cores can be employed as a proxy of the local temperature history. However, it has proven to be challenging to quantify the magnitude of past temperature change solely from the measured isotopic composition. Thus, in a pursuit of improving the accuracy of temperature reconstructions, this PhD dissertation investigates some of the paleoclimatic interpretations that can be made from ice core $\delta^{18}\text{O}$ and δD variability. The work has led to two published papers and one submitted manuscript, all presented in this thesis.

The first study presents temperature reconstruction techniques that only depend on the magnitude of diffusive smoothing on the $\delta^{18}\text{O}$ and δD signals. The objective is to evaluate the performance of such diffusion-based reconstruction techniques in terms of accuracy and precision. By utilizing the methods on both synthetic generated data and ice core data from Greenland and Antarctica, the study finds that single diffusion approaches have higher precision (1.1°C) than methods that rely on the differential diffused signal of $\delta^{18}\text{O}$ and δD (1.9°C).

The second study examines how to estimate the diffusion length from power spectra of newer, continuously measured water isotope data sets that have lower instrument noise levels. Such power spectra reveal a deviation from the conventional power spectral structure, which complicates the currently used diffusion estimation approaches. By performing tests with synthetic data, the results show that noise and system smoothing occurring through the continuous flow analysis system can explain the observed power spectra. This led to the proposal of two modified techniques that can be used to estimate the diffusion length of continuously measured water isotopes.

The third study analyzes the $\delta^{18}\text{O}$ variability of three ice cores drilled on Renland, East Greenland. The objective is to examine their common signal and how it correlates with regional temperatures back in time. While it is shown that the data can be merged into robust seasonal stacks, the linear relation between $\delta^{18}\text{O}$ and regional temperature changes with time. The unstable covariation coincides with a fluctuating amount of southward exported sea ice along the East Greenland coast. Although, an explanation for the varying $\delta^{18}\text{O}$ -temperature relation remains unknown, the study demonstrates that it can be complicated to perform regression-based temperature reconstructions for some ice core drill sites.

Ultimately, preliminary work on a high resolution diffusion length profile from the West Antarctic Ice Sheet Divide is presented. The results indicate remarkably high diffusion during the transition from glacial to interglacial. An investigation is initiated to examine whether the elevated diffusion reflects warmer temperatures than previously inferred or if it is a consequence of perplexing post-depositional processes. While this work is unfinished, it emphasizes some of the challenges ahead of the water isotope diffusion community.

RESUMÉ

Polare iskernes stabile vand isotoper kan bruges som en proxy af den lokale temperaturhistorie. Det er dog svært at kvantificere størrelsen af fortidens temperaturændringer udelukkende fra en målt isotopsammensætning, og denne PhD afhandling undersøger hvilke paleoklimatiske fortolkninger, som man kan lave på baggrund af iskernes $\delta^{18}\text{O}$ og δD variabilitet i jagten på at forbedre rekonstruktioner af fortidens klima. Der er udført tre delstudier, og arbejdet har ledt til to publicerede artikler og et indsendt manuskript.

Det første studie præsenterer temperatur-rekonstruktionsteknikker, som udelukkende afhænger af størrelsen på den diffusion, som har afdæmpet $\delta^{18}\text{O}$ og δD signaler. Formålet er at evaluere nøjagtighed og præcision af diffusionsbaserede rekonstruktionsteknikker. Ved at anvende metoderne på både syntetiske data samt iskerne-data fra Grønland og Antarktis konstateres i studiet, at diffusionsteknikker baseret udelukkende på $\delta^{18}\text{O}$ eller δD har højere præcision (1.1°C) end metoder som afhænger af forskellen mellem $\delta^{18}\text{O}$ og δD (1.9°C).

Det andet studie undersøger, hvordan man estimerer diffusionslængden med numerisk spektralanalyse af nye kontinuerligt målte vand-isotop datasæt, som har et lavere instrumentelt støjniveau. Disse effektspektre afslører en afvigelse fra den konventionelle spektral-struktur, hvilket komplicerer de nuværende diffusion-estimeringsrutiner. Fænomenet er undersøgt ved at udføre tests med syntetiske data, og resultaterne viser, at det kontinuerlig målte analysesystem introducerer støj og signalafdæmpning, hvilket kan forklare de observerede effektspektre. Her foreslås derfor to modificerede teknikker til at estimere diffusionslængden af kontinuerligt målte vand isotoper.

Det tredje studie analyserer $\delta^{18}\text{O}$ variabiliteten af tre iskerner fra Renland, Øst Grønland. Formålet er at undersøge deres fælles signal, og hvorvidt det korrelerer med den regionale temperatur tilbage i tiden. På trods af, at $\delta^{18}\text{O}$ dataene kan blive forenet til robuste sæson-signaler, varierer den lineære relation mellem $\delta^{18}\text{O}$ og temperaturen med tiden. Den instabile samvariation har sammenfald med fluktuationer i mængde af havis, som er eksporteret syd langs den Grønlandske østkyst. Selvom der ikke er bevist en årsag til den varierende $\delta^{18}\text{O}$ -temperatursammenhæng, så demonstrerer studiet, at det kan være kompliceret at udføre temperaturrekonstruktioner på baggrund af regression.

Til sidst præsenteres et indledende arbejde af en højopløst diffusionslængde profil fra WAIS Divide (Antarktis). Resultaterne indikerer bemærkelsesværdigt høj diffusion ved overgangen

mellem istiden og mellemistiden. En undersøgelse er påbegyndt for at efterforske, hvorvidt den høje diffusion reflekterer temperaturer varmere end hidtil antaget, eller om det er en konsekvens af komplekse post-nedbørs-processer. Selvom arbejdet ikke er færdigt så indikerer det nogle af de fremtidige udfordringer, som studier i vand-isotop-diffusion har foran sig.

CONTENTS

I	MOTIVATION AND BACKGROUND	1
1	INTRODUCTION AND OUTLINE	3
2	SCIENTIFIC BACKGROUND	9
2.1	Stable water isotopes	9
2.2	Ice cores as a climate archive	10
2.3	Post-depositional processes	12
2.3.1	Surface effects	12
2.3.2	Densification	12
2.3.3	Diffusion	14
2.3.4	Thinning	15
II	PAPERS	19
3	MOLECULAR DIFFUSION OF STABLE WATER ISOTOPES IN POLAR FIRN AS A PROXY FOR PAST TEMPERATURES	21
3.1	Abstract	21
3.2	Introduction	22
3.3	Theory	24
3.3.1	Diffusion of water isotope signals in firn	24
3.3.2	Isotope diffusion in the solid phase	27
3.4	Reconstructing firn temperatures from ice core data	27
3.4.1	The single isotopologue diffusion	28
3.4.2	The differential diffusion signal	32
3.4.3	The diffusion length ratio	35
3.5	Results	37
3.5.1	Synthetic data test	37
3.5.2	Ice core data test	40
3.5.3	The fractionation factors	41
3.6	Discussion	42
3.6.1	Synthetic data	42
3.6.2	Ice core data	46

3.6.3	The fractionation factors	50
3.6.4	Outlook with respect to ice core measurements	50
3.7	Conclusion	52
4	A GENERALIZED APPROACH TO ESTIMATING DIFFUSION LENGTH OF STABLE WATER ISOTOPES FROM ICE-CORE DATA	58
4.1	Abstract	58
4.2	Introduction	59
4.3	Isotope diffusion theory	60
4.4	Water-isotope data	61
4.5	Estimating diffusion length from ice-core data	62
4.6	Understanding PSDs of different ice-core datasets	65
4.7	Generalizing the diffusion estimation technique	71
4.7.1	Technique 1: Adding white noise	72
4.7.2	Technique 2: 3-function model	72
4.7.3	Uncertainty of diffusion-length estimation	75
4.8	Evaluating fitting techniques	75
4.9	Discussion	79
4.10	Conclusion	80
5	VARYING REGIONAL $\delta^{18}\text{O}$ -TEMPERATURE RELATIONSHIP IN HIGH RES- OLUTION STABLE WATER ISOTOPES FROM EAST GREENLAND	84
5.1	Abstract	84
5.2	Introduction	85
5.3	The ice cores	86
5.4	Diffusion correction	88
5.5	Chronology	90
5.6	$\delta^{18}\text{O}$ variability on Renland	91
5.7	The temperature signature in $\delta^{18}\text{O}$	94
5.7.1	Correlation with instrumental temperature records	94
5.7.2	Correlation with the HIRHAM5 2 m temperature output	97
5.8	The North Atlantic Oscillation's imprint on $\delta^{18}\text{O}$	99
5.9	The impact of sea ice fluctuations on the stable water isotopes	100
5.9.1	Fram Strait sea ice export	100
5.9.2	Sea ice concentration and sea surface temperature	101
5.10	Discussion	104
5.11	Conclusion	105

III	FUTURE WORK AND CONCLUSION	110
6	A DIFFUSION-BASED RECONSTRUCTION OF WAIS DIVIDE TEMPERATURE	112
6.1	Estimating the firn diffusion	113
6.2	Evaluating the temperature reconstruction	115
6.2.1	The period 12-19 ka	118
6.2.2	The cold glacial	120
6.2.3	Borehole temperature reconstruction	121
6.3	Pressure-independent temperature reconstructions	123
6.4	Discussion and outlook: What should be examined in the future	124
7	CONCLUSION	129
IV	APPENDICES	131
A	MOLECULAR DIFFUSION OF STABLE WATER ISOTOPES IN POLAR FIRN AS A PROXY FOR PAST TEMPERATURES	133
A.1	Firn diffusivity	133
A.2	The firn temperature profile	134
A.3	Ice diffusivity	135
A.4	Generating synthetic data	136
A.5	Discrete sampling diffusion	137
A.6	Figures	140
A.6.1	NEEM - late Holocene	140
A.6.2	NEEM - CFA data section	141
A.6.3	NEEM - discrete data section	143
A.6.4	NGRIP - late Holocene	144
A.6.5	NGRIP - early Holocene core 1	145
A.6.6	NGRIP - early Holocene core 2	146
A.6.7	GRIP - late Holocene	147
A.6.8	GRIP - mid Holocene	148
A.6.9	GRIP - early Holocene	149
A.6.10	EDML	151
A.6.11	Dome C	152
A.6.12	Dome Fuji	153
A.6.13	WAIS Divide	154
B	VARYING REGIONAL $\delta^{18}\text{O}$ -TEMPERATURE RELATIONSHIP IN HIGH RESOLUTION STABLE WATER ISOTOPES FROM EAST GREENLAND	157

B.1 Firm diffusivity	157
B.2 Significance analysis	158
B.3 Figures	159

Part I

MOTIVATION AND BACKGROUND

INTRODUCTION AND OUTLINE

This PhD thesis investigates to what extent climate variability can be reconstructed based on various temperature proxies. In paleoclimatology, a proxy often describes the preserved characteristics of past meteorological conditions such as temperature, humidity or the accumulation rate at a given site. Proxies are used as a substitute for direct measurements which remain unrecorded far back in time and they are accessible through climate archives such as tree rings, corals, speleothems, lake/ocean sediment cores and ice cores. A common measurement conducted on these climate archives is of the stable water isotopes $\delta^{18}\text{O}$ and δD which often are used as a proxy for the hydrological cycle.

This thesis utilizes ice cores from Greenland and Antarctica to analyze how variability in $\delta^{18}\text{O}$ and δD can be used as a temperature proxy. The ice caps on Greenland and Antarctica represent respectively up to $\sim 3\text{ km}$ and $\sim 4.5\text{ km}$ thick data archives of past precipitation and past atmospheric composition (where the latter has been encapsulated in air bubbles). This results in ice sheets being the highest resolution record of past climate variability. This information can be acquired by drilling ice cores. Several expeditions have been conducted and the spatial coverage of some of the large drilling campaigns are shown in Fig. 1.1. Currently, Greenland ice cores are covering the past 127,500 years while Antarctic ice cores cover up to the last 800,000 years (EPICA members 2004; NEEM members, 2013). These climate records reveal a unique insight into past temperature variability. Figure 1.2 shows the $\delta^{18}\text{O}$ variability recorded in three ice cores from Greenland. As the $\delta^{18}\text{O}$ signal qualitatively is a measure of past temperatures, it illustrates that the past 127,500 years consisted of two warm periods (interglacials) and one long cold period (glacial). On Greenland, the glacial period was characterized by up to 25°C colder temperatures than the current interglacial (the Holocene period which began $\sim 11,700$ years ago) (Dahl-Jensen et al., 1998). The $\delta^{18}\text{O}$ series indicate that the Holocene period did not experience any long-term high frequency temperature variability and it is often referred to as a stable period within the ice coring community. Contrary to the Holocene, the glacial period was controlled by several abrupt climate transitions reflected by increasing temperatures of up to $8 - 16^\circ\text{C}$ within a few decades followed by a gradual cooling

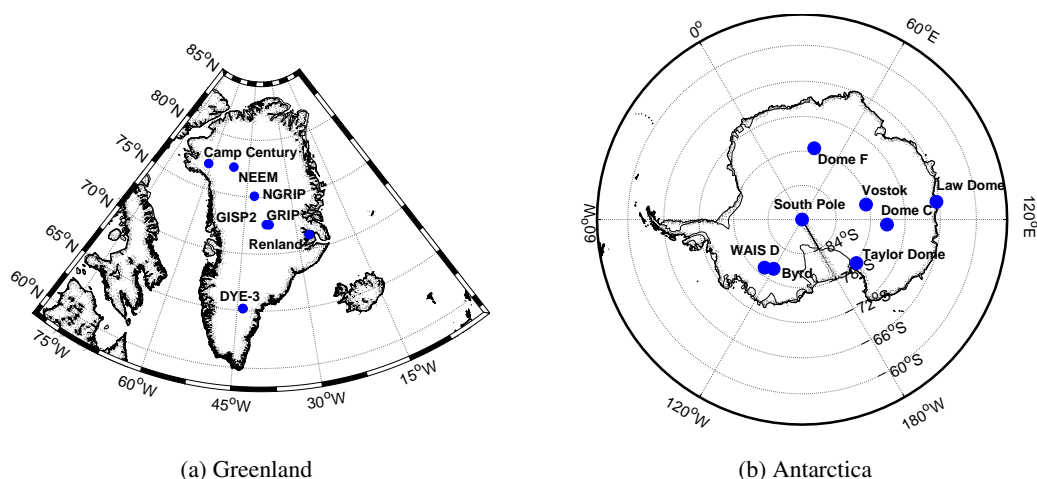


Figure 1.1. Locations of some drill sites located on Greenland and Antarctica.

(Severinghaus and Brook, 1999; Lang et al., 1999; Landais et al., 2004b; Landais et al., 2004a). These sudden changes are called Dansgaard-Oeschger events (DO events) (Dansgaard et al., 1993), and 25 main events have been identified in ice cores from Greenland (Rasmussen et al., 2014). In present day, a proper understanding of the trigger mechanism behind the DO events is considered a holy grail within paleoclimatology. It has been hypothesized that it could result from an overturning of the Atlantic Meridional Circulation due to an influx of freshwater (Bond et al., 1999; Clark et al., 2002) while other studies have found that it connects well with changes in the ice sheet thickness (Zhang et al., 2014) or with the global ice volume (Lohmann and Ditlevsen, 2018). As the majority of DO event related research is based on the interpretation of $\delta^{18}\text{O}$ as a proxy for past temperature, it is crucial to have a fundamental understanding of what paleoclimatic information that can be extracted from the $\delta^{18}\text{O}$ signal stored in ice cores. Accurate estimates of the magnitude and frequency of past temperature changes have important implications for how we interpret Earth's natural climate variability. Especially as Earth currently experiences a rapid temperature increase caused by the anthropological emission of greenhouse gases (e.g. CO_2 , CH_4 , N_2O) (IPCC/Field et al., 2014). Thus, it is a paleoclimatic tool necessary to improve projections of future climate.

The focus of this PhD thesis is to evaluate what paleoclimatic interpretations can be made from the stable water isotopes $\delta^{18}\text{O}$ and δD of polar ice cores. The main part of the thesis comprises of two published papers and one submitted manuscript currently in review. While each paper treats the features of isotopic variability from a different perspective, all rely on the theory of diffusion processes and how it attenuates the $\delta^{18}\text{O}$ oscillations in the ice. Hence, there will inevitably be some repetitions throughout this thesis as all the papers and appendices are provided in full length in order to ensure consistency with the peer-reviewed publications. The

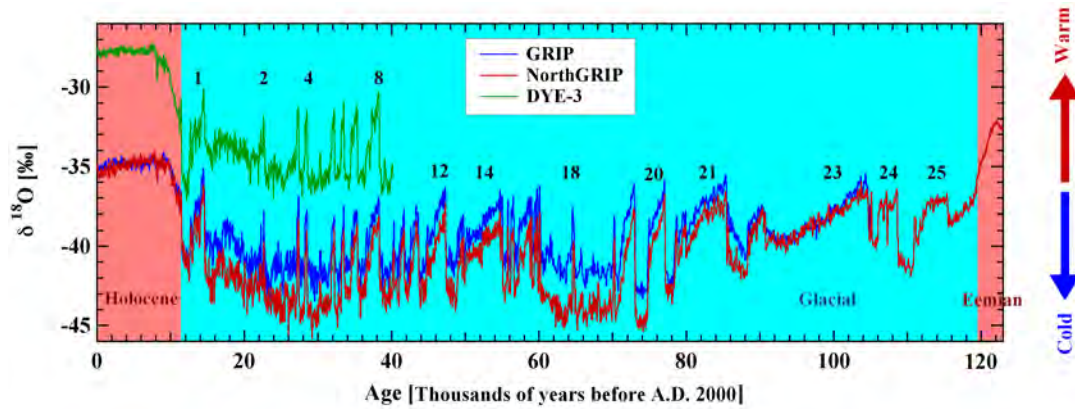


Figure 1.2. $\delta^{18}\text{O}$ measurements on three ice cores from Greenland showing the two interglacial and glacial periods. Numbers mark the DO events. Picture adopted from http://www.iceandclimate.nbi.ku.dk/research/climatechange/glacial_interglacial/the_glacial_instability/

thesis is structured such that it begins by introducing the scientific background theory relevant to understand why ice core $\delta^{18}\text{O}$ and δD can be utilized as a temperature proxy (Chapter 2). It then present the three papers in the chronological order of which the work was conducted.

Chapter 3 presents the paper Holme et al., 2018a which reviews the accuracy and precision of all existing techniques that use the diffusion of $\delta^{18}\text{O}$ and δD to reconstruct past temperature. This is done by utilizing all methods on both synthetic data as well as $\delta^{18}\text{O}$ and δD measurements from Greenlandic and Antarctic ice cores. Based on the results, the paper compares the performance of a technique that employ only the diffusion of either $\delta^{18}\text{O}$ or δD (single diffusion) with methods that utilize the differential diffusion signal of both $\delta^{18}\text{O}$ and δD (dual diffusion). Thus, the work examines how uncertainties from the firn diffusion model and from the data affect the different diffusion-based temperature reconstructions techniques. Appendix A contains all the additional theory and figures used in the published work.

Chapter 4 contains the paper Kahle et al., 2018 which constitutes the work I did in collaboration with the first author Emma C. Kahle. The study addresses and discusses newly discovered power spectral features of stable water isotopes measured on continuous flow analysis systems. The work is based on the water isotope measurements of two Antarctic ice cores: the WAIS Divide (West Antarctic Ice Sheet) ice core and SPICEcore (South Pole Ice Core project). The study suggests new routines to accurately and efficiently estimate the diffusion length of high resolution stable water isotopes. The proposed methods improve the understanding of power spectral $\delta^{18}\text{O}$ and δD data and the study has implications for the diffusion-based temperature reconstruction techniques described in Chapter 3 as continuous flow analysis measurements are becoming more common within the community.

Chapter 5 presents the submitted manuscript Holme et al., 2018b, in review which examines the $\delta^{18}\text{O}$ variability of three ice cores drilled on the Renland peninsula, East Greenland. The objective is to examine how well the isotopic signal correlates with the regional temperature variation as Renland's isotope hydrology could be connected with the fluctuating sea ice cover. The work has implications for studies that perform regression-based temperature reconstructions of $\delta^{18}\text{O}$ from instrumental temperature records. In addition to the scientific analysis and writing, I assisted in measuring the $\delta^{18}\text{O}$, δD data (the RECAP core) on a continuous flow analysis system in the beginning of this PhD (fall of 2015). Appendix B constitutes of the accompanying appendices to the submitted work.

Chapter 6 serves as an outlook of the thesis. It shows how a technique outlined in Holme et al., 2018a can be utilized on a high resolution diffusion length profile presented in Kahle et al., 2018. Thus, it provides a diffusion-based temperature reconstruction for WAIS Divide and it discusses the implications of the results.

Chapter 7 summarizes the combined conclusion of all the work conducted in this PhD thesis.

Co-author agreements for the three presented papers are submitted electronically together with this dissertation. The thesis includes separate bibliographies for each chapter as it is a synopsis of papers. Thus, there will inevitably exist some overlapping references.

REFERENCES

- Bond, G. C., W. Showers, M. Elliot, M. Evans, R. Lotti, I. Hajdas, G. Bonani, and S. J. Johnsen (1999). "The North Atlantic's 1-2 kyr Climate Rhythm' Relation to Heinrich Events, Dansgaard/Oeschger Cycles and the Little Ice Age". In: *Geophysical Monograph* 112, pp. 35–68.
- Clark, P. U., N. G. Pisias, T. F. Stocker, and A. J. Weaver (2002). "The role of the thermohaline circulation in abrupt climate change". In: *Nature* 415, pp. 863–869.
- Dahl-Jensen, D., K. Mosegaard, N. Gundestrup, G. D Clow, S. J. Johnsen, A. W. Hansen, and N. Balling (1998). "Past temperatures directly from the Greenland Ice Sheet". In: *Science* 282.5387, pp. 268–271.
- Dansgaard, W. et al. (1993). "Evidence for general instability of past climate from a 250-kyr ice-core record". In: *Nature* 364, pp. 218–220.
- EPICA members/Laurent, A., C. Barbante, P. R. F. Barnes, J. M. Barnola, M. Bigler, E. Castellano, O. Cattani, J. Chappellaz, D. Dahl-Jensen, B. Delmonte, et al. (2004). "Eight glacial cycles from an Antarctic ice core". In: *Nature* 429, pp. 623–628.

- Holme, C., V. Gkinis, M. Lanzky, V. Morris, M. Olesen, A. Thayer, B. H. Vaughn, and B. M. Vinther (2018b, in review). “Varying regional $\delta^{18}\text{O}$ –temperature relationship in high resolution stable water isotopes from East Greenland”. In: *review: Climate of the Past Discussions*. URL: <https://doi.org/10.5194/cp-2018-169>.
- Holme, C., V. Gkinis, and B. M. Vinther (2018a). “Molecular diffusion of stable water isotopes in polar firn as a proxy for past temperatures”. In: *Geochemica et Cosmochimica Acta* 225, pp. 128–145.
- IPCC/Field, B. et al. (2014). “Climate Change 2014: Impacts, Adaptation and Vulnerability. Part A: Global and Sectoral Aspects. Contribution of the Working Group II to the Fifth Assessment Report of the Intergovernmental Panel on Climate Change”. In: *Technical Report*.
- Kahle, E. C., C. Holme, T. R. Jones, V. Gkinis, and E. J. Steig (2018). “A generalized approach to estimating diffusion length of stable water isotopes from ice–core data”. In: *Journal of Geophysical Research: Earth Surface* 123, pp. 2377–2391.
- Landais, A., J. M. Barnola, V. Masson-Delmotte, J. Jouzel, J. Chappellaz, N. Caillon, C. Huber, M. Leuenberger, and S. J. Johnsen (2004a). “A continuous record of temperature evolution over a whole sequence of Dansgaard–Oeschger during Marine Isotope Stage 4 (76 to 62 kyr BP)”. In: *Geophysical Research Letters* 31 (L22211), pp. 221–232.
- Landais, A., N. Caillon, C. Goujon, A. Grachev, J. M. Barnola, J. Chappellaz, J. Jouzel, V. Masson-Delmotte, and M. Leuenberger (2004b). “Quantification of rapid temperature change during DO event 12 and phasing with methane inferred from air isotopic measurements”. In: *Earth and Planetary Science Letters* 225, pp. 221–232.
- Lang, C., M. Leuenberger, J. Schwander, and S. J. Johnsen (1999). “ 16°C Rapid Temperature Variation in Central Greenland 70,000 Years Ago”. In: *Science* 286 (5441), pp. 934–937.
- Lohmann, J. and P. D. Ditlevsen (2018). “Random and externally controlled occurrences of Dansgaard–Oeschger events”. In: *Climate of the Past* 14, pp. 609–617.
- NEEM members/Dahl-Jensen, D., M.R. Albert, A. Aldahan, N. Azuma, D. Balslev-Clausen, M. Baumgartner, A-M. Berggren, M. Bigler, T. Binder, T. Blunier, et al. (2013). “Eemian interglacial reconstructed from a Greenland folded ice core”. In: *Nature* 493.7433, p. 489.
- Rasmussen, S. O., M. Bigler, S. P. Blockley, T. Blunier, S. L. Buchardt, H. B. Clausen, I. Cvijanovic, D. Dahl-Jensen, S. J. Johnsen, H. Fischer, et al. (2014). “A stratigraphic framework for abrupt climatic changes during the Last Glacial period based on three synchronized Greenland ice-core records: refining and extending the INTIMATE event stratigraphy”. In: *Quaternary Science Reviews* 106, pp. 14–28.

Severinghaus, J. P. and E. J. Brook (1999). “Abrupt Climate Change at the End of the Last Glacial Period Inferred from Trapped Air in Polar Ice”. In: *Science* 286 (5441), pp. 930–934.

Zhang, X., G. Lohmann, G. Knorr, and C. Purcell (2014). “Abrupt glacial climate shifts controlled by ice sheet changes”. In: *Nature* 512, pp. 290–294.

SCIENTIFIC BACKGROUND

This chapter describes the relevant background theory behind the papers in Chapters 3, 4 and 5.

2.1 STABLE WATER ISOTOPES

A water molecule is in common speech expressed as H_2O but water molecules exist in various forms with different masses in nature. The variants of a chemical element such as hydrogen (H) or oxygen (O) is called an isotope. An isotope contains the same number of protons in each atom but they differ in the amount of neutrons. The three known stable oxygen isotopes are ^{16}O [99.759%], ^{17}O [0.037%] and ^{18}O [0.204%], where the integer denotes the mass number which is the number of protons and neutrons in the nucleus, and the brackets mark the isotope's abundance in nature (Mook, 2000). Similarly, the two stable hydrogen isotopes are ^1H [99.985%] and ^2H [0.0155%] where the latter often is referred to as deuterium (D). These oxygen and hydrogen isotopes combine into different isotopologues such as H_2^{16}O , H_2^{17}O , H_2^{18}O and HD^{16}O . An example of water molecules with different oxygen isotopes is shown in Fig. 2.1.

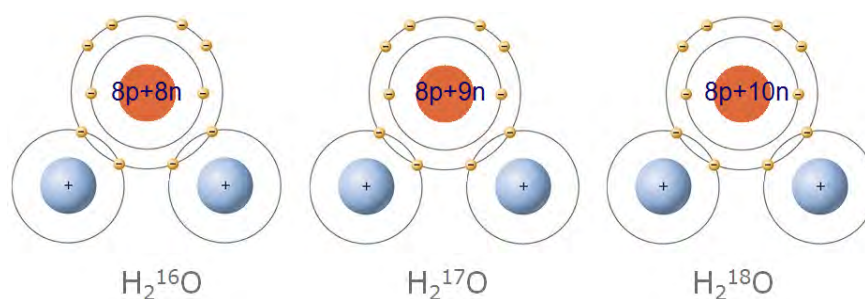


Figure 2.1. Three different isotopologues containing different oxygen isotopes but the same hydrogen isotope. p refers to protons and n refers to neutrons. Picture adopted from http://www.iceandclimate.nbi.ku.dk/research/past_atmos/past_temperature_moisture/

Apart from the fact that water isotopologues occur in various abundances in nature, they have different masses. The abundant H_2^{16}O is light while the rare H_2^{18}O and HD^{16}O are heavy. The difference in mass gives them different physical properties. This is seen from the kinetic energy of a molecule which is determined by temperature (T):

$$kT = \frac{1}{2}m\bar{v}^2, \quad (1)$$

where k is the Boltzmann constant, m is the molecular mass and \bar{v} is the average molecular velocity. As the temperature is the same for the molecules, they have equal $1/2m\bar{v}^2$. Thus, the heavier isotopic molecules have lower diffusion velocities and smaller collision frequencies than the light and abundant H_2^{16}O . Moreover, all particles have three modes of motion: translation (movement of the molecule as a whole), vibration of the molecule's atoms with respect to each other and rotation of the molecule around a specific molecular axis. This results in the heavier molecules having higher binding energies. Consequently, H_2^{18}O and HD^{16}O have lower vapor pressures than H_2^{16}O which causes the lighter isotopes (H and ^{16}O) to be preferentially fractionated into the water vapor phase. This results in two relevant properties traceable in the hydrological cycle: (1) The heavy H_2^{18}O and HD^{16}O have a lower tendency toward evaporation and (2) a higher tendency toward condensation than the light H_2^{16}O (Mook, 2000).

Isotope hydrology is typically expressed through the δ -notation (in ‰), which is defined as the relation between the isotopic abundance ratio (R) with a reference value ($R_{reference}$) and its deviation from unity:

$$\delta = \left(\frac{R}{R_{reference}} - 1 \right) \cdot 1000\text{‰}, \quad (2)$$

where the isotopic abundance ratio is:

$$R = \frac{^{18}\text{O}}{^{16}\text{O}}, \quad R = \frac{^{17}\text{O}}{^{16}\text{O}}, \quad R = \frac{\text{D}}{\text{H}}. \quad (3)$$

The $R_{reference}$ value is based on VSMOW (Vienna Standard Mean Ocean Water). Measurements regarding the amount of ^{18}O , ^{17}O and D isotopes in a sample are thus expressed through $\delta^{18}\text{O}$, $\delta^{17}\text{O}$ and δD .

2.2 ICE CORES AS A CLIMATE ARCHIVE

In present time, water deposited as glacier ice covers around 10% of the Earth's land surface (Cuffey and Paterson, 2010). The majority of this ice coverage is located on the great ice sheets on Greenland and Antarctica. This ice has a distinct isotopic signature that contains in-

formation about its journey from the evaporation site in the subtropics to its condensation site (Dansgaard, 1954; Dansgaard, 1964). Figure 2.2 illustrates how a water mass with an initial δD value of 0‰ is transported from the subtropical ocean to the ice cap. During this journey, the water in the air parcel gets increasingly depleted in heavy isotopes with distance. This is because the heavy $H_2^{18}O$ and $HD^{16}O$ have a lower tendency toward evaporation, thus causing the evaporated water to be more depleted in heavy isotopes which results in a lower and negative δD value. The air parcel is then moved northward where it is exposed to a gradual cooling. Water will then condense out of the air mass along the poleward transport as the amount of moisture it is able to contain is exponentially related to temperature (the Clausius-Clapeyron relation). As the heavy water molecules have a higher tendency toward condensation than the light molecules, the decrease in δ will continue until the water is deposited as snow on the ice sheet. This distillation process leaves a temperature signature imprinted in the stable water isotopes of the snow. For instance, the winter season experiences cold temperatures which forces the air parcel to rain out more water than during the warm summer season. Thus, low temperatures result in low δ values and high temperatures result in high δ values. Assuming that the Greenland accumulation is deposited uniformly over the year, this phenomena manifests as annual oscillations in δ with ice sheet depth. As the $\delta^{18}O$ and δD have been found to correlate with the temperature at the time of condensation (Dansgaard, 1954; Dansgaard, 1964), ice sheets function as a climate archive. Thus, it is possible to access past climate variability by drilling ice cores in polar regions.

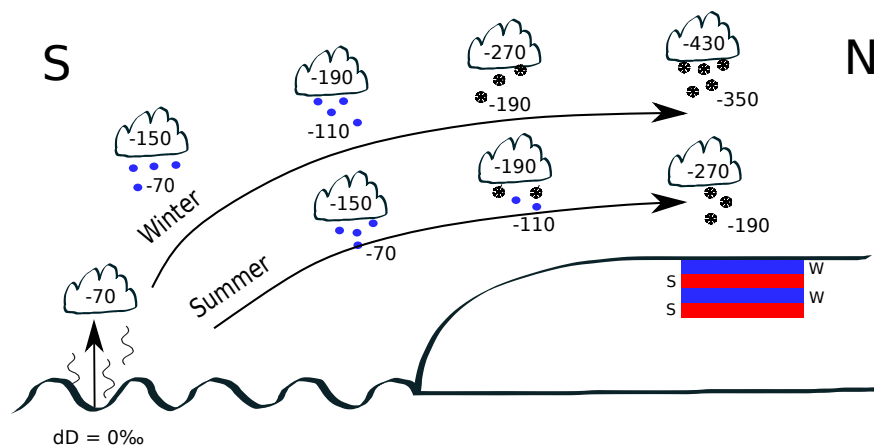


Figure 2.2. The transport of a water mass from the subtropics to its deposition on Greenland.

2.3 POST-DEPOSITIONAL PROCESSES

From the snow is deposited on the ice sheet to the time it is acquired as an ice core, several post-depositional processes have affected the layering and isotopic composition of the snow. Some of these processes are restricted to the surface such as wind scattering of the snow while others occur during the transformation of snow to glacier ice. Thus, in order to accurately interpret the measured ice core $\delta^{18}\text{O}$ signal, it is crucial to have a fundamental understanding of how such processes affect the layered isotope variability. Short descriptions of how surface effects, densification, diffusion and thinning influence the precipitated $\delta^{18}\text{O}$ signal are therefore provided below.

2.3.1 *Surface effects*

After the snow has been deposited on the ice sheet, it is directly in contact with the overlying atmosphere. Thus, the snow is exposed to wind erosion which causes snow drifting. This can redistribute the deposited snow which can create Sastrugi (surface undulations of the snow). Such snow scattering influences how the isotopic composition is layered and it manifests as blue deposition noise in the power spectral density of the $\delta^{18}\text{O}$ signal (Fisher et al., 1985) (increasing amplitude towards higher frequencies). This blue spectral characteristic is however quickly diffused into a red power spectral signature (increasing amplitude towards lower frequencies) due to firn diffusion which acts during the compression of snow to ice (Fisher et al., 1985; Johnsen et al., 1997). Densification and diffusion processes are outlined in Sec. 2.3.2 and 2.3.3.

Besides the wind-induced deposition noise, snow located on the surface is also exposed to sublimation. Sublimation is the direct phase transition from solid phase to vapor phase, which implies that a deposited snow layer can be reduced (mass loss) despite cold temperatures below freezing point. This mass loss has however only been found to play a minor role on changes in isotopic composition of surface snow (Neumann and Waddington, 2004; Steen-Larsen et al., 2014).

2.3.2 *Densification*

The compaction of snow is called densification and it describes how firn (snow that survived a season) with an initial density of $\rho_o = 330 - 410 \text{ kg/m}^3$ is compressed into glacier ice with a density of $\rho_i = 917 \text{ kg/m}^3$. Commonly, this process is divided into three zones that are sepa-

rated by the critical density ($\rho_c = 550 \text{ kg/m}^3$) and the bubble close-off density ($\rho_{pc} \sim 800 - 830 \text{ kg/m}^3$) (Herron and Langway, 1980). In zone 1 ($\rho < \rho_c$), firn becomes denser due to grain-growth and a packing/rearrangement of the snow grains (Alley, 1987). In zone 2 ($\rho_c < \rho < \rho_{pc}$), density is increased through sintering (grain deformation at the interface between grains) while density is increased through compression of bubbles in zone 3 ($\rho_{pc} < \rho < \rho_i$). Several studies have examined the densification rate of snow (e.g. Herron and Langway, 1980; Arnaud et al., 2000; Arthern et al., 2010; Freitag et al., 2013). Herron and Langway, 1980 defined an empirical model based on a subset of equations calibrated to density measurements, the Arnaud et al., 2000 model is based on the physics of grain sliding and plastic deformation, Arthern et al., 2010 presents a semi-empirical model based on normal grain growth and grain-size dependent creep of material around pores while Freitag et al., 2013 models densification by accounting for the effect of impurities. Throughout this PhD thesis, the Herron and Langway, 1980 parameterization is used to simulate the densification rate ($d\rho/dz$). The model is simple and it depends on surface temperature (T) and overburden pressure where the latter is parameterized through accumulation rate (A) and surface density:

$$\frac{d\rho}{dz} = \begin{cases} \frac{k_0 r}{\rho_i} \rho (\rho_i - \rho) & \text{for } \rho \leq \rho_c \\ \frac{k_1 r A^{-0.5}}{\rho_i} \rho (\rho_i - \rho) & \text{for } \rho > \rho_c \end{cases} \quad (4)$$

where $r = \rho_i / \rho_{water}$ and k_0, k_1 are temperature dependent Arrhenius-type rate coefficients:

$$k_0 = f_0 \cdot 11 \exp \left[-\frac{10160}{RT} \right], \quad (5a)$$

$$k_1 = f_1 \cdot 575 \exp \left[-\frac{21400}{RT} \right]. \quad (5b)$$

Here R is the molar gas constant and f_0 and f_1 are two adjustable parameters not included in the original approach by Herron and Langway, 1980. Following the approach of Johnsen et al., 2000, the two parameters f_0 and f_1 are fitting parameters that are estimated by minimizing the least squares between the model and the measured density profile at the drill site. This facilitates an optimal extrapolation of lower or higher densities than what is measured. Figure 2.3 shows the measured and modeled density at NEEM (map in Fig. 1.1). Based on this, it is evident that the fitted Herron and Langway, 1980 model can match the measured density profile well.

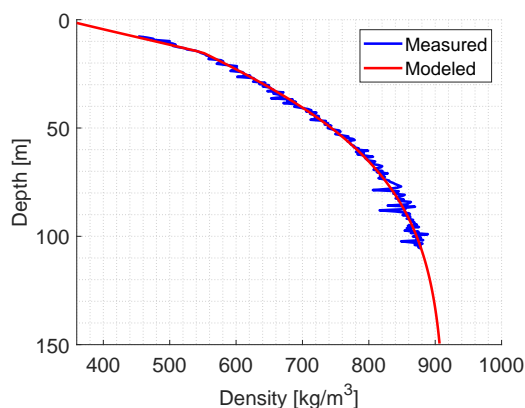


Figure 2.3. Measured density profile from NEEM (blue) and a modeled profile using a Herron and Langway, 1980 model (red). $A = 0.22$ mice/yr, $T = -29^\circ\text{C}$, $\rho_o = 340\text{kg/m}^3$, $f_0 = 0.909$ and $f_1 = 0.975$.

2.3.3 Diffusion

During densification, vapor in the open snow pores are interconnected. This causes a molecular exchange which alters the original isotopic composition in the snow. Diffusion of water isotopes are divided into two processes (1) firn diffusion which smoothens the signal until the pore close-off and (2) ice diffusion which starts dominating when ice becomes warmer (near bedrock) and older. As Chapter 3 provides descriptive and mathematical explanations of what drives the diffusion of water isotopes, nothing substantial is added here besides a short example of how firn diffusion alters the isotopic composition with depth.

Figure 2.4 shows the $\delta^{18}\text{O}$ signal with depth for the NEGIS firn core ($75^\circ 37.61' \text{N}$; $35^\circ 56.49' \text{W}$) and an ice core from Renland ($71^\circ 18' 17'' \text{N}$; $26^\circ 43' 24'' \text{W}$). From the figure, it is evident that the annual $\delta^{18}\text{O}$ oscillations already are obliterated within the top 7-9 meters of the NEGIS firn core while they persist in the Renland ice core. The varying impact of firn diffusion on the annual $\delta^{18}\text{O}$ signal is a consequence of the two sites' difference in annual accumulation rate (A ; which mitigates diffusion) and mean surface temperature (T ; which enhances diffusion) (NEGIS: $T = -28^\circ\text{C}$, $A = 0.11$ m ice/year; Renland: $T = -18^\circ\text{C}$, $A = 0.47$ m ice/year; (Johnsen et al., 1992; Vallelonga et al., 2014)). The relation between the two opposed forcings and their impact on firn diffusion is illustrated in Fig. 3.2 (p. 26). In general, wavelengths shorter than 0.20 m become heavily attenuated (Fig. 3.4 on p. 31 and Johnsen et al., 2000). Thus, annual layers with a size above this quantity have preserved annual $\delta^{18}\text{O}$ oscillations. This explains why the annual $\delta^{18}\text{O}$ oscillations remain largely unaffected by diffusion for Renland and why the NEGIS $\delta^{18}\text{O}$ variability quickly becomes smoothed.

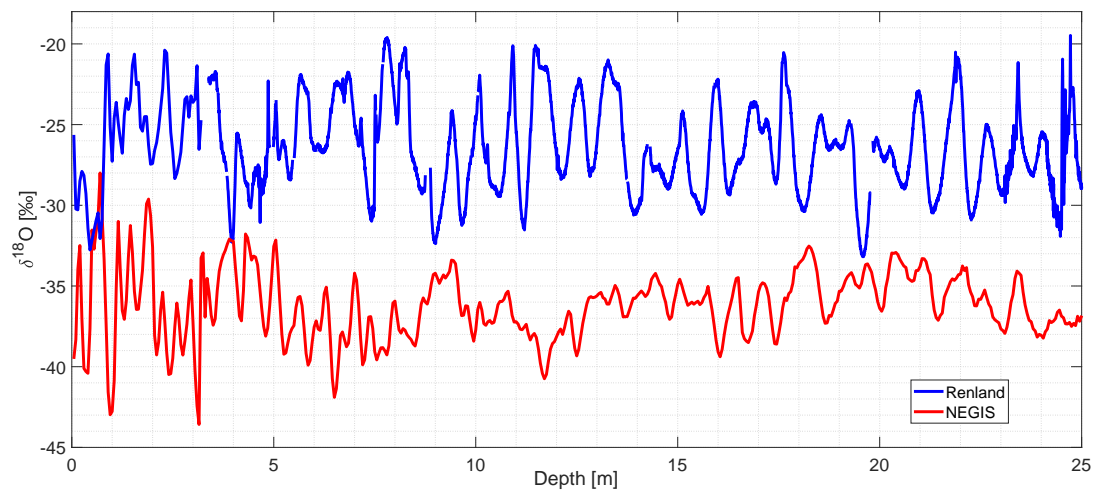


Figure 2.4. $\delta^{18}\text{O}$ variability with depth for the Renland 2015 ice core (blue) and NEGIS firn core (red).

2.3.4 Thinning

After the snow has been transformed into solid ice, the annual layers continue to thin as they are advected toward the bedrock. This results from the ice flow which stretches the layers horizontally and the continuous deposition of younger ice on the surface which steadily increases the overburden pressure applied on a layer. The vertical compression of annual layers with depth can be described by the thinning function. The thinning function depends on the ice flow and its accurate estimate is imperative for the interpretation of accumulation rate and diffusion of water isotopes (Gkinis et al., 2014). For instance, the amount of thinning the layers experienced needs to be known if the past accumulation history is to be reconstructed from the annual layer thickness chronology. Moreover, the thinning rate influences the magnitude of solid ice diffusion a layer endures as it reduces the annual layer thickness while it increases the vertical isotopic gradient (Hammer et al., 1978) (Sec. 3.3.2). Furthermore, it has a direct influence on the reconstruction of past firn diffusion (and temperature) from stable water isotope data (Sec. 3.4.1) and inaccurate estimates will lead to biases in the temperature or accumulation rate reconstructions (Gkinis et al., 2014).

Throughout this dissertation, previously published thinning profiles are used. The thinning rate functions are commonly modeled using the Dansgaard and Johnsen, 1969 model (D-J model - some studies refer to it as the kink model) which computes the vertical ice flow velocity with depth ($w(z)$). The D-J model is characterized by a separation of the horizontal velocity ($u(z)$) into two domains: (1) one with a constant velocity for $h < z \leq H$ and (2) one with a linearly decreasing velocity toward bedrock $0 \leq z \leq h$ (0 is the bedrock and H is surface) -

illustration in Fig. 2.5. The transition between these two zones is called the kink height (h). From the continuity equation, it is then possible to derive an expression for $w(z)$ where the accumulation rate (A), basal melt rate ($-w_0$) and fraction of bottom sliding (f_b) are included (Grinsted and Dahl-Jensen, 2002):

$$w(z) = \begin{cases} w_0 - \frac{Rh(f_b+1)}{2} - R(z-H) & \text{for } h \leq z \leq H \\ w_0 - Rz \left(f_b + (1-f_b) \frac{z}{2h} \right) & \text{for } 0 \leq z \leq h \end{cases} \quad (6)$$

where

$$R = \frac{\partial u_{surf}}{\partial x} = \frac{A + w_0 - (dH/dt)}{H - (1-f_b)h/2} \quad (7)$$

Here $\partial u_{surf}/\partial x$ is the horizontal change in surface velocity and dH/dt is the change in ice sheet thickness with time (t). From Eq. 6, a calculation of $w(z)$ can be made if the past accumulation rate, basal melt, sliding, ice sheet thickness and kink height are known.

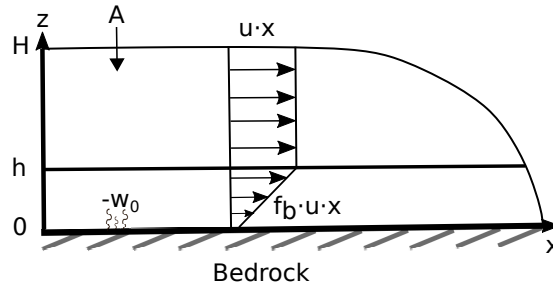


Figure 2.5. A Dansgaard and Johnsen, 1969 model which shows how the horizontal velocity first is uniform from the ice sheet surface (H) down to the kink height (h), after which it decreases linearly down toward the bedrock.

The total thinning (\mathcal{S}) of the annual layer (λ) at depth z can be expressed through the strain rate ($\dot{\epsilon}_z(z) = d\lambda/(\lambda(z)dz)$):

$$\mathcal{S}(z) = \exp\left(\int_0^z \dot{\epsilon}_z(z') dz'\right) = \exp\left(\int_0^z d\lambda/\lambda(z')\right) = \frac{\lambda(z)}{\lambda_0} \quad (8)$$

where $\lambda(z)$ and λ_0 are the thickness of an annual layer at respectively depth z and at the surface. As the annual layer thickness can be expressed through the vertical velocity ($\lambda = w \cdot \tau$ where $\tau = 1$ yr), the thinning function can be reduced to:

$$\mathcal{S}(z) = \frac{w(z)}{A_0} \quad (9)$$

where A_0 is the initial accumulation rate in meters of ice equivalent at the surface. Thus, from Eq. 6 and 9, a thinning rate profile with depth can be calculated.

While the thinning function can be modeled if past accumulation rate and the other ice flow related parameters are known, the D-J model is often/rather inverted using the annual layer thickness chronology and/or borehole temperature measurements as constraints (Grinsted and Dahl-Jensen, 2002; Rasmussen et al., 2013; Buizert et al., 2015). Thus, it is possible to make a Monte Carlo–tuned simulation where the D-J model is inverted such that depth-age relations from the model and measurements are minimized. This ensures that the depth-age relation from the ice flow model matches the annual layers and more importantly the precisely dated volcanic reference markers.

REFERENCES

- Alley, R. B. (1987). “Firn densification by grain-boundary sliding: A first model”. In: *Journal de Physique* 48, pp. C249–C256.
- Arnaud, L., J. M. Barnola, and P. Duval (2000). *Physical modeling of the densification of snow/finn and ice the upper part of polar ice sheets*.
- Arthern, R. J., D. G. Vaughan, A. M. Rankin, R. Mulvaney, and E. R. Thomas (2010). “In situ measurements of Antarctic snow compaction compared with predictions of models”. In: *Journal of Geophysical Research: Earth Surface* 115 (F03011).
- Buizert, C. et al. (2015). “The WAIS Divide deep ice core WD2014 chronology – Part 1: Methane synchronization (68–31 ka BP) and the gas age–ice age difference”. In: *Climate of the Past* 11, pp. 153–173.
- Cuffey, K. M. and W. S. B. Paterson (2010). *The Physics of Glaciers*. 4th. Elsevier.
- Dansgaard, W. (1964). “Stable isotopes in precipitation”. In: *Tellus B* 16.4, pp. 436–468.
- Dansgaard, W. (1954). “The ^{18}O -abundance in fresh water”. In: *Geochimica et Cosmochimica Acta* 6.5–6, pp. 241–260.
- Dansgaard, W. and S. J. Johnsen (1969). “A Flow Model and a Time Scale for the Ice Core from Camp Century, Greenland”. In: *Journal of Glaciology* 8.53, pp. 215–223.
- Fisher, D. A., N. Reeh, and H. B. Clausen (1985). “Stratigraphic noise in time series derived from ice cores”. In: *Annals of Glaciology* 7, pp. 76–83.
- Freitag, J., S. Kipfstuhl, T. Laepple, and F. Wilhelms (2013). “Impurity-controlled densification: a new model for stratified polar firn”. In: *Journal of Glaciology* 59, pp. 1163–1169.
- Gkinis, V., S. B. Simonsen, S. L. Buchardt, J. W. C. White, and B. M. Vinther (2014). “Water isotope diffusion rates from the NorthGRIP ice core for the last 16,000 years - glaciological and paleoclimatic implications”. In: *Earth and Planetary Science Letters* 405.

- Grinsted, A. and D. Dahl-Jensen (2002). "A Monte Carlo-tuned model of the flow in the North-GRIP area". In: *Annals of Glaciology* 35, pp. 527–530. DOI: 10.3189/172756402781817130.
- Hammer, C. U., H. B. Clausen, W. Dansgaard, N. Gundestrup, S. J. Johnsen, and N. Reeh (1978). "Dating of Greenland ice cores by flow models, isotopes, volcanic debris, and continental dust". In: *Journal of Glaciology* 20.82, pp. 3–26.
- Herron, M. M. and C. C. Langway (1980). "Firn Densification: An Empirical Model". In: *Journal of Glaciology* 25.93.
- Johnsen, S. J., H. B. Clausen, K. M. Cuffey, G. Hoffmann, J. Schwander, and T. Creyts (2000). "Diffusion of stable isotopes in polar firn and ice: the isotope effect in firn diffusion". In: *Physics of Ice Core Records*, pp. 121–140.
- Johnsen, S. J., H. B. Clausen, W. Dansgaard, N. S. Gundestrup, M. Hansson, P. Jonsson, J. P. Steffensen, and A. E. Sveinbjornsdottir (1992). "A "deep" ice core from East Greenland". In: *Meddelelser om Groenland, Geoscience* 29, pp. 3–22.
- Johnsen, S. J. et al. (1997). "The $\delta^{18}\text{O}$ record along the Greenland Ice Core Project deep ice core and the problem of possible Eemian climatic instability". In: *Journal of Geophysical Research* 102, pp. 26397–26410.
- Mook, J. (2000). *Environmental Isotopes in the Hydrological Cycle Principles and Applications*. International Atomic Energy Agency.
- Neumann, T. A. and E.D. Waddington (2004). "Effects of firn ventilation on isotopic exchange". In: *Journal of Glaciology* 50, pp. 183–194.
- Rasmussen, S. O., P. M. Abbott, T. Blunier, A. J. Bourne, E. Brook, S. L. Buchardt, C. Buizert, J. Chappellaz, H. B. Clausen, E. Cook, et al. (2013). "A first chronology for the North Greenland Eemian Ice Drilling (NEEM) ice core". In: *Climate of the Past* 9.6, pp. 2713–2730.
- Steen-Larsen, H. C. et al. (2014). "What controls the isotopic composition of Greenland surface snow?" In: *Climate of the Past* 10 (1), pp. 377–392.
- Vallelonga, P., K. Christianson, R. B. Alley, S. Anandakrishnan, J. E. M. Christian, D. Dahl-Jensen, V. Gkinis, C. Holme, R. W. Jacobel, N. B. Karlsson, et al. (2014). "Initial results from geophysical surveys and shallow coring of the Northeast Greenland Ice Stream (NEGIS)". In: *The Cryosphere* 8.4, pp. 1275–1287.

Part II

PAPERS

MOLECULAR DIFFUSION OF STABLE WATER ISOTOPES IN POLAR FIRN AS A PROXY FOR PAST TEMPERATURES

The following chapter is a copy of the paper Holme et al. (2018a):

Holme, C., Gkinis, V. and B. M. Vinther (2018). Molecular diffusion of stable water isotopes in polar firn as a proxy for past temperatures. *Geochimica et Cosmochimica Acta*, 225, 128–145. DOI:10.1016/j.gca.2018.01.015

3.1 ABSTRACT

Polar precipitation archived in ice caps contains information on past temperature conditions. Such information can be retrieved by measuring the water isotopic signals of $\delta^{18}\text{O}$ and δD in ice cores. These signals have been attenuated during densification due to molecular diffusion in the firn column, where the magnitude of the diffusion is isotopologue specific and temperature dependent. By utilizing the differential diffusion signal, dual isotope measurements of $\delta^{18}\text{O}$ and δD enable multiple temperature reconstruction techniques. This study assesses how well six different methods can be used to reconstruct past surface temperatures from the diffusion-based temperature proxies. Two of the methods are based on the single diffusion lengths of $\delta^{18}\text{O}$ and δD , three of the methods employ the differential diffusion signal, while the last uses the ratio between the single diffusion lengths. All techniques are tested on synthetic data in order to evaluate their accuracy and precision. We perform a benchmark test to thirteen high resolution Holocene data sets from Greenland and Antarctica, which represent a broad range of mean annual surface temperatures and accumulation rates. Based on the benchmark test, we comment on the accuracy and precision of the methods. Both the benchmark test and the synthetic data test demonstrate that the most precise reconstructions are obtained when using the single isotope diffusion lengths, with precisions of approximately 1.0°C . In the benchmark test, the single isotope diffusion lengths are also found to reconstruct consistent

temperatures with a root-mean-square-deviation of 0.7°C. The techniques employing the differential diffusion signals are more uncertain, where the most precise method has a precision of 1.9°C. The diffusion length ratio method is the least precise with a precision of 13.7°C. The absolute temperature estimates from this method are also shown to be highly sensitive to the choice of fractionation factor parameterization.

3.2 INTRODUCTION

Polar precipitation stored for thousands of years in the ice caps of Greenland and Antarctica contains unique information on past climatic conditions. The isotopic composition of polar ice, commonly expressed through the δ notation has been used as a direct proxy of the relative depletion of a water vapor mass in its journey from the evaporation site to the place where condensation takes place (Epstein et al., 1951; Mook, 2000). Additionally, for modern times, the isotopic signal of present day shows a good correlation with the temperature of the cloud at the time of precipitation (Dansgaard, 1954; Dansgaard, 1964) and as a result it has been proposed and used as a proxy of past temperatures (Jouzel and Merlivat, 1984; Jouzel et al., 1997; Johnsen et al., 2001).

The use of the isotopic paleothermometer presents some notable limitations. The modern day linear relationship between $\delta^{18}\text{O}$ and temperature commonly referred to as the “spatial slope” may hold for present conditions, but studies based on borehole temperature reconstruction (Cuffey et al., 1994; Johnsen et al., 1995) as well as the thermal fractionation of the $\delta^{15}\text{N}$ signal in polar firn (Severinghaus et al., 1998; Severinghaus and Brook, 1999) have independently underlined the inaccuracy of the spatial isotope slope when it is extrapolated to past climatic conditions. Even though qualitatively the $\delta^{18}\text{O}$ signal comprises past temperature information, it fails to provide a quantitative picture on the magnitudes of past climatic changes.

Johnsen, 1977; Whillans and Grootes, 1985 and Johnsen et al., 2000 set the foundations for the quantitative description of the diffusive processes the water isotopic signal undergoes in the porous firn layer from the time of deposition until pore close-off. Even though the main purpose of Johnsen et al., 2000 was to investigate how to reconstruct the part of the signal that was attenuated during the diffusive processes, the authors make a reference to the possibility of using the assessment of the diffusive rates as a proxy for past firn temperatures.

The temperature reconstruction method based on isotope firn diffusion requires data of high resolution. Moreover, if one would like to look into the differential diffusion signal, data sets of both $\delta^{18}\text{O}$ and δD are required. Such data sets have until recently not been easy to obtain especially due to the challenging nature of the δD analysis (Bigeleisen et al., 1952; Vaughn

et al., 1998). With the advent of present commercial high-accuracy, high-precision Infra-Red spectrometers (Crosson, 2008; Brand et al., 2009), simultaneous measurements of $\delta^{18}\text{O}$ and δD have become easier to obtain. Coupling of these instruments to Continuous Flow Analysis systems (Gkinis et al., 2011; Maselli et al., 2013; Emanuelsson et al., 2015; Jones et al., 2017) can also result in measurements of ultra-high resolution, a necessary condition for accurate temperature reconstructions based on water isotope diffusion.

A number of existing works have presented past firn temperature reconstructions based on water isotope diffusion. Simonsen et al., 2011 and Gkinis et al., 2014 used high resolution isotopic datasets from the NorthGRIP ice core (NGRIP members, 2004). The first study makes use of the differential diffusion signal, utilizing spectral estimates of high-resolution dual $\delta^{18}\text{O}$ and δD datasets covering the GS-1 and GI-1 periods in the NorthGRIP ice core (Rasmussen et al., 2014). The second study presents a combined temperature and accumulation history of the past 16,000 years based on the power spectral density (PSD hereafter) signals of high resolution $\delta^{18}\text{O}$ measurements of the NorthGRIP ice core. More recently, Wel et al., 2015 introduced a slightly different approach for reconstructing the differential diffusion signal and testing it on dual $\delta^{18}\text{O}$, δD high resolution data from the EDML ice core (Oerter et al., 2004). By artificially forward-diffusing the δD signal the authors estimate differential diffusion rates by maximizing the correlation between the $\delta^{18}\text{O}$ and δD signal. In this work we attempt to test the various approaches in utilizing the temperature reconstruction technique.

We use synthetic, as well as real ice core data sets that represent Holocene conditions from a variety of drilling sites on Greenland and Antarctica. Our objective is to use data sections that originate from parts of the core as close to present day as possible. By doing this we aim to minimize possible uncertainties and biases in the ice flow thinning adjustment that is required for temperature interpretation of the diffusion rate estimates. Such a bias has been shown to exist for the NorthGRIP ice core (Gkinis et al., 2014), most likely due to the Dansgaard and Johnsen, 1969 ice flow model overestimating the past accumulation rates for the site. In order to include as much data as possible, approximately half of the datasets used here have an age of 9-10 ka. This age coincides with the timing of the early Holocene Climate Optimum around 5-9 ka (HCO hereafter). For Greenlandic drill sites, temperatures were up to 3°C warmer than present day during the HCO (Dahl-Jensen et al., 1998). Another aspect of this study is that it uses water isotopic data sets of $\delta^{18}\text{O}$ and δD measured using different analytical techniques, namely Isotope Ratio Mass Spectroscopy (IRMS hereafter) as well as Cavity Ring Down Spectroscopy (CRDS hereafter). Two of the data sets presented here were obtained using Continuous Flow Analysis (CFA hereafter) systems tailored for water isotopic analysis (Gkinis et al., 2011). All data sections are characterized by a very high sampling resolution typically of 5 cm or better.

3.3 THEORY

3.3.1 Diffusion of water isotope signals in firn

The porous medium of the top 60 – 80m of firn allows for a molecular diffusion process that attenuates the water isotope signal from the time of deposition until pore close-off. The process takes place in the vapor phase and it can be described by Fick's second law as (assuming that the water isotope ratio signal (δ) approximates the concentration):

$$\frac{\partial \delta}{\partial t} = D(t) \frac{\partial^2 \delta}{\partial z^2} - \dot{\epsilon}_z(t) z \frac{\partial \delta}{\partial z} \quad (10)$$

where $D(t)$ is the diffusivity coefficient, $\dot{\epsilon}_z(t)$ the vertical strain rate and z is the vertical axis of a coordinate system, with its origin being fixed within the considered layer. The attenuation of the isotopic signal results in loss of information. However, the dependence of $\dot{\epsilon}_z(t)$ and $D(t)$ on temperature and accumulation presents the possibility of using the process as a tool to infer these two paleoclimatic parameters. A solution to Eq. 10 can be given by the convolution of the initial isotopic profile δ' with a Gaussian filter \mathcal{G} as:

$$\delta(z) = \mathcal{S}(z) [\delta'(z) * \mathcal{G}(z)] \quad (11)$$

where the Gaussian filter is described as:

$$\mathcal{G}(z) = \frac{1}{\sigma \sqrt{2\pi}} e^{-\frac{z^2}{2\sigma^2}}, \quad (12)$$

and \mathcal{S} is the total thinning of the layer at depth z described by

$$\mathcal{S}(z) = e^{\int_0^z \dot{\epsilon}_z(z') dz'} . \quad (13)$$

In Eq. 12, the standard deviation term σ^2 represents the average displacement of a water molecule along the z -axis and is commonly referred to as the diffusion length. The σ^2 quantity is a direct measure of diffusion and its accurate estimate is critical to any attempt of reconstructing temperatures that are based on the isotope diffusion thermometer. The diffusion length is directly related to the diffusivity coefficient and the strain rate (as the strain rate is approximately proportional to the densification rate in the firn column) and it can therefore be regarded as a measure of firn temperature.

The differential equation describing the evolution of σ^2 with time is given by (Johnsen, 1977):

$$\frac{d\sigma^2}{dt} - 2\dot{\epsilon}_z(t)\sigma^2 = 2D(t) . \quad (14)$$

In the case of firm the following approximation can be made for the strain rate:

$$\dot{\epsilon}_z(t) \approx -\frac{d\rho}{dt} \frac{1}{\rho}, \quad (15)$$

with ρ representing the density. Then for the firm column, Eq. 14 can be solved hereby yielding a solution for σ^2 :

$$\sigma^2(\rho) = \frac{1}{\rho^2} \int_{\rho_o}^{\rho} 2\rho^2 \left(\frac{d\rho}{dt} \right)^{-1} D(\rho) d\rho, \quad (16)$$

where ρ_o is the surface density. Under the assumption that the diffusivity coefficient $D(\rho)$ and the densification rate $\frac{d\rho}{dt}$ are known, integration from surface density ρ_o to the close-off density ρ_{co} can be performed yielding a model based estimate for the diffusion length. In this work we make use of the Herron–Langway densification model (H–L hereafter) and the diffusivity rate parametrization introduced by Johnsen et al., 2000 (Appendix A.1). $\frac{d\rho}{dt}$ depends on temperature and overburden pressure and $D(\rho)$ depends on temperature and firm connectivity. Our implementation of Eq. 16 includes a seasonal temperature signal that propagates down in the firm (Appendix A.2). The seasonal temperature variation affects the firm diffusion length non-linearly in the upper 10 – 12 m due to the saturation vapor pressure’s exponential dependence on temperature.

In Fig. 3.1 we evaluate Eq. 16 for all three isotopic ratios of water ($\delta^{18}\text{O}$, $\delta^{17}\text{O}$, δD) using boundary conditions characteristic of ice core sites from central Greenland and the East Antarctic Ice Cap. In Fig. 3.1, the transition between zone 1 and zone 2 densification (at the critical density $\rho_c = 550\text{kgm}^{-3}$) is evident as a kink in both the densification and diffusion model. For the first case we consider cold and dry conditions (case A hereafter) representative of Antarctic ice coring sites (e.g. Dome C, Vostok) with a surface temperature $T_{\text{sur}} = -55^\circ\text{C}$ and annual accumulation $A = 0.032\text{myr}^{-1}\text{ice eq.}$ For the second case we consider relatively warm and humid conditions (case B hereafter) representative of central Greenlandic ice coring sites (e.g. GISP2, GRIP, NorthGRIP) with a surface temperature $T_{\text{sur}} = -29^\circ\text{C}$ and annual accumulation $A = 0.22\text{myr}^{-1}\text{ice eq.}$ The general impact of surface temperature and accumulation rate on the firm diffusion length can be seen in Fig. 3.2.

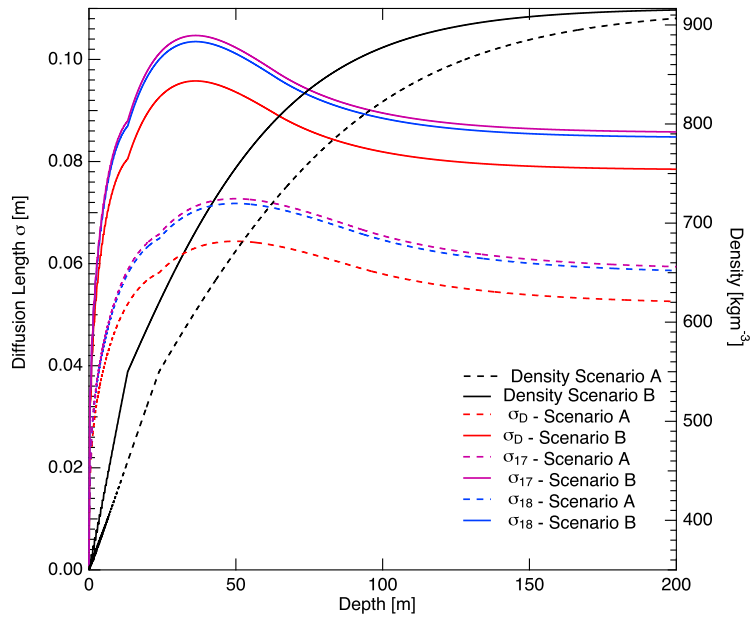


Figure 3.1. Diffusion length and density profiles (black) for case A (dashed lines: $T_{\text{sur}} = -55^{\circ}\text{C}$, $A = 0.032 \text{ myr}^{-1}$) and B (solid curves: $T_{\text{sur}} = -29^{\circ}\text{C}$, $A = 0.22 \text{ myr}^{-1}$). The increase in diffusion of the $\delta^{18}\text{O}$ (blue color), $\delta^{17}\text{O}$ (purple color) and δD (red color) isotope signals are partially due to the compaction of the firm which moves the ice closer together.

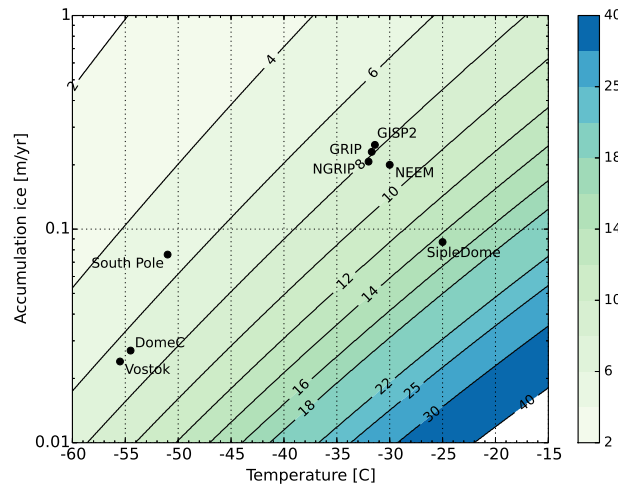


Figure 3.2. Modeled firm diffusion lengths [cm] for $\delta^{18}\text{O}$ as a function of temperature and accumulation rate (with $\rho_{\text{co}} = 804 \text{ kgm}^{-3}$ and $\rho_{\text{o}} = 330 \text{ kgm}^{-3}$) from Gkinis et al., 2014. The contours indicate lines of constant diffusion length and the colorbar represents the diffusion length in cm. Here the combined impact of temperature and accumulation rate on the diffusion length is evident; while warm temperatures induce high diffusion lengths, a high accumulation rate reduces the diffusion length estimate. The firm diffusion lengths corresponding to a few ice core sites are plotted as a reference.

3.3.2 Isotope diffusion in the solid phase

Below the close-off depth, diffusion occurs in solid ice driven by the isotopic gradients within the lattice of the ice crystals. This process is several orders of magnitude slower than firn diffusion. Several studies exist that deal with the estimate of the diffusivity coefficient in ice (Itagaki, 1964; Blinks et al., 1966; Delibaltas et al., 1966; Ramseier, 1967; Livingston et al., 1997). The differences resulting from the various diffusivity coefficients are small and negligible for the case of our study (for a brief comparison between the different parameterizations, the reader is referred to Gkinis et al., 2014). As done before by other similar firn diffusion studies (Johnsen et al., 2000; Simonsen et al., 2011; Gkinis et al., 2014) we make use of the parametrization given in Ramseier, 1967 as:

$$D_{\text{ice}} = 9.2 \cdot 10^{-4} \cdot \exp\left(-\frac{7186}{T}\right) \text{m}^2\text{s}^{-1}. \quad (17)$$

Assuming that a depth–age scale as well as a thinning function are available for the ice core a solution for the ice diffusion length is given by (Appendix A.3 for details):

$$\sigma_{\text{ice}}^2(t') = S(t')^2 \int_0^{t'} 2D_{\text{ice}}(t) S(t)^{-2} dt. \quad (18)$$

In Fig. 3.3 we have calculated ice diffusion lengths for four different cores (NGRIP, NEEM, Dome C, EDML). For the calculation of D_{ice} we have used the borehole temperature profile of each core and assumed a steady state condition. As the temperature of the ice increases closer to the bedrock, σ_{ice} increases nonlinearly due to D_{ice} exponential temperature dependence. When approaching these deeper parts of the core, the warmer ice temperatures enhance the effect of ice diffusion which then becomes an important and progressively dominating factor in the calculations. For the special case of the Dome C core (with a bottom age exceeding 800,000 years), σ_{ice} reaches values as high as 15 cm.

3.4 RECONSTRUCTING FIRN TEMPERATURES FROM ICE CORE DATA

Here we outline the various temperature reconstruction techniques that can be employed for paleotemperature reconstructions. In order to avoid significant overlap with previously published works e.g. Johnsen, (1977), Johnsen et al., (2000), Simonsen et al., (2011), Gkinis et al., (2014), and Wel et al., (2015) we occasionally point the reader to any of the latter or/and refer to specific sections in the Appendix A. We exemplify and illustrate the use of various techniques using synthetic data prepared such that they resemble two representative regimes of ice coring

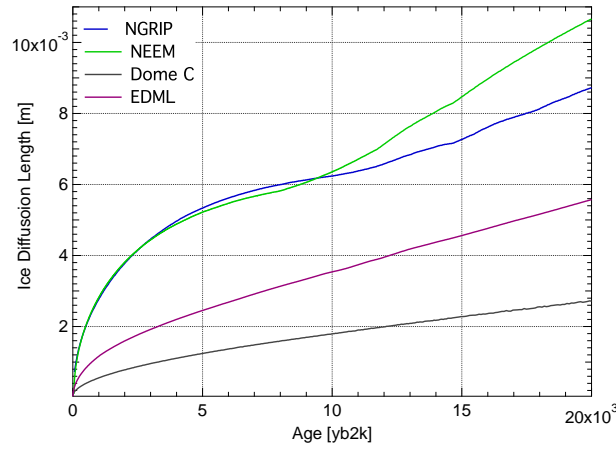


Figure 3.3. The ice diffusion length plotted with respect to age [b2k] for some selected sites from Greenland (NGRIP and NEEM) and Antarctica (Dome C and EDML).

sites on the Greenland summit and the East Antarctic Plateau.

3.4.1 *The single isotopologue diffusion*

As shown in Eq. 11, the impact of the diffusion process can be mathematically described as a convolution of the initial isotopic profile with a Gaussian filter. A fundamental property of the convolution operation is that it is equivalent to multiplication in the frequency domain. The transfer function for the diffusion process will be given by the Fourier transform of the Gaussian filter that will itself be a Gaussian function described by (Abramowitz and Stegun, 1964; Gkinis et al., 2014):

$$\mathfrak{F}[\mathcal{G}(z)] = \hat{\mathcal{G}} = e^{-\frac{k^2\sigma^2}{2}}. \quad (19)$$

In Eq. 19, $k = 2\pi f$ where f is the frequency of the isotopic time series. In Fig. 3.4 we illustrate the effect of the diffusion transfer function on a range of wavelengths for $\sigma = 1, 2, 4$ and 8 cm. Frequencies corresponding to wavelengths on the order of 50 cm and above remain largely unaltered while signals with wavelengths shorter than 20 cm are heavily attenuated.

A data-based estimate of the diffusion length σ can be obtained by looking at the power spectrum of the diffused isotopic time series. Assuming a noise signal $\eta(k)$, Eq. 19 provides a model describing the power spectrum as:

$$P_s = P_0(k)e^{-k^2\sigma^2} + |\hat{\eta}(k)|^2, \quad f \in [0, f_{Nq}] \quad (20)$$

where $f_{\text{Nq}} = 1/(2\Delta)$ is the Nyquist frequency that is defined by the sampling resolution Δ . $P_0(k)$ is the spectral density of the compressed profile without diffusion. It is assumed independent of k (now P_0) due to the strong depositional noise encountered in high resolution δ ice core series (Johnsen et al., 2000). Theoretically $|\hat{\eta}(k)|^2$ refers to white measurement noise. As we will show later, real ice core data sometimes have a more red noise behavior. A generalized model for the noise signal can be described well by autoregressive process of order 1 (AR-1). Its power spectral density is defined as (Kay and Marple, 1981):

$$|\hat{\eta}(k)|^2 = \frac{\sigma_\eta^2 \Delta}{|1 - a_1 \exp(-ik\Delta)|^2}, \quad (21)$$

where a_1 is the AR-1 coefficient and σ_η^2 is the variance of the noise signal.

In Fig. 3.5, an example of power spectra based on a synthetic time series is shown. A description of how the synthetic time series is generated is provided in Appendix A.4. The diffusion length used for the power spectrum in Fig. 3.5 is equal to 8.50 cm. The spectral estimate of the time series \mathbb{P}_s is calculated using Burg's spectral estimation method (Kay and Marple, 1981) and specifically the algorithm presented in Andersen, 1974. Using a least-squares approach we optimize the fit of the model P_s to the data-based \mathbb{P}_s by varying the four parameters P_0 , σ , a_1 and σ_η^2 . In the case of Fig. 3.5, the $|P_s - \mathbb{P}_s|^2$ least squares optimization resulted in $P_0 = 0.32 \text{‰}^2 \cdot \text{m}$, $\sigma = 8.45 \text{ cm}$, $a_1 = 0.05$ and $\sigma_\eta^2 = 0.005 \text{‰}^2$.

Assuming a diffusion length $\hat{\sigma}_i^2$ is obtained for depth z_i by means of $|P_s - \mathbb{P}_s|^2$ minimization, one can calculate the equivalent diffusion length at the bottom of the firn column σ_{firn}^2 in order to estimate firn temperatures by means of Eq. 16. In order to do this, one needs to take into account three necessary corrections - (1) sampling diffusion, (2) ice diffusion and (3) thinning. The first concerns the artifactually imposed diffusion due to the sampling of the ice core. In the case of a discrete sampling scheme with resolution Δ the additional diffusion length is (Appendix A.5 for derivation):

$$\sigma_{\text{dis}}^2 = \frac{2\Delta^2}{\pi^2} \ln\left(\frac{\pi}{2}\right). \quad (22)$$

In the case of high resolution measurements carried out with CFA measurement systems, there exist a number of ways to characterize the sampling diffusion length. Typically the step or impulse response of the CFA system can be measured yielding a Gaussian filter specific for the CFA system (Gkinis et al., 2011; Maselli et al., 2013; Emanuelsson et al., 2015; Jones et al., 2017). The Gaussian filter can be characterized by a diffusion length σ_{cfa}^2 that can be directly used to perform a sampling correction. The second correction concerns the ice diffusion as described in Sec. 3.3.2. The quantities σ_{ice}^2 and σ_{dis}^2 can be subtracted from $\hat{\sigma}_i^2$ yielding a

scaled value of σ_{firn}^2 due to ice flow thinning. As a result, we can finally obtain the diffusion length estimate at the bottom of the firn column σ_{firn}^2 (in meters of ice eq.):

$$\sigma_{\text{firn}}^2 = \frac{\widehat{\sigma}_i^2 - \sigma_{\text{dis}}^2 - \sigma_{\text{ice}}^2}{\mathcal{S}(z)^2}. \quad (23)$$

Subsequently, a temperature estimate can be obtained by numerically finding the root of (for a known $A(z)$):

$$\left(\frac{\rho_{\text{co}}}{\rho_i}\right)^2 \sigma^2(\rho = \rho_{\text{co}}, T(z), A(z)) - \sigma_{\text{firn}}^2 = 0 \quad (24)$$

where σ^2 is the result of the integration in Eq. 16 from surface to close-off density ($\rho_o \rightarrow \rho_{\text{co}}$). In this work we use a Newton-Raphson numerical scheme (Press et al., 2007) for the calculation of the root of the equation.

The accuracy of the σ_{firn}^2 estimation and subsequently of the temperature reconstruction obtained based on it, depends on the three correction terms σ_{ice}^2 , σ_{dis}^2 and the ice flow thinning $\mathcal{S}(z)$. For relatively shallow depths where σ_{ice}^2 is relatively small compared to $\widehat{\sigma}_i^2$, ice diffusion can be accounted for with simple assumptions on the borehole temperature profile and the ice flow. In a similar way, σ_{dis}^2 is a well constrained parameter and depends only on the sampling resolution Δ for discrete sampling schemes or the smoothing of the CFA measurement system.

Equation 23 reveals an interesting property of the single isotopologue temperature estimation technique. As seen, the result of the σ_{firn}^2 calculation depends strongly on the ice flow thinning quantity $\mathcal{S}(z)^2$. Possible errors in the estimation of $\mathcal{S}(z)^2$ due to imperfections in the modelling of the ice flow will inevitably be propagated to the σ_{firn}^2 value thus biasing the temperature estimation. Even though this appears to be a disadvantage of the method, in some instances, it can be a useful tool for assessing the accuracy of ice flow models. Provided that for certain sections of the ice core there is a temperature estimate available based on other reconstruction methods (borehole thermometry, $\delta^{15}\text{N}/\delta^{40}\text{Ar}$) it is possible to estimate ice flow induced thinning of the ice core layers. Following this approach Gkinis et al., 2014 proposed a correction in the existing accumulation rate history for the NorthGRIP ice core.

The annual spectral signal interference

Depending on the ice core site temperature and accumulation conditions, spectral signatures of an annual isotopic signal can be apparent as a peak located at the frequency range that corresponds to the annual layer thickness. The resulting effect of such a spectral signature, is the artifactual biasing of the diffusion length estimation towards lower values and thus colder temperatures. Figure 3.6 shows the PSD of the δD series for a mid Holocene section from the

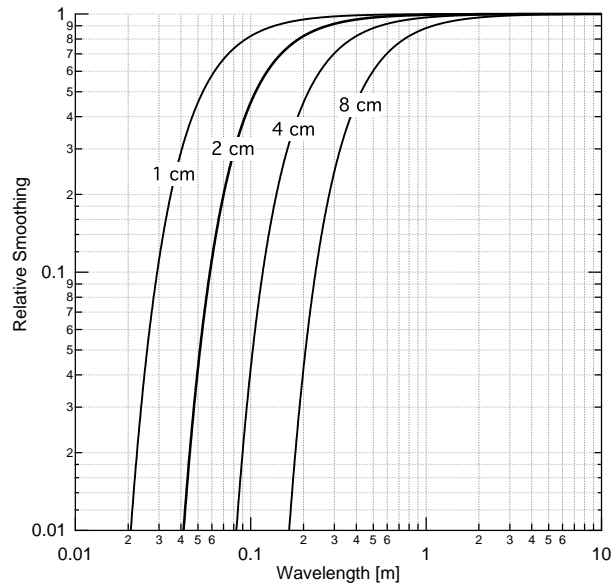


Figure 3.4. The smoothing effect of the diffusion transfer function demonstrated on a range of different wavelengths for $\sigma = 1, 2, 4$ and 8 cm.

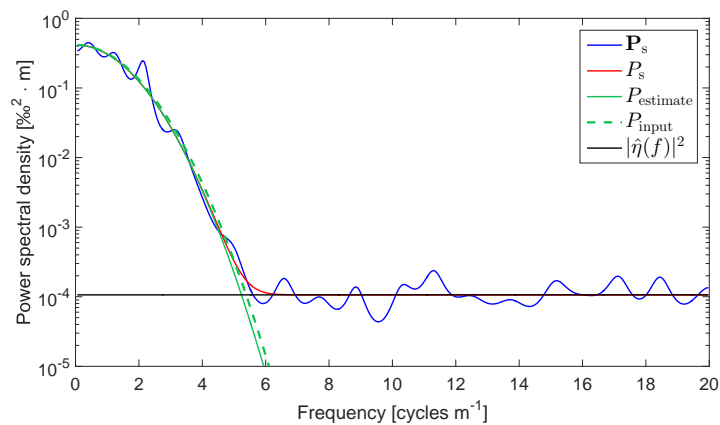


Figure 3.5. PSD of a synthetic $\delta^{18}\text{O}$ time series plotted with respect to frequency (blue curve). The red curve represents the complete model fit (Eq. 20). The green dashed curve represents the input diffusion and the solid green curve represents the estimated diffusion length of the signal (uncorrected for sampling diffusion). The black curve represents the noise part of the fit.

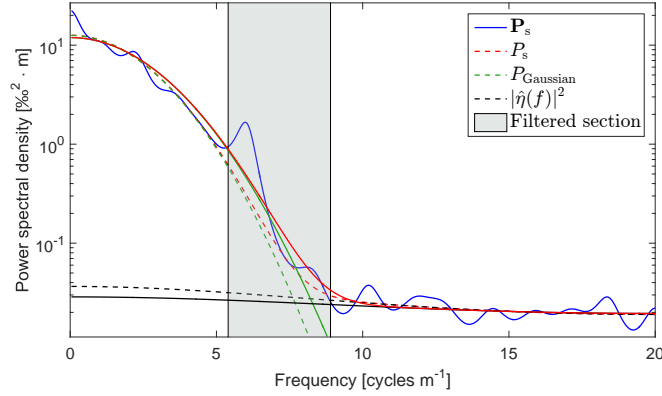


Figure 3.6. The interference of the annual spectral signal is seen in the PSD of the δD GRIP mid Holocene section. The regular fit is represented by the solid lines and the dashed lines represent the case where the weight function $w(f)$ has filtered out this artifactual bias.

GRIP ice core (drill site characteristics in Table 3.3). A prominent spectral feature is visible at $f \approx 6 \text{ cycles m}^{-1}$. This frequency is comparable to the expected frequency of the annual signal at $6.1 \text{ cycles m}^{-1}$ as estimated from the annual layer thickness reconstruction of the GICC05 timescale (Vinther et al., 2006).

In order to evade the influence of the annual spectral signal on the diffusion length estimation, we propose the use of a weight function $w(f)$ in the spectrum as:

$$w(f) = \begin{cases} 0 & f_\lambda - df_\lambda \leq f \leq f_\lambda + df_\lambda \\ 1 & f < f_\lambda - df_\lambda, f > f_\lambda + df_\lambda \end{cases} \quad (25)$$

where f_λ is the frequency of the annual layer signal based on the reconstructed annual layer thickness λ and df_λ is the range around the frequency f_λ at which the annual signal is detectable. The weight function is multiplied with the optimization norm $|P_s - \mathbb{P}_s|^2$. Figure 3.6 also illustrates the effect of the weight function on the estimation of P_s and subsequently the diffusion length value. When the weight function is used during the optimization process, there is an increase in the diffusion length value by 0.3 cm, owing essentially to the exclusion of the annual signal peak from the minimization of $|P_s - \mathbb{P}_s|^2$. While the value of f_λ can be roughly predicted, the value of df_λ usually requires visual inspection of the spectrum.

3.4.2 The differential diffusion signal

A second-order temperature reconstruction technique is possible based on the differential signal between $\delta^{18}\text{O}$ and δD . Due to the difference in the fractionation factors and the air diffusivities

between the oxygen and deuterium isotopologues, a differential diffusion signal is created in the firn column. Based on the calculation of the diffusion lengths presented in Fig. 3.1 we then compute the differential diffusion lengths $^{17}\Delta\sigma^2$ and $^{18}\Delta\sigma^2$ where

$$^{17}\Delta\sigma^2 = \sigma_{^{17}\text{O}}^2 - \sigma_{\text{D}}^2 \text{ and } ^{18}\Delta\sigma^2 = \sigma_{^{18}\text{O}}^2 - \sigma_{\text{D}}^2. \quad (26)$$

As it can be seen in Fig. 3.7 the differential diffusion length signal is slightly larger for the case of $^{17}\Delta\sigma^2$ when compared to $^{18}\Delta\sigma^2$.

One obvious complication of the differential diffusion technique is the requirement for dual measurements of the water isotopologues, preferably performed on the same sample. The evolution of IRMS techniques targeting the analysis of δD (Bigeleisen et al., 1952; Vaughn et al., 1998; Gehre et al., 1996; Begley and Scrimgeour, 1997) in ice cores has allowed for dual isotopic records at high resolutions. With the advent of CRDS techniques and their customization for CFA measurements, simultaneous high resolution measurements of both $\delta^{18}\text{O}$ and δD have become a routine procedure.

The case of $\delta^{17}\text{O}$ is more complicated as the greater abundance of ^{13}C than ^{17}O rules out the possibility for an IRMS measurement at mass/charge ratio (m/z) of 45 or 29 using CO_2 equilibration or reduction to CO respectively. Alternative approaches that exist include the electrolysis method with CuSO_4 developed by Meijer and Li, 1998 as well as the fluorination method presented by Baker et al., 2002 and implemented by Barkan and Luz, 2005 for dual-inlet IRMS systems. These techniques target the measurement of the $^{17}\text{O}_{\text{excess}}$ parameter and are inferior for $\delta^{17}\text{O}$ measurements at high precision and have a very low sample throughput. As a result, high resolution $\delta^{17}\text{O}$ measurements from ice cores are currently non-existent. Recent innovations however in CRDS spectroscopy (Steig et al., 2014) allow for simultaneous triple isotopic measurements of δD , $\delta^{18}\text{O}$ and $\delta^{17}\text{O}$ in a way that a precise and accurate measurement for both $\delta^{17}\text{O}$ and $^{17}\text{O}_{\text{excess}}$ is possible. Therefore high resolution ice core datasets of δD , $\delta^{18}\text{O}$ and $\delta^{17}\text{O}$ should be expected in the near future.

The following analysis is focused on the $^{18}\Delta\sigma^2$ signal but it applies equally to the $^{17}\Delta\sigma^2$. The stronger attenuation of the $\delta^{18}\text{O}$ signal with respect to the δD signal can be visually observed in the power spectral densities of the two signals. As seen in Fig. 3.8 the $\mathbb{P}_{\text{S}18}$ signal reaches the noise level at a lower frequency when compared to the \mathbb{P}_{SD} signal. At low frequencies with high signal to noise ratio we can calculate the logarithm of the ratio of the two power spectral densities as (i.e. neglecting the noise term):

$$\ln\left(\frac{P_{\text{D}}}{P_{18}}\right) \approx k^2(\sigma_{^{18}\text{O}}^2 - \sigma_{\text{D}}^2) + \ln\left(\frac{P_{0\text{D}}}{P_{018}}\right) = ^{18}\Delta\sigma^2 k^2 + C. \quad (27)$$

As seen in Eq. 27 and Fig. 3.8 (synthetic generated $\delta^{18}\text{O}$ and δD data as in Sec. 3.4.1) an estimate of the $^{18}\Delta\sigma^2$ parameter can be obtained by a linear fit of $\ln(P_{\text{D}}/P_{18})$ in the low frequency area, thus requiring only two parameters ($^{18}\Delta\sigma^2$ and C) to be tuned. An interesting aspect of the differential diffusion method, is that in contrast to the single isotopologue diffusion length, $^{18}\Delta\sigma_{\text{firm}}^2$ is a quantity that is independent of the sampling and solid ice diffusion thus eliminating the uncertainties associated with these two parameters. This can be seen by simply using Eq. 23:

$$^{18}\Delta\sigma_{\text{firm}}^2 = \frac{\hat{\sigma}_{18}^2 - \sigma_{\text{dis}}^2 - \sigma_{\text{ice}}^2}{\mathcal{L}(z)^2} - \frac{\hat{\sigma}_{\text{D}}^2 - \sigma_{\text{dis}}^2 - \sigma_{\text{ice}}^2}{\mathcal{L}(z)^2} = \frac{\hat{\sigma}_{18}^2 - \hat{\sigma}_{\text{D}}^2}{\mathcal{L}(z)^2}. \quad (28)$$

Accurate estimates of the thinning function however still play a key role in the differential diffusion technique. One more complication of the differential diffusion technique is the selection of the frequency range in which one chooses to apply the linear regression. Often visual inspection is required in order to designate a cut-off frequency until which the linear regression can be applied. In most cases identifying the cut-off frequency, or at least a reasonable area around it is reasonably straight-forward. Though in a small number of cases, spectral features in the low frequency area seem to have a strong influence on the slope of the linear regression and thus on the $^{18}\Delta\sigma^2$. As a result, visual inspection of the regression result is always advised in order to avoid biases.

Another way of estimating the differential diffusion signal is to subtract the single diffusion spectral estimates σ_{18}^2 and σ_{D}^2 . Theoretically this approach should be inferior to the linear fit approach due to the fact that more degrees of freedom are involved in the estimation of σ_{18}^2 and σ_{D}^2 (8 versus 2; 3 if the cutoff frequency is included). Here we will test both approaches.

Linear correlation method

An alternative way to calculate the differential diffusion signal $^{18}\Delta\sigma^2$ is based on the assumption that the initial precipitated isotopic signal presents a deuterium excess signal d_{xs} that is invariable with time and as a consequence of this, the correlation signal between $\delta^{18}\text{O}$ and δD (hereafter $r_{\delta^{18}\text{O}/\delta\text{D}}$) is expected to have a maximum value at the time of deposition. The d_{xs} signal is defined as the deviation from the meteoric water line $d_{\text{xs}} = \delta\text{D} - 8 \cdot \delta^{18}\text{O}$ (Craig, 1961; Dansgaard, 1964). From the moment of deposition, the difference in diffusion between the $\delta^{18}\text{O}$ and δD signals results in a decrease of the $r_{\delta^{18}\text{O}/\delta\text{D}}$ value. Hence, diffusing the δD signal with a Gaussian kernel of standard deviation equal to $^{18}\Delta\sigma^2$ will maximize the value of $r_{\delta^{18}\text{O}/\delta\text{D}}$ (Wel et al., 2015) as shown in Fig. 3.9. Thus, the $^{18}\Delta\sigma^2$ value is found when the $r_{\delta^{18}\text{O}/\delta\text{D}}$ value has its maximum.

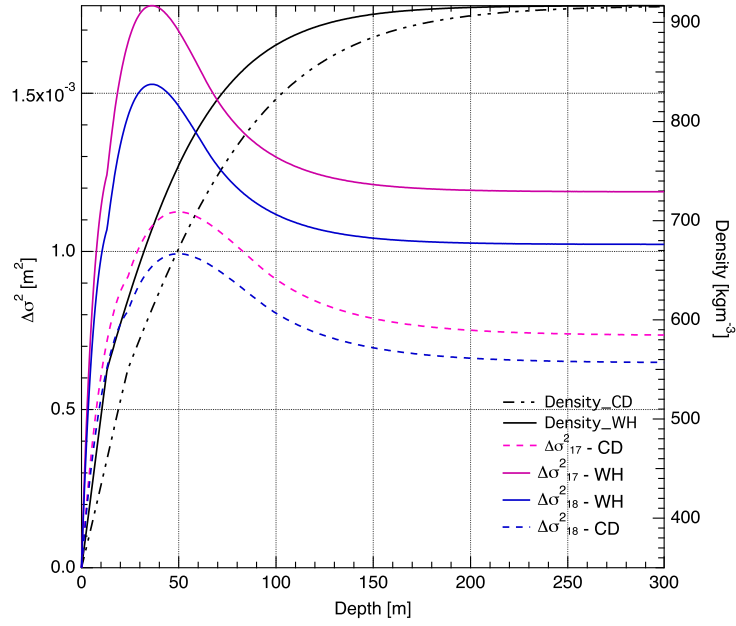


Figure 3.7. Differential diffusion length profiles for cases A (dashed lines) and B (solid lines) for $^{18}\Delta\sigma^2$ (blue) and $^{17}\Delta\sigma^2$ (purple). The density profiles are given in black.

This type of estimation is independent of spectral estimates of the $\delta^{18}\text{O}$ and δD time series and does not pose any requirements for measurement noise characterization or selection of cut-off frequencies. However uncertainties related to the densification and ice flow processes, affect this method equally as they do for the spectrally based differential diffusion temperature estimation. In this study, we test the applicability of the method on synthetic and real ice core data. We acknowledge that the assumption that the d_{xs} signal is constant with time is not entirely consistent with the fact that there is a small seasonal cycle in the d_{xs} signal (Johnsen et al., 1989). It is thus likely to result in inaccuracies.

3.4.3 The diffusion length ratio

A third way of using the diffusion lengths as proxies for temperature can be based on the calculation of the ratio of two different diffusion lengths. From Eq. 16 we can evaluate the ratio of two different isotopologues j and k as:

$$\frac{\sigma_j^2(\rho)}{\sigma_k^2(\rho)} = \frac{\frac{1}{\rho^2} \int 2\rho^2 \left(\frac{d\rho}{dt}\right)^{-1} D_j(\rho) d\rho}{\frac{1}{\rho^2} \int 2\rho^2 \left(\frac{d\rho}{dt}\right)^{-1} D_k(\rho) d\rho}, \quad (29)$$

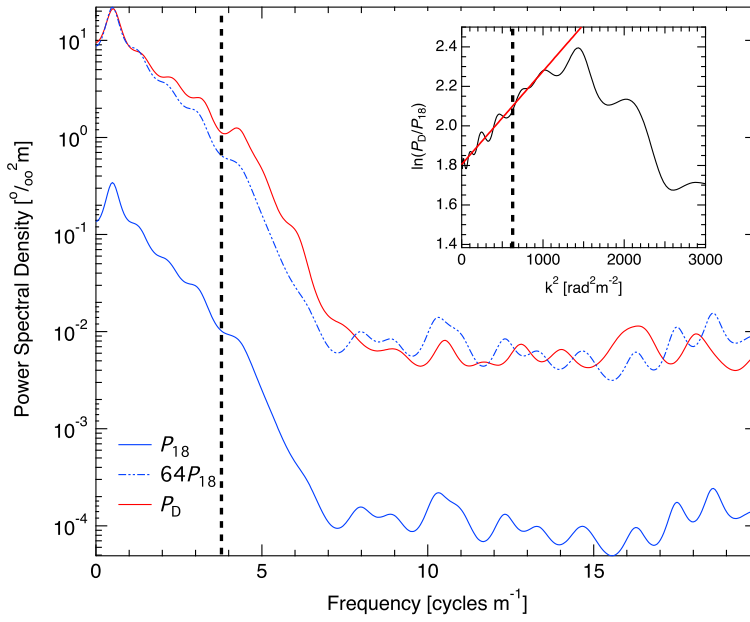


Figure 3.8. PSDs of synthetic $\delta^{18}\text{O}$ (blue) and δD (red) with respect to frequency where the inner subplot shows the $\ln(P_D/P_{18})$ relation with respect to k^2 . The $^{18}\Delta\sigma^2$ value is determined from the slope of the linear fit in the subplot. The chosen cutoff frequency is marked by the vertical dashed line in both plots.

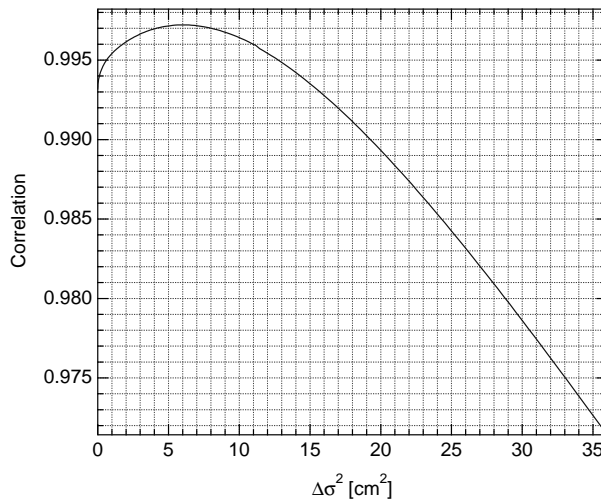


Figure 3.9. Correlation coefficient ($r_{\delta^{18}\text{O}/\delta\text{D}}$) between the $\delta^{18}\text{O}$ and the forward-diffused δD series as a function of the estimated $^{18}\Delta\sigma^2$. The synthetic data represent a case A climate.

and by substituting the firm diffusivities as defined in Appendix A.1 and according to Johnsen et al., 2000 we get:

$$\frac{\sigma_j^2(\rho)}{\sigma_k^2(\rho)} = \frac{D_{aj}\alpha_k}{D_{ak}\alpha_j} \frac{\frac{1}{\rho^2} \int 2\rho^2 \left(\frac{d\rho}{dt}\right)^{-1} \frac{m p}{RT\tau} \left(\frac{1}{\rho} - \frac{1}{\rho_{ice}}\right) d\rho}{\frac{1}{\rho^2} \int 2\rho^2 \left(\frac{d\rho}{dt}\right)^{-1} \frac{m p}{RT\tau} \left(\frac{1}{\rho} - \frac{1}{\rho_{ice}}\right) d\rho} = \frac{D_{aj}\alpha_k}{D_{ak}\alpha_j}. \quad (30)$$

As a result, the ratio of the diffusion lengths is dependent on temperature through the parameterizations of the fractionation factors (α) and carries no dependence to parameters related to the densification rates nor the atmospheric pressure. Additionally, it is a quantity that is independent of depth. Here we give the analytical expressions of all the isotopologues combinations by substituting the diffusivities and the fractionation factors:

$$\sigma_{18}^2 / \sigma_D^2 = 0.93274 \cdot \exp(16288/T^2 - 11.839/T) \quad (31)$$

$$\sigma_{17}^2 / \sigma_D^2 = 0.933 \cdot \exp(16288/T^2 - 6.263/T) \quad (32)$$

$$\sigma_{18}^2 / \sigma_{17}^2 = 0.99974 \cdot \exp(-5.57617/T) \quad (33)$$

A data-based diffusion length ratio estimate can be obtained by estimating the single diffusion length values as described in Sec. 3.4.1 and thereafter applying the necessary corrections as in Eq. 23. An interesting aspect of the ratio estimation is that it is not dependent on the ice flow thinning as seen below

$$\left(\frac{\sigma_{18}^2}{\sigma_D^2}\right)_{\text{firm}} = \frac{\hat{\sigma}_{18}^2 - \sigma_{\text{dis}}^2 - \sigma_{\text{ice}}^2}{\hat{\sigma}_D^2 - \sigma_{\text{dis}}^2 - \sigma_{\text{ice}}^2}. \quad (34)$$

while the method still depends on the sampling and ice diffusion.

3.5 RESULTS

3.5.1 Synthetic data test

A first order test for the achievable accuracy and precision of the presented diffusion temperature reconstruction techniques can be performed using synthetic isotopic data. We generate synthetic time series of $\delta^{17}\text{O}$, $\delta^{18}\text{O}$ and δD using an AR-1 process and subsequently applying numerical diffusion with diffusion lengths as calculated for case A and B (as presented in Fig. 3.1). The time series are then sampled at a resolution of 2.5 cm and white measurement noise is added. Eventually, estimates of diffusion lengths for all three isotopologues are obtained using

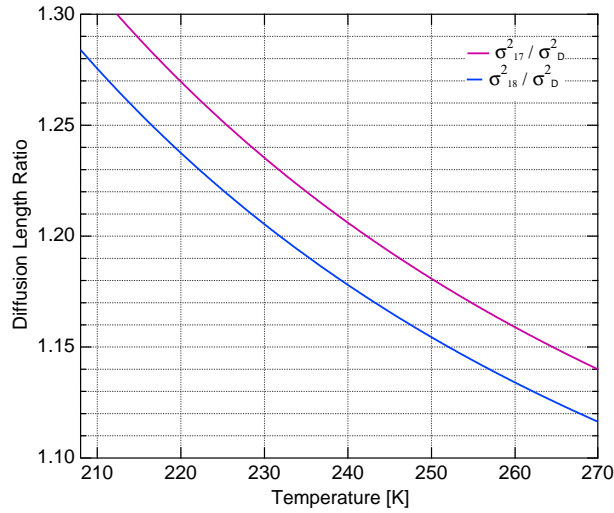


Figure 3.10. The diffusion length ratios $\sigma_{18}^2 / \sigma_D^2$ and $\sigma_{17}^2 / \sigma_D^2$ with respect to temperature. The $\sigma_{18}^2 / \sigma_{17}^2$ is almost constant at 0.975 and omitted here due to its very low temperature sensitivity.

the techniques we have described in the previous sections. A more detailed description of how the synthetic data are generated is outlined in Appendix A.4.

The process of time series generation is repeated 500 times. For each iteration, the quantities σ_{17} , σ_{18} , σ_D , $^{17}\Delta\sigma^2$, $^{18}\Delta\sigma^2$ and the ratios $\sigma_{18}^2 / \sigma_D^2$, $\sigma_{17}^2 / \sigma_D^2$ and $\sigma_{18}^2 / \sigma_{17}^2$ are estimated. The differential diffusion signals are estimated using the three different techniques as described in Sec. 3.4.2. We designate the subtraction technique with I, the linear regression with II and the correlation method with III. For every value of the diffusion estimates we calculate a firm temperature where the uncertainties related to the firm diffusion model (A , ρ_{co} , ρ_o , surface pressure P , \mathcal{S} and σ_{ice} in Table 3.1) are included. For the total of the 500 iterations we calculate a mean firm temperature \bar{T} , a standard deviation and a mean bias as:

$$\text{MB} = \frac{1}{N} \sum_{i=1}^N T_i - T_{\text{sur}} = \bar{T} - T_{\text{sur}}, \quad (35)$$

where $i = 1, 2, \dots, N$ signifies the iteration number, T_i is the synthetic data-based estimated temperature and T_{sur} is the model forcing surface temperature for the case A and B scenarios. The results of the experiment are presented in Table 3.2 and the calculated mean biases are illustrated in Fig. 3.11. The diffusion length ratio approach yields very large uncertainty bars (see Table 3.2) and thus these results are not included in Fig. 3.11.

Table 3.1. The standard deviations of the input parameters. Most of the standard deviations are expressed as a percentage of the mean input value.

Parameter	A	ρ_{co}	ρ_o	P	\mathcal{S}	σ_{ice}
Uncertainty	$\pm 5\%A_{\text{mean}}$	$\pm 20\text{kgm}^{-3}$	$\pm 30\text{kgm}^{-3}$	$\pm 2\%P_{\text{mean}}$	$\pm 1\%\mathcal{S}_{\text{mean}}$	$\pm 2\%\sigma_{ice_{\text{mean}}}$

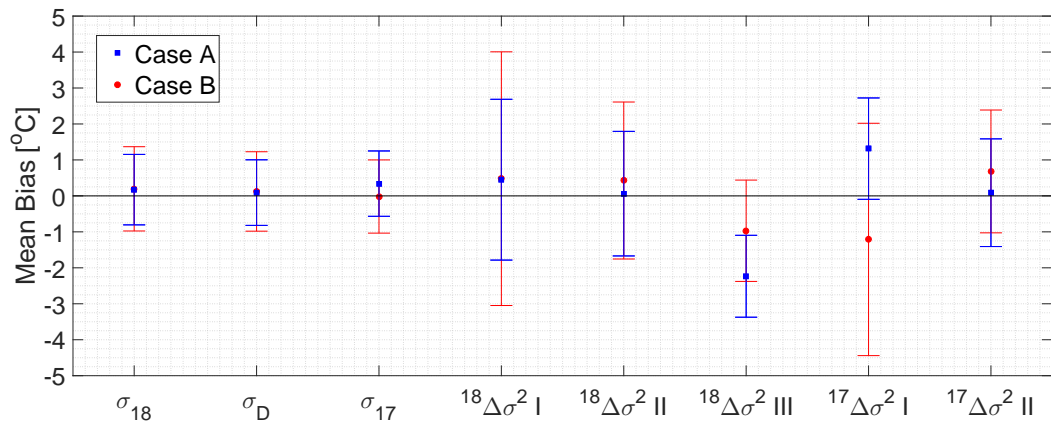


Figure 3.11. Mean biases for the single and differential diffusion techniques. The error bars represent 1 std of the estimated temperatures.

Table 3.2. Simulations with synthetic data of a case A ($T_{\text{sur}} = -55.0^\circ\text{C}$) and B ($T_{\text{sur}} = -29.0^\circ\text{C}$). The diffusion lengths in the tabular are the firm diffusion lengths. Thus, this is before sampling, ice diffusion and thinning affected the input diffusion length. The estimated firm diffusion lengths are after correcting for sampling, ice diffusion and thinning (with their corresponding uncertainties).

	Case A			Case B		
	Applied diffusion	Est. diffusion	Est. T [$^\circ\text{C}$]	Applied diffusion	Est. diffusion	Est. T [$^\circ\text{C}$]
σ_{18}	5.82 cm	5.85 ± 0.14 cm	-54.8 ± 1.0	8.50 cm	8.51 ± 0.20 cm	-28.8 ± 1.2
σ_D	5.22 cm	5.23 ± 0.12 cm	-54.9 ± 0.9	7.86 cm	7.86 ± 0.18 cm	-28.9 ± 1.1
σ_{17}	5.90 cm	5.97 ± 0.11 cm	-54.7 ± 0.9	8.59 cm	8.54 ± 0.13 cm	-29.0 ± 1.0
$^{18}\Delta\sigma^2 \text{ I}$	6.6 cm^2	$6.9 \pm 1.1 \text{ cm}^2$	-54.6 ± 2.2	10.3 cm^2	$10.7 \pm 2.0 \text{ cm}^2$	-28.5 ± 3.5
$^{18}\Delta\sigma^2 \text{ II}$	6.6 cm^2	$6.7 \pm 0.8 \text{ cm}^2$	-54.9 ± 1.7	10.3 cm^2	$10.5 \pm 1.2 \text{ cm}^2$	-28.6 ± 2.2
$^{18}\Delta\sigma^2 \text{ III}$	6.6 cm^2	$5.5 \pm 0.3 \text{ cm}^2$	-57.2 ± 1.1	10.3 cm^2	$9.7 \pm 0.6 \text{ cm}^2$	-30.0 ± 1.4
$^{17}\Delta\sigma^2 \text{ I}$	7.5 cm^2	$8.3 \pm 0.7 \text{ cm}^2$	-53.7 ± 1.4	12.0 cm^2	$12.2 \pm 2.0 \text{ cm}^2$	-30.2 ± 3.2
$^{17}\Delta\sigma^2 \text{ II}$	7.5 cm^2	$7.5 \pm 0.5 \text{ cm}^2$	-54.9 ± 1.5	12.0 cm^2	$12.4 \pm 1.0 \text{ cm}^2$	-28.3 ± 1.7
$\sigma_{18}^2 / \sigma_{17}^2$	0.975	0.960 ± 0.027	—	0.977*	$0.993 \pm 0.035^*$	—
$\sigma_{18}^2 / \sigma_D^2$	1.24	1.25 ± 0.04	-56.6 ± 11.1	1.17	1.17 ± 0.03	-28.2 ± 19.3
$\sigma_{17}^2 / \sigma_D^2$	1.28	1.31 ± 0.03	-62.8 ± 7.0	1.20	1.18 ± 0.04	-16.1 ± 27

3.5.2 Ice core data test

We also use a number of high resolution, high precision ice core data, in order to benchmark the diffusion temperature reconstruction techniques that we have presented. The aim of this benchmark test is to utilize the various reconstruction techniques for a range of boundary conditions that is (a) as broad as possible with respect to mean annual surface temperature and accumulation and (b) representative of existing polar ice core sites. Additionally, we have made an effort in focusing on ice core data sets that reflect conditions as close as possible to present. As a result, the majority of the data sets presented here are from relatively shallow depths. This serves a twofold purpose. Firstly, it reduces the uncertainties regarding the ice flow that are considerably larger for the deeper parts of the core. Secondly, choosing to work with data sections as close to late Holocene conditions as possible, allows for a comparison of the estimated temperature to the site's present temperature. Although this is technically not a true comparison as the sites' surface temperatures have very likely varied during the Holocene, we consider it as a rough estimate of each techniques accuracy. For those cases where it was not possible to obtain late Holocene isotopic time series, due to limited data availability, we have used data originating from deeper sections of the ice cores with an age of about 10ka b2k reflecting conditions of the early Holocene. In Table 3.3 we provide relevant information for each data set as well as the present temperature and accumulation conditions for each ice core site. For five out of thirteen ice core data sets, we used a weight function of $w(f_\lambda - 0.5 \leq f \leq f_\lambda + 3) = 0$ in order to remove the annual peak (see figures in Appendix A.6).

The data sets were produced using a variety of techniques both with respect to the analysis itself (IRMS/CRDS), as well as with respect to the sample resolution and preparation (discrete/CFA). The majority of the data sets were analyzed using CRDS instrumentation. In particular the L1102i, L2120i and L2130i variants of the Picarro CRDS analyzer were utilized for both discrete and CFA measurements of $\delta^{18}\text{O}$ and δD . The rest of the data sets were analyzed using IRMS techniques with either CO_2 equilibration or high temperature carbon reduction. For the case of the NEEM early Holocene data set, we work with two data sections that span the same depth interval and consist of discretely sampled and CFA measured data respectively. Additionally, the Dome C and Dome F data sections represent conditions typical for the East Antarctic Plateau and are sampled using a different approach (2.5cm resolution discrete samples for the Dome C section and high resolution CFA measurements for the Dome F section).

In a way similar to the synthetic data test, we apply the various reconstruction techniques on every ice core data section. No reconstruction techniques involving $\delta^{17}\text{O}$ are presented here

due to lack of $\delta^{17}\text{O}$ data. In order to achieve an uncertainty estimate for every reconstruction, we perform a sensitivity test that is based on $N = 1000$ iterations. Assuming that every ice core section consists of J $\delta^{18}\text{O}$ and δD points, then a repetition is based on a data subsection with size J' that varies in the interval $[J/2, J]$. This “jittering” of the subsection size happens around the midpoint of every section and J' is drawn from a uniform distribution. Similar to the synthetic data tests, we also introduce uncertainties originating from the firn densification model, the ice flow model and ice diffusion (through the parameters: A , ρ_{co} , ρ_o , P , \mathcal{S} and σ_{ice}). For every reconstruction method and every ice core site, we calculate a mean and a standard deviation for the diffusion estimate, as well as a mean and a standard deviation for the temperature. Results are presented in Table 3.4. The estimated temperatures for ice cores covering the late-mid Holocene and early Holocene are shown in Fig. 3.12 and 3.13 respectively.

3.5.3 *The fractionation factors*

We also test how the choice of the parameterization of the isotope fractionation factors (α_{18} , α_{D}) influences the reconstructed temperatures of ice core sections. This is especially relevant for temperatures below -40°C , as the confidence of the parameterized fractionation factors has been shown to be low for such cold temperatures (Ellehoj et al., 2013). The low confidence is partly a consequence of two things a) it is difficult to avoid kinetic fractionation in the measurement system and b) the water vapor pressure becomes small which makes it difficult to measure. The experiments are typically performed with a vapor source with a known isotopic composition that condenses out under controlled equilibrium conditions. For temperatures below -40°C , single crystals have been observed growing against the flow of vapor in the tubes and chambers of the experimental setup (Ellehoj et al., 2013). This indicates that the water vapor experiences kinetic fractionation which disturbs the equilibrium process. In order to avoid this, most models generally extrapolate the warmer experiments to cover colder temperatures. Such extrapolations were performed in the parameterizations of Majoube, 1970 (α_{18}) and Merlivat and Nief, 1967 (α_{D}) which we used in the firn diffusivity parameterization (Appendix A.1). Their experiments were conducted down to a minimum temperature of -33°C , and then extrapolated to colder temperatures. Similarly, Ellehoj et al., 2013 estimated new values of α_{18} and α_{D} by measuring in the range -40°C to 0°C . Their results showed a α_{D} parameterization that deviated significantly from that of Merlivat and Nief, 1967. A more recent study by Lamb et al., 2017 measured the value of α_{D} in the range -87°C to -39°C . Their inferred equilibrium fractionation factors required a correction for kinetic effects. By including such a correction and extrapolating to warmer temperatures, they obtained a parameterization of α_{D}

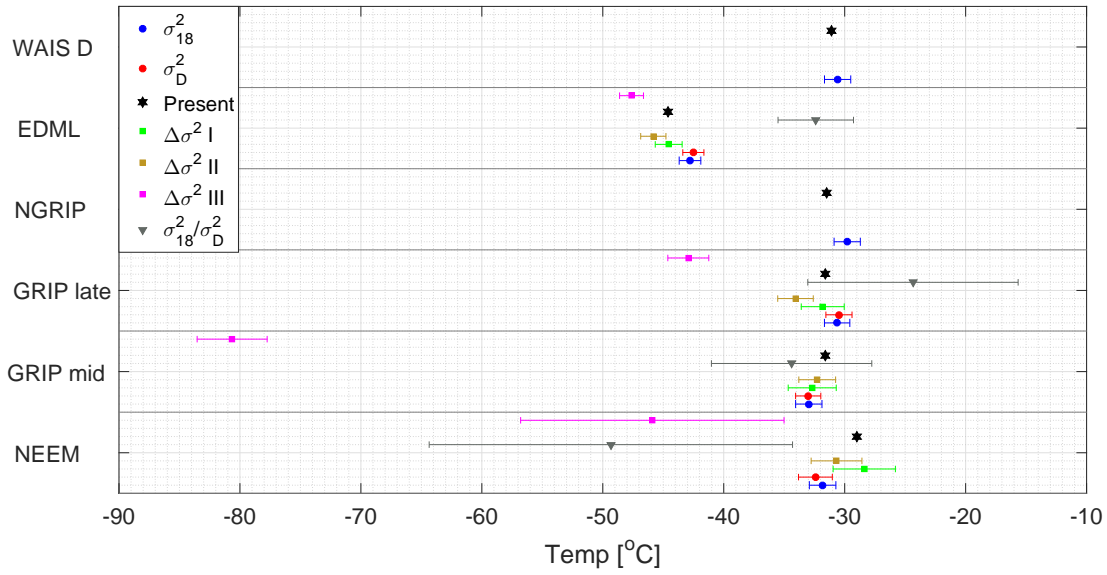


Figure 3.12. Late-mid Holocene section with reconstructed temperatures from the σ_{18}^2 (blue circles), σ_D^2 (red circles), $\Delta\sigma^2$ I (green squares), $\Delta\sigma^2$ II (brown squares), $\Delta\sigma^2$ III (magenta squares) and σ_{18}^2/σ_D^2 (grey triangles) methods. The black stars represent the present annual mean temperatures at the sites.

with a slightly weaker temperature dependence than that of Merlivat and Nief, 1967. Moreover, their α_D deviated significantly from the results of Ellehoj et al., 2013. Such discrepancies between the fractionation factor parameterizations underline the importance of addressing how great an impact the potential inaccuracies have on the diffusion-based temperature proxy.

In this test, the procedure followed is common to that in Sec. 3.5.2 where a set of $N = 1000$ repetitions is performed and both “jittering” of the data sets length and perturbation of input model variables takes place. The results are displayed in Fig. 3.14, where the temperatures resulting from the parameterizations of Majoube, 1970 (α_{18}) and Merlivat and Nief, 1967 (α_D) are compared to the temperatures resulting from the parameterizations of Ellehoj et al., 2013 (α_{18} , α_D) and Lamb et al., 2017 (α_D). In the latter case, the parameterization of α_{18} from Majoube, 1970 is used for the dual diffusion length methods.

3.6 DISCUSSION

3.6.1 Synthetic data

Based on the results of the sensitivity experiment with synthetic data, the following can be inferred. Firstly, the three techniques based on the single isotope diffusion, perform similarly and

Table 3.3. Ice core data sections and the corresponding drill site characteristic. Sources of data: (Steig et al., 2013)¹, (Oerter et al., 2004)², (Svensson et al., 2015)³, (Gkinis, 2011)⁴, (Gkinis et al., 2011)⁵. Drill site characteristic sources: (Banta et al., 2008)^a, (Oerter et al., 2004; Veres et al., 2013)^b, (Watanabe et al., 2003; Kawamura et al., 2003)^c, (Lorius et al., 1979)^d, (NGRIP members, 2004; Gkinis et al., 2014)^e, (Johnsen et al., 2000)^f, (Guillevic et al., 2013; Rasmussen et al., 2013)^g.

Site Sections	Depth [m]	Age [kab2k]	Present T [°C]	A [miceyr ⁻¹]	P [Atm]	Thinning	Meas.	Analysis	Δ [cm]
GRIP mid ^f	753 – 776	3.7	-31.6	0.23	0.65	0.71	δD, δ ¹⁸ O	2130	2.5
GRIP late ^f	514 – 531	2.4	-31.6	0.23	0.65	0.79	δD, δ ¹⁸ O	2130	2.5
WAIS 2005A ^{a,1}	120 – 150	0.5	-31.1	0.22	0.77	0.97	δ ¹⁸ O	1102	5.0
EDML ^{b,2}	123 – 178	1.6	-44.6	0.08	0.67	0.93	δD, δ ¹⁸ O	IRMS	5.0
NEEM ^g	174 – 194	0.8	-29.0	0.22	0.72	0.31	δD, δ ¹⁸ O	2120	2.5
NGRIP ^e	174 – 194	0.9	-31.5	0.20	0.67	0.49	δ ¹⁸ O	IRMS	2.5
Dome F ^{c,3}	302 – 307	9.6	-57.3	0.04	0.61	0.93	δD, δ ¹⁸ O	CFA1102	0.5
Dome C ^{d,4}	308 – 318	9.9	-53.5	0.04	0.65	0.93	δD, δ ¹⁸ O	IRMS	2.5
GRIP early ^f	1449 – 1466	9.4	-31.6	0.23	0.65	0.42	δD, δ ¹⁸ O	2130	2.5
NEEM dis ^{g,5}	1380 – 1392	10.9	-29.0	0.22	0.72	0.31	δD, δ ¹⁸ O	2120	5.0
NEEM CFA ^{g,5}	1382 – 1399	10.9	-29.0	0.22	0.72	0.31	δD, δ ¹⁸ O	CFA1102	0.5
NGRIP I ^e	1300 – 1320	9.1	-31.5	0.18	0.67	0.55	δ ¹⁸ O	IRMS	5.0
NGRIP II ^e	1300 – 1320	9.1	-31.5	0.18	0.67	0.55	δ ¹⁸ O	IRMS	5.0

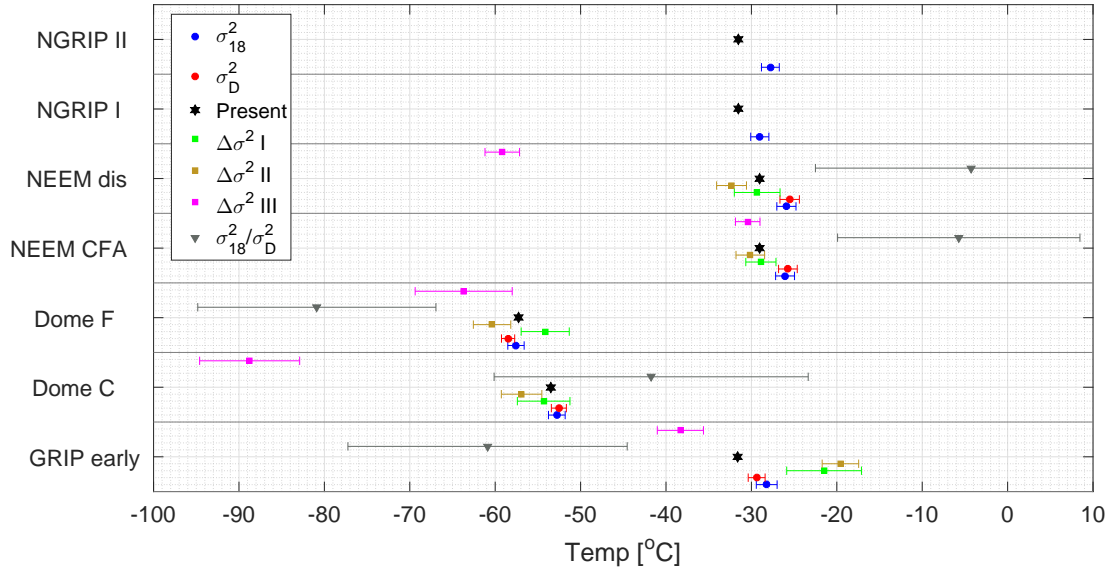


Figure 3.13. Early Holocene section with reconstructed temperatures from the σ_{18}^2 (blue circles), σ_D^2 (red circles), $\Delta\sigma^2$ I (green squares), $\Delta\sigma^2$ II (brown squares), $\Delta\sigma^2$ III (magenta squares) and σ_{18}^2/σ_D^2 (grey triangles) methods. The black stars represent the present annual mean temperatures at the sites.

Table 3.4. Ice core results with the estimated firn diffusion lengths and their corresponding temperatures [$^{\circ}\text{C}$]. The units for the σ_{18} and the σ_D values are expressed in cm and the unit for $^{18}\Delta\sigma^2$ is expressed in cm^2 .

Site Name	σ_{18}	σ_D	$^{18}\Delta\sigma^2$ I	$^{18}\Delta\sigma^2$ II	$^{18}\Delta\sigma^2$ III	σ_{18}^2/σ_D^2
GRIP mid	$7.83 \pm 0.17 \text{ cm}$	$7.20 \pm 0.16 \text{ cm}$	$9.4 \pm 1.0 \text{ cm}^2$	$9.6 \pm 0.7 \text{ cm}^2$	$0.2 \pm 0.1 \text{ cm}^2$	1.18 ± 0.02
	$-33.0 \pm 1.1 \text{ }^{\circ}\text{C}$	$-33.0 \pm 1.0 \text{ }^{\circ}\text{C}$	$-32.7 \pm 2.0 \text{ }^{\circ}\text{C}$	$-32.3 \pm 1.5 \text{ }^{\circ}\text{C}$	$-80.6 \pm 2.9 \text{ }^{\circ}\text{C}$	$-34.4 \pm 6.6 \text{ }^{\circ}\text{C}$
GRIP late	$8.52 \pm 0.12 \text{ cm}$	$7.92 \pm 0.16 \text{ cm}$	$9.9 \pm 0.8 \text{ cm}^2$	$8.6 \pm 0.5 \text{ cm}^2$	$4.8 \pm 0.5 \text{ cm}^2$	1.16 ± 0.02
	$-30.6 \pm 1.1 \text{ }^{\circ}\text{C}$	$-30.5 \pm 1.1 \text{ }^{\circ}\text{C}$	$-31.8 \pm 1.8 \text{ }^{\circ}\text{C}$	$-34.1 \pm 1.5 \text{ }^{\circ}\text{C}$	$-43.0 \pm 1.7 \text{ }^{\circ}\text{C}$	$-24.4 \pm 8.7 \text{ }^{\circ}\text{C}$
WAIS 2005A	$7.05 \pm 0.11 \text{ cm}$	—————	—————	—————	—————	—————
	$-31.7 \pm 1.1 \text{ }^{\circ}\text{C}$	—————	—————	—————	—————	—————
EDML	$7.72 \pm 0.09 \text{ cm}$	$7.12 \pm 0.08 \text{ cm}$	$8.9 \pm 0.3 \text{ cm}^2$	$8.1 \pm 0.3 \text{ cm}^2$	$7.1 \pm 0.2 \text{ cm}^2$	1.18 ± 0.01
	$-42.8 \pm 0.9 \text{ }^{\circ}\text{C}$	$-42.5 \pm 0.9 \text{ }^{\circ}\text{C}$	$-44.6 \pm 1.1 \text{ }^{\circ}\text{C}$	$-45.9 \pm 1.0 \text{ }^{\circ}\text{C}$	$-47.6 \pm 1.0 \text{ }^{\circ}\text{C}$	$-32.4 \pm 3.1 \text{ }^{\circ}\text{C}$
NEEM	$7.98 \pm 0.22 \text{ cm}$	$7.20 \pm 0.32 \text{ cm}$	$11.8 \pm 1.6 \text{ cm}^2$	$10.2 \pm 1.1 \text{ cm}^2$	$4.5 \pm 2.0 \text{ cm}^2$	1.23 ± 0.05
	$-31.8 \pm 1.1 \text{ }^{\circ}\text{C}$	$-32.4 \pm 1.4 \text{ }^{\circ}\text{C}$	$-28.4 \pm 2.6 \text{ }^{\circ}\text{C}$	$-30.7 \pm 2.1 \text{ }^{\circ}\text{C}$	$-45.9 \pm 10.1 \text{ }^{\circ}\text{C}$	$-49.3 \pm 15.0 \text{ }^{\circ}\text{C}$
NGRIP	$9.24 \pm 0.20 \text{ cm}$	—————	—————	—————	—————	—————
	$-29.8 \pm 1.1 \text{ }^{\circ}\text{C}$	—————	—————	—————	—————	—————
Dome F	$5.76 \pm 0.15 \text{ cm}$	$4.92 \pm 0.06 \text{ cm}$	$9.0 \pm 1.8 \text{ cm}^2$	$5.4 \pm 0.8 \text{ cm}^2$	$4.4 \pm 1.9 \text{ cm}^2$	1.37 ± 0.08
	$-57.6 \pm 1.0 \text{ }^{\circ}\text{C}$	$-58.5 \pm 0.8 \text{ }^{\circ}\text{C}$	$-54.2 \pm 2.8 \text{ }^{\circ}\text{C}$	$-60.4 \pm 2.2 \text{ }^{\circ}\text{C}$	$-63.7 \pm 5.7 \text{ }^{\circ}\text{C}$	$-80.9 \pm 14.0 \text{ }^{\circ}\text{C}$
Dome C	$6.97 \pm 0.15 \text{ cm}$	$6.34 \pm 0.08 \text{ cm}$	$8.4 \pm 1.9 \text{ cm}^2$	$6.7 \pm 1.1 \text{ cm}^2$	$0.4 \pm 0.4 \text{ cm}^2$	1.21 ± 0.05
	$-52.8 \pm 1.0 \text{ }^{\circ}\text{C}$	$-52.5 \pm 0.9 \text{ }^{\circ}\text{C}$	$-54.3 \pm 3.0 \text{ }^{\circ}\text{C}$	$-56.9 \pm 2.3 \text{ }^{\circ}\text{C}$	$-88.8 \pm 5.9 \text{ }^{\circ}\text{C}$	$-42.8 \pm 18.4 \text{ }^{\circ}\text{C}$
GRIP early	$9.31 \pm 0.24 \text{ cm}$	$8.25 \pm 0.09 \text{ cm}$	$18.7 \pm 4.0 \text{ cm}^2$	$20.4 \pm 1.9 \text{ cm}^2$	$6.6 \pm 1.1 \text{ cm}^2$	1.27 ± 0.06
	$-28.2 \pm 1.2 \text{ }^{\circ}\text{C}$	$-29.4 \pm 1.0 \text{ }^{\circ}\text{C}$	$-21.5 \pm 4.4 \text{ }^{\circ}\text{C}$	$-19.6 \pm 2.1 \text{ }^{\circ}\text{C}$	$-38.4 \pm 2.7 \text{ }^{\circ}\text{C}$	$-60.9 \pm 16.4 \text{ }^{\circ}\text{C}$
NEEM dis	$10.33 \pm 0.19 \text{ cm}$	$9.72 \pm 0.20 \text{ cm}$	$12.1 \pm 1.8 \text{ cm}^2$	$10.0 \pm 0.9 \text{ cm}^2$	$1.6 \pm 0.2 \text{ cm}^2$	1.13 ± 0.02
	$-25.9 \pm 1.1 \text{ }^{\circ}\text{C}$	$-25.5 \pm 1.1 \text{ }^{\circ}\text{C}$	$-29.3 \pm 2.7 \text{ }^{\circ}\text{C}$	$-32.3 \pm 1.8 \text{ }^{\circ}\text{C}$	$-59.2 \pm 2.0 \text{ }^{\circ}\text{C}$	$-4.2 \pm 18.3 \text{ }^{\circ}\text{C}$
NEEM CFA	$10.27 \pm 0.19 \text{ cm}$	$9.65 \pm 0.18 \text{ cm}$	$12.3 \pm 1.1 \text{ cm}^2$	$11.4 \pm 0.9 \text{ cm}^2$	$11.2 \pm 0.6 \text{ cm}^2$	1.13 ± 0.01
	$-26.1 \pm 1.1 \text{ }^{\circ}\text{C}$	$-25.7 \pm 1.1 \text{ }^{\circ}\text{C}$	$-29.0 \pm 1.8 \text{ }^{\circ}\text{C}$	$-30.1 \pm 1.7 \text{ }^{\circ}\text{C}$	$-30.4 \pm 1.4 \text{ }^{\circ}\text{C}$	$-5.7 \pm 14.2 \text{ }^{\circ}\text{C}$
NGRIP I	$9.68 \pm 0.16 \text{ cm}$	—————	—————	—————	—————	—————
	$-29.0 \pm 1.1 \text{ }^{\circ}\text{C}$	—————	—————	—————	—————	—————
NGRIP II	$10.14 \pm 0.17 \text{ cm}$	—————	—————	—————	—————	—————
	$-27.8 \pm 1.0 \text{ }^{\circ}\text{C}$	—————	—————	—————	—————	—————

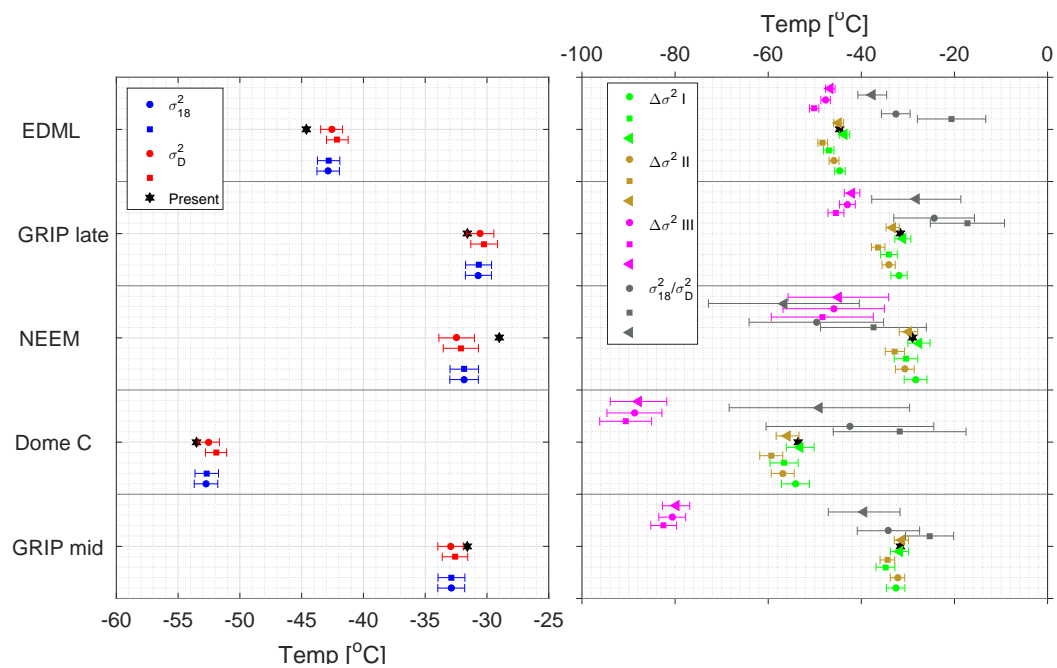


Figure 3.14. Temperature reconstructions based on different fractionation factor parameterizations. The left figure shows the single isotopologue methods and the right figure shows the dual isotope methods. Circles correspond to fractionation factors from Majoube, (1970) and Merlivat and Nief, (1967), squares correspond to fractionation factors from Ellehoj et al., (2013) and triangles from Lamb et al., (2017) and Majoube, (1970).

of all the techniques tested, yield the highest precision with a $s_{\bar{T}} \approx 1.0^\circ\text{C}$ (the average precision $s_{\bar{T}}$ of each technique is calculated by averaging the variances of all simulations). Additionally, the estimated temperatures \bar{T} are within $1s_{\bar{T}}$ of the forcing temperature T_{sur} , a result pointing to a good performance with respect to the accuracy of the temperature estimation.

The precision of the differential diffusion techniques is slightly inferior to single diffusion with the subtraction technique being the least precise of all three differential diffusion approaches ($s_{\bar{T}} \approx 2.6^\circ\text{C}$). A possible reason for this result may be the fact that the subtraction technique relies on the tuning of 8 optimization parameters as described in Sec. 3.4.1 and 3.4.2. Both the linear fit and the correlation techniques yield precision estimates of 1.8°C and 1.3°C , respectively. Despite the high precision of the correlation technique, the tests shows that the technique has a bias toward colder temperatures. The linear fit is therefore the most optimal of the differential diffusion techniques. All 10 experiments utilizing differential diffusion methods, yield an accuracy that lies within the $2s_{\bar{T}}$ range ($1s_{\bar{T}}$ range for 9 out of 10 experiments). We can conclude that experiments involving the estimation of the diffusion length ratio indicate that the latter are practically unusable due to very high uncertainties with $s_{\bar{T}}$ averaging to a value of $\approx 16^\circ\text{C}$ for all four experiments. A general trend that seems to be apparent for all the experiments, is that the results for the case A forcing yield slightly lower uncertainties when compared to those for the case B forcing, likely indicating a temperature and accumulation influence in the performance of all the reconstruction techniques.

3.6.2 Ice core data

3.6.2.1 The estimation of diffusion length from spectra

From the spectra presented in Appendix A.6, we can see that the diffusion plus noise model (Eq. 20) provides good fits to the ice core data. For ice core sections with a resolution equal to (or higher than) 2.5 cm, we start seeing a difference in the spectral signature of the noise tail between the data from Greenland and Antarctica. The low accumulation Antarctic ice core sites seem to best represent the diffusion plus white noise model used in the synthetic data test. For instance, the PSD of Dome C in Fig. A.32 (Appendix A.6) resembles well that of the synthetic data in Fig. 3.5, whereas a slightly more red noise tail is evident for the high accumulation sites on Greenland. We don't know why the noise for some of the Greenlandic sites behaves differently, but the white noise of the Antarctic ice core data coincides well with isotopic signals that likely comprise of a few events per year and is whiten due to post depositional effects such as snow relocation. Nonetheless, the AR-1 noise model in Eq. 20 describes both the red and white noise well.

An example of how sample resolution plays a role in assessing the value of the estimated diffusion length, can be seen when visually comparing the spectra of the NEEM early Holocene data in Fig. A.8 and A.11. The lack of sufficient resolution in Fig A.11 (discrete 5 cm data) results in a poorly resolved noise signal. On the contrary, the 0.5 cm resolution of the CFA obtained data (both datasets are from approximately the same depth interval) allows for a much better insight into the noise characteristics of the isotopic time series and therefore a more robust diffusion length estimation. Despite differences in the resolution of the power spectra, the fitting procedure provides similar estimates of the firn diffusion lengths as seen in Table 3.4. This result indicates that even though the diffusion length can be estimated with less certainty, the diffusion length is still preserved in the signal which underlines how powerful a technique the spectral estimation of diffusion length is.

In this study, the annual peak is removed in five out of thirteen cases. However, we do not see any distinguished multiannual variability manifested as spectral peaks. A correction similar to that of the annual peak filter is therefore not implemented. This does not necessarily mean that there is no imprint in those bands to start with, but our analysis does not indicate this and these signals are either too weak to noticeably affect the fits of the assumed model (i.e. diffusion plus noise) or they cannot be resolved at all because their power lies lower than the measurement noise.

3.6.2.2 *The temperature reconstructions*

The precision $s_{\bar{T}}$ of each reconstruction technique has been quantified by averaging the variances of the reconstructed temperatures (Table 3.4). In accordance with the results from the synthetic data test, the most precise reconstructions are obtained when using the single isotope diffusion methods. The single diffusion methods have a $s_{\bar{T}}$ of 1.1 °C, while the differential diffusion methods $^{18}\Delta\sigma^2$ I, II and III have a $s_{\bar{T}}$ of 2.6 °C, 1.9 °C and 4.8 °C, respectively. The correlation-based technique is hereby shown to be the least precise differential diffusion method. This differs from the result of the synthetic data, where the correlation-based technique had the most precise results. Of the differential diffusion methods, the linear fit of the logarithmic ratio provides the most precise results, with a precision similar to that found from the synthetic data (Sec. 3.6.1). Of all the tested techniques, the diffusion length ratio method is the least precise with a $s_{\bar{T}}$ of 11.8 °C. A similar precision was found from the synthetic data.

The perturbations of the model parameters help achieve a realistic view on the overall precision and it facilitates a comparison between the single and the differential diffusion techniques. Nonetheless, we want to emphasize that the presented precisions do not represent the absolute obtainable precision of the diffusion-based temperature reconstruction techniques. While the

uncertainties presented in Table 3.1 represents typical Holocene values estimated for Central Greenland and the East Antarctic Ice Cap, the input parameters' uncertainties in the firn diffusion model are essentially both depth and site dependent. For instance, we have a better knowledge about the ice flow thinning at a low accumulation site e.g. Dome C compared to that of a high accumulation site e.g. NGRIP for early Holocene ice core data, This is a result of the Dome C site's early Holocene period being at a depth of 300m while the NGRIP site's early Holocene period is at a depth of 1300m. Additionally, it is more more difficult to estimate the glacial accumulation rate at sites where the present day values already are very low. Basically, inferring a change between 3cm/yr and 1.5cm/yr (and how stable this 1.5cm/yr estimate is during the glacial) is much harder and with higher uncertainties compared to going from 23cm/yr to 10cm/yr (where annual layer thickness information is available from chemistry). Similarly, ρ_{co} and ρ_o are better known for Holocene conditions and likely close to present day values while glacial conditions represent a regime at which those values may change more considerably. Thus, when utilizing the diffusion techniques on long ice core records, we propose that the uncertainties of such model parameters and corrections should be based on specific characteristics of the ice core site and the part (or depth) of the core under consideration.

It is not possible to quantify the accuracy of the methods when applied on short ice core data sections, as the reconstructed temperatures represent the integrated firn column temperature. Even though the firn diffusion model has a polythermal firn layer due to the seasonal temperature variation, we can only estimate a single value of the diffusion length from the data (the exact temperature gradients a layer has experienced is unknown). The reconstructed temperatures should therefore not necessarily be completely identical to present day annual temperatures. However, clear outliers can still be inferred from the data as Holocene temperature estimates that deviate with 30°C from the present day annual mean temperatures are unrealistic.

First we address the correlation-based and diffusion length ratio techniques as these two methods result in temperatures that clearly deviate with present day annual mean temperatures (Fig. 3.12 and 3.13). Besides the low precision of the diffusion length ratio method, temperature estimates using the the correlation-based and diffusion length ratio techniques are highly inconsistent with the results of the other techniques, with root-mean-square deviations (RMSD) varying from 21 °C to 34 °C. In addition, it can be seen that the correlation-based method results in significantly different temperatures for the discretely and continuously measured NEEM section. A similar difference is not found from the spectral-based methods. Instead, these provide consistent temperatures independent of the processing scheme. The generally poor performance of the correlation-based method on ice core data contradicts the high accuracy

and precision of the synthetic reconstructions, and is most likely caused by an oversimplification of the relationship between δD and $\delta^{18}O$. The generation of the synthetic data is based on the assumption that $\delta D = 8 \cdot \delta^{18}O + 10\%$. However, this premise neglects the time dependent d_{xs} signal. The correlation-based method can therefore be used to accurately reconstruct synthetic temperatures, while the accuracy and precision are much lower for ice core data, as such data has been influenced by the d_{xs} signal. In addition, these temperature estimates have been shown to be dependent on the sampling process. The correlation-based method therefore yields uncertain estimates of the differential diffusion length.

The temperature estimates originating from the σ_{18}^2 and σ_D^2 methods are found to have a RMSD of $0.7^\circ C$. This shows that the σ_{18}^2 and σ_D^2 methods result in similar temperatures, which is consistent with the high accuracies found from the synthetic data test. Furthermore, the early Holocene ice core data from Greenland consistently shows reconstructed temperatures warmer than present day (Fig. 3.13), which corresponds well with a HCO of around $3^\circ C$ warming as found by Dahl-Jensen et al., (1998) and Vinther et al., (2009). With the exception of WAIS D, the estimated temperatures for the late-mid Holocene using the σ_{18}^2 and σ_D^2 methods are either slightly warmer or colder than present day (Fig. 3.12). These sections represent ages ranging from 0.9 to 3.7 ka and it is not unreasonable to assume that the sites' surface temperatures have varied in time. We emphasize that some of the presented ice core sections are as short as 15 m, and that such temperature estimates will potentially be more similar to present day when averaged over a long time series.

The temperature estimates of the $^{18}\Delta\sigma^2$ I method are similar to the present day annual temperature in six out of nine cases. However, the results of the $^{18}\Delta\sigma^2$ I and II techniques have a RMSD of $3.8^\circ C$. The seemingly accurate performance of the $^{18}\Delta\sigma^2$ I method could be either a coincidence or correct. Two of the similar temperature results are from the NEEM early Holocene data that likely should have had warmer surface temperatures than present day. It is therefore difficult to select the most accurate results as both of the differential diffusion techniques before performed well in the accuracy test with the synthetic data. One should therefore not have a preferred technique without utilizing both methods on longer ice core sections. Basically, the reconstructed temperatures could be similar when the temperatures have been averaged over a longer record. Besides the internal differences in the results of the differential techniques, most of the temperature estimates do not match the results of the single diffusion lengths.

3.6.3 *The fractionation factors*

The temperature estimates resulting from the different fractionation factor parametrizations are shown in Fig. 3.14. For each method, the influence of the choice of parametrization on the reconstructed temperatures has been quantified by calculating the RMSD between temperature estimates of two parametrizations. Comparing the parametrizations of Ellehoj et al., (2013) to those of Majoube, (1970) and Merlivat and Nief, (1967), the RMSDs of reconstructions that are based on the single diffusion lengths σ_{18}^2 and σ_D^2 are 0.04°C and 0.4°C . Thus, it is evident that the choice of fractionation factors has an insignificant effect on the results of the σ_{18}^2 method and a small effect on the results of the σ_D^2 method. The choice of parameterization has a greater effect on the temperatures of the $^{18}\Delta\sigma^2$ techniques, where the temperature estimate of the $^{18}\Delta\sigma^2$ I, II and III techniques have RMSDs of 2.3°C , 2.3°C and 2.2°C , respectively. Comparing the parametrization of Lamb et al., (2017) to that of Merlivat and Nief, (1967), the temperatures of the $^{18}\Delta\sigma^2$ I, II and III techniques have RMSDs of 0.9°C , 0.9°C and 1.0°C , respectively. In general, smaller RMSDs are found when comparing with temperature estimates based on the Lamb et al., (2017) parametrization. For instance, comparing the temperatures of the σ_{18}^2/σ_D^2 technique based on Lamb et al., (2017) with those of Merlivat and Nief, (1967), the σ_{18}^2/σ_D^2 technique yields a RMSD of 5.9°C , while the RMSD is 11.0°C when comparing the results based on the parametrizations of Ellehoj et al., (2013) with those of Majoube, (1970) and Merlivat and Nief, (1967). There are two reasons to why the RMSDs are smaller when comparing with the Lamb et al., (2017) parametrization: the parametrized α_D of Merlivat and Nief, (1967) differs more with that of Ellehoj et al., (2013) than with that of Lamb et al., (2017), and the same α_{18} parametrization is used when comparing with Lamb et al., (2017).

The σ_{18}^2/σ_D^2 method is significantly more influenced by the fractionation factors. The high RMSDs imply that even if the diffusion length ratio is estimated with high confidence, the method is still too sensitive to the choice of parameterization. This makes the method less suitable as a paleoclimatic thermometer.

3.6.4 *Outlook with respect to ice core measurements*

It is obvious from the analysis we present here that the type of isotopic analysis chosen has an impact on the quality of the power spectral estimates and subsequently on the diffusion length estimation. One such important property of the spectral estimation that is directly dependent on the nature of the isotopic analysis is the achievable Nyquist frequency, defined by the sampling resolution Δ of the isotopic time series. The value of the Nyquist frequency f_{Nq} sets the limit in

the frequency space until which a power spectral estimate can be obtained. The higher the value of f_{Nq} , the more likely it is that the noise part $|\hat{\eta}(k)|^2$ of the power spectrum will be resolved by the spectral estimation routine. The deeper the section under study, the higher the required f_{Nq} due to the fact that the ice flow thinning results in a progressively lower value for the diffusion length and as a result the diffusion part of the spectrum extends more into the higher frequencies. This effect manifests particularly in the case of the early Holocene Greenland sections of this study. For the case of the NEEM early Holocene record, one can observe the clear benefit of the higher sampling resolution by comparing the discrete ($\Delta = 5$ cm) to the the CFA ($\Delta = 0.5$ cm) data set. Characterizing the noise signal $|\hat{\eta}(k)|^2$ is more straight forward in the case of the CFA data. On the contrary, at these depths of the NEEM core, the resolution of 5 cm results in the spectral estimation not being able to resolve the noise signal.

The diffusion of the sampling and measurement process itself is a parameter that needs to be thoroughly addressed particularly during the development and construction of a CFA system as well as during the measurement of an ice core with such a system. Ideally, one would aim for (a) a dispersive behavior that resembles as close as possible that of Gaussian mixing, (b) a measurement system diffusion length σ_{cfa} that is as low as possible and (c) a diffusive behavior that is stable as a function of time. Real measurements with CFA systems indicate that most likely due to surface effects in the experimental apparatus that lead to sample memory, the transfer functions of such systems depart from the ideal model of Gaussian dispersion showing a slightly skewed behavior. For some systems, this behavior resembles more that of a slightly skewed Log-Normal distribution (Gkinis et al., 2011; Maselli et al., 2013; Emanuelsson et al., 2015) or a more skewed distribution that in the case of Jones et al., (2017) requires the product of two Log-Normal distributions to be accurately modeled. The result of this behavior to the power spectral density is still a matter of further study as high resolution datasets obtained with CFA systems are relatively recent.

Additionally the accuracy of the depth registration is essential in order for accurate spectral estimates to be possible. Instabilities in melt rates of the ice stick under consideration can in principle be addressed and a first-order correction can be available assuming a length encoder is installed in the system. Such a correction though does not take into account the fact that due to the constant sample flow rate through the CFA system, the constant mixing volume of the system's components (sample tubing, valves etc) will cause a variable mixing as melt rates change. The magnitudes and importance of these variations are not easy to assess and more work will be required in the future in order to characterize and correct for these effects.

Due to the recent advances in laser spectroscopy we expect measurements of the $\delta^{17}\text{O}$ signal to be a common output from analyzed ice cores. As we showed with synthetic data, such

a signal can also be used to reconstruct temperatures. Especially the differential diffusion length of $\delta^{17}\text{O}$ and δD showed higher precision than that of $\delta^{18}\text{O}$ and δD . Such measurements however, require that laboratories around the world have access to well calibrated standards. Calibration protocols for $\delta^{17}\text{O}$ have been suggested (Schoenemann et al., 2013) although there is still a lack of $\delta^{17}\text{O}$ values for the International Atomic Energy Agency standards VSMOW (Vienna Standard Mean Ocean Water) and SLAP (Standard Light Antarctic Precipitation).

3.7 CONCLUSION

This study assessed the performance of six different diffusion-based temperature reconstruction techniques. By applying the methods on synthetic data, first order tests of accuracy and bias were demonstrated and evaluated. Moreover, this approach facilitated precision estimates of each method. The precision of each technique was further quantified by utilizing every variety of the diffusion-based temperature proxy on thirteen high resolution data sets from Greenland and Antarctica. The results showed that the single diffusion length methods yielded similar temperatures and that they are the most precise of all the presented reconstruction techniques. The most precise of the three differential diffusion length techniques was the linear fit of the logarithmic ratio. The most uncertain way of reconstructing past temperatures was by employing the diffusion length ratio method. The results from the correlation-based method were inconsistent to the results obtained through the spectral-based methods, and the method was considered to yield uncertain estimates of the differential diffusion length.

It was furthermore shown that the choice of fractionation factor parametrization only had a small impact on the results from the single diffusion length methods, while the influence was slightly higher for the differential diffusion length methods. The diffusion length ratio method was highly sensitive to the fractionation factor parametrization, and the method is not suitable as a paleoclimatic thermometer.

In conclusion, despite that the dual diffusion techniques seem to be the more optimal choices due to their independence of sampling and ice diffusion or densification and thinning processes, the uncertain estimates should outweigh the theoretical advantages for Holocene ice core data.

REFERENCES

Abramowitz, M. and A. Stegun I (1964). *Handbook of Mathematical Functions with Formulas, Graphs, and Mathematical Tables*. 9th. Dover.

- Andersen, N. (1974). "On The Calculation Of Filter Coefficients For Maximum Entropy Spectral Analysis". In: *Geophysics* 39.1.
- Baker, L., I. A. Franchi, J. Maynard, I. P. Wright, and C. T. Pillinger (2002). "A technique for the determination of O-18/O-16 and O-17/O-16 isotopic ratios in water from small liquid and solid samples". In: *Analytical Chemistry* 74.7, pp. 1665–1673.
- Banta, J. R., J. R. McConnell, M. M. Frey, R. C. Bales, and K. Taylor (2008). "Spatial and temporal variability in snow accumulation at the West Antarctic Ice Sheet Divide over recent centuries". In: *Journal of Geophysical Research* 113.
- Barkan, E. and B. Luz (2005). "High precision measurements of O-17/O-16 and O-18/O-16 ratios in (H₂O)". In: *Rapid Communications In Mass Spectrometry* 19.24, pp. 3737–3742.
- Begley, I. S. and C. M. Scrimgeour (1997). "High-precision $\delta^2\text{H}$ and $\delta^{18}\text{O}$ measurement for water and volatile organic compounds by continuous-flow pyrolysis isotope ratio mass spectrometry". In: *Analytical Chemistry* 69.8, pp. 1530–1535.
- Bigeleisen, J., M. L. Perlman, and H. C. Prosser (1952). "Conversion Of Hydrogenic Materials To Hydrogen For Isotopic Analysis". In: *Analytical Chemistry* 24.8, pp. 1356–1357.
- Blicks, H., O. Dengel, and N. Riehl (1966). "Diffusion Von Protonen (tritonen) In Reinen Und Dotierten Eis-einkristallen". In: *Physik Der Kondensierten Materie* 4.5, pp. 375–381.
- Brand, W. A., H. Geilmann, E. R. Crosson, and C. W. Rella (2009). "Cavity ring-down spectroscopy versus high-temperature conversion isotope ratio mass spectrometry; a case study on $\delta^2\text{H}$ and $\delta^{18}\text{O}$ of pure water samples and alcohol/water mixtures". In: *Rapid Communications in Mass Spectrometry* 23.12, pp. 1879–1884.
- Craig, H. (1961). "Isotopic Variations in Meteoric Water". In: *Science* 133.3465, pp. 1702–1703.
- Crosson, E. R. (2008). "A cavity ring-down analyzer for measuring atmospheric levels of methane, carbon dioxide, and water vapor". In: *Applied Physics B-Lasers And Optics* 92.3, pp. 403–408.
- Cuffey, K. M., R. B. Alley, P. M. Grootes, J. M. Bolzan, and S. Anandakrishnan (1994). "Calibration Of the Delta-O-18 isotopic paleothermometer for central Greenland, using borehole temperatures". In: *Journal Of Glaciology* 40.135, pp. 341–349.
- Dahl-Jensen, D., K. Mosegaard, N. Gundestrup, G. D Clow, S. J. Johnsen, A. W. Hansen, and N. Balling (1998). "Past temperatures directly from the Greenland Ice Sheet". In: *Science* 282.5387, pp. 268–271.
- Dansgaard, W. (1964). "Stable isotopes in precipitation". In: *Tellus B* 16.4, pp. 436–468.
- Dansgaard, W. (1954). "The ^{18}O -abundance in fresh water". In: *Geochimica et Cosmochimica Acta* 6.5–6, pp. 241–260.

- Dansgaard, W. and S. J. Johnsen (1969). “A flow model and a time scale for the ice core from Camp Century, Greenland”. In: *Journal of Glaciology* 8.53.
- Delibaltas, P., O. Dengel, D. Helmreich, N. Riehl, and H. Simon (1966). “Diffusion Von ^{18}O In Eis-einkristallen”. In: *Physik Der Kondensierten Materie* 5.3, pp. 166–170.
- Ellehoj, M. D., H. C. Steen-Larsen, S. J. Johnsen, and M. B. Madsen (2013). “Ice-vapor equilibrium fractionation factor of hydrogen and oxygen isotopes: Experimental investigations and implications for stable water isotope studies”. In: *Rapid Communications in Mass Spectrometry* 27, pp. 2149–2158.
- Emanuelsson, B. D., W. T. Baisden, N. A. N. Bertler, E. D. Keller, and V. Gkinis (2015). “High-resolution continuous-flow analysis setup for water isotopic measurement from ice cores using laser spectroscopy”. In: *Atmos. Meas. Tech.* 8.7, pp. 2869–2883.
- Epstein, S., R. Buchsbaum, H. Lowenstam, and H.C. Urey (1951). “Carbonate-water isotopic temperature scale”. In: *Geological Society of America Bulletin* 62.4, p. 417.
- Gehre, M., R. Hoefling, P. Kowski, and G. Strauch (1996). “Sample preparation device for quantitative hydrogen isotope analysis using chromium metal”. In: *Analytical Chemistry* 68.24, pp. 4414–4417.
- Gkinis, V. (2011). “High resolution water isotope data from ice cores”. PhD thesis. University of Copenhagen.
- Gkinis, V., T. J. Popp, T. Blunier, M. Bigler, S. Schupbach, E. Kettner, and S. J. Johnsen (2011). “Water isotopic ratios from a continuously melted ice core sample”. In: *Atmospheric Measurement Techniques* 4.11, pp. 2531–2542.
- Gkinis, V., S. B. Simonsen, S. L. Buchardt, J. W. C. White, and B. M. Vinther (2014). “Water isotope diffusion rates from the NorthGRIP ice core for the last 16,000 years - glaciological and paleoclimatic implications”. In: *Earth and Planetary Science Letters* 405.
- Guillevic, M. et al. (2013). “Spatial gradients of temperature, accumulation and $\delta^{18}\text{O}$ -ice in Greenland over a series of Dansgaard—Oeschger events”. In: *Climate of the Past* 9, pp. 1029–1051.
- Herron, M. M. and C. C. Langway (1980). “Firn Densification: An Empirical Model”. In: *Journal of Glaciology* 25.93.
- Itagaki, Kazuhiko (1964). “Self-Diffusion in Single Crystals of Ice”. In: *J. Phys. Soc. Jpn.* 19.6, pp. 1081–1081.
- Johnsen, S. J. (1977). “Stable Isotope Homogenization of Polar Firn and Ice”. In: *Isotopes and Impurities in Snow and Ice*, pp. 210–219.

- Johnsen, S. J., H. B. Clausen, K. M. Cuffey, G. Hoffmann, J. Schwander, and T. Creyts (2000). “Diffusion of stable isotopes in polar firn and ice: the isotope effect in firn diffusion”. In: *Physics of Ice Core Records*, pp. 121–140.
- Johnsen, S. J., D. Dahl-Jensen, W. Dansgaard, and N. Gundestrup (1995). “Greenland paleotemperatures derived from GRIP bore hole temperature and ice core isotope profiles”. In: *Tellus B-Chemical And Physical Meteorology* 47.5, pp. 624–629.
- Johnsen, S. J., D. Dahl-Jensen, N. Gundestrup, J. P. Steffensen, H. B. Clausen, H. Miller, V. Masson-Delmotte, A. E. Sveinbjörnsdóttir, and J. W. C. White (2001). “Oxygen isotope and palaeotemperature records from six Greenland ice-core stations: Camp Century, Dye-3, GRIP, GISP2, Renland and NorthGRIP”. In: *Journal of Quaternary Science* 16.4.
- Johnsen, S. J., W. Dansgaard, and J. W. C. White (1989). “The origin of Arctic precipitation under present and glacial conditions”. In: *Tellus* 41B, pp. 452–468.
- Jones, T. R., J. W. C. White, E. J. Steig, B. H. Vaughn, V. Morris, V. Gkinis, B. R. Markle, and S. W. Schoenemann (2017). “Improved methodologies for continuous-flow analysis of stable water isotopes in ice cores”. In: *Atmos. Meas. Tech* 10, pp. 617–632.
- Jouzel, J. and L. Merlivat (1984). “Deuterium and oxygen 18 in precipitation: modeling of the isotopic effects during snow formation”. In: *Journal of Geophysical Research-Atmospheres* 89.D7, pp. 11749–11759.
- Jouzel, J. et al. (1997). “Validity of the temperature reconstruction from water isotopes in ice cores”. In: *Journal Of Geophysical Research-Oceans* 102.C12, pp. 26471–26487.
- Kawamura, K., T. Nakazawa, S. Aoki, S. Sugawara, Y. Fujii, and O. Watanabe (2003). “Atmospheric CO₂ variations over the last three glacial-interglacial climatic cycles deduced from the Dome Fuji deep ice core, Antarctica using a wet extraction technique”. In: *Tellus* 55B, pp. 126–137.
- Kay, S. M. and S. L. Marple (1981). “Spectrum Analysis - A Modern Perspective”. In: *Proceedings of the IEEE* 69.11.
- Lamb, K. D., B. W. Clouser, M. Bolot, L. Sarkozy, V. Ebert, H. Saathoff, O. Möhler, and E. J. Moyer (2017). “Laboratory measurements of HDO/H₂O isotopic fractionation during ice deposition in simulated cirrus clouds”. In: *PNAS* 114.L22, pp. 5612–5617.
- Livingston, F. E., G. C. Whipple, and S. M. George (1997). “Diffusion of HDO into single-crystal (H₂O)-O-16 ice multilayers: Comparison with (H₂O)-O-18”. In: *Journal of Physical Chemistry B* 101.32, pp. 6127–6131.
- Lorius, C., L. Merlivat, J. Jouzel, and M. Pourchet (1979). “A 30,000-yr isotope climatic record from Antarctic ice”. In: *Nature* 280, pp. 644–648.

- Majoube, M. (1970). “Fractionation factor of ^{18}O between water vapour and ice”. In: *Nature* 226.1242.
- Maselli, O. J., D Fritzsche, L. Layman, J. R. McConnell, and H. Meyer (2013). “Comparison of water isotope-ratio determinations using two cavity ring-down instruments and classical mass spectrometry in continuous ice-core analysis”. In: *Isotopes in Environmental and Health Studies*, pp. 1–12. ISSN: 1025-6016. DOI: 10.1080/10256016.2013.781598.
- Meijer, H. A. J. and W. J. Li (1998). “The use of electrolysis for accurate delta O-17 and delta O-18 isotope measurements in water”. In: *Isotopes In Environmental And Health Studies* 34.4, pp. 349–369.
- Merlivat, L. and G. Nief (1967). “Fractionnement Isotopique Lors Des Changements Detat Solide-Vapeur Et Liquide-Vapeur De Leau A Des Temperatures Inferieures A 0 Degrees C”. In: *Tellus* 19.1, pp. 122–127.
- Mook, J. (2000). *Environmental Isotopes in the Hydrological Cycle Principles and Applications*. International Atomic Energy Agency.
- NGRIP members (2004). “High-resolution record of Northern Hemisphere climate extending into the last interglacial period”. In: *Nature* 431.7005, pp. 147–151.
- Oerter, H., W. Graf, H. Meyer, and F. Wilhelms (2004). “The EPICA ice core Droning Maud Land: first results from stable-isotope measurements”. In: *Ann. Glaciol.* 39, pp. 307–312.
- Press, W. H., S. A. Teukolsky, W. T. Vetterling, and B. P. Flannery (2007). *Numerical Recipes: The Art of Scientific Computing*. Cambridge University Press.
- Ramseier, R. O. (1967). “Self-Diffusion Of Tritium In Natural And Synthetic Ice Monocrystals”. In: *Journal Of Applied Physics* 38.6, pp. 2553–2556.
- Rasmussen, S. O. et al. (2013). “A first chronology for the North Greenland Eemian Ice Drilling (NEEM) ice core”. In: *Climate of the Past* 9, pp. 2713–2730.
- Rasmussen, S. O. et al. (2014). “A stratigraphic framework for abrupt climatic changes during the Last Glacial period based on three synchronized Greenland ice-core records: refining and extending the INTIMATE event stratigraphy”. In: *Quaternary Science Reviews* 106, pp. 14–28.
- Schoenemann, S. W., A. J. Schauer, and E. J. Steig (2013). “Measurement of SLAP2 and GISP $\delta^{17}\text{O}$ and proposed VSMOW-SLAP normalization for $\delta^{17}\text{O}$ and $^{17}\text{O}_{\text{excess}}$ ”. In: *Rapid Commun. Mass Spectrom.* 27, pp. 582–590.
- Severinghaus, J. P. and E. J. Brook (1999). “Abrupt Climate Change at the End of the Last Glacial Period Inferred from Trapped Air in Polar Ice”. In: *Science* 286 (5441), pp. 930–934.

- Severinghaus, J. P., T. Sowers, E. J. Brook, R. B. Alley, and M. L. Bender (1998). “Timing of abrupt climate change at the end of the Younger Dryas interval from thermally fractionated gases in polar ice”. In: *Nature* 391.6663, pp. 141–146.
- Simonsen, S. B., S. J. Johnsen, T. J. Popp, B. M. Vinther, V. Gkinis, and H. C. Steen-Larsen (2011). “Past surface temperatures at the NorthGRIP drill site from the difference in firn diffusion of water isotopes”. In: *Climate of the Past* 7.
- Steig, E. J., V. Gkinis, A. J. Schauer, S. W. Schoenemann, K. Samek, J. Hoffnagle, K. J. Dennis, and S. M. Tan (2014). “Calibrated high-precision ^{17}O -excess measurements using cavity ring-down spectroscopy with laser-current-tuned cavity resonance”. In: *Atmos. Meas. Tech.* 7.8, pp. 2421–2435.
- Steig, E. J. et al. (2013). “Recent climate and ice-sheet change in West Antarctica compared to the past 2000 years”. In: *Nature Geoscience* 6.
- Svensson, A. et al. (2015). “On the occurrence of annual layers in Dome Fuji ice core early Holocene Ice”. In: *Climate of the Past* 11, pp. 1127–1137.
- Vaughn, B. H., J. W. C. White, M. Delmotte, M. Trolier, O. Cattani, and M. Stievenard (1998). “An automated system for hydrogen isotope analysis of water”. In: *Chemical Geology* 152.3-4, pp. 309–319.
- Veres, D. et al. (2013). “The Antarctic ice core chronology (AICC2012): an optimized multi-parameter and multi-site dating approach for the last 120 thousand years”. In: *Climate of the Past* 9.
- Vinther, B. M. et al. (2006). “A synchronized dating of three Greenland ice cores throughout the Holocene”. In: *Journal Of Geophysical Research-Atmospheres* 111.D13102.
- Vinther, B. M. et al. (2009). “Holocene thinning of the Greenland ice sheet”. In: *Nature* 461.
- Watanabe, O., H. Shoji, K. Satow, H. Motoyama, Y. Fujii, H. Narita, and Aoki S. (2003). “Dating of the Dome Fuji, Antarctica deep ice core”. In: *Mem. Natl Inst. Polar Res., Spec. Issue* 57, pp. 25–37.
- Wel, G. van der, H. Fischer, H. Oerter, H. Meyer, and H. A. J. Meijer (2015). “Estimation and calibration of the water isotope differential diffusion length in ice core records”. In: *The Cryosphere* 9.4, pp. 1601–1616.
- Whillans, I. M. and P. M. Grootes (1985). “Isotopic diffusion in cold snow and firn”. In: *Journal of Geophysical Research - Atmospheres* 90, pp. 3910–3918.

A GENERALIZED APPROACH TO ESTIMATING DIFFUSION LENGTH OF STABLE WATER ISOTOPES FROM ICE-CORE DATA

The following chapter is a copy of the paper Kahle et al. (2018):

Kahle, E. C., **Holme, C.**, Jones, T. R., Gkinis, V., & Steig, E. J. (2018). A generalized approach to estimating diffusion length of stable water isotopes from ice-core data. *Journal of Geophysical Research: Earth Surface*, 123, pp: 2377–2391. DOI:10.1029/2018JF004764

4.1 ABSTRACT

Diffusion of water vapor in the porous firn-layer of ice sheets damps high-frequency variations in water-isotope profiles. Through spectral analysis, the amount of diffusion can be quantified as the “diffusion length,” the mean cumulative diffusive-displacement of water molecules relative to their original location at time of deposition. In this study, we use two types of ice-core data, obtained from either continuous-flow analysis or discrete sampling, to separate diffusional effects occurring in the ice sheet from those arising through analytical processes in the laboratory. In both Greenlandic and Antarctic ice cores, some characteristics of the power spectral density of a dataset depend on the water-isotope measurement process. Due to these spectral characteristics, currently established approaches for diffusion estimation do not work equally well for newer, continuously-measured datasets with lower instrument noise levels. We show how smoothing within the continuous-flow analysis system can explain these spectral differences. We propose two new diffusion-estimation techniques, which can be applied to either continuously- or discretely-measured datasets. We evaluate these techniques and demonstrate their viability for future use. The results of this study have the potential to improve climate interpretation of ice-core records as well as models of firn densification and diffusion.

4.2 INTRODUCTION

Water-isotope data have long been used as a climate proxy, based on the temperature-dependent distillation of water isotopes in the atmosphere (Epstein et al., 1951; Dansgaard, 1954; Dansgaard, 1964). Post-depositional processes occurring in an ice sheet alter the original climate signal recorded in the water-isotope ratios. The most dominant alteration to the signal occurs due to diffusion in the firn column, snowfall in the upper tens of meters of an ice sheet that has yet to be fully compressed into ice. Because firn is permeable, water molecules diffuse in the vapor phase along gradients of concentration and temperature (Johnsen, 1977; Whillans and Grootes, 1985). In ice-core research, using water-isotope data to analyze the diffusion process yields information about past firn conditions, including surface temperature, as well as ice-sheet thinning history (Gkinis et al., 2014). Further, if high-frequency climate information, as existed at the ice sheet surface, is to be reconstructed from water-isotope data, a diffusion correction must be applied (Jones et al., 2018).

The diffusion process damps the high-frequency climate variations recorded in a water-isotope profile. The amount of diffusion can be characterized as the “diffusion length,” which represents the mean cumulative diffusive-displacement in the vertical direction of water molecules relative to their original location in the firn at the time of deposition. Through spectral analysis, the diffusion length can be estimated for a section of data based on the damping of its high frequencies. Estimates of diffusion length have been made for many ice cores in both Greenland and Antarctica (Simonsen et al., 2011; Gkinis et al., 2014; Wel et al., 2015; Jones et al., 2017b; Holme et al., 2018a), typically yielding diffusion lengths on the order of ~ 5 to 10 cm at the base of the firn column.

Existing methods for estimating diffusion length do not work equally well for all datasets. In particular, new data obtained using continuous-flow analysis systems with high-precision laser spectrometers have somewhat different spectral characteristics than those obtained by older measurement methods (Jones et al., 2017b). These differences affect the estimation of diffusion lengths, and therefore can also affect climate reconstructions. In this paper, we discuss the spectral structure of continuously-measured data, including possible sources of additional noise that are not present in discretely-measured data and perhaps not perceptible in continuously-measured data with lower instrument precision. We then describe two new approaches for determining diffusion length that can be applied to any high-resolution water-isotope dataset. We use new and previously-published data from ice cores in Greenland and Antarctica to demonstrate the effectiveness of these approaches, and we discuss the broader implications of these improved methods.

4.3 ISOTOPE DIFFUSION THEORY

Water-isotope vapor diffusion occurs in the firn column, where interconnected air pathways allow water vapor to diffuse. At the base of the firn column, firn densification ultimately traps individual air bubbles in solid ice (i.e. the bubble close-off depth), causing vapor diffusion to cease. Solid-phase diffusion continues below the firn layer but is orders of magnitude slower than vapor diffusion in the firn. Vertical strain (compaction of the firn layer and ice thinning by extensional flow) act to progressively reduce the diffusion length. The accumulated solid-ice diffusion begins to compete with the vertical strain only at depth within the ice sheet where the ice is warmer due to geothermal heating. For ice-core sites like NEEM and WAIS Divide, solid ice diffusion is not detected until ages greater than 50ka (Gkinis et al., 2014).

The effects of diffusion, firn compaction, and ice thinning on the isotope profile can be described by Fick's second law:

$$\frac{\partial \delta}{\partial t} = D \frac{\partial^2 \delta}{\partial z^2} - \dot{\epsilon} z \frac{\partial \delta}{\partial z}, \quad (36)$$

where δ is the isotope ratio, D is the diffusivity coefficient, z is the vertical coordinate assuming an origin fixed on a sinking layer of firn, and $\dot{\epsilon}$ is the vertical strain rate (Johnsen, 1977; Whillans and Grootes, 1985). The term $\dot{\epsilon} z$ can be thought of as the vertical velocity.

The diffusion length σ can be calculated from the diffusivity D and the vertical strain rate $\dot{\epsilon}$ by:

$$\frac{d\sigma^2}{dt} - 2\dot{\epsilon}(t)\sigma^2 = 2D(t). \quad (37)$$

Note that the diffusivity $D(t)$ at a given depth in the firn is less than the diffusivity of water vapor in air and the instantaneous value of $D(t)$ is given as follows (following Johnsen et al., (2000)):

$$D = \frac{m p D_a}{R T \alpha \tau} \left(\frac{1}{\rho} - \frac{1}{\rho_{ice}} \right) \quad (38)$$

where m is the molar weight of water, p is the saturation pressure over ice at absolute temperature T , D_a is the diffusivity in air, R is the gas constant, α is the fractionation factor, τ is the tortuosity factor of the firn, ρ is density of the firn, and ρ_{ice} is the density of ice. The diffusivity is different for $\delta^{18}\text{O}$ and δD because D_a and α are different for each isotope ratio.

As shown by Johnsen, (1977), and subsequently used in many studies (Whillans and Grootes, 1985; Cuffey and Steig, 1998; Johnsen et al., 2000; Simonsen et al., 2011; Gkinis et al., 2014; Wel et al., 2015; Jones et al., 2017b; Holme et al., 2018a), the solution to Equation 36 has the

same form as the well-known solution to the heat equation. This solution for the isotope profile at time t and depth z is given by:

$$\delta(z,t) = S(t) \frac{1}{\sigma\sqrt{2\pi}} \int_{-\infty}^{\infty} \delta(z,0) \exp\left(-\frac{(z-u)^2}{2\sigma^2}\right) du. \quad (39)$$

A complete derivation of this solution is available in textbooks (e.g. Lasaga, (2014)). The factor $S(t)$ is the total thinning a layer has experienced due to ice flow from $t = 0$ to $t = t'$:

$$S(t') = \exp\left(\int_0^{t'} \dot{\epsilon}(t) dt\right), \quad (40)$$

Equation 39 is equivalent to the convolution of the initial isotope profile, $\delta(z,0)$, with a Gaussian filter of standard deviation equal to the diffusion length σ (Johnsen et al., 2000):

$$\mathcal{G} = \frac{1}{\sigma\sqrt{2\pi}} \exp\left(\frac{-z^2}{2\sigma^2}\right). \quad (41)$$

4.4 WATER-ISOTOPE DATA

Traditionally, water-isotope data are measured discretely by cutting small sections of the core (~ 1 to 50 cm) to produce a sample. The isotope ratio of each discrete sample is determined by mass spectrometry (Johnsen et al., 1972; Brand et al., 2009; Schoenemann et al., 2013) or with newer laser spectroscopy instruments (Kerstel et al., 1999; Lis et al., 2008; Gupta et al., 2009). In the past decade, it has also become common for ice-core water-isotope measurements to be made using continuous-flow analysis (CFA) systems. CFA systems allow for continuous injection of a stream of water-vapor sample from a continuously melted ice stick into the cavity of a laser spectrometer, yielding data of high resolution and precision (Gkinis et al., 2011a; Emanuelsson et al., 2015; Jones et al., 2017a). A typical nominal resolution for CFA datasets is 0.5 cm.

Various CFA systems exist; in this work we consider datasets measured with two different CFA systems (Gkinis et al., 2010; Gkinis et al., 2011a; Jones et al., 2017a). We use previously-published data from the WAIS Divide ice core (WDC) (Jones et al., 2017b) and sections of data from a new ice core at the South Pole (SPC), both measured with the CFA system at the Institute of Arctic and Alpine Research (INSTAAR) at the University of Colorado. Details of the SPC ice-core project are given in Casey et al., (2014). A Picarro L2130-*i* laser spectrometer was used for $\delta^{18}\text{O}$ and δD measurements; details are given in Jones et al., (2017a). We use the first 2800 m of WDC, corresponding to approximately the last 30,000 years. We use two sections of SPC, one from the Holocene and one from the last glacial period. For comparison, we use data

Table 4.1. Summary of the datasets used in this paper and plotted in Figure 4.2. *Second section of SPC is plotted in Figure 4.4.

Core	Analysis Method	Depths (m)	Resolution (m)
Dome C	discrete	308-318	0.025
NEEM	discrete	174-194	0.025
EDML	discrete	123-173	0.05
WDC	discrete	260-290	0.05
GRIP	discrete	753-776	0.025
NGRIP	discrete	1300-1320	0.05
Dome F	continuous	302-307	0.005
NEEM	continuous	1382-1399	0.005
SPC	continuous	450-500	0.005
SPC	continuous	1060-1075*	0.005
WDC	continuous	450-500	0.005

from NEEM and Dome F (Gkinis et al., 2011a; Svensson et al., 2015) measured on a second CFA system at the University of Copenhagen. We also use discrete datasets from Greenlandic and Antarctic ice cores, including GRIP, EDML, NEEM, WDC, NGRIP, and Dome C (Oerter et al., 2004; Gkinis et al., 2011a; Gkinis, 2011; Steig et al., 2013; Gkinis et al., 2014; Holme et al., 2018a). These datasets are summarized in Table 4.1.

4.5 ESTIMATING DIFFUSION LENGTH FROM ICE-CORE DATA

To estimate the extent of diffusion from ice-core data, we begin with the description of isotope diffusion outlined above. The computation of the convolution that yields Equation 39 can be performed in the frequency domain, using the convolution theorem:

$$\delta(z, t) = \delta(z, 0) * \mathcal{G} \quad \Rightarrow \quad \hat{\delta}(z, t) = \hat{\delta}(z, 0) \cdot \hat{\mathcal{G}}, \quad (42)$$

where $*$ represents convolution and $\hat{}$ represents the Fourier transform. The Fourier transform of a Gaussian is itself a Gaussian, and therefore the transfer function of the diffusion process is given by:

$$\mathcal{F}(\mathcal{G}) = \hat{\mathcal{G}} = \exp\left(\frac{-k^2 \sigma^2}{2}\right), \quad (43)$$

where $k = 2\pi f$ and f is the frequency of the signal.

Combining Equations 42 and 43, the expected loss in the amplitude of the signal at frequency f is given by:

$$\Gamma = \Gamma_0 \exp\left(\frac{-k^2 \sigma^2}{2}\right), \quad (44)$$

where Γ_0 and Γ are the amplitudes of the signal at frequency f , before and after diffusion. Based on Equation 44, we can compute the expected power spectral density (PSD) of an ice-core section as:

$$P = P_0 \exp(-k^2 \sigma^2), \quad (45)$$

where P_0 and P are the PSDs of the signal before and after diffusion. We assume that P_0 is constant (white noise) over short core sections, as discussed and justified in Johnsen et al., (2000) and Gkinis et al., (2014).

Spectral estimates of ice-core data sections will also be affected by noise generated during the laboratory measurement process. Taking this effect into account, the idealized model for the PSD of ice-core data is given by:

$$P = P_0 \exp(-k^2 \sigma^2) + |\hat{\eta}|^2 \quad (46)$$

where $|\hat{\eta}|^2$ is the measurement noise.

The diffusion length σ can be calculated by optimizing the fit between Equation 46 and the PSD of a section of ice-core data. Repeating this method over consecutive, windowed sections of data yields diffusion-length estimates through the length of an ice-core record. Various spectral-estimation techniques can be used to produce the PSD of the data. In this work, we use Burg's spectral estimation algorithm (Burg, 1975), following the approach of Gkinis et al., (2014). Burg's method is preferable for this application because it is based on a predictive autoregressive model and ice-core data are intrinsically autoregressive. In Figure 4.1 we give examples of estimated PSDs of a data section from the Dome F ice core for both $\delta^{18}\text{O}$ and δD (Svensson et al., 2015). The record was measured using the CFA approach presented in Gkinis et al., (2011a) with a nominal resolution of 0.5 cm. Note that the differences in the sloping of the spectra of $\delta^{18}\text{O}$ and δD are due to differences in how the CFA system affects each isotope ratio.

Based on Equation 46, two strategies emerge for estimating diffusion lengths from high-resolution ice-core data. A first-order approach is to use the first term of Equation 46 as the power spectral model P and tune σ to fit the power spectral estimate P' in a least squares sense in a range of low frequencies $[2, f_c]$ (Jones et al., 2017b). The value of f_c is manually chosen such that P' is dominated by the diffusion signal in this range of frequencies; as a result, measurement noise does not significantly affect the quality of the fit. A second approach is to include the noise signal $|\hat{\eta}|^2$ in the fit, using a 2-function model and thus fitting the model of P as described in Equation 46 to the spectral estimate P' across the full range of frequencies. The advantage of the latter technique compared to the first-order approach is that it does not

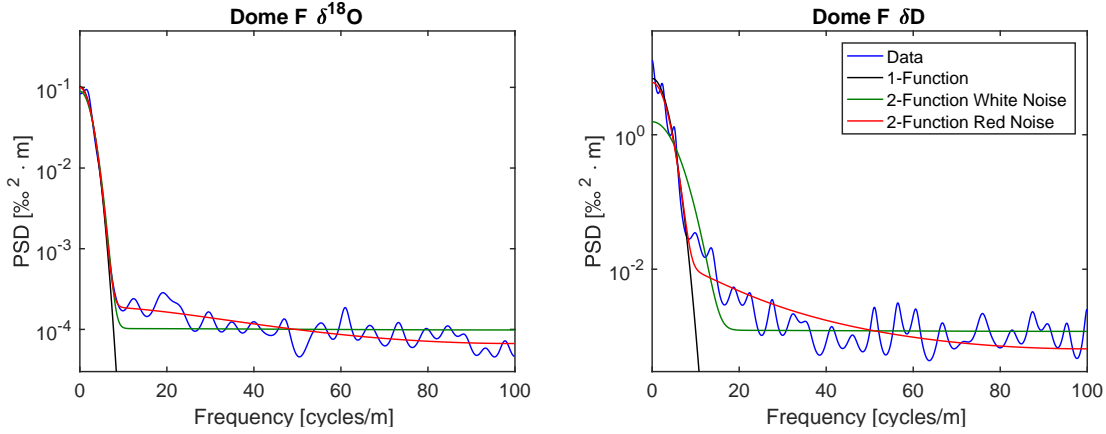


Figure 4.1. First-order (black curve) and 2-function models applied to the PSD of a section of Dome F data from 302-307 m depth. For the 2-function model we use both white noise (green curve) and red noise (red curve).

involve the subjective step of manually choosing the value of f_c . However, considering the full frequency range requires an accurate model for the measurement noise; otherwise, biases in the estimation of the diffusion length σ can emerge.

In Figure 4.1, both approaches are applied to the Dome F data section. For the first-order approach, we select $f_c = 20$ cycles/m (black line). For the 2-function model (green line), we first assume the measurement noise $|\hat{\eta}|^2$ is white. However, this approach results in a slight misfit in the range of frequencies 10-25 cycles/m. Next, assuming that the measurement noise is slightly red, as presented in Gkinis et al., (2011a) and Gkinis et al., (2014) and Holme et al., (2018a), we obtain a more satisfactory fit (red line). Red noise behavior is expected due to smoothing and memory effects in the measurement system. The spectral model used for the latter case is:

$$P = P_0 e^{-k^2 \sigma^2} + \frac{\zeta_\eta^2 \Delta}{|1 - a_1 \exp(-ik\Delta)|^2}, \quad (47)$$

where a_1 , the AR-1 coefficient, and ζ_η^2 , the variance of the red noise, are variable parameters in the fit. The AR-1 coefficient determines the strength of correlation between two consecutive points in the series. For the $\delta^{18}\text{O}$ PSD in the left panel, the values for σ obtained with these different fitting approaches are 5.42, 5.11 and 5.34 cm, respectively. Although all three fits appear similar in the frequency range where the diffusive damping occurs, the anomalous value of 5.11 cm for the white-noise case illustrates how the misfit of the model can affect the estimation of diffusion length.

For some datasets, the problem of the misfit can lead to large errors in the estimation of diffusion length. Using the same section of ice from Dome F, but this time considering the δD signal, we observe a larger misfit (right panel). While the first-order approach using the cut-off frequency still produces a satisfactory fit to the part of the spectrum dominated by the

diffusion signal, the 2-function model assuming white noise fails to yield an adequate fit. As seen in the spectrum, the power in the data in the range of frequencies 15-25 cycles/m deviates strongly from the expected model. Assuming red noise, the fit is significantly better with an AR-1 coefficient $\alpha_1 = 0.64$, a value significantly higher than that used for the fit of the $\delta^{18}\text{O}$ signal. The resulting diffusion-length values for each fit on the δD PSD are 4.82, 2.79, and 4.62 cm, respectively. The 2-function model with the white noise assumption clearly does not effectively fit the data, while the red noise assumption and the first-order approach each fit the diffusion-damped frequencies well. Considering the inherent subjectivity of the cut-off frequency selection in the first-order approach and an evident misfit of the red-noise 2-function model (in the frequency range 15-25 cycles/m), it is not possible to judge which of the latter two diffusion-length estimates is more accurate.

4.6 UNDERSTANDING PSDS OF DIFFERENT ICE-CORE DATASETS

In Figure 4.2 we present a collection of estimated PSDs from sections of various ice-core records and measurement techniques (discrete and CFA). The data have been normalized, showing the consistent effects of diffusive damping of high frequencies as well as measurement noise. Differences in measurement noise level can be explained by differences in the precision of the instrument used as well as by differences in data processing. In some cases, in the range of frequencies between ~ 10 and 25 cycles/m (vertical dashed lines), the PSD deviates from the model of Equation 47, as in the δD section presented from Dome F. We plot δD for each dataset, except where only $\delta^{18}\text{O}$ is available (NGRIP, WDC discrete), since those data tend to exhibit the deviation more strongly than the $\delta^{18}\text{O}$ data.

In general, the PSDs of data from CFA systems tend to deviate from the theoretical spectrum (Equation 47) more strongly than those of discretely-measured data. This creates a problem for the estimation of diffusion length from CFA data. Figure 4.3 illustrates this problem on data sections from WDC and SPC, which exhibit greater deviation than the continuous Dome F and NEEM data. Even assuming $|\hat{\eta}|^2$ to be red noise, the misfit of the 2-function model on the WDC and SPC sections is greater than that on the Dome F δD data shown in Figure 4.1. This suggests that differences in the CFA systems used play a significant role in affecting the spectra. Various CFA systems may affect measured data slightly differently. For example, the Copenhagen CFA system used for Dome F and NEEM uses a lower-precision (older-generation) Picarro instrument (Picarro L2120-*i*) than the INSTAAR system (L2130-*i*) used for WDC and SPC. Further, the Copenhagen CFA vaporizes the sample differently, which may result in a smaller smoothing effect on the data. Importantly, there is no evidence that

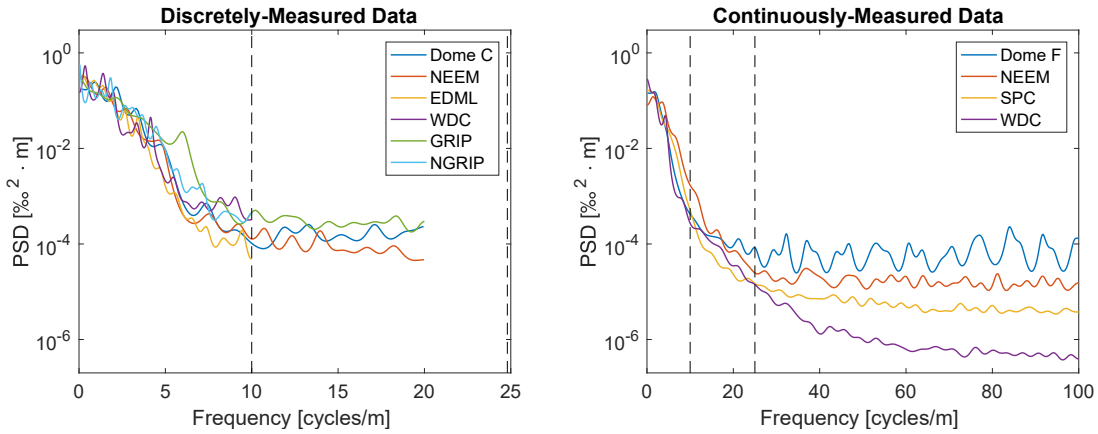


Figure 4.2. Estimated PSDs for discretely-measured (left panel) and continuously-measured (right panel) datasets. All data has been normalized by dividing by its standard deviation before making the spectral estimate. δD is plotted for all datasets, except where not available (NGRIP and WDC discrete). Discrete cores tend to follow the model of Equation 47, while continuous cores tend to deviate from that model between frequencies of 10 and 25 cycles/m and beyond (range highlighted by vertical dashed lines on each panel). Note the relatively constant value (i.e, white noise) of the PSDs for the discretely-measured data between 10 and 25 cycles/m.

the character of the deviation from Equation 47 changes with measurement time, for a given measurement system. We use replicate ice samples from the same section of ice core measured on the INSTAAR CFA system at different times. Figure 4.4 plots the PSDs from measurements of SPC from 1060 m to 1075 m depth. The blue and red curves show the original and replicate measurements, respectively. The PSDs do not differ significantly.

The influence of the CFA system on the spectral properties of the data may arise in a number of components of the system. Liquid-phase mixing takes place throughout the tubing of the CFA system. In particular, liquid water reservoirs, such as degassing and filtering units, may

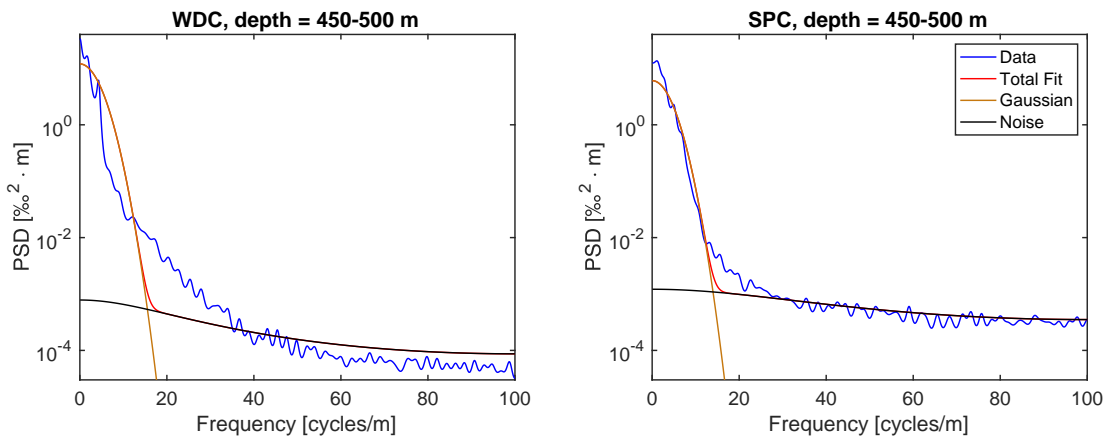


Figure 4.3. 2-function model (Equation 47) applied to WDC and SPC at 450-500 m depth. With only two functions, the model is unable to effectively fit the entire data spectrum.

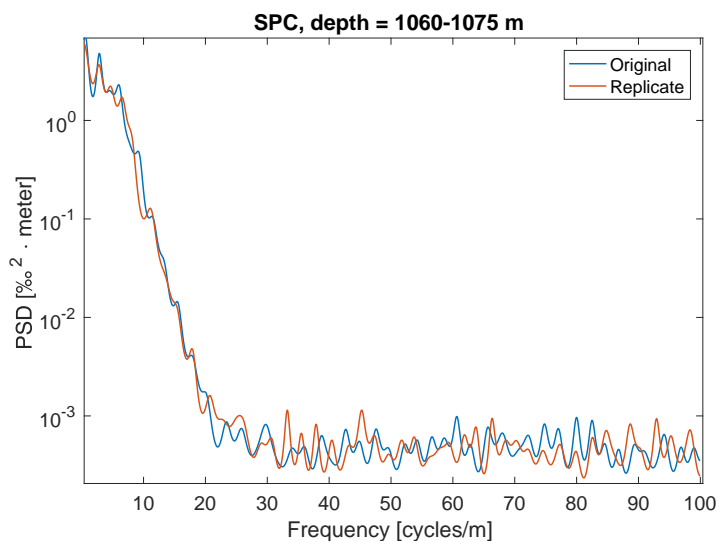


Figure 4.4. PSDs from replicate measurements of the same depths of SPC from 1060-1075 m. The blue curve shows the measurement from the original piece of ice. The red curve shows the measurement of a different sample from the same ice depth.

enhance these effects. Attenuation of the signal due to mixing in the vapor phase can also be significant. Sample vaporization takes place at an operating pressure of ~ 1 atm (Gkinis et al., 2011a; Jones et al., 2017a), while the operating pressure within the instrument cavity is only ~ 65 mbar (Crosson, 2008). Under the higher pressure, significant smoothing occurs between the time of vaporization and the time of injection into the cavity. Additionally, memory effects arise from the particular nature of hydrogen bonding of the water molecule. Due to this intermolecular bonding, water molecules may adsorb to surfaces within the system downstream of the point of vaporization, potentially affecting subsequent measurements (Aemisegger et al., 2012). Some studies suggest the length, strength, and number of hydrogen bonds per molecule are different between H_2O and HDO (Soper and Benmore, 2008), which helps explain the stronger memory effects observed in the δD signal in comparison to the $\delta^{18}\text{O}$ signal.

The influence of the CFA system on the spectral properties of the data may arise in a number of places, as meltwater from an ice sample is transferred through tubing and various reservoirs (Gkinis et al., 2011a). For example, when sample water is pumped into the debubbler (a 2 ml open-top vial that allows air bubbles to escape), some smoothing occurs. Also, smoothing occurs in the vapor phase when the sample is vaporized under relatively high pressure before it is injected into the Picarro instrument. The volumes of these reservoirs for the liquid and vapor phases affect how much smoothing occurs in a particular CFA system. Memory effects occur within the laser cavity of the Picarro instrument (Aemisegger et al., 2012). Because a stream of vapor is continuously pumped through the cavity, the isotopic memory from previous

Table 4.2. The parameters characterizing the CFA system smoothing as estimated from the fit in Figure 4.5.

Isotope	C_1 [‰]	C_2 [‰]	μ_1 [sec]	μ_2 [sec]	σ_1 [sec]	σ_2 [sec]
$\delta^{18}\text{O}$	59.76	-44.31	3.65	12.58	0.502	75.48
δD	626.67	-349.61	3.70	597.30	0.512	1647.79

vapor, probably due to adsorption of water molecules to the cavity walls, will affect subsequent measurements.

We examine whether the effect of diffusive system smoothing can explain the spectral characteristics in continuous data PSDs by comparing real data to synthetic data with simulated smoothing. To characterize the smoothing of the system, we introduce an isotopic step-change into the INSTAAR CFA system, using ice that has been prepared in the laboratory from isotopically-distinct waters. The response of the system to the step change can be described as the product of two lognormal cumulative distribution functions (CDF):

$$\delta_{step}(t) = C_1 \cdot \left[1 + \operatorname{erf} \left(\frac{\ln(t) - \mu_1}{\sigma_1 \sqrt{2}} \right) \right] \cdot \left[1 + \operatorname{erf} \left(\frac{\ln(t) - \mu_2}{\sigma_2 \sqrt{2}} \right) \right] + C_2, \quad (48)$$

where t is time, μ_1 and μ_2 are the position of the distributions, σ_1 , and σ_2 are the standard deviations of the CDFs and C_1 and C_2 are scaling factors.

To estimate the extent of system smoothing, we fit Equation 48 to the isotopic step-change, as shown in panels a) and b) of Figure 4.5. The resulting system-smoothing parameters are shown in Table 4.2. These are representative values and will vary slightly due to small changes in the system through time. The impulse response function calculated by the derivative of the step response is shown in panel c) of Figure 4.5 for both $\delta^{18}\text{O}$ and δD . The δD response is slightly wider, which suggests it is smoothed more within the system, confirming the result of Jones et al., (2017a). This difference may explain why the PSD of δD deviates more strongly from Equation 47 than the PSD of $\delta^{18}\text{O}$. To simulate system smoothing, we apply the impulse response function as a filter on synthetic data.

We generate synthetic data by performing the following steps. First, to simulate data that represent the isotopic signal in surface snow, we generate an AR-1 process with a resolution of 0.1 cm and add white noise (ε_n) as:

$$\delta_n = a_1 \cdot \delta_{n-1} + \varepsilon_n. \quad (49)$$

The parameters involved in the generation of synthetic data are chosen such that the resulting δ_{final} time series visually resembles the WDC data (in this example from the depth interval

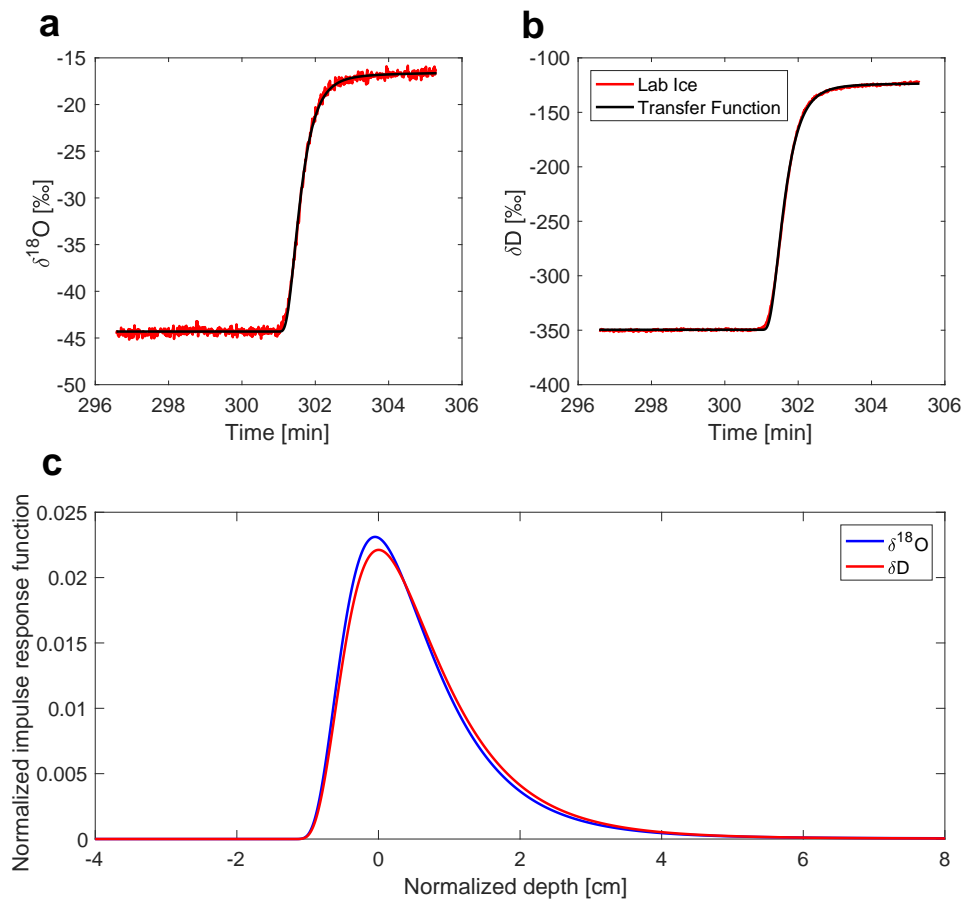


Figure 4.5. The characterization of the CFA system response to an isotopic step change. Panels a) and b) show the transfer function of Equation 48 fit to the isotopic step-change of the laboratory-prepared ice sample. The estimated parameters are listed in Table 4.2. Panel c) shows the normalized impulse response functions for $\delta^{18}\text{O}$ and δD plotted with respect to a normalized depth (assuming an average melt rate of 2.5 cm/min).

450 – 467 m). Typical values for the autoregressive coefficient a_1 lie around $a_1 = 0.3$, while the standard deviation of ε_n is approximately 11 ‰ and 87.6 ‰ for $\delta^{18}\text{O}$ and δD , respectively.

Next, we introduce firn diffusion by convolving δ_n with a Gaussian filter (\mathcal{G}) with a standard deviation σ equal to 5.61 cm and 5.08 cm for $\delta^{18}\text{O}$ and δD , respectively:

$$\delta_{ice} = \delta_n * \mathcal{G}_{firn}. \quad (50)$$

Using the results of the step-response test we account for the smoothing imposed by the CFA system and perform one more convolution operation where the transfer function is the impulse response of the CFA system:

$$\delta_{cfa} = \delta_{ice} * \mathcal{G}_{cfa}, \quad (51)$$

where \mathcal{G}_{cfa} is the derivative of Equation 48. Last, we sample the data at a 0.5 cm resolution and add white measurement noise:

$$\delta_{final} = \delta_{0.5} + \varepsilon_{meas}, \quad (52)$$

where $\varepsilon_{meas} = 0.05$ ‰ and 0.15 ‰ for $\delta^{18}\text{O}$ and δD , respectively.

The sequence of steps described in equations 49–52 yields a PSD presented as the light grey curve in Figure 4.6. This curve can be described to a very good approximation by the model of Equation 47, but does not match the PSD of the WDC data (blue and red curves). We find that one way to approximate the WDC behavior is to slightly modify equation 50 by adding a white noise component ε as:

$$\delta_{ice} = \delta_n * \mathcal{G}_{firn} + \varepsilon. \quad (53)$$

Figure 4.6 shows the results of adding increasing levels of white noise ε (dark grey and black curves). With this noise addition, the PSDs of the synthetic data begin to resemble that of the WDC data, suggesting that there is a source of noise between the process of diffusion in the ice sheet and the process of smoothing within the CFA system. This source of noise may include the varying rate of sample flow through the system as well as temperature-dependent instrument noise. Nonetheless, Figure 4.6 gives a visual confirmation that, with the addition of white noise, the convolution of synthetic data with the system impulse response results in a time series that is similar to the measured WDC data. Later, we use this approach to generating synthetic data to evaluate new methods of estimating diffusion length.

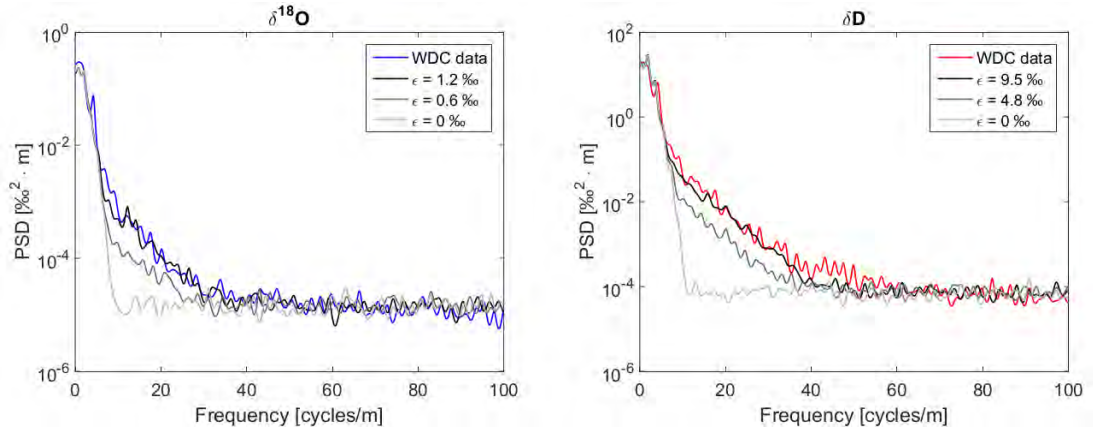


Figure 4.6. A comparison of PSDs from actual WDC data and from synthetic data with progressive levels of white noise added during the system smoothing process for both $\delta^{18}\text{O}$ and δD .

Table 4.3. Summary of models for the PSD of ice-core data. *Variable is manually selected and is not subject to fitting through optimization.

Model Name	Description	Variable Parameters
First-Order	$P = P_0 \exp(-k^2 \sigma^2)$	P_0, σ
2-Function	$P = P_0 \exp(-k^2 \sigma^2) + \hat{\eta} ^2$ where $ \hat{\eta} ^2 = \frac{\zeta_{\eta}^2 \Delta}{ 1 - a_1 \exp(-ik\Delta) ^2}$	$P_0, \sigma, \zeta_{\eta}, a_1$
Noise-Adding	$P = P_0 \exp(-k^2 \sigma^2) + \hat{\eta} ^2$ where data PSD has been altered	$P_0, \sigma, \zeta_{\eta}, a_1$ <i>noise added to data*</i>
3-Function Double-Noise	$P = P_0 \exp(-k^2 \sigma^2) + \hat{\eta} ^2 + \hat{\eta}' ^2$	$P_0, \sigma, \zeta_{\eta}, a_1, \zeta_{\eta}', a_1'$
3-Function Double-Gaussian	$P = P_0 \exp(-k^2 \sigma^2) + P_0' \exp(-k^2 \sigma'^2) + \hat{\eta} ^2$	$P_0, \sigma, P_0', \sigma', \zeta_{\eta}, a_1$
3-Function FND	$P = P_0 \exp(-k^2 \sigma^2) + \phi_0 e^{-(k\psi)^2} 1 - \Phi(-ik\psi) ^2 + \hat{\eta} ^2$ where $\Phi(\psi) = \frac{1}{2} \text{erfc}(-\frac{\psi}{2})$	$P_0, \sigma, \phi_0, \psi, \zeta_{\eta}, a_1$

4.7 GENERALIZING THE DIFFUSION ESTIMATION TECHNIQUE

As discussed in Section 4.5, neither of the existing techniques for estimating diffusion lengths fully capture the spectral properties of continuous data. We consider two new techniques to address this problem. First, we add white noise to the data to mask the deviation in the mid-frequency range where the influence of the CFA appears to be most significant. Second, we add a third function to Equation 47, intended to capture the influence of the CFA-system smoothing on the spectrum. We illustrate these methods with δD data, which are more strongly affected than $\delta^{18}\text{O}$ by the CFA system. As we will show, both the noise-adding and 3-function techniques are effective.

4.7.1 *Technique 1: Adding white noise*

For this technique, we add normally-distributed noise to the data in the depth domain, which increases the high-frequency noise level in the frequency domain. This approach is equivalent to adding white noise as a constant to the data in the frequency domain and yields identical results. The resulting PSD masks the deviation, and the model of Equation 47 can effectively fit the altered PSD. Panel a) of Figure 4.7 illustrates this technique applied to a WDC data section.

We used a sensitivity test to evaluate the optimal magnitude of noise (standard deviation) to be added to the data. Adding too little noise does not effectively mask the deviation, but adding too much noise risks obscuring information. The test used a 500-year moving window throughout the WDC record. For each windowed section, 100 diffusion lengths were estimated by adding an increasing white noise level to the data in each window. A diffusion length was estimated for each tested noise level on each 500-year window. We define the optimal noise level as that at which the diffusion-length estimates stop changing with increasing noise. This level can be found when the gradient of diffusion length with respect to the added noise level approaches zero. Panels b) and c) of Figure 4.7 show how this gradient changes for both $\delta^{18}\text{O}$ and δD throughout the WDC core. The optimal noise level is selected for each age as the lowest noise level that results in a gradient within $0.1 \text{ cm}/\text{‰}$ of $0 \text{ cm}/\text{‰}$. For WDC, we found that the optimal added noise is Gaussian-distributed noise with a standard deviation of 0.4 ‰ for $\delta^{18}\text{O}$ and 3.0 ‰ for δD .

4.7.2 *Technique 2: 3-function model*

This technique adds a third function to the model in Equation 47 to improve the fit to the data PSD. We tested the additions of three different functions, and determined which addition results in the most effective model. The three functions we tested were 1) a second autoregressive noise function, 2) a second Gaussian function, and 3) a folded normal distribution (FND) (Tsagris et al., 2014). The primary motivation for adding any of these functions is to better fit the mid-frequency range (10-25 cycles/meter) of the PSD. Additionally, there is a physical justification for using the FND model. As the absolute value of a Gaussian distribution, a FND is a function that smooths in only one direction. Since water is continuously flowing in one direction through the CFA system, the application of a FND is intended to mimic this one-sided effect. These models and those described earlier are summarized in Table 4.3. For each model,

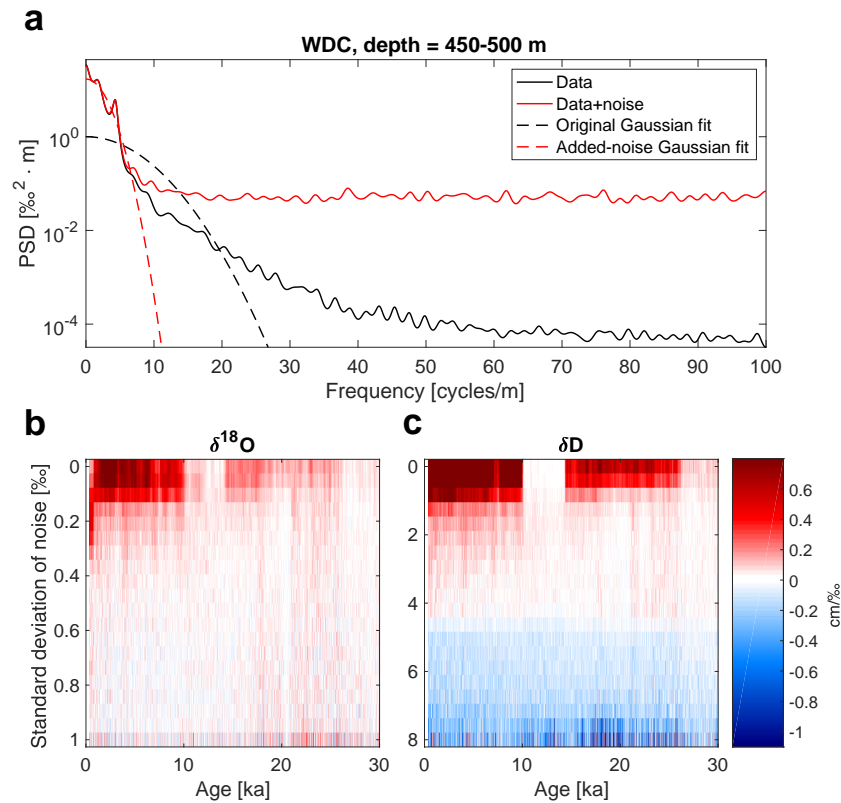


Figure 4.7. The noise-adding technique applied to a δD section from WDC. Panel a) shows the unmodified data (solid black curve) and the data with noise added (solid red curve). The dashed lines represent the Gaussian functions fit using the 2-function fitting technique before and after adding noise to the data. With the added noise, the dashed red curve is able to effectively fit the data spectrum. Panels b) and c) demonstrate the sensitivity test for determining the optimal added noise level. For WDC, the gradient of estimated diffusion lengths with respect to noise level plotted as a function of age. At each age, the lowest noise level with a gradient of approximately zero is chosen as the optimal noise level to be added. Note that the strength of the colors is not symmetric, but the color bar is linear.

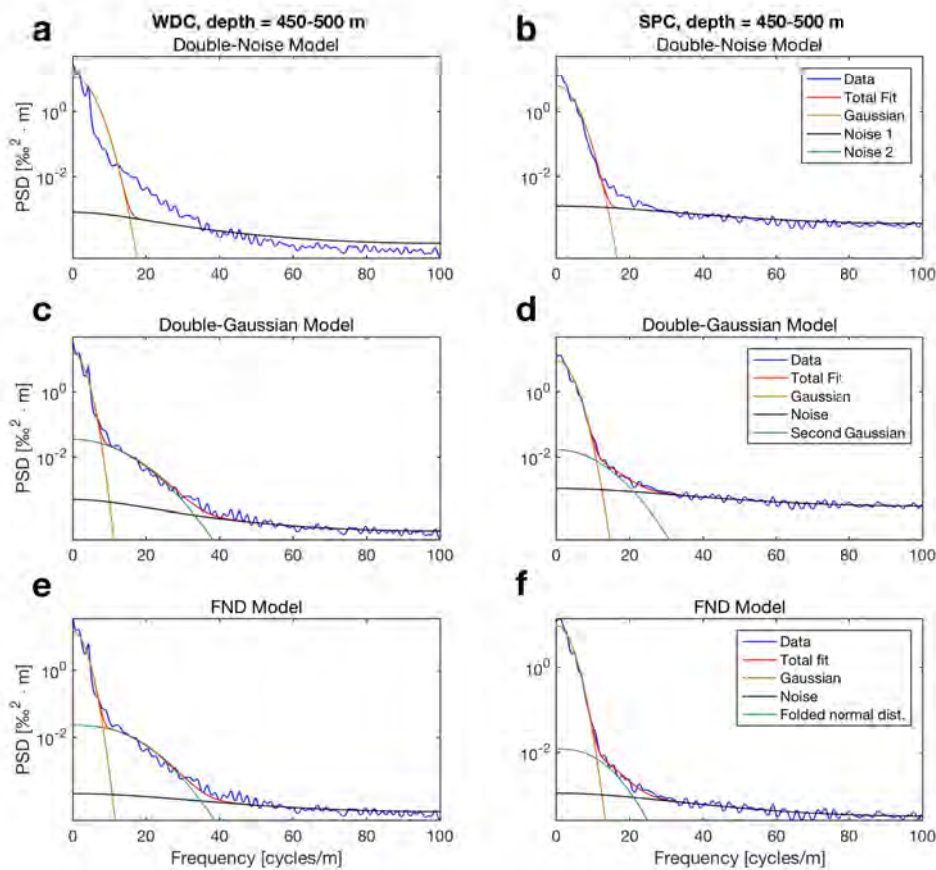


Figure 4.8. Each of the 3-function models applied to data sections from WDC and SPC PSDs. The double-noise model does not fit the full spectrum well, while both the double-Gaussian and FND models capture the full shape of the PSDs.

the parameter space is constrained such that the model can vary but remains within reasonable limits.

The results of applying the 3-function models are shown in Figure 4.8 for WDC and SPC. Panels a) and b) show the model that sums a Gaussian function and two autoregressive noise functions, henceforth the “double-noise model”. With the addition of an autoregressive noise function, the total fit is visually improved for SPC, as compared to the 2-function model in Figure 4.3, but is still unable to effectively match the spectrum for WDC. Panels c) and d) show the model that sums two Gaussian functions and one autoregressive noise function, henceforth the “double-Gaussian model”. Again, there is a visual improvement in the total fit as compared to the 2-function model fit, now in both SPC and WDC. Finally, panels e) and f) show the model that sums one Gaussian, one autoregressive noise function, and one FND function, henceforth the “FND model”. Due to the close relationship between a Gaussian and a FND function, the fits are very similar in panels c) and e) and in panels d) and f).

Table 4.4. Summary of performance of diffusion-estimate techniques on WDC δD data using 500-year windows.

Age of window [ka]	Noise-Adding $\sigma \pm 1$ Standard Deviation [cm]	Double-Gaussian $\sigma \pm 1$ Standard Deviation [cm]
1	5.59 ± 0.41	5.53 ± 0.43
5	3.91 ± 0.17	3.76 ± 0.19
10	2.95 ± 0.19	2.87 ± 0.20
15	3.13 ± 0.20	3.11 ± 0.21
20	2.00 ± 0.13	2.10 ± 0.15

4.7.3 Uncertainty of diffusion-length estimation

To describe the uncertainty of the diffusion length estimated by each of these techniques, we use the 95th percent confidence bounds from the PSD estimate. To create a conservative estimate of uncertainty, we find the most extreme diffusion lengths possible given these PSD bounds, an approach similar to that of Jones et al., (2017b). The upper bound on diffusion length is found from the Gaussian function fit over a combination of the lowest frequencies of the upper PSD estimate bound with the highest frequencies of the lower PSD estimate bound. This combination yields the narrowest Gaussian function possible, and thus the greatest diffusion length. Conversely, the lower bound on diffusion length is found from combining the lowest frequencies of the lower PSD estimate bound with the high frequencies of the upper PSD estimate bound, resulting in the broadest Gaussian function possible and thus the smallest diffusion length. The frequency that separates the fit from the lower to upper PSD estimate bound is chosen at the lower-frequency side of the diffusion Gaussian, which maximizes the difference in the uncertainty bounds and thus creates a conservative estimate. Because the shape of the spectrum changes with depth, the separation frequency varies. Figure 4.9 demonstrates this approach with the double-Gaussian model, with dashed lines representing the upper and lower bounds on the fits of each function of the model. Table 4.4 lists diffusion-length estimates plus or minus one standard deviation for five windows throughout the WDC core.

4.8 EVALUATING FITTING TECHNIQUES

To evaluate each fitting technique, we evaluate how reliably the techniques can be used to determine the known diffusion length of synthetic data. We construct synthetic data as described in Section 4.6. Qualitatively, both techniques result in effective fits on the synthetic data. To quantify the performance of each technique, we use a Monte Carlo-like procedure. Each Monte Carlo iteration builds a unique time series having the same diffusion length, but a

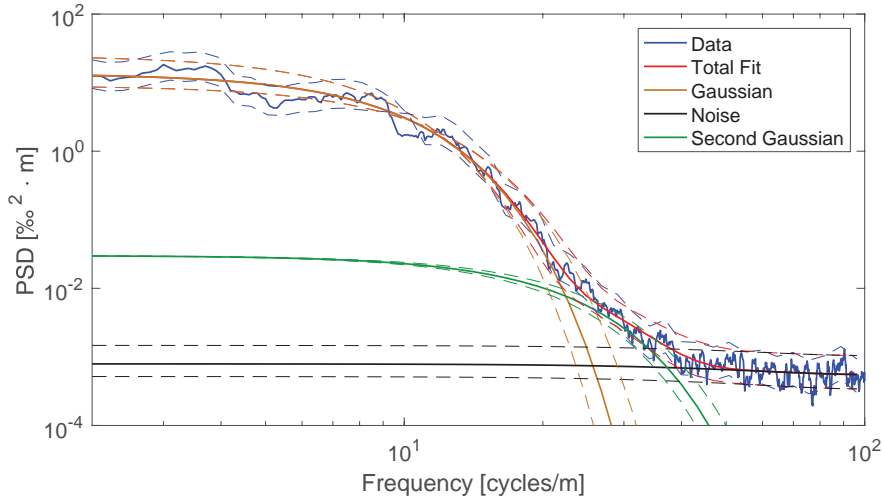


Figure 4.9. Illustration of uncertainty estimation for diffusion-length estimate for WDC δD data from 2505-2521 m depth. Solid lines show the data and the fit of each function. Dashed lines show the 95% confidence bounds for the spectral estimate of the data and the corresponding fits of the parameterization for upper and lower bounds. To estimate uncertainty for the diffusion-length estimate, the solid yellow curve yields the value and the dashed yellow curves yield the upper and lower bounds of 95% confidence. Axes are plotted in log-log space to expand the view of the lower frequencies and emphasize the fits of the diffusion length and its bounds (yellow curves).

different noise realization. We then use both techniques to estimate diffusion lengths for 100 iterations of synthetic data. Table 4.5 gives the mean, standard deviation, and root mean square error of the diffusion-length estimates for both δD and $\delta^{18}O$. Both techniques accurately estimate the input diffusion length, the noise-adding technique with a RMSE of 0.25 cm for both $\delta^{18}O$ and δD , and the double-Gaussian model with a RMSE of 0.22 cm for $\delta^{18}O$ and 0.18 cm for δD . Thus, these values compare well with our estimates of uncertainty from Section 6.3.

As a second means of evaluation, we compared the effectiveness of each resulting fit over the entire WDC record. We calculated the adjusted coefficient of determination (\bar{r}^2) as a metric of goodness-of-fit with the data. The coefficient of determination (r^2) is calculated by comparing the variability of the estimation errors with the variability of the original values. The adjusted coefficient of determination (\bar{r}^2) takes into account the number of variable parameters (p) as follows (Theil, 1961):

$$\bar{r}^2 = 1 - (1 - r^2) \frac{n-1}{n-p-1}, \quad (54)$$

where n is the sample size. For the noise-adding technique, $p = 5$; for the 3-function models, $p = 6$. Figure 4.10 plots the \bar{r}^2 values as a function of age for WDC. The \bar{r}^2 values of the double-Gaussian and FND models are indistinguishable, so we show only the double-Gaussian result in the figure. All four techniques provide good fits ($\bar{r}^2 > 0.9$) to the data, but the best

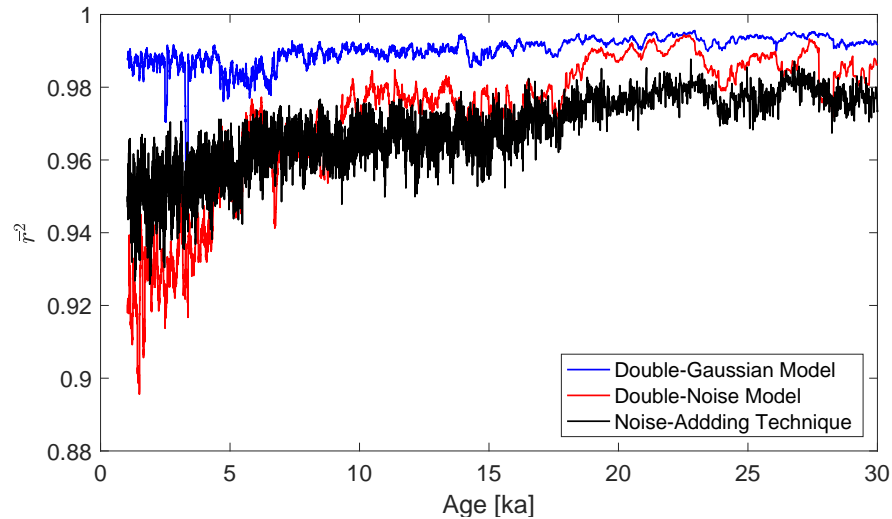


Figure 4.10. For WDC, the adjusted coefficient of determination (\bar{r}^2) plotted against age for each fitting technique. FND results are identical to the double-Gaussian results and are not shown.

fits are obtained with the double-Gaussian and FND models. For simplicity and computational efficiency, we prefer the double-Gaussian over the FND model.

Third, we compared the resulting diffusion-length estimates from the double-Gaussian model and the noise-adding technique. The left panel of Figure 4.11 shows the diffusion-length estimates from both techniques plotted with respect to age along with confidence bounds showing two standard deviations. The diffusion-length estimates were calculated over a moving 500-year window, shifting 100 years for each consecutive estimate. Both techniques reconstruct similar diffusion lengths throughout the record.

A fourth way of validating the techniques is by comparison with the technique using the first-order model, as discussed in Section 4.5, above. The right panel of Figure 4.11 shows this comparison for the WDC record, using the same data windows as in Jones et al., 2017b. The estimated diffusion lengths for all three techniques match within uncertainty bounds. As each of these techniques is independent of one another, the confidence bounds together provide insight into how well diffusion lengths can currently be estimated from ice-core data.

We conclude that the best technique for estimating diffusion length is the double-Gaussian parameterization of the 3-function model. Although the FND model is better justified theoretically than the double-Gaussian model, it is effectively equivalent, though less computationally straightforward. The noise-adding technique produces similar results to the double-Gaussian model, but risks masking information in the signal, while the double-noise model does not fit the data as well as any of the other methods.

Table 4.5. Summary of performance of diffusion-estimate techniques on synthetic data of known input diffusion length.

Isotope	Input σ [cm]	Mean \pm 1 Standard Deviation [cm]		RMSE [cm]	
		Noise-Adding	Double-Gaussian	Noise-Adding	Double-Gaussian
$\delta^{18}\text{O}$	5.61	5.60 ± 0.25	5.68 ± 0.20	0.25	0.22
δD	5.08	5.16 ± 0.23	5.09 ± 0.18	0.25	0.18

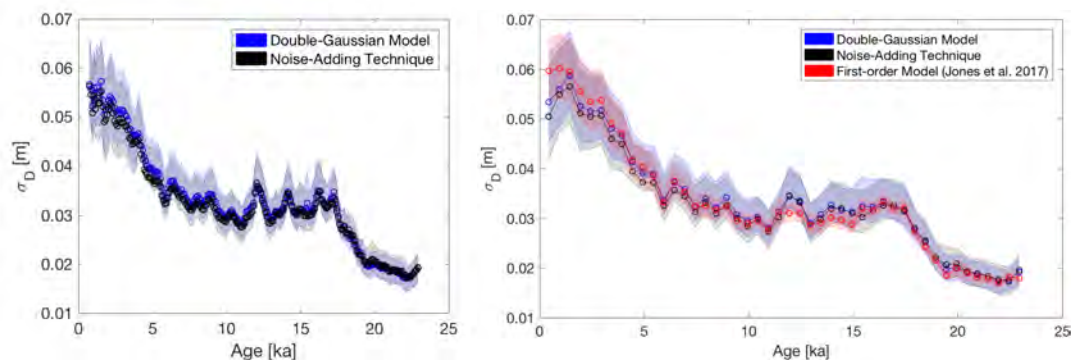


Figure 4.11. The left panel shows a comparison of diffusion-length estimates for the double-Gaussian model and noise-adding technique shown for δD for WDC. Confidence bounds show two standard deviations. The right panel shows a comparison of WDC δD diffusion-length estimates from the double-Gaussian model and noise-adding technique with those from Jones et al., (2017b). All diffusion lengths have been estimated on the same windows defined by Jones et al., (2017b). Confidence bounds show two standard deviations.

4.9 DISCUSSION

The double-Gaussian technique provides a more efficient approach to estimating diffusion length than the manual cut-off method (Jones et al., 2017b), but yields essentially identical results, and generalizes the application of previously-developed methods (Gkinis et al., 2014) to data from CFA systems. While our approach is nominally automated, in practice, we find that small alterations to the bounds of the fit parameters may be required to ensure that an accurate fit is obtained for each data window analyzed. For a given ice-core record, the general shape and magnitude of the PSDs will shift with increasing depth. Choice of different parameter bounds for distinct regimes within a dataset (e.g., Holocene and Glacial) may be necessary, as we have found with our results from the WAIS Divide ice core (Figure 4.11). Fine tuning of the upper bound on the P_0 parameter of the second Gaussian is particularly important as it separates the region of the PSD affected by diffusion from that affected by system smoothing.

With an approach that takes the above considerations into account, the double-Gaussian model can be used to produce diffusion-length estimates at sufficiently high resolution to recover relatively small features within the isotope-diffusion signal. For example, the high-resolution diffusion-length record in the left panel of Figure 4.11 resolves small peaks during the transition out of the glacial period (at ~ 12 , 14, and 17.5 ka) in the WAIS Divide ice core, while these features are subtle or altogether absent in the lower-resolution record in the right panel. Further investigation is required to determine whether these features reflect meaningful variations in climate or firn processes. In this context, a comparison with total air content from WDC would be helpful. This record is currently in development (Jon Edwards, pers. comm., 2017). If the comparison shows that total air content is also elevated where water-isotope diffusion lengths are anomalously high, this would suggest that anomalously low density firn could account for the exceptionally high diffusion lengths obtained at ~ 12 , 14, and 17.5 ka in the WAIS Divide ice core (as was previously suggested in Jones et al., 2017a).

In addition to providing informative comparisons with other proxy records, high-resolution diffusion-length records can also be used to improve current firn densification and diffusion models. With input temperature and accumulation-rate histories, firn models produce synthetic, high-resolution water-isotope data. Comparison of diffusion lengths of these synthetic data with those from ice-core data can be used to evaluate what mechanisms within the model impact the resulting diffusion-length record. Current generation firn models do not reproduce the variability observed in the WDC diffusion-length record of Jones et al., (2017b). A model-data comparison approach could be used to examine what variables and boundary conditions are required to reproduce specific features in an ice-core diffusion-length record. This approach

has the potential to both improve understanding of the climate signal as well as to improve firn models.

4.10 CONCLUSION

In this study we examine the diffusion signal in water-isotope data from a collection of ice-core records. We observe that the power spectral density of sections of water-isotope data can differ based on how the data are measured. In some cases, mostly with data measured on continuous-flow analysis systems, the PSD deviates from a simple model of diffusion plus instrument noise. We show that this deviation can be explained through modeling of the CFA system smoothing. Previous diffusion-length estimation techniques cannot effectively model these PSDs. We propose four new estimation techniques and find that the most effective method is the double-Gaussian parameterization of the 3-function model. These automated methods are efficient and effective in fitting all frequencies of the PSD. We validate the methods against one another, against synthetic data with known diffusion length, and against results estimated independently by Jones et al., (2017b). These methods can be used to determine diffusion lengths on water-isotope data from any ice-core record of sufficiently high resolution regardless of measurement technique. Diffusion-length records resulting from these automated methods have the potential to improve interpretation of ice-core and climate records as well as models of firn densification and isotope diffusion.

REFERENCES

- Aemisegger, F., P. Sturm, P. Graf, H. Sodemann, S. Pfahl, A. Knohl, and H. Wernli (2012). “Measuring variations of $\delta^{18}\text{O}$ and $\delta^2\text{H}$ in atmospheric water vapour using two commercial laser-based spectrometers: An instrument characterisation study”. In: *Atmospheric Measurement Techniques* 5 (7), p. 1491.
- Brand, W. A., H. Geilmann, E. R. Crosson, and C. W. Rella (2009). “Cavity ring-down spectroscopy versus high-temperature conversion isotope ratio mass spectrometry; a case study on $\delta^2\text{H}$ and $\delta^{18}\text{O}$ of pure water samples and alcohol/water mixtures”. In: *Rapid Communications in Mass Spectrometry* 23.12, pp. 1879–1884.
- Burg, J. P. (1975). “Maximum entropy spectral analysis”. PhD thesis.
- Casey, K. A., T. J. Fudge, T. A. Neumann, E. J. Steig, M. G. P. Cavitte, and D. D. Blankenship (2014). “The 1500 m South Pole ice core: Recovering a 40 ka environmental record”. In: *Annals of Glaciology* 55 (68), pp. 137–146.

- Crosson, E. R. (2008). "A cavity ring-down analyzer for measuring atmospheric levels of methane, carbon dioxide, and water vapor". In: *Applied Physics B-Lasers And Optics* 92.3, pp. 403–408.
- Cuffey, K. M. and E. J. Steig (1998). "Isotopic diffusion in polar firn: implications for interpretation of seasonal climate parameters in ice-core records, with emphasis on central Greenland". In: *Journal of Glaciology* 44.147, pp. 273–284.
- Dansgaard, W. (1964). "Stable isotopes in precipitation". In: *Tellus B* 16.4, pp. 436–468.
- Dansgaard, W. (1954). "The ^{18}O -abundance in fresh water". In: *Geochimica et Cosmochimica Acta* 6.5–6, pp. 241–260.
- Emanuelsson, B. D., W. T. Baisden, N. A. N. Bertler, E. D. Keller, and V. Gkinis (2015). "High-resolution continuous-flow analysis setup for water isotopic measurement from ice cores using laser spectroscopy". In: *Atmos. Meas. Tech.* 8.7, pp. 2869–2883.
- Epstein, S., R. Buchsbaum, H. Lowenstam, and H.C. Urey (1951). "Carbonate-water isotopic temperature scale". In: *Geological Society of America Bulletin* 62.4, p. 417.
- Gkinis, V. (2011). "High resolution water isotope data from ice cores". PhD thesis. University of Copenhagen.
- Gkinis, V., T. J. Popp, T. Blunier, M. Bigler, S. Schupbach, E. Kettner, and S. J. Johnsen (2011a). "Water isotopic ratios from a continuously melted ice core sample". In: *Atmospheric Measurement Techniques* 4 (11), pp. 2531–2542.
- Gkinis, V., T. J. Popp, S. J. Johnsen, and T. Blunier (2010). "A continuous stream flash evaporator for the calibration of an ir cavity ring-down spectrometer for the isotopic analysis of water". In: *Isotopes in Environmental and Health Studies* 46 (4), pp. 463–475.
- Gkinis, V., S. B. Simonsen, S. L. Buchardt, J. W. C. White, and B. M. Vinther (2014). "Water isotope diffusion rates from the NorthGRIP ice core for the last 16,000 years - glaciological and paleoclimatic implications". In: *Earth and Planetary Science Letters* 405.
- Gupta, P., D. Noone, J. Galewsky, C. Sweeney, and B. H. Vaughn (2009). "Demonstration of high-precision continuous measurements of water vapor isotopologues in laboratory and remote field deployments using wavelength-scanned cavity ring-down spectroscopy (WS-CRDS) technology". In: *Rapid Communications in Mass Spectrometry* 23 (16), pp. 2534–2542.
- Holme, C., V. Gkinis, and B. M. Vinther (2018a). "Molecular diffusion of stable water isotopes in polar firn as a proxy for past temperatures". In: *Geochimica et Cosmochimica Acta* 225, pp. 128–145.
- Johnsen, S. J. (1977). "Stable Isotope Homogenization of Polar Firn and Ice". In: *Isotopes and Impurities in Snow and Ice*, pp. 210–219.

- Johnsen, S. J., H. B. Clausen, K. M. Cuffey, G. Hoffmann, J. Schwander, and T. Creyts (2000). “Diffusion of stable isotopes in polar firn and ice: the isotope effect in firn diffusion”. In: *Physics of Ice Core Records*, pp. 121–140.
- Johnsen, S. J., H. B. Clausen, W. Dansgaard, and C. C. Langway (1972). “Oxygen isotope profiles through Antarctic and Greenland ice sheets”. In: *Nature* 235 (5339), pp. 429–434.
- Jones, T. R., K. M. Cuffey, J. W. C. White, E. J. Steig, C. Buizert, B. R. Markle, J. R. McConnell, and M. Sigl (2017a). “Water isotope diffusion in the WAIS Divide ice core during the Holocene and last glacial”. In: *Journal of Geophysical Research: Earth Surface* 122, pp. 290–309.
- Jones, T. R., W. H. Roberts, E. J. Steig, K. M. Cuffey, B. R. Markle, and J. W. C. White (2018). “Southern Hemisphere climate variability forced by Northern Hemisphere ice-sheet topography”. In: *Nature* 554 (7692), p. 351.
- Jones, T. R., J. W. C. White, E. J. Steig, B. H. Vaughn, V. Morris, V. Gkinis, B. R. Markle, and S. W. Schoenemann (2017b). “Improved methodologies for continuous-flow analysis of stable water isotopes in ice cores”. In: *Atmos. Meas. Tech* 10, pp. 617–632.
- Kerstel, E. T., R. Van Trigt, J. Reuss, and H. A. J. Meijer (1999). “Simultaneous determination of the $^2\text{H}/^1\text{H}$, $^{17}\text{O}/^{16}\text{O}$, and $^{18}\text{O}/^{16}\text{O}$ isotope abundance ratios in water by means of laser spectrometry”. In: *Analytical Chemistry* 71 (23), pp. 5297–5303.
- Lasaga, A. C. (2014). *Kinetic theory in the earth sciences*. Princeton, NJ: Princeton University Press.
- Lis, G., L. I. Wassenaar, and M. J. Hendry (2008). “High-precision laser spectroscopy D/H and $^{18}\text{O}/^{16}\text{O}$ measurements of microliter natural water samples”. In: *Analytical Chemistry* 80 (1), pp. 287–293.
- Oerter, H., W. Graf, H. Meyer, and F. Wilhelms (2004). “The EPICA ice core Droning Maud Land: first results from stable-isotope measurements”. In: *Ann. Glaciol.* 39, pp. 307–312.
- Schoenemann, S. W., A. J. Schauer, and E. J. Steig (2013). “Measurement of SLAP2 and GISP $\delta^{17}\text{O}$ and proposed VSMOW-SLAP normalization for $\delta^{17}\text{O}$ and $^{17}\text{O}_{\text{excess}}$ ”. In: *Rapid Communications in Mass Spectrometry* 27 (5), pp. 582–590.
- Simonsen, S. B., S. J. Johnsen, T. J. Popp, B. M. Vinther, V. Gkinis, and H. C. Steen-Larsen (2011). “Past surface temperatures at the NorthGRIP drill site from the difference in firn diffusion of water isotopes”. In: *Climate of the Past* 7.
- Soper, A. K. and C. J. Benmore (2008). “Quantum differences between heavy and light water”. In: *Physical Review Letters* 101 (6), p. 065502.
- Steig, E. J. et al. (2013). “Recent climate and ice-sheet change in West Antarctica compared to the past 2000 years”. In: *Nature Geoscience* 6.

- Svensson, A. et al. (2015). “On the occurrence of annual layers in Dome Fuji ice core early Holocene Ice”. In: *Climate of the Past* 11, pp. 1127–1137.
- Theil, H. (1961). *Economic forecast and policy, vol. XV of Contributions to Economic Analysis*. Amsterdam, Netherlands: North-Holland Publishing Company.
- Tsagris, M., C. Beneki, and H. Hassani (2014). “On the Folded Normal Distribution”. In: *Mathematics* 2, pp. 12–28.
- Wel, G. van der, H. Fischer, H. Oerter, H. Meyer, and H. A. J. Meijer (2015). “Estimation and calibration of the water isotope differential diffusion length in ice core records”. In: *The Cryosphere* 9 (4), pp. 1601–1616.
- Whillans, I. M. and P. M. Grootes (1985). “Isotopic diffusion in cold snow and firn”. In: *Journal of Geophysical Research* 90 (D2), pp. 3910–3918.

VARYING REGIONAL $\delta^{18}\text{O}$ -TEMPERATURE RELATIONSHIP IN
HIGH RESOLUTION STABLE WATER ISOTOPES FROM EAST
GREENLAND

The following chapter is a copy of the submitted manuscript Holme et al., 2018b, in review:

Holme, C., Gkinis, V., Lanzky, M., Morris, V., Olesen, M., Thayer, A., Vaughn, B. H., and Vinther, B. M. (2018). Varying regional $\delta^{18}\text{O}$ -temperature relationship in high resolution stable water isotopes from East Greenland. In: *Climate of the Past Discussions*, <https://doi.org/10.5194/cp-2018-169>, in review.

5.1 ABSTRACT

This study examines the stable water isotope signal ($\delta^{18}\text{O}$) of three ice cores drilled on the Renland peninsula (East Greenland coast). While ice core $\delta^{18}\text{O}$ measurements qualitatively are a measure of the local temperature history, the $\delta^{18}\text{O}$ variability actually reflects the integrated hydrological activity that the deposited ice experienced from the evaporation source to the condensation site. Thus, as Renland is located next to a fluctuating sea ice cover, the transfer function used to infer past temperatures from the $\delta^{18}\text{O}$ variability is potentially influenced by variations in the local moisture conditions. The objective of this study is therefore to evaluate the $\delta^{18}\text{O}$ variability of ice cores drilled on Renland and examine what amount that can be attributed to regional temperature variations. In the analysis, three ice cores are utilized to create stacked summer, winter and annually averaged $\delta^{18}\text{O}$ signals (AD 1801-2014). The imprint of temperature on $\delta^{18}\text{O}$ is first examined by correlating the $\delta^{18}\text{O}$ stacks with instrumental temperature records from East Greenland (AD 1895-2014) and Iceland (AD 1830-2014) and with the regional climate model HIRHAM5 (AD 1980-2014). The results show that the $\delta^{18}\text{O}$ variability correlates with regional temperatures on both a seasonal and an annual scale between 1910-2014 while $\delta^{18}\text{O}$ is uncorrelated with Iceland temperatures between 1830-1909.

Our analysis indicates that the unstable regional $\delta^{18}\text{O}$ -temperature correlation does not result from changes in weather patterns through respectively strengthening and weakening of the North Atlantic Oscillation. Instead, the results imply that the varying $\delta^{18}\text{O}$ -temperature relation is connected with the volume flux of sea ice exported through Fram Strait (and south along the coast of East Greenland). Notably, the $\delta^{18}\text{O}$ variability only reflects the variations in regional temperature when the temperature anomaly is positive and the sea ice export anomaly is negative. It is hypothesized that this could be caused by a larger sea ice volume flux during cold years which suppresses the Iceland temperature signature in the Renland $\delta^{18}\text{O}$ signal. However, more isotope-enabled modeling studies with emphasis on coastal ice caps are needed in order to quantify the mechanisms behind this observation. As the amount of Renland $\delta^{18}\text{O}$ variability that reflects regional temperature varies with time, the results have implications for studies performing regression-based $\delta^{18}\text{O}$ -temperature reconstructions based on ice cores drilled in the vicinity of a fluctuating sea ice cover.

5.2 INTRODUCTION

Polar ice caps store deposited precipitation as stratified ice layers thousands of years back in time. This precipitation consists of stable water isotopes ($\delta^{18}\text{O}$, δD) that work as a direct proxy of the relative depletion of a water vapor mass in its transport from the evaporation source to the site where condensation takes place (Epstein et al., 1951; Mook, 2000). This traceability manifests as a correlation between $\delta^{18}\text{O}$ and the temperature in the cloud at the time of condensation (Dansgaard, 1954; Dansgaard, 1964). Thus, a relationship between $\delta^{18}\text{O}$ and temperature is preserved in annual layers of precipitation on an ice cap. Hence, by drilling ice cores at polar sites such as Antarctica and Greenland, it is possible to access past temperatures imprinted in the $\delta^{18}\text{O}$ signal. Several studies have examined the relation between temperature and ice core $\delta^{18}\text{O}$, and its linear or quadratic relationship has regularly been used as a transfer function to infer past temperature (Jouzel and Merlivat, 1984; Johnsen et al., 1989; Jouzel et al., 1997; Johnsen et al., 2001; Ekaykin et al., 2017). While it is evident that $\delta^{18}\text{O}$ and temperature covary, the $\delta^{18}\text{O}$ signal is also affected by changes in sea ice and atmospheric circulation (Noone and Simmonds, 2004; Steig et al., 2013). Changes in the atmospheric circulation can be triggered by climatic oscillation modes (e.g. the North Atlantic Oscillation, Southern Annual Mode, Pacific Decadal Oscillation etc.) which affect the $\delta^{18}\text{O}$ variability as they influence precipitation patterns (Vinther et al., 2010; Ekaykin et al., 2017). Additionally, changes in sea ice extent affect the local moisture conditions which particularly influence the coastal precipitated $\delta^{18}\text{O}$ variability (Bromwich and Weaver, 1983; Noone and Simmonds, 2004). Such

variations have implications for a simple regression-based reconstruction of temperature from $\delta^{18}\text{O}$ as the variability patterns between the ice core isotope signal and the oscillation modes and sea ice extent can have varied in strength back in time. Furthermore, in studies that analyze the relationship between polar precipitated $\delta^{18}\text{O}$ and temperature, the temperature record is often substantially shorter than the $\delta^{18}\text{O}$ series. While this is inevitable when performing temperature reconstructions, utilizing a short temperature record complicates the possibility of verifying if the estimated $\delta^{18}\text{O}$ -temperature relation is stable with time.

The aim of this study is to examine how much of the $\delta^{18}\text{O}$ variability (AD 1801-2014) from a stack of ice cores drilled on the Renland peninsula, Eastern Greenland, can be attributed to temperature variations (map in Fig. 5.1). In the analysis, seasonally averaged $\delta^{18}\text{O}$ time series have been compared with regional temperatures through instrumental temperature records located on the coasts of East Greenland (AD 1895-2014) and Iceland (AD 1821-2014) and the regional atmospheric climate model HIRHAM5 2 m temperature output (AD 1980-2014). The $\delta^{18}\text{O}$ signal is divided into its seasonal components as it potentially improves the reconstruction of variability in weather regimes and past temperatures (Vinther et al., 2003b; Vinther et al., 2010; Zheng et al., 2018). As Renland is located at the coast, its hydrological conditions are connected with the sea ice that annually is transported south along the coast of East Greenland. Relatively small loss in regional sea ice extent ($\approx 10\%$ or less) has previously been found to influence local Greenland moisture source water vapor which is traceable in the corresponding ice core deuterium excess values (Klein and Welker, 2016). The deuterium excess signal ($d_{\text{xs}} = \delta\text{D} - 8 \cdot \delta^{18}\text{O}$, (Dansgaard, 1964)) contains information about the kinetic fractionation occurring when moisture evaporates from the ocean surface and ice core d_{xs} has been found to correlate with relative humidity and sea surface temperature at the source region (Jouzel and Merlivat, 1984; Johnsen et al., 1989). Thus, besides investigating the regional $\delta^{18}\text{O}$ -temperature relationship, this study examines if changes in the Arctic sea ice extent can be detected in the Renland stable water isotopes.

5.3 THE ICE CORES

The Renland ice cap has an area of 1200km^2 with an average ice thickness of a few hundred meters. It is separated from the main Greenlandic ice sheet as a small peninsula on the east coast of Greenland (map in Fig. 5.1). The ice cap experiences a high annual accumulation rate of around 0.47m ice/year with an annual surface temperature of -18°C . Renland has probably never been overridden by the Inland ice as it is surrounded by deep branches of the Scoresbysund Fjord which effectively drains the Inland ice (Johnsen et al., 1992). Additionally,

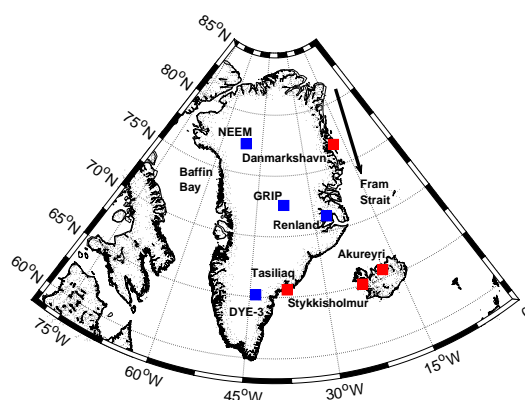


Figure 5.1. Locations of ice core drill sites (blue squares) and the instrumental temperature records (red squares). Sea ice exported from Fram Strait is represented by the black arrow.

the small width of the ice cap which is constrained by the surrounding mountains prohibits the ice elevation from significant increases from present day height. As a result, the ice cap has not experienced any ice sheet elevation changes for the past 8000 years (except for slight uplift due to isostatic rebound) (Vinther et al., 2009). This implies that lapse-rate controlled temperature variations resulting from a varying ice sheet thickness will be negligible.

This study utilizes three ice cores drilled on Renland in the analyses (Table 5.1). Two cores were drilled next to each other in the year 1988 (main (M) and shallow (S) cores) while the third was drilled approximately 2 km away in 2015 as part of the REland ice CAP project (RECAP). The 1988 M and RECAP cores extend over the past 120 ka while the 1988 S core only covers the time back to the year 1801. Despite two cores covering the past interglacial and glacial period, the study focuses on the period AD 1801-2014 as we here have three overlapping ice core records and instrumental temperature recordings. Moreover, the separation of the summer and winter signals is better facilitated when the annual layers not are obliterated due to diffusion and ice thinning.

The records from 1988 were measured on a Isotope Ratio Mass Spectroscopy (IRMS) with a discrete resolution of 5.0 cm while the RECAP core was measured using cavity ringdown spectroscopy (Picarro L2130) on a Continuous Flow Analysis (CFA) system with a nominal resolution of 0.5 cm. For the RECAP core, the years 2011-2014 are covered by the snow pit core A6 drilled next to the drill site. The A6 core was measured discretely with a sample size of 5.0 cm on a Picarro L2130. This was done as the porous snow in the upper firn column easily inhibits a stable measurement flow in the CFA analysis which complicates precise water isotope measurements.

Table 5.1. The subset of the three ice cores used in this study: processing information, analysis and coordinates.

Cores	Coordinates	Time span	Depth span	Meas.	Resolution	Analysis
RECAP	71° 18' 18" N; 26° 43' 24" W; 2315 m.a.s.l.	1801 – 2014	111.7 m	$\delta^{18}\text{O}$, δD	0.5 cm	CFA-L2130
1988 M	71° 18' 17" N; 26° 43' 24" W; 2340 m.a.s.l.	1801 – 1987	92.5 m	$\delta^{18}\text{O}$	5.0 cm	IRMS
1988 S	71° 18' 17" N; 26° 43' 24" W; 2340 m.a.s.l.	1801 – 1987	91.6 m	$\delta^{18}\text{O}$	5.0 cm	IRMS

5.4 DIFFUSION CORRECTION

Firn diffusion dampens the annual oscillations in the $\delta^{18}\text{O}$ data. This takes place while firn (snow that survived a season) is transformed into ice in the top 60-80 meters of the ice sheet. During this densification process, air in the open porous firn is interconnected which enables the stable water isotopes in the firn air to mix with the snow grains (Johnsen, 1977). This molecular diffusion process makes the $\delta^{18}\text{O}$ signal become increasingly more smooth with depth until pore close-off. The firn diffusion of stable water isotopes imposes two challenges on the analysis presented in this study. First, the diffusion of the annual oscillations creates artificial trends in summer and winter season time series of $\delta^{18}\text{O}$ (Vinther et al., 2010). Secondly, it introduces a bias when comparing the ice cores drilled in 1988 with the ice core drilled in 2015. For instance, the $\delta^{18}\text{O}$ signal representing the year 1987 has only experienced 1 year of firn diffusion in the 1988 ice cores while it has experienced 28 years of firn diffusion in the 2015 core. The $\delta^{18}\text{O}$ signal for overlapping years will therefore be more attenuated in the 2015 core.

As this study compares the seasonally averaged $\delta^{18}\text{O}$ signals of three ice cores drilled in different years, it is necessary to ensure that each $\delta^{18}\text{O}$ record has the same firn diffusive properties with depth. This is typically achieved by correcting each $\delta^{18}\text{O}$ record such that the effect of increasing smoothing with depth is removed by deconvolving the measured $\delta^{18}\text{O}$ signal to restore the originally deposited signal. However, Renland frequently experiences summer melting which causes steep isotopic gradients in the firn. Such high frequency gradients complicate a deconvolution of the measured $\delta^{18}\text{O}$ signal (Cuffey and Steig, 1998; Vinther et al., 2010). Instead, this study forward diffuses the three $\delta^{18}\text{O}$ records with depth such that each $\delta^{18}\text{O}$ series has been influenced by the same amount of firn diffusion. Diffusion of stable water isotopes is typically described by the diffusion length (σ) which is the average vertical displacement of a water molecule (units in meters). Thus, the $\delta^{18}\text{O}$ series are forward diffused ($\delta^{18}\text{O}_{fd}$) such that each record has the same σ with depth. Despite that such a smoothing procedure slightly mixes the summer and winter signals, a distinction of the seasonal components is still possible due to Renland's thick annual layers greatly exceeding the diffusion length.

The procedure below outlines in three steps how this was done separately for the 2015, 1988 M and 1988 S cores.

Step 1: First, the amount of diffusion that the measured $\delta^{18}\text{O}$ signal already has experienced with depth is computed through the diffusion length's density dependence (for origin see Gkinis et al., 2014; Holme et al., 2018a):

$$\sigma^2(\rho) = \frac{1}{\rho^2} \int_{\rho_0}^{\rho} 2\rho^2 \left(\frac{d\rho}{dt} \right)^{-1} D(\rho) d\rho \quad (55)$$

where $D(\rho)$ is the firm diffusivity and $d\rho/dt$ is the densification rate. This study uses the firm diffusivity parameterization of Johnsen et al., 2000 (described in Appendix B.1) that employs the site-dependent parameters of temperature (-18°C), accumulation rate (0.47 m ice/year), surface pressure (0.75 atm) and density. Density is here modeled with depth by fitting a Herron and Langway, 1980 densification model to density measurements from the drill sites. From Eq. 55, it is possible to calculate the diffusion length that each layer has experienced ($\sigma^2(\rho)$) (left subplot in Fig. B.1).

Step 2: Equation 55 can be used to calculate the auxiliary diffusion needed to transform a $\delta^{18}\text{O}$ record into having a uniform diffusion length independent of depth. An auxiliary diffusion ($\sigma^2(\rho)_{aux}$) is calculated as the difference between the final diffusion length at the pore close-off density ($\sigma^2(\rho_{pc} = 804.3 \text{ kg/m}^3)$) and the diffusion length at a given layer in meters of ice-equivalent depth:

$$\sigma^2(\rho)_{aux} = \left(\left(\frac{\rho_{pc}}{\rho_i} \right)^2 \sigma^2(\rho_{pc}) - \left(\frac{\rho(z)}{\rho_i} \right)^2 \sigma^2(\rho) \right) \cdot \left(\frac{\rho_i}{\rho(z)} \right)^2 \quad (56)$$

where the fraction $\rho_i/\rho(z)$ ultimately is multiplied in order to transform the $\sigma^2(\rho)_{aux}$ from representing ice-equivalent depth to density-equivalent depth (as the annual oscillations are squeezed during firm compaction). Using Eq. 56, an auxiliary diffusion profile with respect to density (and thus depth) is calculated for an ice core (left subplot in Fig. B.1).

Step 3: Forward diffusion is then simulated through a convolution of the measured data ($\delta^{18}\text{O}_{meas}$) with a Gaussian filter (\mathcal{G}) with a standard deviation equal the auxiliary diffusion length as this is mathematically equivalent to firm diffusion (Johnsen, 1977):

$$\delta^{18}\text{O}_{fd}(z) = \delta^{18}\text{O}_{meas} * \mathcal{G} \quad (57)$$

where

$$\mathcal{G}(z) = \frac{1}{\sigma_{aux} \sqrt{2\pi}} e^{-z^2/(2\sigma_{aux}^2)} \quad (58)$$

As the auxiliary diffusion length decreases with depth, the width of the Gaussian filter changes accordingly. Thus, the convolution (using the σ_{aux} for the corresponding depth) is applied on a moving 2m section which is shifted in small steps equal to the sampling interval. For each convolved data section, only the midpoint of the sliding window is retained as the new forward diffused $\delta^{18}\text{O}_{fd}$ value. In order to avoid tail-problems when diffusing the top 2 meter measurements, the $\delta^{18}\text{O}_{meas}$ data were extended by using its prediction filter coefficients estimated from a maximum entropy method algorithm by Andersen, 1974. This assumes that the extended series has the same spectral properties as the original series. After applying this smoothing routine on the entire record, a $\delta^{18}\text{O}_{fd}$ series with constant σ is obtained. A comparison between $\delta^{18}\text{O}_{fd}$ and $\delta^{18}\text{O}_{meas}$ is shown in Fig. B.1.

5.5 CHRONOLOGY

It is important to ensure that the chronologies of the three ice cores are synchronous before comparing the $\delta^{18}\text{O}$ variability. The two cores drilled in 1988 were manually dated by counting the summer maxima and winter minima in the $\delta^{18}\text{O}$ series and verified by identifying signals of volcanic eruptions in the electrical conductivity measurements (Vinther et al., 2003b; Vinther et al., 2010). For the 2015 RECAP core, the period 1801-2007 was dated with the annual layer algorithm (StratiCounter) presented in Winstrup et al., 2012 and the years 2007-2014 were manually counted similar to the 1988 cores (the RECAP chronology is presented in Simonsen et al., 2018, in review). The annual layer algorithm uses signals in the ice core that all have annual oscillations or peaks such as the chemical impurities (Na^+ , Ca , SO_4^{2-} and NH_4^+), electrical conductivity and stable water isotopes. Even though the model automatically count years, the chronology is still restricted by the same volcanic eruptions as in the 1988 cores. The model marks a year when Na^+ has a peak which indicates winter. Na^+ is a result of the transport of salt from the ocean and it peaks during winter due the strong winds during the fall. As the timing of this winter peak might not be similar to the timing of the $\delta^{18}\text{O}$ series' winter minima (used for the 1988 cores), this study has tuned the RECAP dating presented Simonsen et al., 2018, in review slightly. For each year, this is done by tuning the timing of the summer and winter in the dated RECAP record to match with the maximum and minimum of the $\delta^{18}\text{O}$ series. The chronology is only shifted a maximum of a few months and it is only changed within a given year. This ensures that the modified dating profile remains consistent with the original chronology while it facilitates an optimal comparison between the manually dated and the automatically dated stable water isotopes profiles.

Table 5.2. Correlation coefficients (r) calculated for different combinations of $\delta^{18}\text{O}$ records for the period 1801-1987 ($p < 0.05$).

Season	r (2015/1988 M)	r (2015/1988 S)	r (1988 M/1988 S)
Winter	0.63	0.60	0.78
Summer	0.66	0.65	0.82
Annual	0.64	0.66	0.84

In order to analyze the seasonal signals of the $\delta^{18}\text{O}$ series we need to distinguish between snow deposited during summer and winter. Under the assumption that $\delta^{18}\text{O}$ and temperature extremes in the Greenland region occur simultaneously, Vinther et al., 2010 found best to define the summer and winter seasons such that they each contain 50% of the annual accumulation. Besides maximizing the amount of utilized data, this definition ensures that the winter and summer signals contain no overlapping data. This study has therefore defined the summer and winter seasons similar to Vinther et al., 2010. The summer, winter and annually averaged $\delta^{18}\text{O}$ data used in this study are thus seasonal/annual averages of the forward diffused $\delta^{18}\text{O}$ series.

5.6 $\delta^{18}\text{O}$ VARIABILITY ON RENLAND

The three ice cores' $\delta^{18}\text{O}$ data as a representative of the isotope hydrology on Renland is first evaluated by calculating Pearson correlation coefficients and signal to noise variance ratios (SNR) on the forward diffused $\delta^{18}\text{O}$ records in the overlapping period 1801-1987. The correlation coefficient is a metric that describes the linear relation between two signals and it has been calculated for different combinations of the presented ice cores (Table 5.2). For all correlation coefficient calculations throughout this study, the level of significance is estimated based on a Monte Carlo routine described in Appendix B.2. From the results displayed in Table 5.2, it is evident that the lowest correlation coefficients are found for the winter averaged data with values ranging from 0.60 – 0.78 while the summer and annually averaged signals have higher values ranging from approximately 0.64 – 0.84. The high correlation coefficients indicate that there is a strong linear relationship between the $\delta^{18}\text{O}$ records. This is further illustrated by the visual covariation of the annually averaged $\delta^{18}\text{O}$ records in Fig. 5.2. In all instances, the highest correlations are found when correlating the two ice cores drilled in 1988. This might be attributed to the use of similar dating method and their close proximity. Nonetheless, all the presented ice cores correlated significantly during the 1801-1987 period.

The $\delta^{18}\text{O}$ variability can be further analyzed by examining the mean single series SNR which provides an insight into the amount of signal and noise in the $\delta^{18}\text{O}$ series. Noise can

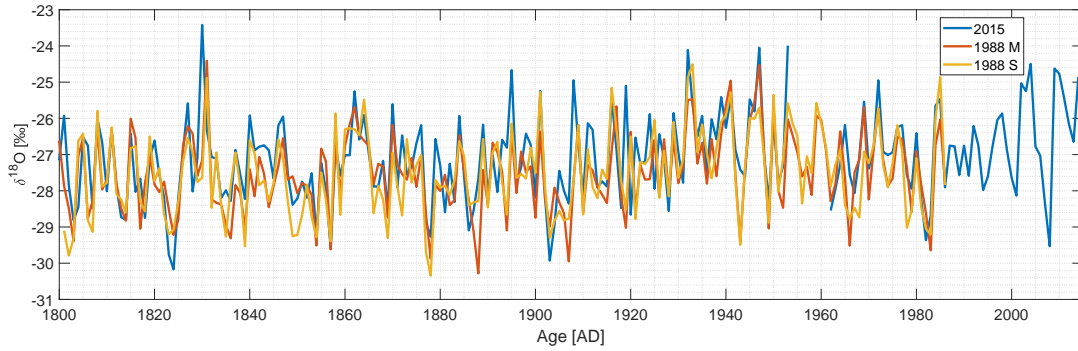


Figure 5.2. Annually averaged $\delta^{18}\text{O}$ for respectively the RECAP 2015 (blue), 1988 M (red) and 1988 S (yellow) cores with age.

originate from depositional effects such as wind shuffling of snow, melt layers and from dating uncertainties (± 1 year) in between the three cores. By averaging n (3) overlapping ice core data records, the mean single series SNR is calculated by comparing the variance of an averaged record (VAR_s) with the mean of the variances ($\overline{\text{VAR}}$) for the n individual records (Johnsen et al., 1997; Vinther et al., 2006):

$$\text{SNR} = \frac{\text{VAR}_s - \frac{\overline{\text{VAR}}}{n}}{\overline{\text{VAR}} - \text{VAR}_s} \quad (59)$$

The SNR results are shown in Table 5.3. Similar to the high correlation, it is evident that merging the two 1988 records results in the highest SNR values. Moreover, the summer averaged signal has a higher SNR compared to the winter averaged signal which probably is a consequence of winters having more windy conditions that generates redeposition of snow. A similar pattern have previously been found for the seasonal isotopes of GRIP ($n = 5$; SNR summer: 0.70, winter: 0.51), Dye-3 ($n = 2$; SNR summer: 1.73, winter: 1.56) and NEEM ($n = 4$; SNR summer: 1.28, winter: 0.64) (map in Fig. 5.1) (Vinther, 2003a; Zheng et al., 2018). This comparison also shows that the SNR values of the three Renland ice cores are high compared to GRIP, Dye-3 and NEEM which likely can be attributed to a combination of a high accumulation rate and a good cross-dating between the compared cores.

From this analysis, the study can comment on two things. First, the two 1988 cores have the most robust common signal of all the tested combinations. As this was for two adjacently drilled ice cores, utilizing all three records still result in a larger spatial atmospheric representativeness of the region. Secondly, the high SNR and correlation coefficients imply that the chronologies from the annual layer detection algorithm and the manual counting are consistent. This has implications for future ice core science as manual layer counting can be a slow and inefficient procedure. Thus, manual counting can effectively be replaced with the StratiCounter

Table 5.3. Mean signal to noise variance ratios calculated for the summer, winter and annually averaged data using respectively two and three cores in the period 1801-1987.

Merged cores	SNR winter	SNR summer	SNR annual
1988 M, 2015	1.65	1.73	1.73
1988 M, 1988 S	3.53	4.46	5.05
1988 M, 1988 S, 2015	2.01	2.36	2.43

software by Winstrup et al., 2012 for ice cores where several datasets that contain observable annual peaks or oscillations are available.

The high combined SNR values and correlation coefficients indicate that it is beneficial to combine the time series into a stacked $\delta^{18}\text{O}$ record. We choose to employ all three ice cores as that increases the spatial representativeness of $\delta^{18}\text{O}$ while it provides water isotopic variability for the years 1988-2014. A stacked record is typically created by averaging the time series but the time span 1801-2014 consists of an inhomogeneous amount of data records as only the RECAP core contains data in the 1988-2014 period while it also has a gap between 1954-1961 due to missing ice samples. Thus, it is important to implement a variance correction in order to avoid bias issues when averaging time series with nonuniform length (Osborn et al., 1997; Jones et al., 2001). This variance correction (c) can be expressed directly through the SNR values in Table 5.3 and the number of records (m) used in the averaging for the given year (derivation can be found in Vinther et al., 2006):

$$c = \sqrt{\frac{\text{SNR}}{\text{SNR} + \frac{1}{m}}} \quad (60)$$

Before stacking, the three time series are standardized based on the period of overlap (1801-1987) ($\delta^{18}\text{O}_{\text{std}}$ has mean = 0 and standard deviation = 1). An average $\delta^{18}\text{O}_{\text{avr}}$ value is then calculated by multiplying c onto the mean $\delta^{18}\text{O}_{\text{std}}$ for each year:

$$\delta^{18}\text{O}_{\text{avr}} = c \cdot \frac{1}{m} \sum_{i=1}^m \delta^{18}\text{O}_{\text{std}_i} \quad (61)$$

The amplitude and variability of the original $\delta^{18}\text{O}$ series are then restored by using the average variance ($\overline{\text{VAR}}$) and the average ($\overline{\delta^{18}\text{O}}$) of the three time series (from the period where the time series were standardized):

$$\delta^{18}\text{O}_{\text{stack}} = \delta^{18}\text{O}_{\text{avr}} \cdot \sqrt{\overline{\text{VAR}} + \overline{\delta^{18}\text{O}}} \quad (62)$$

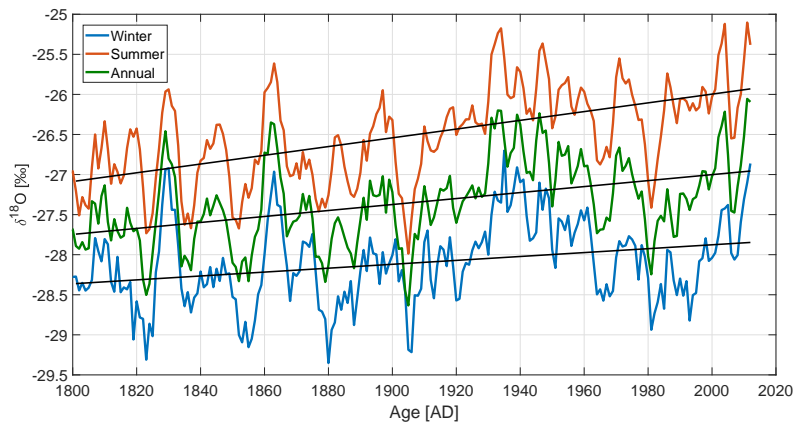


Figure 5.3. Summer (red), winter (blue) and annually averaged (green) $\delta^{18}\text{O}$ stacks together with their corresponding linear trends (black lines) for the period 1801–2014. A moving average of 5 years has been applied on all the time series. For the unfiltered series, the reader is referred to Figs. 5.4, B.2 and B.3.

Figure 5.3 shows the summer, winter and annual $\delta^{18}\text{O}_{\text{stack}}$ series for the period 1801–2014. In the figure, a 5 year moving average has been applied on the stacked records in order filter out any remaining high frequency noise variability. From the figure, it is evident that the summer averaged signal is less depleted than the annual and winter averaged signals. Moreover, the summer signal has the largest trend in $\delta^{18}\text{O}$ with an increase of $0.54\text{‰}/\text{century}$ while the winter and annually averaged data show lower increases of respectively $0.24\text{‰}/\text{century}$ and $0.37\text{‰}/\text{century}$. The amount of variability that correlates with temperature will be examined in Sect. 5.7.

5.7 THE TEMPERATURE SIGNATURE IN $\delta^{18}\text{O}$

5.7.1 Correlation with instrumental temperature records

The relationship between Renland $\delta^{18}\text{O}$ variability and temperature is first investigated by comparing the stacked $\delta^{18}\text{O}$ series with instrumental temperature records. This study uses the nearest and longest temperatures recordings from Greenland (Tasiilaq and Danmarkshavn) and Iceland (Akureyri and Stykkisholmur) - locations are shown in Fig. 5.1. The Greenland temperature records are available from the Danish Meteorological Institute (<http://www.dmi.dk/laer-om/generelt/dmi-publikationer/tekniske-rapporter/>) and the Iceland temperatures are available from the Icelandic Met Office (<http://en.vedur.is/climatology/data/#a>). For the temperature measurements, the seasons have been de-

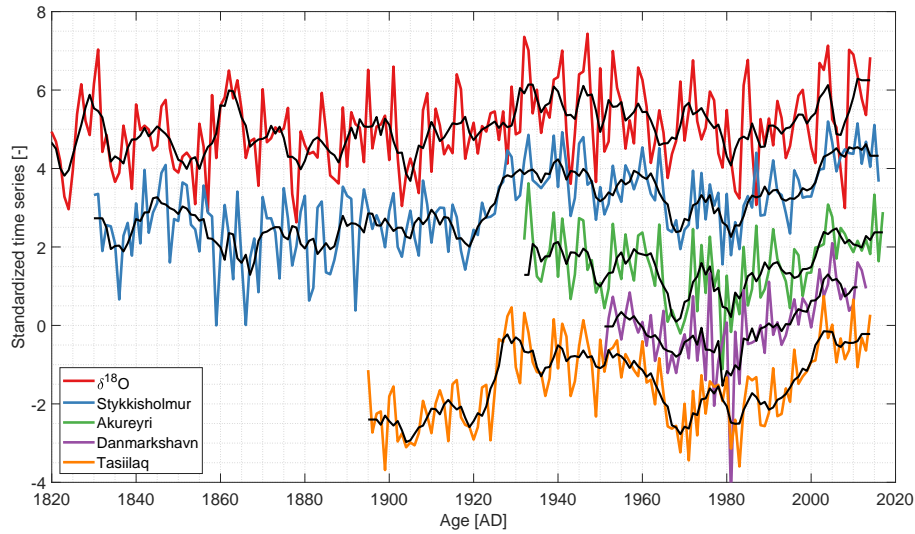


Figure 5.4. Annually averaged $\delta^{18}\text{O}$ and temperature series. For visualization, the time series have been standardized and shifted vertically. The black curves represent a moving average of 5 years.

Table 5.4. Correlation coefficients between the $\delta^{18}\text{O}$ stack and instrumental temperature records ($p < 0.05$) on both a 1 year resolution and with a 5 year moving mean applied (in bold).

Record	Stykkisholmur	Akureyri	Danmarkshavn	Tasiilaq
Period	1830 – 2014	1931 – 2014	1951 – 2014	1895 – 2014
r winter	0.29 / 0.51	0.30 / 0.56	0.21 / 0.51	0.41 / 0.64
r summer	0.40 / 0.58	0.45 / 0.69	0.30 / 0.62	0.37 / 0.61
r annual	0.48 / 0.62	0.40 / 0.58	0.35 / 0.63	0.50 / 0.72

finer similar to Vinther et al., 2010 with summer extending from May-October and winter from November-April. Figure 5.4 shows the annually averaged $\delta^{18}\text{O}$ stack together with the annually averaged temperature measurements (winter and summer averages are shown in Fig. B.2 and B.3). Visually, the past 100 years of summer, winter and annually averaged $\delta^{18}\text{O}$ signals of Renland covary with the regional temperature. However, the years 1830-1910 show periods with both anticorrelation and correlation. Besides the visual covariation, correlation coefficients between the temperature recordings and the $\delta^{18}\text{O}$ stacks are calculated and shown in Table 5.4. The correlations with the winter averaged data are in general the lowest while annual and summer signals have similar high correlations at all the sites. The best correlation with the Renland $\delta^{18}\text{O}$ signal is found for the annual averages at Tasiilaq ($r = 0.50$). Additionally, applying a 5 year moving mean on the $\delta^{18}\text{O}$ and temperature series increases all the correlations (i.e. the Tasiilaq correlation coefficient increases to $r = 0.72$).

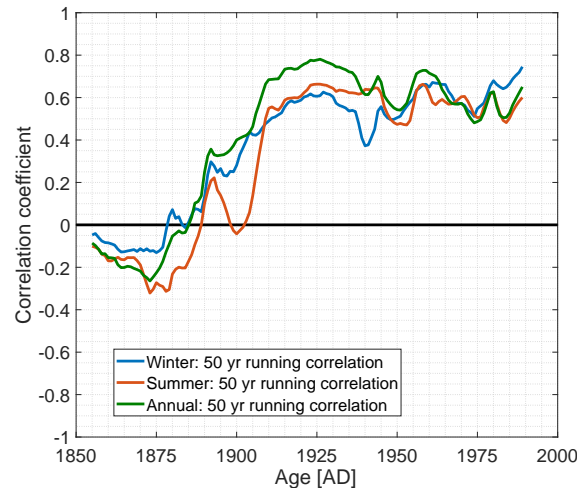


Figure 5.5. Running correlation of 50 years between the Stykkisholmur temperature and the $\delta^{18}\text{O}$ stack for respectively winter (blue), summer (red) and annual averages (green). Both the $\delta^{18}\text{O}$ and temperature data were first smoothed with a 5 year moving mean. Each year represents the midpoint of the running window.

The high correlation between $\delta^{18}\text{O}$ and temperature implies that the region's temperature variability is imprinted in the Renland $\delta^{18}\text{O}$ stack. Conventionally, a simple interpretation in terms of local temperature can then be achieved by using the linear relation between $\delta^{18}\text{O}$ and temperature. However, this requires that the linear relationship between temperature and $\delta^{18}\text{O}$ is stable throughout time. In order to examine this, correlation coefficients between Stykkisholmur temperature and $\delta^{18}\text{O}$ have been calculated on a 50 year running window and shown in Fig. 5.5. Here Stykkisholmur is chosen as it has the longest temperature record while we selected a window size of 50 years in order to include enough independent data as the time series have been smoothed with a 5 year moving mean. This analysis indicates that the Stykkisholmur temperature and the $\delta^{18}\text{O}$ stack only correlates in the period 1910-2014. For winter, summer and annual averages, the average correlation in the period 1910-2014 is 0.56, 0.65 and 0.66 while it severely reduces to -0.02 , -0.02 and 0.004 in the 1830-1909 period. Thus, the high correlation coefficients presented in Table 5.4 is only a result of the high correlations in the 1910-2014 period. This could explain why the highest $\delta^{18}\text{O}$ -temperature correlation was found at Tasiilaq as it only extended back to 1895. Consequently, the regional $\delta^{18}\text{O}$ -temperature relationship between Renland isotopes and the Iceland temperature record is not constant through time. While it remains unknown if the temperature on Iceland and Renland was similar between 1830-1909, it is certain that the Renland $\delta^{18}\text{O}$ variability does not represent the temperature variability at Iceland in said period. Thus, even though the $\delta^{18}\text{O}$ variability probably reflects the local temperature on Renland, the results show that the decorrelation scale of this $\delta^{18}\text{O}$ -temperature relationship was different in the 1830-1909 period.

5.7.2 Correlation with the HIRHAM5 2 m temperature output

The spatial extent of the correlation between the $\delta^{18}\text{O}$ signal and temperature is further investigated by using 2 m temperature output from the regional climate model, HIRHAM5 (Christensen et al., 2007). This particular HIRHAM5 simulation (Langen et al., 2017) covers the entire Greenlandic region including Iceland. At the lateral boundaries and over the ocean, the model is driven with the European Re-Analysis dataset, ERA-Interim (Dee et al., 2011). This study uses monthly averaged data (1980-2014) on a horizontal resolution of 0.05° (~ 5.5 km) converted to summer and winter temperatures by averaging May-October and November-April, respectively. The RECAP core is used instead of the stacked record as the analysis is on data from the satellite era, which is minimally available in the 1988 cores. The correlation maps are shown in Fig. 5.6. The results show significant positive correlations between the winter signals of HIRHAM5 2 m temperature and the RECAP $\delta^{18}\text{O}$. Moreover, the high correlations ($r > 0.5$) that extend over most of Greenland, irrespectively of the ice divide, indicate that the winter temperature variability over Greenland is imprinted in the Renland $\delta^{18}\text{O}$ signal. Results furthermore show that there is no statistically significant correlation between $\delta^{18}\text{O}$ and temperature east of Renland in areas regularly covered by sea ice. For the summer and annually averaged signals, the correlations are lower ($r \sim 0.4 - 0.5$) and they only cover the east coast region. This local spatial pattern is consistent with Vinther et al., 2010 who found that the summer averaged $\delta^{18}\text{O}$ data from different Greenlandic ice cores were less internally coherent than the corresponding winter data. This could explain why the summer $\delta^{18}\text{O}$ variability of the RECAP core only correlates with the local temperatures on the coast of East Greenland. Moreover, the variance in summer averaged temperatures over Greenland is very low as shown in Fig. 5.7. The low variance is due to the HIRHAM5 summer temperatures reaching a maxima just below 0°C at places with constant ice cover. For instance, Fig. 5.8 shows the monthly averaged HIRHAM5 temperature from a grid point on Renland where it is evident that the monthly averaged temperature fluctuations during summer are very small. Thus, the small temperature fluctuations can limit the possibility of interpreting the spatial extent of summer and annual temperature variability imprinted in the $\delta^{18}\text{O}$ signal.

All in all, these results support the correlations from Sect. 5.7.1 that showed high correlations between $\delta^{18}\text{O}$ and temperature in the 1910-2014 period.

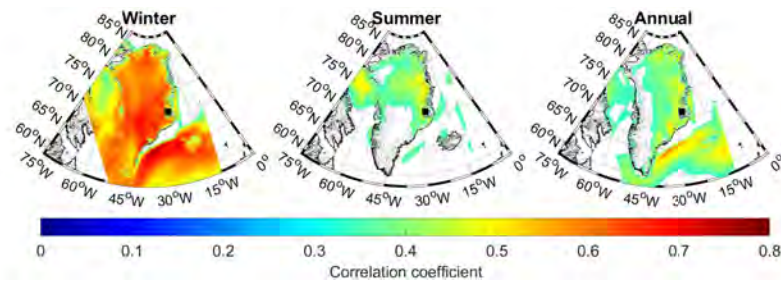


Figure 5.6. Figures showing the correlation between winter (left), summer (middle) and annually (right) averaged RECAP $\delta^{18}\text{O}$ and HIRHAM5 temperatures. Only correlations with $p < 0.05$ are shown.

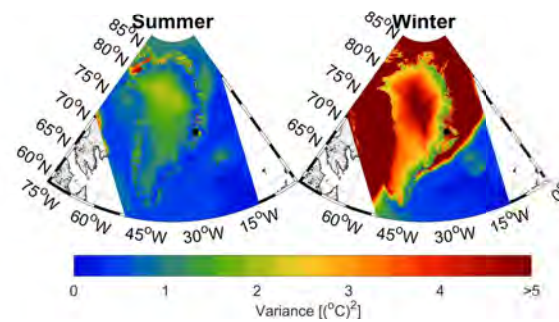


Figure 5.7. Variances of the summer (left) and winter averaged temperatures (right). A maximum variance of $5(\text{°C})^2$ is displayed in order to emphasize the small variance in the summer averaged signal.

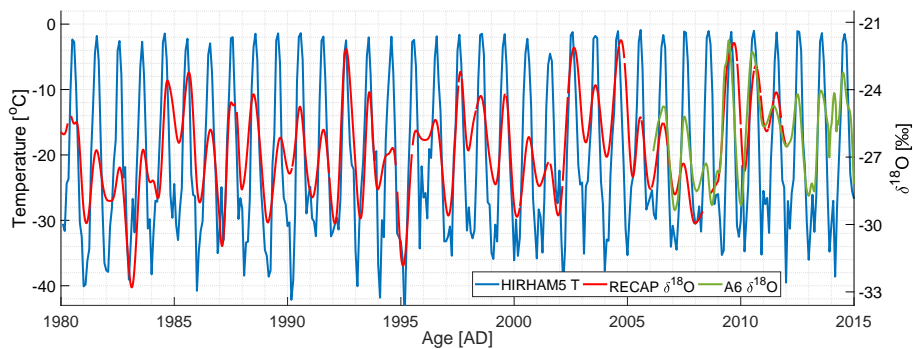


Figure 5.8. Monthly averaged 2 m temperature from a grid point on Renland (blue curve) plotted together with the forward diffused $\delta^{18}\text{O}$ from the RECAP ice core (red curve) and A6 snow pit core (green curve).

5.8 THE NORTH ATLANTIC OSCILLATION'S IMPRINT ON $\delta^{18}\text{O}$

The North Atlantic Oscillation (NAO) describes fluctuations in atmospheric pressure at sea level between Iceland and the Azores. A strengthening and weakening of respectively the low pressure system over Iceland and high pressure system over the Azores control both the direction and strength of westerly winds and storm tracks over the North Atlantic. Such changes in the NAO have previously been found to have an imprint on precipitation in western Greenland (Appenzeller et al., 1999). Correspondingly, the winter isotope signal of West and South Greenland ice cores have previously been found to anticorrelate with the atmospheric circulation changes from NAO (Vinther et al., 2003b; Vinther et al., 2010). Despite that Vinther et al., 2010 showed that ice cores drilled on the Greenland east coast revealed no connection with the NAO, this study examines said correlation in order to determine if changes in the NAO can be linked to the varying $\delta^{18}\text{O}$ -temperature relationship.

While the NAO is best described through a principal component analysis of multiple sea level pressure records in the North Atlantic region, this study uses an approximation where the NAO index is based on pressure observations only near the two centers of action of the surface pressure field (the Azores/Iberian Peninsula and Iceland). Such an approximation was carried out by Jones et al., 1997 who reconstructed the NAO variation back to 1821 (and since extended up to present time). This study uses a slightly modified version of this NAO index by Vinther et al., 2003c who improved the NAO record in the period 1821-1856 by using extra pressure series.

The connection between the NAO index and seasonally (and annually) averaged $\delta^{18}\text{O}$ stacks is examined by estimating their correlation. Correlation coefficients have been calculated on 5 year moving averages of the NAO and $\delta^{18}\text{O}$ stacks and shown in Table 5.5 (the annual NAO record is plotted in Fig. 5.9). The level of significance is estimated based on a Monte Carlo routine described in Appendix B.2. In the complete 1821-2014 period, the summer, winter and annually averaged NAO and $\delta^{18}\text{O}$ data are uncorrelated with coefficients of 0.01, -0.05 and 0.02, respectively. If we instead examine the time before and after the $\delta^{18}\text{O}$ -temperature correlation terminated (the year 1909), the summer and annually averaged data yield positive correlations of 0.29 and 0.30 between 1821-1909 while the winter and annually averaged data yield negative correlations -0.25 and -0.22 between 1910-2014. Thus, there is a varying relation between the NAO and the $\delta^{18}\text{O}$ data and the weak $\delta^{18}\text{O}$ -NAO anticorrelation coincides with a covarying $\delta^{18}\text{O}$ -temperature relation. However, the weak correlations during 1821-1919 imply that the NAO only can account for around 8 – 9% of the corresponding

Table 5.5. Correlation coefficients between the $\delta^{18}\text{O}$ stack and NAO index. Both time series have been smoothed with a 5 year moving mean. Only the numbers in bold are statistically significant ($p < 0.05$).

Period	1821 – 1909	1910 – 2014	1821 – 2014
r winter	0.15 ($p = 0.16$)	-0.25 ($p = 0.01$)	-0.05 ($p = 0.52$)
r summer	0.29 ($p < 0.01$)	-0.15 ($p = 0.13$)	0.01 ($p = 0.85$)
r annual	0.30 ($p < 0.01$)	-0.22 ($p = 0.02$)	0.02 ($p = 0.82$)

$\delta^{18}\text{O}$ variability. It therefore seems unlikely that respectively strengthening and weakening of the NAO cause changes in the $\delta^{18}\text{O}$ -temperature relation.

5.9 THE IMPACT OF SEA ICE FLUCTUATIONS ON THE STABLE WATER ISOTOPES

5.9.1 Fram Strait sea ice export

In this section, it is investigated if there is a connection between the Renland $\delta^{18}\text{O}$ variability and the sea ice export (SIE) through the Fram Strait (map in Fig. 5.1). Multi-year sea ice from the Arctic Ocean is exported southward through Fram Strait along the eastern coast of Greenland into the Greenland Sea. Fluctuations in this sea ice volume flux have a direct effect on the amount of open water located east and northeast of Renland. As $\delta^{18}\text{O}$ is an integrated signal of the hydrological activity along the moisture transport pathway from evaporation source to deposition, the open water which facilitates moist and mild climatic conditions will likely affect the isotopic composition of the precipitation deposited on Renland. Essentially, besides the temperature dependence of isotopic fractionation during local condensation, $\delta^{18}\text{O}$ contains information about the amount of water mass that is removed from the air during the poleward transport and the continuous contribution of local water mixing with the transported water mass (Noone and Simmonds, 2004).

This analysis uses a Fram Strait SIE record covering the period 1820-2000 reconstructed by Schmith and Hansen, 2002. It is an ice volume flux record [km^3/yr] based on historical observations of multi-year sea ice obtained from ship logbooks and ice charts. As the record represents the annual SIE, only the annually averaged $\delta^{18}\text{O}$ stack is used in the analysis. Figure 5.9 shows the SIE together with the annually averaged $\delta^{18}\text{O}$ stack and the RECAP d_{xs} record (d_{xs} is only available for the RECAP core). A correlation analysis is carried out in order to quantify any covariation of the records. For a moving average of 5 years applied on the time series, there is an anticorrelation of -0.54 ($p < 0.01$) between the annual SIE and $\delta^{18}\text{O}$ while there is no significant correlation between d_{xs} and the SIE ($r = -0.08$). From the correlation

analyses, it is clear that $\delta^{18}\text{O}$ anticorrelates with SIE while it correlates with temperature (Sect. 5.7.1). In order to examine if these correlations apply simultaneously, correlation coefficients have been calculated on a 50 year running window. The level of significance is estimated based on a Monte Carlo routine described in Appendix B.2. The results are plotted in Fig. 5.10. In the past 100 years, the Stykkisholmur temperature record is found to correlate with Renland $\delta^{18}\text{O}$ while it (as similar to $\delta^{18}\text{O}$) anticorrelates with SIE through Fram Strait. This likely indicates that warm temperatures result in less sea ice that can be exported away from the Arctic Ocean. However, this pattern ceases to exist previous to the early 1900s such that neither the $\delta^{18}\text{O}$ signal or temperature share any correlation with the SIE. This synchronous decrease in correlation indicates that the uncorrelated $\delta^{18}\text{O}$ –temperature relation cannot be explained by dating errors in the ice core chronologies. Furthermore, as discussed in Sect. 5.8 and shown as running correlations in Fig. 5.10, the varying $\delta^{18}\text{O}$ –temperature correlation cannot be a consequence of the NAO controlling the $\delta^{18}\text{O}$ variability. Moreover, Fig. 5.10 also shows that changes in local moisture source regions are not traceable through the d_{xs} –SIE correlation.

In order to examine this $\delta^{18}\text{O}$ –temperature correlation hiatus, the connection between the SIE anomaly and the $\delta^{18}\text{O}$ –temperature relation is plotted in Fig. 5.11 (SIE anomaly is here defined as the deviation from the mean flux). As a 5 year moving mean has been applied on the time series, only every 5 point is used in the analysis. From the figure, it is clear that on years when the normalized temperature is positive ($T_{\text{norm}} = T - T_{\text{mean}}$), there is always a negative SIE anomaly and a high $\delta^{18}\text{O}$ –temperature correlation of 0.83. Whereas, for $T_{\text{norm}} < 0$ there is no $\delta^{18}\text{O}$ –temperature correlation ($r = 0.02$) which coincides with a combination of both positive and negative SIE anomalies. Besides showing that higher temperatures coincide with less multi-year sea ice being transported south (likely due to an already lower extent of sea ice), it appears that lower temperatures coincide with more fluctuations in the SIE which possibly reduce the $\delta^{18}\text{O}$ –temperature correlation. These results imply that the $\delta^{18}\text{O}$ variability can be dominated by other climatic conditions such as SIE, and does not only represent variations in regional temperature for an extended period of time.

5.9.2 *Sea ice concentration and sea surface temperature*

The Arctic sea ice concentration (SIC) data (fractional ice cover in percentage) from the ERA-Interim reanalysis (Dee et al., 2011) has been correlated with the RECAP $\delta^{18}\text{O}$ and d_{xs} series and the results are shown in Figs. 5.12 and 5.13 (1980–2014). Similar to Sect. 5.7.2, summer refers to May–October and winter refers to November–April. In the case of d_{xs} , only the annually averaged data is used as its seasonal components is smeared out after the $\delta^{18}\text{O}$ and

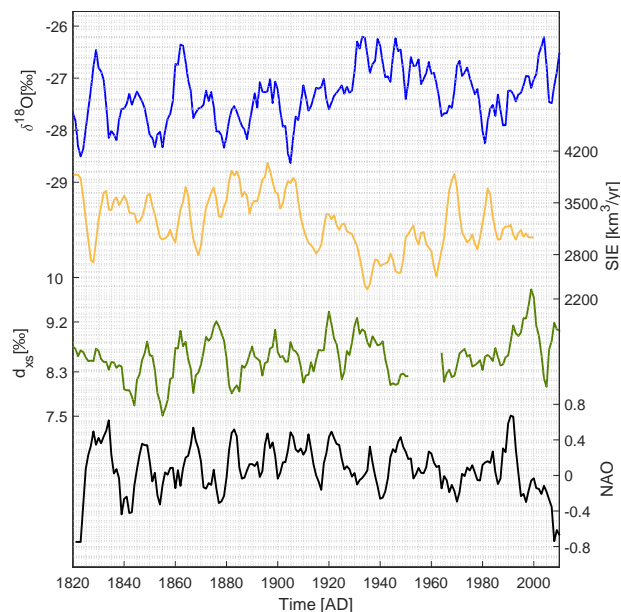


Figure 5.9. Annually averaged $\delta^{18}\text{O}$ stack (blue curve), Fram Strait SIE (yellow curve), d_{xs} (green curve) and NAO index (black curve). A 5 year moving average has been applied on all the data.

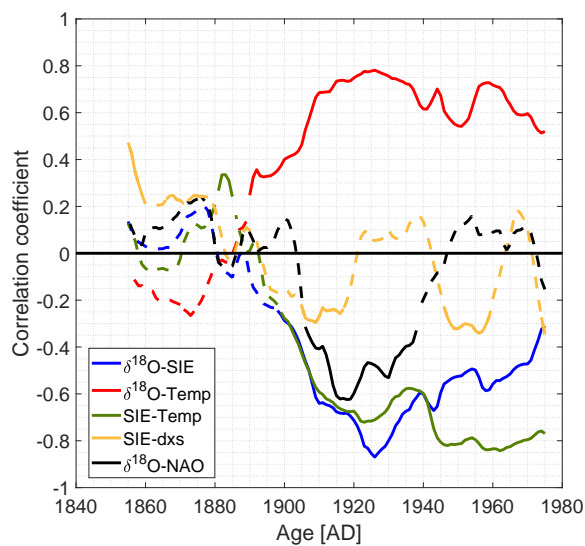


Figure 5.10. Running correlations of 50 years between Stykkisholmur temperature and the $\delta^{18}\text{O}$ stack (red), SIE and the $\delta^{18}\text{O}$ stack (blue), SIE and Stykkisholmur temperature (green), the $\delta^{18}\text{O}$ stack and the NAO index (black) and d_{xs} with SIE (yellow). The solid lines represent significant correlation ($p < 0.05$) while the dashed lines are insignificant $p > 0.05$. Each year represents the midpoint of the running window.

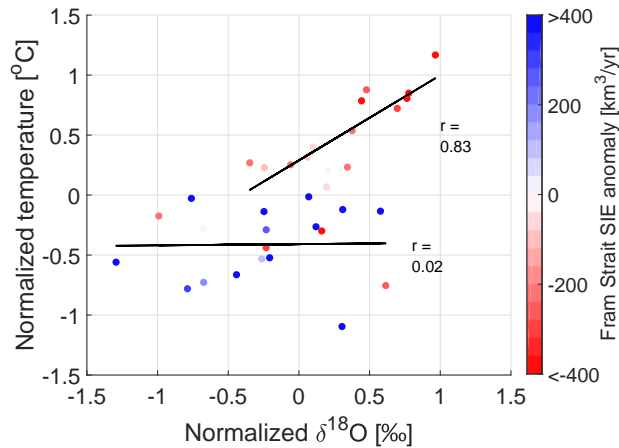


Figure 5.11. Normalized annual temperature plotted with respect to normalized annual $\delta^{18}\text{O}$ where colors indicate strength of the Fram Strait sea ice export anomaly. A 5 year moving average has been applied to all the time series but only every 5 point is displayed and used in the analysis. The solid black lines represent linear fits between $\delta^{18}\text{O}$ and temperature for positive and negative temperature anomalies.

δD data have been forward diffused. The results show a large patch of anticorrelation between $\delta^{18}\text{O}$ and SIC in the Baffin Bay area ($r \approx -0.4$) outside West Greenland for both winter and annually averaged data. Presumably, this indicates that the climate at Renland is similar to the climate at Baffin Bay which controls the advance and retreat of the sea ice extent. A similar connection was found in Sect. 5.7.2 which showed that winter averaged $\delta^{18}\text{O}$ signal correlated with temperatures all over Greenland. Resembling anticorrelations between NEEM $\delta^{18}\text{O}$ and Baffin Bay SIC have previously been found (Steen-Larsen et al., 2011; Zheng et al., 2018). Moreover, the results are consistent with Faber et al., 2017 who found that changes in the Baffin Bay sea ice coverage can impact the $\delta^{18}\text{O}$ precipitation over Greenland (by using an atmospheric general circulation model coupled with water isotopologue tracing (isoCAM3)). Furthermore, the analysis shows only a small patch of correlation between the $\delta^{18}\text{O}$ series and the SIC south of Fram Strait. However, this is not necessarily inconsistent with the significant anticorrelation presented in Sect. 5.9.1. Possibly, this nuance can be explained by the SIE representing the annual discharge of multi-year sea ice (ice volume flux) while the SIC represents the fractional ice cover in percentage (area).

The connection between the Renland stable water isotopes and the local climate conditions is further investigated by correlating the RECAP d_{xs} signal with the Arctic SIC and sea surface temperature (SST). Figure 5.13 shows that there exists small patches of positive correlation patterns between the d_{xs} signal and the SIC in the Arctic Ocean and south of Baffin Bay. As these areas are very small, it is difficult to evaluate the connection between the extent of SIC

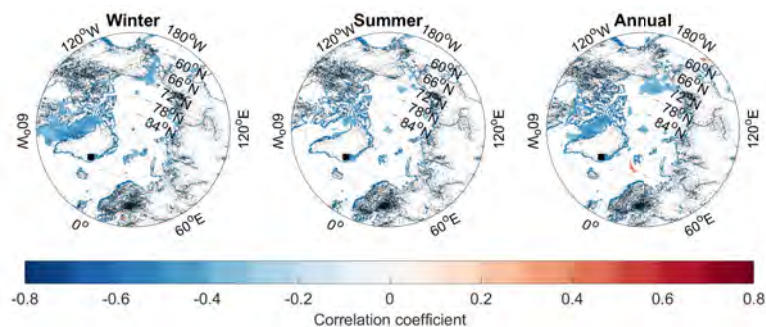


Figure 5.12. Maps showing the correlation coefficients between the ERA-Interim sea ice concentration and the RECAP $\delta^{18}\text{O}$ data for the 1980-2014 period ($p < 0.05$).

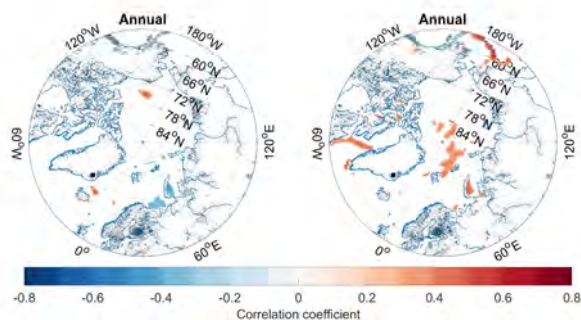


Figure 5.13. Maps showing the d_{XS} -SST (left) and d_{XS} -SIC (right) correlation coefficients between annually averaged data from RECAP and ERA-Interim covering the 1980-2014 period ($p < 0.05$).

and d_{XS} at Renland. The d_{XS} signal is further examined by checking if it reflects the local SST variability. This has been done by correlating the d_{XS} signal with the SST data in the Arctic region from ERA-Interim data (1980-2014). From Fig. 5.13, it is evident that there barely exists patches with significant correlation. Thus, it is difficult to assess whether the RECAP d_{XS} record directly reflects the local SST or SIC variability during the 1980-2014 period. More analysis on what controls the Renland d_{XS} signal is needed in future research.

5.10 DISCUSSION

The analysis showed that the strength of the SIE have varied in the past and that its fluctuations could be connected with the regional $\delta^{18}\text{O}$ -temperature relationship. Despite the apparent connection, this study has not proved any causality between the $\delta^{18}\text{O}$ -temperature relation and

the Fram Strait SIE. Still, a proposed hypothesis for this connection is that the fluctuating SIE conditions during cold years impose changes in the location of the local moisture sources which suppress the imprint of Iceland temperature variability in Renland $\delta^{18}\text{O}$. It is likely that this connection has its strongest impact on ice cores drilled at the coastal regions near sea ice as Vinther et al., 2010 found that the $\delta^{18}\text{O}$ records of Greenlandic ice cores drilled in South and Central Greenland correlated well with a Southwest Greenland instrumental temperature series in the period 1785-1980 (Vinther et al., 2006). With reference to this temperature series, Fig. B.4 shows that these temperatures do not have a stable linear covariation with the Renland $\delta^{18}\text{O}$ stack (winter averages are here chosen as that constitutes the longest and most homogeneous record). Besides that Renland obviously is located far away from the Southwest Greenland instrumental temperature stations, this contrariety might result from the isotope distillation process being more manifested as a temperature variability in the $\delta^{18}\text{O}$ signal when the precipitation has journeyed further and risen in altitude more than that of the coastal region, further depleting the $\delta^{18}\text{O}$ signal. In order to evaluate this hypothesis, more studies using isotope-enabled modeling are needed. The impact of changes in sea ice on the Arctic $\delta^{18}\text{O}$ precipitation has previously been investigated by Faber et al., 2017 who found that the $\delta^{18}\text{O}$ precipitation on Greenland only responded to perturbations of the Baffin Bay sea ice coverage. However, they used a horizontal resolution of $\sim 1.4^\circ \times 1.4^\circ$ which barely resolved the Renland Ice Cap of $\sim 1200\text{km}^2$. Thus, a further examination of how changes in sea ice extent is connected with the coastal Greenlandic precipitation on a higher spatial resolution grid is essential in order to evaluate this hypothesis.

Moreover, while this study found that the Renland $\delta^{18}\text{O}$ signal anticorrelated with variations in the sea ice extent outside West Greenland (Sect. 5.9.2), a similar pattern was found with the HIRHAM5 temperature correlations presented in Sect. 5.7.2. It is therefore likely that the connection represents a reduced sea ice coverage due to increasing temperatures rather than an actual interconnection between Renland $\delta^{18}\text{O}$ and Baffin Bay sea ice.

5.11 CONCLUSION

This study found that by quantifying the mean signal to noise variance ratios, a robust seasonal $\delta^{18}\text{O}$ signal (1801-2014) could be extracted by stacking three ice cores from Renland. This $\delta^{18}\text{O}$ stack was correlated with instrumental temperature records from East Greenland and Iceland and with the HIRHAM5 2m temperature output. Results showed that there were high correlations between $\delta^{18}\text{O}$ and regional temperatures on both a seasonal and annual scale between 1910-2014. A similar anticorrelation was found between the $\delta^{18}\text{O}$ stack and the amount

of sea ice exported through Fram Strait. However, both correlations stopped in the 1830-1909 period. The results indicated that the varying regional temperature variability in the $\delta^{18}\text{O}$ signal could not be explained by the North Atlantic Oscillation. Instead, the linear $\delta^{18}\text{O}$ -temperature relation depended on whether the temperatures were warmer or colder than the temperature anomaly. Warm years were associated with a high correlation and accompanied by less sea ice transported south along the coast while cold years were associated with zero correlation that accompanied a fluctuating amount of sea ice along the coast. These results implied that changes in the extent of open water outside Renland might affect the local moisture conditions. Hence, greater sea ice flux along the coast of Greenland may suppress the Iceland temperature signature in the $\delta^{18}\text{O}$ signal; however, this was not confirmed by correlations between d_{xs} and sea surface temperature in the Arctic region. Thus, more high resolution isotope-enabled modeling focused on the effect of Arctic sea ice on coastal precipitation are needed in order to quantify this process.

These results have implications for ice core temperature reconstructions based on the linear relationship between $\delta^{18}\text{O}$ variability and local temperature records. For Renland, the linear $\delta^{18}\text{O}$ -temperature relationship was unstable with time which implied that the annual-to-decadal variability of $\delta^{18}\text{O}$ measured in an ice core could not be directly attributed to temperature variability. Similar conditions might apply for other ice cores drilled in the vicinity of a fluctuating sea ice cover. This reinforces the interpretation that $\delta^{18}\text{O}$ is an integrated signal of all the hydrological activity that a vapor mass experiences from the evaporation at the source to its condensation at the drill site.

REFERENCES

- Andersen, N. (1974). "On The Calculation Of Filter Coefficients For Maximum Entropy Spectral Analysis". In: *Geophysics* 39.1.
- Appenzeller, C., J. Schwander, S. Sommer, and T. F. Stocker (1999). "The North Atlantic Oscillation and its imprint on precipitation and ice accumulation in Greenland". In: *Geophysical Research Letters* 25.11, pp. 1939–1942.
- Bromwich, D. H. and C. J. Weaver (1983). "Latitudinal displacement from main moisture source controls $\delta^{18}\text{O}$ of snow in coastal Antarctica". In: *Nature* 301, pp. 145–147.
- Christensen, O. B., M. Drews, J. H. Christensen, K. Dethloff, K. Ketelsen, I. Hebestadt, and A. Rinke (2007). *The HIRHAM Regional Climate Model Version 5*. Technical Report 06-17. Danish Climate Centre, DMI.

- Cuffey, K. M. and E. J. Steig (1998). “Isotopic diffusion in polar firn: implications for interpretation of seasonal climate parameters in ice-core records, with emphasis on central Greenland”. In: *Journal of Glaciology* 44.147, pp. 273–284.
- Dansgaard, W. (1964). “Stable isotopes in precipitation”. In: *Tellus B* 16.4, pp. 436–468.
- Dansgaard, W. (1954). “The ^{18}O -abundance in fresh water”. In: *Geochimica et Cosmochimica Acta* 6.5–6, pp. 241–260.
- Dee, D. P., S. M. Uppala, A. J. Simmons, P. Berrisford, P. Poli, S. Kobayashi, U. Andrae, M. A. Balmaseda, G. Balsamo, d. P. Bauer, et al. (2011). “The ERA-Interim reanalysis: Configuration and performance of the data assimilation system”. In: *Quarterly Journal of the royal meteorological society* 137.656, pp. 553–597.
- Ekaykin, A. A., D. O. Vladimirova, V. Y. Lipenkov, and V. Masson–Delmotte (2017). “Climatic variability in Princess Elizabeth Land (East Antarctica) over the last 350 years”. In: *Climate of the Past* 13, pp. 61–71.
- Epstein, S., R. Buchsbaum, H. Lowenstam, and H.C. Urey (1951). “Carbonate-water isotopic temperature scale”. In: *Geological Society of America Bulletin* 62.4, p. 417.
- Faber, A.-K., B. M. Vinther, J. Sjolte, and R.A. Pedersen (2017). “How does sea ice influence $\delta^{18}\text{O}$ of Arctic precipitation?” In: *Atmospheric Chemistry and Physics* 17, pp. 5865–5876.
- Gkinis, V., S. B. Simonsen, S. L. Buchardt, J. W. C. White, and B. M. Vinther (2014). “Water isotope diffusion rates from the NorthGRIP ice core for the last 16,000 years - glaciological and paleoclimatic implications”. In: *Earth and Planetary Science Letters* 405.
- Herron, M. M. and C. C. Langway (1980). “Firn Densification: An Empirical Model”. In: *Journal of Glaciology* 25.93.
- Holme, C., V. Gkinis, M. Lanzky, V. Morris, M. Olesen, A. Thayer, B. H. Vaughn, and B. M. Vinther (2018b, in review). “Varying regional $\delta^{18}\text{O}$ -temperature relationship in high resolution stable water isotopes from East Greenland”. In: *review: Climate of the Past Discussions*. URL: <https://doi.org/10.5194/cp-2018-169>.
- Holme, C., V. Gkinis, and B. M. Vinther (2018a). “Molecular diffusion of stable water isotopes in polar firn as a proxy for past temperatures”. In: *Geochemica et Cosmochimica Acta* 225, pp. 128–145.
- Johnsen, S. J. (1977). “Stable Isotope Homogenization of Polar Firn and Ice”. In: *Isotopes and Impurities in Snow and Ice*, pp. 210–219.
- Johnsen, S. J., H. B. Clausen, K. M. Cuffey, G. Hoffmann, J. Schwander, and T. Creyts (2000). “Diffusion of stable isotopes in polar firn and ice: the isotope effect in firn diffusion”. In: *Physics of Ice Core Records*, pp. 121–140.

- Johnsen, S. J., H. B. Clausen, W. Dansgaard, N. S. Gundestrup, M. Hansson, P. Jonsson, J. P. Steffensen, and A. E. Sveinbjörnsdóttir (1992). “A “deep” ice core from East Greenland”. In: *Meddelelser om Groenland, Geoscience* 29, pp. 3–22.
- Johnsen, S. J., D. Dahl-Jensen, N. Gundestrup, J. P. Steffensen, H. B. Clausen, H. Miller, V. Masson-Delmotte, A. E. Sveinbjörnsdóttir, and J. W. C. White (2001). “Oxygen isotope and palaeotemperature records from six Greenland ice-core stations: Camp Century, Dye-3, GRIP, GISP2, Renland and NorthGRIP”. In: *Journal of Quaternary Science* 16.4.
- Johnsen, S. J., W. Dansgaard, and J. W. C. White (1989). “The origin of Arctic precipitation under present and glacial conditions”. In: *Tellus* 41B, pp. 452–468.
- Johnsen, S. J. et al. (1997). “The $\delta^{18}\text{O}$ record along the Greenland Ice Core Project deep ice core and the problem of possible Eemian climatic instability”. In: *Journal of Geophysical Research* 102, pp. 26397–26410.
- Jones, P. D., T. Jonsson, and D. Wheeler (1997). “Extension to the North Atlantic oscillation using early instrumental pressure observations from Gibraltar and south-west Iceland”. In: *International Journal of Climatology* 17 (13), pp. 1433–1450.
- Jones, P. D., T. J. Osborn, K. R. Briffa, C. K. Folland, E. B. Horton, L. V. Alexander, D. E. Parker, and N. A. Rayner (2001). “Adjusting for sampling density in grid box land and ocean surface temperature time series”. In: *Journal of Geophysical Research* 106.D4, pp. 3371–3380.
- Jouzel, J. and L. Merlivat (1984). “Deuterium and oxygen 18 in precipitation: modeling of the isotopic effects during snow formation”. In: *Journal of Geophysical Research-Atmospheres* 89.D7, pp. 11749–11759.
- Jouzel, J. et al. (1997). “Validity of the temperature reconstruction from water isotopes in ice cores”. In: *Journal Of Geophysical Research-Oceans* 102.C12, pp. 26471–26487.
- Klein, E. S. and J. M. Welker (2016). “Influence of sea ice on ocean water vapor isotopes and Greenland ice core records”. In: *Geophysical Research Letters* 43, 12, 475–b12, 483.
- Langen, P. L., R. S. Fausto, B. Vandecrux, R. H. Mottram, and J. E. Box (2017). “Liquid Water Flow and Retention on the Greenland Ice Sheet in the Regional Climate Model HIRHAM5: Local and Large-Scale Impacts”. In: *Front. Earth Sci.*
- Mook, J. (2000). *Environmental Isotopes in the Hydrological Cycle Principles and Applications*. International Atomic Energy Agency.
- Noone, D. and I. Simmonds (2004). “Sea ice control of water isotope transport to Antarctica and implications for ice core interpretation”. In: *Journal of Geophysical Research* 109 (D07105).

- Osborn, T., K. R. Briffa, and P. D. Jones (1997). “Adjusting Variance for sample-size in tree-ring chronologies and other regional mean time series”. In: *Dendrochronologies* 15.
- Schmith, T. and C. Hansen (2002). “Fram Strait Ice Export during the Nineteenth and Twentieth Centuries Reconstructed from a Multiyear Sea Ice Index from Southwestern Greenland”. In: *Journal of Climate* 16, pp. 2782–2791.
- Simonsen, M. F. et al. (2018, in review). “Ice core dust particle size reveals past glacier extent in East Greenland”. In: *In review in Nature Communication* .
- Steen-Larsen, H. C. et al. (2011). “Understanding the climatic signal in the water stable isotope records from the NEEM shallow firn/ice cores in northwest Greenland”. In: *Journal of Geophysical Research* 116 (D6).
- Steig, E. J. et al. (2013). “Recent climate and ice-sheet change in West Antarctica compared to the past 2000 years”. In: *Nature Geoscience* 6.
- Vinther, B. M. (2003a). “Seasonal $\delta^{18}\text{O}$ Signals in Greenland Ice Cores”. MA thesis. Denmark: University of Copenhagen.
- Vinther, B. M., K. K. Andersen, A. W. Hansen, T. Schmith, and P. D. Jones (2003c). “Improving the Gibraltar/Reykjavik NAO Index”. In: *Geoph. Res. Lett.* 30.23.
- Vinther, B. M., S. J. Johnsen, K. K. Andersen, H. B. Clausen, and A. W. Hansen (2003b). “NAO signal recorded in the stable isotopes of Greenland ice cores”. In: *Geoph. Res. Lett.* 30.7.
- Vinther, B. M., P. D. Jones, H. B. Briffa K. R. and Clausen, K. K. Andersen, D. Dahl-Jensen, S. J. Johnsen, and H. B. Clausen (2010). “Climatic signals in multiple highly resolved stable isotope records from Greenland”. In: *Quaternary Science Reviews* 29.3-4, pp. 522–538.
- Vinther, B. M. et al. (2006). “A synchronized dating of three Greenland ice cores throughout the Holocene”. In: *Journal Of Geophysical Research-Atmospheres* 111.D13102.
- Vinther, B. M. et al. (2009). “Holocene thinning of the Greenland ice sheet”. In: *Nature* 461.
- Winstrup, M., A. M. Svensson, S. O. Rasmussen, O. Winther, E. J. Steig, and A. E. Axelrod (2012). “An automated approach for annual layer counting in ice cores”. In: *Clim. of the Past* 8, pp. 1881–1895.
- Zheng, M., J. Sjolte, F. Alolphi, B. M. Vinther, H. C. Steen-Larsen, T. J. Popp, and R. Muscheler (2018). “Climate information preserved in seasonal water isotope at NEEM: relations with temperature, circulation and sea ice”. In: *Clim. of the Past* 14, pp. 1067–1078.

Part III

FUTURE WORK AND CONCLUSION

A DIFFUSION-BASED RECONSTRUCTION OF WAIS DIVIDE TEMPERATURE

This chapter serves as an outlook based on the results presented in Chapters 3 and 4. In Chapter 4, high resolution diffusion length profiles of the WAIS Divide core's $\delta^{18}\text{O}$, δD measurements were estimated with depth (and age). Such diffusion length profiles contain information that can be used to reconstruct past temperature or accumulation variability as outlined in Chapter 3. However, several unexpected irregularities were observed in the diffusion length profiles (Jones et al., 2017a and Chapter 4). The objective of this chapter is therefore to initiate a discussion of whether these spikes in diffusion represent temperature change or if they result from deficiencies in how we interpret firn diffusion.

The WAIS Divide Core (WDC) was drilled on the West Antarctic Ice Sheet (WAIS) in an elevation of 1776 m (Fig. 6.1) (Fudge et al., 2016). It is characterized by a present-day annual surface temperature of -30°C and high accumulation rates of $\sim 0.22\text{ m ice/yr}$ at present times (Buizert et al., 2015). Thus, the drill site has a high resemblance with the Greenlandic drill sites NEEM, GRIP and NGRIP. The past temperature signal from the WDC has previously been reconstructed from the δD data where the temperature signature was calibrated to optimize the fit to measured borehole temperatures, while simultaneously being optimized to fit to $\delta^{15}\text{N}$ data in a firn densification model (Cuffey et al., 2016). While the reconstructed magnitude of its long-term temperature variability (e.g. the glacial to interglacial temperature change) is constrained by how heat propagates through the ice sheet (and therefore likely accurate), the short-term temperature variability is reconstructed by assuming that the δD variability directly represents temperature. Although there exists a well-established relationship as outlined in Chapter 2, Chapter 5 shows a case where the $\delta^{18}\text{O}$ signal does not covary with the regional temperature. Similarly, the relationship between $\delta^{18}\text{O}$ and temperature has already been examined for WAIS in Steig et al., 2013 (with the WAIS2015A ice core's $\delta^{18}\text{O}$ variability). Here, the authors observed that instead of being a direct proxy for temperature, the ice core $\delta^{18}\text{O}$ signal rather covaried with atmospheric circulation in a manner similar to temperature.

As the WAIS diffusion length profile (Chapter 4) shows high frequency variability, it is relevant to compare the temperature reconstruction from Cuffey et al., 2016 with a diffusion-based temperature reconstruction which only depends on the post-depositional processes rather than the integrated hydrological activity the deposited snow experienced from the ocean surface to the cloud condensation. Thus, such a comparison enables us to examine if there exists deficiencies in our densification and/or diffusion models or if WAIS was dominated by high frequency temperature variability unresolved in the study by Cuffey et al., 2016.

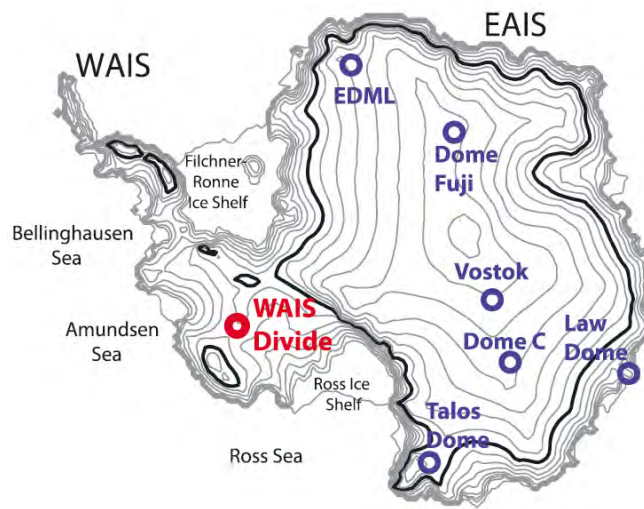


Figure 6.1. Location of the WDC drill site (red circle). Picture is adopted from Fudge et al., 2016.

6.1 ESTIMATING THE FIRN DIFFUSION

In the following, a diffusion-based temperature profile is reconstructed by utilizing the single isotope diffusion length σ_D . Although such a diffusion length profile was presented for the WDC in Chapter 4, this chapter re-estimates the diffusion as our previous study did not take into account the significant annual peak that dominates the power spectral density (PSD). As outlined in Section 3.4.1, such a spectral feature reduces the diffusion length estimate, which will result in artificially colder temperatures. Thus, here the diffusion length is estimated using the noise adding technique (Section 4.7.1) on the PSD where the annual peak has been discarded in the optimization scheme. As we know how the annual layer thickness changes with depth (Buizert et al., 2015; Sigl et al., 2016), we know approximately where to expect an annual peak in the PSD. However, as the location of the annual peak in the PSD of δD is not exactly at the calculated annual layer thickness, the following routine is implemented in order

to accurately locate it in the frequency domain and discard it in the non-linear least squares optimization:

1. Calculate the PSD of δD (\mathbb{P})
2. Fit \mathbb{P} using the noise-adding technique (P_{fit})
3. Detrend the signal: $detrended = \mathbb{P} - P_{fit}$
4. Find annual peak: $f_\lambda = \max(detrended)$
5. Generate weight function:

$$w(f) = \begin{cases} 0 & f \leq 0.5, f_\lambda - 0.8 \leq f \leq f_\lambda + 1.5 \\ 1 & 0.5 < f < f_\lambda - 0.8, f > f_\lambda + 1.5 \end{cases} \quad (63)$$

6. Repeat step 2 with new optimization norm: $|w(f) (P_{fit} - \mathbb{P})|^2$

The routine ensures that we are able to precisely locate and discard the annual peak together with multicentennial climate variability when estimating the diffusion length ($f \leq 0.5$). An example of the weight function is shown in Fig. 6.2 (grey bars for multicentennial variability and the annual peak). Similar to Chapter 4, diffusion lengths are estimated from a 500 year moving window with increments of 100 years.

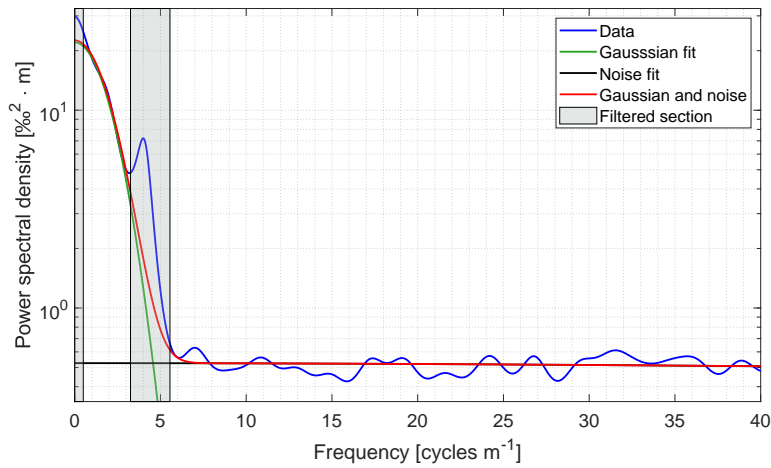


Figure 6.2. Power spectral density of the WDC δD data in the depth 239 – 255 m. The noise adding technique has been applied and the signal is fitted using the two-function fit described in Sec. 4.7.1. The grey bars represent the sections that have been filtered out. While the frequency domain extends up to 100 cycles/m, only the frequency interval $[0, 40 \text{ cycles/m}]$ is shown.

Following the procedure outlined in Sec. 3.4.1, past temperatures are reconstructed by estimating the surface temperature that resulted in a measured firm diffusion length. It is therefore

first necessary to convert the spectral estimated diffusion length ($\widehat{\sigma}_i$) into a diffusion length estimate at the bottom of the firn column (σ_{firn}^2) by correcting for measurement diffusion (σ_{cfa}), ice diffusion (σ_{ice}) and thinning ($\mathcal{S}(z)$):

$$\sigma_{\text{firn}}^2 = \frac{\widehat{\sigma}_i^2 - \sigma_{\text{cfa}}^2 - \sigma_{\text{ice}}^2}{\mathcal{S}(z)^2}. \quad (64)$$

The parameters needed for this correction have already been assessed and estimated in other studies. For instance, the measurement diffusion was estimated in Jones et al., 2017b who found 0.07 cm and 0.08 cm for $\delta^{18}\text{O}$ and δD , respectively. The thinning function was modeled in Buizert et al., 2015, and the ice diffusion length is calculated using the thinning profile and the borehole temperature profile of WDC. These profiles are plotted with respect to age or depth in Fig. 6.3 together with a reconstruction of the accumulation rate profile (Koutnik et al., 2016; Fudge et al., 2016).

Using the properties in Fig. 6.3, past firn diffusion lengths are reconstructed and plotted in Fig. 6.4. From this figure, it is evident that during the glacial to interglacial transition, the WDC have recorded very high firn diffusion lengths.

Moreover, there are a lot of fluctuations in the new diffusion length estimate and whether these results indicate climate variability in terms of temperature, surface pressure or densification processes will be examined in the following sections.

6.2 EVALUATING THE TEMPERATURE RECONSTRUCTION

As the firn diffusion length is a combined measure of temperature (which enhances diffusion) and accumulation (which mitigates diffusion), it is necessary to account for the accumulation rate before properly discussing the explanation behind the diffusive features. This has been done by coupling a Herron and Langway, 1980 model with the Johnsen et al., 2000 diffusion model (as described in Sections 3.3.1 and 3.4.1). Besides the accumulation rate reconstruction, the surface density and surface pressure are needed as input variables. The present-day surface pressure is 0.77 atm (Buizert and Severinghaus, 2016) while the surface density is somewhere between $\rho_o = 390 - 420 \text{ kg/m}^3$ for WAIS. Such surface density is high compared to other drill sites on both Greenland and Antarctica, where the density normally ranges between $330 - 360 \text{ kg/m}^3$. As the temperature reconstruction depends on past surface densities (of which we know nothing), the model is inverted using three different surface densities of 350, 400 and 450 kg/m^3 . Thus, this gives a first order conservative estimate of whether the enhanced

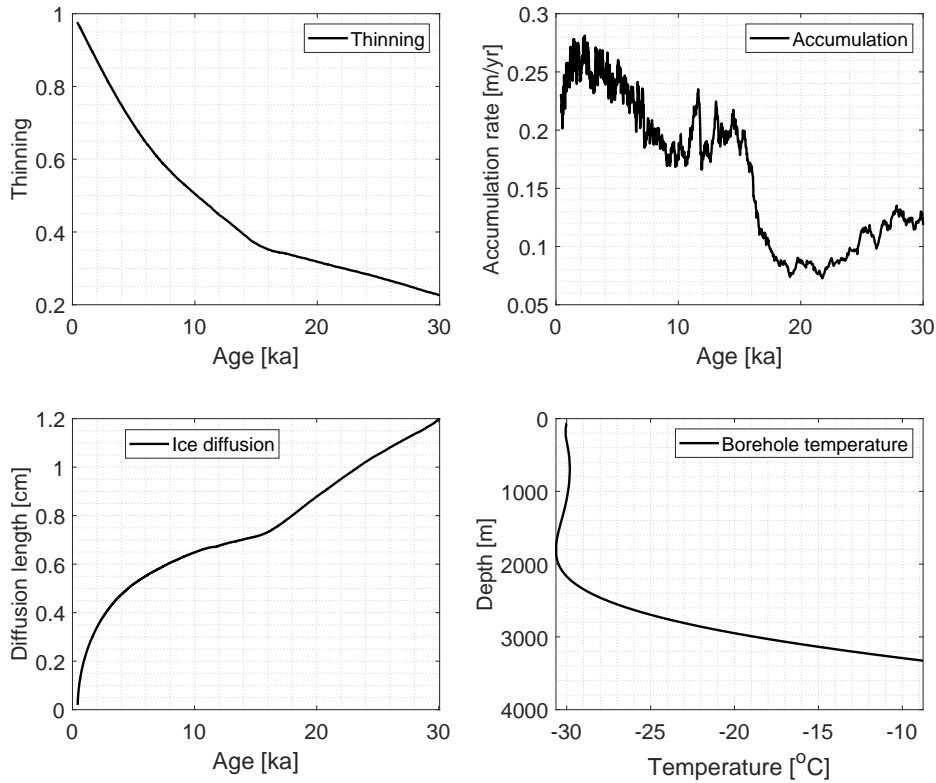


Figure 6.3. Thinning (upper left), accumulation rate (upper right), ice diffusion (lower left) and the borehole temperature profile (lower right). A 10 point moving average is applied on the accumulation rate profile (Koutnik et al., 2016; Buizert et al., 2015; Fudge et al., 2016).

diffusion results from changing surface densities in the past. The diffusion-based temperature reconstructions are plotted in Fig. 6.6.

Figure 6.6 shows that there is a large mismatch between the diffusion-based reconstructions and the reconstruction based on borehole temperatures from Cuffey et al., 2016. It is furthermore evident that the choice of ρ_o has a large impact on the absolute temperature estimate; an increasing ρ_o results in warmer temperatures. A similar result was presented for the WDC in Gkinis et al., 2018, submitted, where we found that the Herron and Langway densification model was very sensitive to changes in ρ_o and that it had a large impact on the diffusion length at WAIS. Thus, besides representing actual temperature variability, large variations in the surface density can potentially reduce some of the temperature oscillations. Nonetheless, the diffusion-based reconstruction with $\rho_o = 400 \text{ kg/m}^3$ agrees well with the reconstruction from Cuffey et al., 2016 during the Holocene (0 - 12 ka).

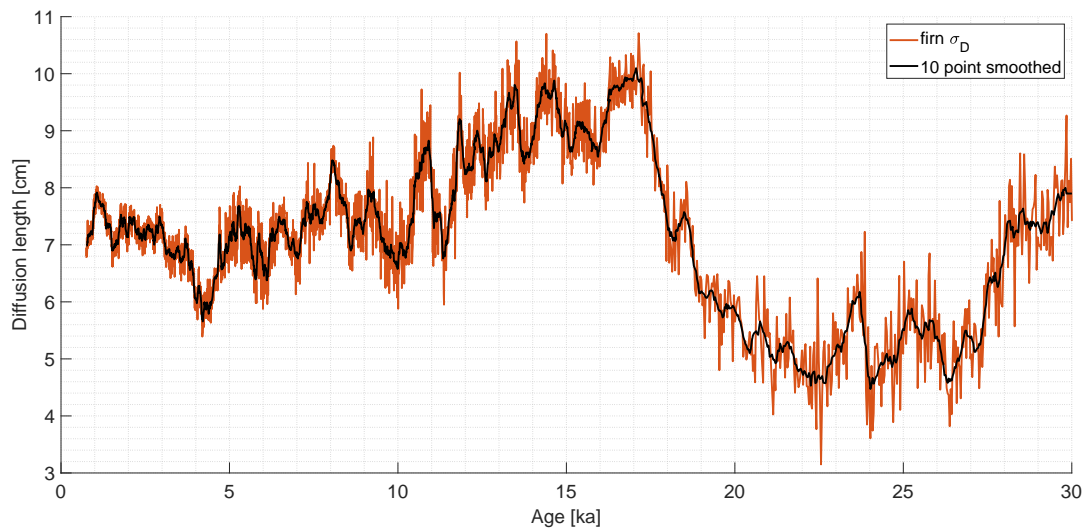


Figure 6.4. Estimated diffusion at bottom of firn column (cm of ice-equivalent) for δD (red) and a 10-point moving average applied (black).

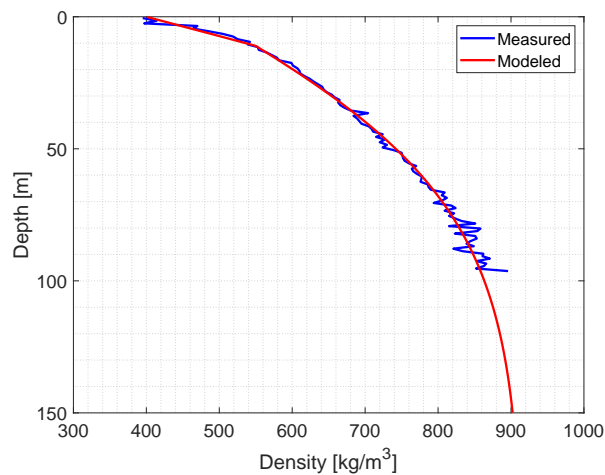


Figure 6.5. Measured density profile from WAIS (the WDC05A core by Todd Sowers) (blue). Red curve is a fitted Herron and Langway model. $f_0 = 0.903$, $f_1 = 0.899$, $\rho_0 = 0.400$, $T = -30^\circ\text{C}$ and $A = 0.22\text{mice/yr}$.

During the Holocene, there is a significant discrepancy between the reconstructions which shows a decrease in temperatures at 4.2 ka. This temperature drop is consistent with other studies that found similar climate variability and it has been referred to as the 4.2 ka event (Weiss et al., 1993). While the event has been hypothesized to be linked to the collapse of ancient civilizations (Cullen et al., 2000; deMenocal, 2001), the spatial pattern remains controversial (Marchant and Hooghiemstra, 2004; Magny et al., 2009). Moreover, to my knowledge, it is the first time that it has been observed in an Antarctic ice core. However, while the signal is clearly

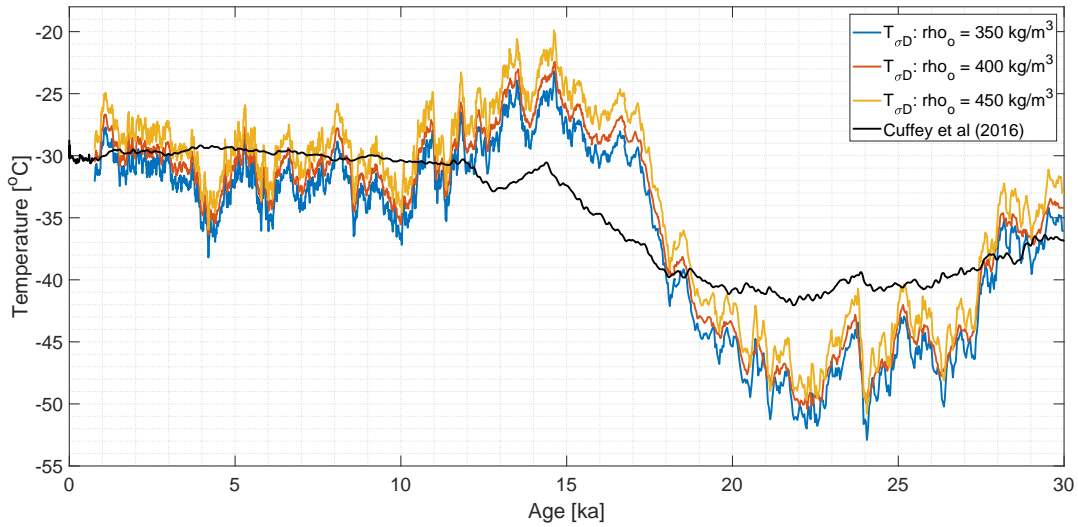


Figure 6.6. Temperature reconstructions using σ_D initiated with surface densities of 350 (blue), 400 (red) and 450 kg/m^3 (yellow) plotted together with the reconstruction based on borehole temperatures from Cuffey et al., 2016 (black).

recorded in the firn diffusion of δD , more analysis is needed to examine how significant this event is compared to the remaining variability.

In relation to the presented temperature reconstruction, there are still two features which uncertainties or variations in ρ_o do not seem to capture: (1) the large temperature/diffusion rise between 12-19 ka and (2) the colder glacial temperatures during the last glacial maximum. These features will be discussed in the Secs. 6.2.1 and 6.2.2.

6.2.1 The period 12-19 ka

The high diffusion length estimated during 12-19 ka has previously been investigated thoroughly by Jones et al., 2017a. They hypothesized that it could arise from (1) thermal gradients in the firn column, (2) changes in firn grain properties that alter vapor access to open pores, or (3) impurity-driven enhancement of solid ice diffusion. Through their analysis, they found that none of the hypotheses were able to explain the high diffusion lengths observed in the WDC. I have provided a small summary of how Jones et al., 2017a conducted their tests below.

6.2.1.1 Thermal gradients

The enhanced diffusion is observed during the glacial to interglacial transition which is a period governed by strong temperature change. Such temperature change generates thermal gradients in the firn. Thermal gradients in the firn have a nonlinear dependence on the saturation vapor

pressure and it increases the diffusion length additionally compared to an isothermal firn layer (as described in Section 3.3.1 and Appendix A.2). In Jones et al., 2017a, the authors tested the influence of thermal gradients by examining how temperature change with depth (dT/dz) (Buizert et al., 2015; Cuffey et al., 2016) altered the tortuosity (the twistedness of pathways through a porous medium). While the dT/dz is the temperature gradient integrated through the firn column (estimated from heat-coupled diffusion, δD and $\delta^{15}N$ measurements), they tested its impact with emphasis on the microstructure of the firn and its residence time. Hence, they did not implement its influence in the saturation vapor pressure or densification model as in Chapter 3. Thus, it was done through the parameter b from the Schwander et al., 1988 tortuosity parameterization (Eq. 104 in Appendix A.1):

$$b = b_0 + k \cdot \text{abs} \left(\frac{dT}{dz} \right). \quad (65)$$

Here k and b_0 are adjustable parameters used to match the destrained σ_{firn}^2 (Fig. 6.4) at 1 ka with the most anomalous part of the record at 17 ka. They found changes in the tortuosity parameter to partially covary with the observed diffusion lengths but the correlations and the large magnitude of implied microstructural change needed was concluded to be an unsatisfactory explanation.

6.2.1.2 *Changing firn grain properties*

Jones et al., 2017a examined if changes in firn grain properties could account for the enhanced diffusion. This was investigated as smaller grains result in more intergranular boundaries and veins per volume of ice which would increase the diffusion (as the solid ice diffusion is driven by isotopic gradients within the lattice of the ice crystals - Sec. 3.3.2). The hypothesis was tested by comparing solid ice diffusion calculations for respectively monocrystalline (Ramseier, 1967) and polycrystalline ice (Lu et al., 2009). Despite that polar ice normally has grain sizes on the order of 1mm (with variations in grain size being related to grain growth and climatic changes (De La Chapelle et al., 1998)), the polycrystalline ice in Lu et al., 2009 (hyperfine grains of ≤ 30 nm on average) was used as an upper bound of how changing firn grain properties could account for the observed enhanced diffusion. While the WDC diffusion lengths varied between the lower case of monocrystalline ice and upper case of polycrystalline ice, the results from Jones et al., 2017a showed that changing firn grain properties could not be the main driver behind the 12-19 ka diffusive features.

6.2.1.3 *Impurity-driven diffusion*

The effect of impurities in the ice on diffusion was investigated. This was partially motivated by previous studies where it was found that elevated impurity concentrations (e.g. Ca^{2+}) led to faster densification (Hörhold et al., 2012; Freitag et al., 2013) (which mitigates diffusion). However, the effect of impurity-driven densification did not apply for the case of WDC as Buizert et al., 2015 only obtained reliable reconstructions of past accumulation rates with less than one-quarter of the total Ca sensitivity from Hörhold et al., 2012; Freitag et al., 2013.

Instead, Jones et al., 2017a examined the effect of impurities on diffusion directly as Lu et al., 2009 found from experiments that impurities in polycrystalline solid ice can increase the diffusivity by an order of magnitude (despite natural polar ice not being polycrystalline). Hence, Jones et al., 2017a tested the influence of Ca^{2+} relative to non-sea salt sulfur as an impurity enhancement of solid ice diffusion. However, the authors found that a simple dependence of the total impurity content on the diffusion lengths cannot explain the diffusive features in the period 12-19 ka.

6.2.2 *The cold glacial*

The cold glacial period (20-25 ka) was not examined in Jones et al., 2017a as they did not attempt to do a diffusion-based temperature reconstruction. A hypothesis that could explain the cold temperatures is that the snow was deposited at a higher elevation. This can be achieved through either a thicker ice sheet or if the ice originated from a location upstream at a higher altitude. A higher elevation leads to colder temperatures due to the atmospheric lapse rate (the decrease of temperature with altitude). However, the diffusion-based reconstruction was on average around 6°C colder than the reconstruction based on the borehole temperature profile. If true, this implies that the ice sheet had a higher elevation of around 600-850 m (not taking into account the effect of a changed thinning function due to thicker ice sheet). Although Cuffey et al., 2016 acknowledges that changes in past elevation and ice thickness impose a relatively large uncertainty on their temperature reconstruction, they state that full ice sheet model simulations yield a last glacial maximum ice sheet thickness ranging from -200 to 300 m relative to present day. Thus, they conclude that the likelihood of past elevation changes having varied significantly is minimal. Moreover, while Koutnik et al., 2016 found that the ice in the WDC was deposited on the ice divide 10-15 km upstream, they concluded that the ice divide has remained stable within a few km for the past 9,700 years. They were unfortunately

not able to extend the study as the geophysical data were unsuitable to constrain the ice flow further back in time.

In order to investigate if past snow was deposited at a higher altitude, one should examine the combined influence of surface temperature and ice thinning on the diffusion length profile in Fig. 6.4. Besides colder temperatures resulting from a higher elevation, a thicker ice sheet would modify the thinning function which influences the destraining of the estimated diffusion length (Eq. 64). Thus, future research should examine if varying ice sheet thickness and/or elevation can explain the cold temperatures during the last glacial maximum.

6.2.3 Borehole temperature reconstruction

From Fig. 6.6, it is evident that the diffusion-based temperature reconstruction does not match the reconstruction based on the borehole temperature profile. However, as high frequency temperature variability gets diffused in the ice sheet, multiple surface temperature scenarios can ultimately result in a similar borehole temperature profile. Thus, the diffusion-based temperature reconstruction might still reflect a plausible climate history. It is possible to test this case by modeling how heat propagates through the ice sheet. If the modeled temperature profile with depth matches the observed borehole temperature profile, the input surface temperature history provides a possible climate scenario.

Temperatures (T) with depth (z) are modeled by simulating the heat propagation through the ice cap. Thus, the temperature history from Fig. 6.6 is used as the surface temperature back in time (the solution for $\rho_0 = 400\text{kg/m}^3$ is used). Heat propagation is then modeled through the non-steady state heat conduction equation:

$$\frac{\partial T}{\partial t} = \kappa \frac{\partial^2 T}{\partial z^2} - \left(w(z) - \left(\frac{\kappa}{\rho} + \frac{\partial \kappa}{\partial \rho} \right) \frac{\partial \rho}{\partial z} \right) \frac{\partial T}{\partial z}, \quad (66)$$

where the vertical velocity ($w(z)$) is computed using a one-dimensional Dansgaard and Johnsen, 1969 flow model (Eq. 6 outlined in Sec. 2.3.4). The ice sheet thickness is assumed constant with time ($dH/dt = 0$), and a compressible firn layer based on the Herron and Langway model is implemented in the top (Fig. 6.5). I use the same temperature-dependent thermal diffusivity parameterizations of firn and ice (κ) as described in Appendix A.2. Moreover, the ice flow parameters and basal temperature (T_b) are displayed in Table 6.1 where the kink height and the sliding coefficient f_b are similar to Cuffey et al., 2016. The basal melt rate ($-w_0$) in both Buizert et al., 2015 and Cuffey et al., 2016 was used as a fitting parameter (and not specified). Instead, I use a basal melt rate of 1.0 cm/yr as documented in WAIS Divide Project

Table 6.1. Ice flow and heat propagation properties used in the forward modeling of the borehole temperature profile.

H	h	$-w_0$	f_b	ρ_o	T_b
3404m	$0.2H$	1.0cm/yr	1.3	400kg/m ³	-6.65°C

Members/Fudge et al., 2013. It should be noted that I use a measured borehole temperature profile that only covers the depth 70 – 3329m (measured in 2011) as I have not acquired the profile from Cuffey et al., 2016 (measured in 2014) with the remaining depth down to 3404m. Thus, I assume a basal temperature of -6.65°C as my boundary condition based on Fig. 1 in Cuffey et al., 2016. Finally, Eq. 66 is solved using the Crank-Nicolson scheme which is a finite-difference method used to numerically solve the heat equation and similar partial differential equations (Durran, 2010).

The simulation of temperatures with depth is initiated in the glacial at 30 ka by solving the steady state heat equation ($\partial T / \partial t = 0$). For each time step, the non-steady state model computes a borehole temperature profile based on the corresponding temperature and accumulation rate from Figs. 6.6 and 6.3. The model then progresses forward in time in increments of 100years where the final iteration is the present day temperature profile.

I assess the validity of the used ice flow model and thermal conductivity parameters by solving Eq. 66 with the temperature reconstruction from Cuffey et al., 2016 (see Fig. 6.7). Despite that the ice flow-heat conduction model used in this study differs slightly from that of Cuffey et al., 2016 (this model is simpler), the modeled temperature profile using the borehole-based temperature reconstruction matches the observed borehole temperature profile relatively well in the top 1500 m. Below, it is evident that my model results in warmer temperatures. This might be attributed to the chosen melt rate of 1.0cm/yr which could be lower than that of Buizert et al., 2015; Cuffey et al., 2016. The residual between data and model would here decrease with an increasing basal melt rate. Nonetheless, it is evident that the presented ice flow-heat propagation model is adequate for this hypothesis testing.

With respect to the diffusion-based temperature reconstruction, the resulting temperature profile with depth is also shown in Fig. 6.7. However, the temperature profile is not similar to the observed borehole profile. In fact, the residual between the data and model vary between -1 to 2°C . Such large discrepancies imply that the diffusion-based temperature reconstruction is an inaccurate temperature history record given the input parameters. Future research should expand on this analysis by testing how sensitive the presented model is to changes in ice sheet thickness and surface density. Moreover, it would be interesting to see if it is possible to

improve the match with the measured temperature profile by increasing the model complexity and instead fit several of the current input parameters (e.g. $-w_0$ and f_b).

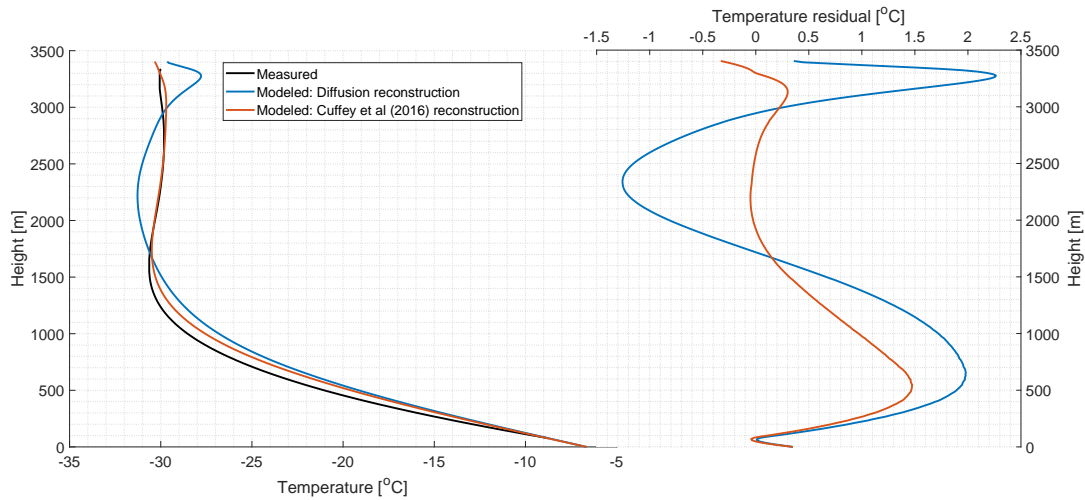


Figure 6.7. Left: Modeled borehole temperature profiles using the reconstructions based on diffusion (blue) and borehole temperatures (red) together with the measured borehole temperature profile (black). Right: The corresponding residuals between the modeled profiles and the measured temperature profile.

6.3 PRESSURE-INDEPENDENT TEMPERATURE RECONSTRUCTIONS

The diffusion-based temperature reconstruction is indirectly dependent on a priori knowledge about the elevation of which the deposited precipitation was exposed to firm diffusion. While the firm diffusion model by Johnsen et al., 2000 does not require a precise altitude, it depends on the diffusivity of water vapor (D_a) which is parameterized through the ambient pressure (P) and temperature (T) (Hall and Pruppacher, 1976) (Appendix A.1):

$$D_a = 2.1 \cdot 10^{-5} \left(\frac{T}{T_0} \right)^{1.94} \left(\frac{P_0}{P} \right). \quad (67)$$

Normally, P is estimated from either pressure measurements at the drill site or it can be calculated back in time from the barometric formula (if the altitude is known). However, our knowledge about past ice sheet elevation (and pressure) is limited which can lead to errors in the temperature reconstructions. This is especially relevant if the currently unstable WAIS (Mercher, 1978) collapsed preceding its current ice sheet size. While such collapses have been found to occur on a multi-millennial scale (Pollard and DeConto, 2009), a study by Steig et al., 2015 found that WAIS collapsed during the last warm interglacial. Thus, in case of high tem-

perature anomalies it is not unreasonable to assume it could affect the stability of WAIS and thereby the ice sheet thickness.

In future diffusion-based research, I propose to discard the assumptions about past elevation by removing the pressure dependency in Eq. 67. For instance, past pressure can be estimated from the total air content (TAC) that is encapsulated in ice bubbles (derived from the ideal gas law (Martinerie et al., 1992)):

$$\text{TAC} = V_{\text{close-off}} \frac{P \cdot T_0}{P_0 \cdot T}. \quad (68)$$

Here $V_{\text{close-off}}$ is the pore volume at the close-off depth which Martinerie et al., 1992 found to be a site-dependent parameter that could be expressed through temperature (another linear expression was presented in Delmotte et al., 1999):

$$V_{\text{close-off}} = (6.95 \cdot 10^{-4} T) - 0.043 \quad (69)$$

or density:

$$V_{\text{close-off}} = \frac{1}{\rho_{co}} - \frac{1}{\rho_i}, \quad (70)$$

where ρ_{co} is the mean density at which the air isolation occurs (bubble close-off density). The TAC measured in bubbles of polar ice has been speculated to be a proxy of past ice sheet elevation (Martinerie et al., 1992). However, it has been difficult to convert the measurements to actual elevation numbers due to the poorly constrained behavior of the porosity at close-off (Delmotte et al., 1999). Instead of quantifying exact elevation changes, I propose to use the TAC data directly in the firm diffusion model. Thus, by using the formulation of TAC in Eq. 68 and the parameterization in Eq. 69 together with the firm air diffusivity in Eq. 67, it is possible to remove the pressure dependence from the vapor diffusivity:

$$D_a = 2.1 \cdot 10^{-5} \left(\frac{T}{T_0} \right)^{0.94} \frac{(6.95 \cdot 10^{-4} T) - 0.043}{\text{TAC}}. \quad (71)$$

Thus, by implementing the TAC data in the Johnsen et al., 2000 model, the firm diffusion model becomes independent of uncertainties on past ice sheet elevation.

6.4 DISCUSSION AND OUTLOOK: WHAT SHOULD BE EXAMINED IN THE FUTURE

From Fig. 6.6, it is evident that part of the diffusion-based temperature reconstruction of the WDC potentially is inaccurate (12-30 ka). However, as the estimated diffusion length certainly

represents an actual climate signal as discussed in Jones et al., 2017a and Chapter 4, the potentially inaccurate reconstruction could be a consequence of large variations in surface and bubble close-off densities back in time (which are assumed to be constant with time), past changes in ice sheet elevation and/or missing complexity in the firn diffusion model.

The influence from past elevation change can be examined further by implementing TAC data in the firn diffusion model as described in Sec. 6.3. Besides removing the elevation dependency, it will also be possible to examine past changes in bubble close-off density when assuming the temperature reconstruction from Cuffey et al., 2016 is correct. A paper describing the TAC data of the WDC is currently in preparation (Edwards et al., 2018, unpublished). From personnel communication with Jon Edwards and Edwards et al., 2016, conference, the TAC data from WDC shows anomalously low pressures during the period 12-19 ka together with a lot of variability. A connection between TAC and temperature has previously been found for periods with large temperature gradients. For instance, Eicher et al., 2016 found that the NGRIP TAC data anticorrelated with rapid Dansgaard-Oeschger warmings. They hypothesized that this might be attributed to the changing firnification processes. Thus, when high resolution WDC TAC data become available in the future, the firn diffusion and densification processes should be investigated further.

It would also be relevant to further examine how sensitive the firn diffusion model is to temperature gradients and changing firn density properties. Such examination has already been initiated by Gkinis et al., 2018, submitted, where we build on the Community Firn Model (CFM) (Lundin et al., 2017; Stevens et al., 2018) which contains a compilation of often used densification models (e.g. Herron and Langway, 1980; Barnola et al., 1991; Goujon et al., 2003; Freitag et al., 2013). In Gkinis et al., 2018, submitted, a newly developed branch of CFM called the iso-CFM is presented which contains a module to calculate diffusion lengths of different water isotopologues for different densification parameterizations and climate scenarios. Thus, the iso-CFM will be a helpful tool in the advances toward a better understanding of firn properties and how they affect our interpretation of firn diffusion.

REFERENCES

- Barnola, J.-M., P. Pimienta, D. Raynaud, and Ye. S. Korotkevich (1991). "CO₂-climate relationship as deduced from the Vostok ice core: A re-examination based on new measurements and on a re-evaluation of the air dating". In: *Tellus B* 43.2, pp. 83–90.
- Buizert, C. and J. P. Severinghaus (2016). "Dispersion in deep polar firn driven by synoptic-scale surface pressure variability". In: *The Cryosphere* 10.5, pp. 2099–2111.

- Buizert, C. et al. (2015). “The WAIS Divide deep ice core WD2014 chronology – Part 1: Methane synchronization (68–31 ka BP) and the gas age–ice age difference”. In: *Climate of the Past* 11, pp. 153–173.
- Cuffey, K. M., G. D. Clow, E. J. Steig, C. Buizert, T. J. Fudge, M. Koutnik, E. D. Waddington, R. B. Alley, and J. P. Severingshaus (2016). “Deglacial temperature history of West Antarctica”. In: *PNAS* 113 (50), pp. 14249–14254.
- Cullen, H. M., P. B. deMenocal, S. Hemming, G. Hemming, F. H. Brown, T. Guilderson, and F. Sirocko (2000). “Climate change and the collapse of the Akkadian empire: Evidence from the deep sea”. In: *Geology* 28.4, pp. 379–382.
- Dansgaard, W. and S. J. Johnsen (1969). “A Flow Model and a Time Scale for the Ice Core from Camp Century, Greenland”. In: *Journal of Glaciology* 8.53, pp. 215–223.
- De La Chapelle, S., O. Castelnau, V. Lipenkov, and P. Duval (1998). “Dynamic recrystallization and texture development in ice as revealed by the study of deep ice cores in Antarctica and Greenland”. In: *Journal of Geophysical Research: Solid Earth* 103.B3, pp. 5091–5105.
- Delmotte, M., D. Raynaud, V. Morgan, and J. Jouzel (1999). “Climatic and glaciological information inferred from air-content measurements of a Law Dome (East Antarctica) ice core”. In: *Journal of Glaciology* 45.150, pp. 255–263.
- deMenocal, P. B. (2001). “Cultural Responses to Climate Change During the Late Holocene”. In: *Science* 292, pp. 667–673.
- Durrant, D. R. (2010). *Numerical Methods for Fluid Dynamics*. Springer, 2nd. Edition.
- Edwards, J. S., E. J. Brook, C. Buizert, J.E. Lee, L.E. Mitchell, J. E. B. Fegyveresi, T. Sowers, R.B. Alley, and J.P. Severinghaus (2016, conference). In: *Millennial scale climate and total air content in the NEEM, GISP2 and WAIS Divide ice cores*. Vol. 285. IPICS 2016.
- Edwards, J. S., J. E. B. Fegyveresi, T. Sowers, R. Alley, J. Severinghaus, C. Buizert, and L. Mitchell (2018, unpublished). “Determining climatic controls on total air content and elevation changes from the WAIS Divide Ice Core”. In: *Manuscript in preparation*.
- Eicher, O., M. Baumgartner, A. Schilt, J. Schmitt, J. Schwander, T. Stocker, and H. Fischer (2016). “Climatic and insolation control on the high-resolution total air content in the NGRIP ice core”. In: *Climate of the Past* 12.6, pp. 1979–1993.
- Freitag, J., S. Kipfstuhl, T. Laepple, and F. Wilhelms (2013). “Impurity-controlled densification: a new model for stratified polar firn”. In: *Journal of Glaciology* 59, pp. 1163–1169.
- Fudge, T. J., B. R. Markle, K. M. Cuffey, C. Buizert, K. C. Taylor, E. J. Steig, E. D. Waddington, H. Conway, and M. Koutnik (2016). “Variable relationship between accumulation and temperature in West Antarctica for the past 31,000 years”. In: *Geophysical Research Letters* 43, pp. 3795–3803.

- Gkinis, V., C. Holme, E. C. Kahle, M. Stevens, E. J. Steig, and B. M. Vinther (2018, submitted). “Numerical experiments on firn isotope diffusion using the Community Firn Model”. In: *Journal of Glaciology*. P. .
- Goujon, C., J.-M. Barnola, and C. Ritz (2003). “Modeling the densification of polar firn including heat diffusion: Application to close-off characteristics and gas isotopic fractionation for Antarctica and Greenland sites”. In: *Journal of Geophysical Research: Atmospheres* 108.D24.
- Hall, W. D. and H. R. Pruppacher (1976). “The Survival of Ice Particles Falling from Cirrus Clouds in Subsaturated Air”. In: *Journal of the Atmospheric Sciences* 33.10, pp. 1995–2006.
- Herron, M. M. and C. C. Langway (1980). “Firn Densification: An Empirical Model”. In: *Journal of Glaciology* 25.93.
- Hörhold, M. W., T. Laepple, J. Freitag, M. Bigler, H. Fischer, and S. Kipfstuhl (2012). “On the impact of impurities on the densification of polar firn”. In: *Earth and planetary science letters* 325, pp. 93–99.
- Johnsen, S. J., H. B. Clausen, K. M. Cuffey, G. Hoffmann, J. Schwander, and T. Creyts (2000). “Diffusion of stable isotopes in polar firn and ice: the isotope effect in firn diffusion”. In: *Physics of Ice Core Records*, pp. 121–140.
- Jones, T. R., K. M. Cuffey, J. W. C. White, E. J. Steig, C. Buizert, B. R. Markle, J. R. McConnell, and M. Sigl (2017a). “Water isotope diffusion in the WAIS Divide ice core during the Holocene and last glacial”. In: *Journal of Geophysical Research: Earth Surface* 122, pp. 290–309.
- Jones, T. R., J. W. C. White, E. J. Steig, B. H. Vaughn, V. Morris, V. Gkinis, B. R. Markle, and S. W. Schoenemann (2017b). “Improved methodologies for continuous-flow analysis of stable water isotopes in ice cores”. In: *Atmos. Meas. Tech* 10, pp. 617–632.
- Koutnik, M., T. J. Fudge, H. Conway, E. D. Waddington, T. A. Neumann, K. M. Cuffey, C. Buizert, and K. C. Taylor (2016). “Holocene accumulation and ice flow near the West Antarctic Ice Sheet Divide ice core site”. In: *Journal of Geophysical Research: Earth Surface* 121, pp. 907–924.
- Lu, H., S. A. McCartney, and V. Sadtschenko (2009). “H/D exchange kinetics in pure and HCl doped polycrystalline ice at temperatures near its melting point: Structure, chemical transport, and phase transitions at grain boundaries”. In: *The Journal of chemical physics* 130.5, p. 054501.
- Lundin, J. M. D., C. M. Stevens, R. Arthern, C. Buizert, A. Orsi, S. R. M. Ligtenberg, S. B. Simonsen, E. Cummings, R. Essery, W. Leahy, et al. (2017). “Firn Model Intercomparison Experiment (FirnMICE)”. In: *Journal of Glaciology* 63.239, pp. 401–422.

- Magny, M., B. Vannière, G. Zanchetta, E. Fouache, G. Touchais, L. Petrika, C. Coussot, A. Walter-Simonnet, and F. Arnaud (2009). “Possible complexity of the climatic event around 4300—3800 cal. BP in the central and western Mediterranean”. In: *The Holocene* 19.6, pp. 823–833.
- Marchant, R. and H. Hooghiemstra (2004). “Rapid environmental change in African and South American tropics around 4000 years before present: a review”. In: *Earth-Science Reviews* 66.3-4, pp. 217–260.
- Martinerie, P., D. Raynaud, D. M. Etheridge, J.-M. Barnola, and D. Mazaudier (1992). “Physical and climatic parameters which influence the air content in polar ice”. In: *Earth and Planetary Science Letters* 112.1-4, pp. 1–13.
- Mercher, J. H. (1978). “West Antarctica ice sheet and CO₂ greenhouse effect: a threat of disaster”. In: *Nature* 271, pp. 321–325.
- Pollard, D. and R. M. DeConto (2009). “Modelling West Antarctic ice sheet growth and collapse through the past five million years”. In: *Nature* 458.7236, p. 329.
- Ramseier, R. O. (1967). “Self-Diffusion Of Tritium In Natural And Synthetic Ice Monocrystals”. In: *Journal Of Applied Physics* 38.6, pp. 2553–2556.
- Schwander, J., B. Stauffer, and A. Sigg (1988). “Air mixing in firn and the age of the air at pore close-off”. In: *Annals of Glaciology*, pp. 141–145.
- Sigl, M., T. J. Fudge, M. Winstrup, J. Cole-Dai, D. Ferris, J. McConnell, K. Taylor, K. Welten, T. Woodruff, F. Adolphi, et al. (2016). “The WAIS Divide deep ice core WD2014 chronology- Part 2: Annual-layer counting (0-31 ka BP)”. In: *Climate of the Past* 12, pp. 769–786.
- Steig, E. J., K. Huybers, H. A. Singh, N. J. Steiger, Q. Ding, D. M.W. Frierson, T. Popp, and J. W.C. White (2015). “Influence of West Antarctic Ice Sheet collapse on Antarctic surface climate”. In: *Geophysical Research Letters* 42.12, pp. 4862–4868.
- Steig, E. J. et al. (2013). “Recent climate and ice-sheet change in West Antarctica compared to the past 2000 years”. In: *Nature Geoscience* 6.
- Stevens, C. M., E. Waddington, H. Conway, and M. Koutnik (2018). *Investigations of physical processes in polar firn through modeling and field measurements*.
- WAIS Divide Project Members/Fudge, T. J., E. J. Steig, B. R. Markle, S. W. Schoenemann, Q. Ding, J. R. Taylor K. C. and McConnell, E. J. Brook, T. Sowers, and J. W. C. and others White (2013). “Onset of deglacial warming in West Antarctica driven by local orbital forcing”. In: *Nature* 500.7463, p. 440.
- Weiss, H., M.-A. Courty, W. Wetterstrom, F. Guichard, L. Senior, R. Meadow, and A. Curnow (1993). “The genesis and collapse of third millennium north Mesopotamian civilization”. In: *Science* 261.5124, pp. 995–1004.

CONCLUSION

This PhD project examined ice core stable water isotope data in a pursuit of improving the understanding of $\delta^{18}\text{O}$ and δD variability as a proxy of past temperatures. This work led to two published papers and one submitted manuscript which amounted to the final dissertation presented here.

The first study evaluated the accuracy and precision of diffusion-based techniques that can be utilized to infer past temperatures. These methods depend on the magnitude of firn diffusive smoothing on $\delta^{18}\text{O}$ and δD rather than the integrated hydrological activity that the deposited snow experienced prior to snowfall. Besides showing that the most precise methods only rely on the diffusion of a single isotopologue in preference to the differential diffusion signal of $\delta^{18}\text{O}$ and δD , the study also addressed that well-characterized power spectra are imperative for accurate estimates of the diffusion length.

The second study showed that the currently established approaches for diffusion estimation did not work equally well for newer, continuously measured data sets with lower instrument noise levels. Simulations with synthetic data showed that a newly discovered red power spectral signature could be explained by noise and system smoothing occurring through the continuous flow analysis system. Two methods were proposed to handle the extra complexity in the power spectral diffusion estimation and the techniques performed both efficiently and accurately.

The third study examined the $\delta^{18}\text{O}$ measurements of three ice cores drilled on Renland, East Greenland. The results showed that the measurements could be merged into robust seasonally averaged stacks and that the $\delta^{18}\text{O}$ stacks correlated with regional temperatures for the past 100 years. However, the relation between Renland $\delta^{18}\text{O}$ and Iceland temperature did not correlate further back in time (AD 1830-1909). While the varying $\delta^{18}\text{O}$ -temperature relation coincided with changes in the volume flux of sea ice exported south along the East Greenland coast, a causality was not proven and it should be investigated further by using isotope-enabled modeling on a high spatial resolution. As the study showed a case where the linear $\delta^{18}\text{O}$ -temperature

relation changes through time, it underlines the challenges with performing regression-based temperature reconstructions.

Chapter 6 presented a case where a diffusion-based temperature reconstruction might not be as straightforward as outlined in Chapter 3. Spectral estimates of diffusion lengths in the WAIS Divide ice core yielded stronger diffusion than predicted between 12-19 ka. To this day, it remains unknown whether the elevated diffusion reflects actual temperature variability or if it represents unrecognized changes in ice flow, densification and/or diffusion properties. Still, it is certain that the observed diffusion signal represents the post-depositional processes that have dampen the isotopic signal. Thus, the diffusion of WAIS Divide stable water isotopes provides a difficult but interesting starting point for the challenges ahead of the water isotope diffusion community.

Part IV

APPENDICES



MOLECULAR DIFFUSION OF STABLE WATER ISOTOPES IN POLAR FIRN AS A PROXY FOR PAST TEMPERATURES

This appendix was published as a supplement to Holme et al., 2018a and it has been included in its full length even though Appendix A.1 overlaps with Appendix B.1.

A.1 FIRN DIFFUSIVITY

We express the diffusivity as a function of firn density ρ and we use (Johnsen et al., 2000):

$$D(\rho) = \frac{m p D_{ai}}{RT \alpha_i \tau} \left(\frac{1}{\rho} - \frac{1}{\rho_{ice}} \right). \quad (72)$$

The terms used in Eq. (72) and the parametrization used for them are described below:

- m : molar weight (kg)
- p : saturation vapor pressure over ice (Pa). We use (Murphy and Koop, 2006):

$$p = \exp \left(9.5504 - \frac{5723.265}{T} + 3.530 \ln(T) - 0.0073 T \right) \quad (73)$$

- D_{ai} : diffusivity of water vapor (for isotopologue i) in air (m^2s^{-1}). For the diffusivity of the abundant isotopologue water vapor D_a we use (Hall and Pruppacher, 1976):

$$D_a = 2.1 \cdot 10^{-5} \left(\frac{T}{T_o} \right)^{1.94} \left(\frac{P_o}{P} \right) \quad (74)$$

with $P_o = 1 \text{ Atm}$, $T_o = 273.15 \text{ K}$ and P, T the ambient pressure (Atm) and temperature (K). Additionally from Merlivat and Jouzel, 1979 $D_{a^2\text{H}} = 0.9755 D_a$ and $D_{a^{18}\text{O}} = 0.9723 D_a$ and from Barkan and Luz, 2007 $D_{a^{17}\text{O}} = 0.98555 D_a$.

- R : molar gas constant $R = 8.3144 \text{ (m}^3\text{PaK}^{-1}\text{mol}^{-1}\text{)}$

- T: Ambient temperature (K)
- α_i : Ice – Vapor fractionation factor. we use the formulations by Majoube, 1970, Merlivat and Nief, 1967 and Barkan and Luz, 2005 for $\alpha_{s/v}^2$, $\alpha_{s/v}^{18}$ and $\alpha_{s/v}^{17}$ respectively.

$$\alpha_{\text{Ice/Vapor}}(^2\text{H}/^1\text{H}) = 0.9098 \exp(16288/T^2) \quad (75)$$

$$\alpha_{\text{Ice/Vapor}}(^{18}\text{O}/^{16}\text{O}) = 0.9722 \exp(11.839/T) \quad (76)$$

$$\alpha_{\text{Ice/Vapor}}(^{17}\text{O}/^{16}\text{O}) = \exp(0.529 \ln[\alpha_{\text{Ice/Vapor}}(^{18}\text{O}/^{16}\text{O})]) \quad (77)$$

- τ : The firn tortuosity. We use Schwander et al., (1988) as in Johnsen et al., 2000. More recent results include Freitag et al., (2002) and Adolph and Albert, (2014).

$$\frac{1}{\tau} = 1 - b \cdot \left(\frac{\rho}{\rho_{\text{ice}}}\right)^2 \quad \rho \leq \frac{\rho_{\text{ice}}}{\sqrt{b}}, \quad b = 1.3 \quad (78)$$

Based on Eq. (104), $\tau \rightarrow \infty$ for $\rho > 804.3 \text{ kg m}^{-3}$

A.2 THE FIRN TEMPERATURE PROFILE

Temperature variations in the firn column affect the amount of firn diffusion. The temperature profile T is modeled by solving the general heat transfer equation:

$$\frac{\partial T}{\partial t} = \kappa \frac{\partial^2 T}{\partial z^2} - \left(w - \left(\frac{\kappa}{\rho} + \frac{\partial \kappa}{\partial \rho} \right) \frac{\partial \rho}{\partial z} \right) \frac{\partial T}{\partial z}, \quad (79)$$

where ρ is the density, w is the vertical velocity and κ is the thermal diffusivity of firn. Here the internal heat production and the heat transport in the horizontal plane have been neglected. The thermal diffusivity of firn depends on density and the thermal diffusivity of ice (κ_{ice}) (Schwander et al., 1997):

$$\kappa = \kappa_{\text{ice}} \left(\frac{\rho}{\rho_i} \right)^{1-0.5(\rho/\rho_i)}, \quad (80)$$

where ρ_i is the density of ice. The thermal diffusivity of ice is defined as (Cuffey and Paterson, 2010):

$$\kappa_{\text{ice}} = \frac{k}{\rho_i c_p} = \frac{9.828 \cdot \exp(-5.7 \cdot 10^{-3} T) \cdot 3.16 \cdot 10^7}{\rho_i (152.5 + 7.122 T)}, \quad (81)$$

where c_p is the specific heat capacity and k is the thermal conductivity of ice. This allows for the computation of changes in thermal diffusivity with density:

$$\frac{\partial \kappa}{\partial \rho} = \kappa \left(\frac{1}{\rho} - \frac{1}{2\rho_i} \right) \left(1 + \ln \left(\frac{\rho}{\rho_i} \right) \right). \quad (82)$$

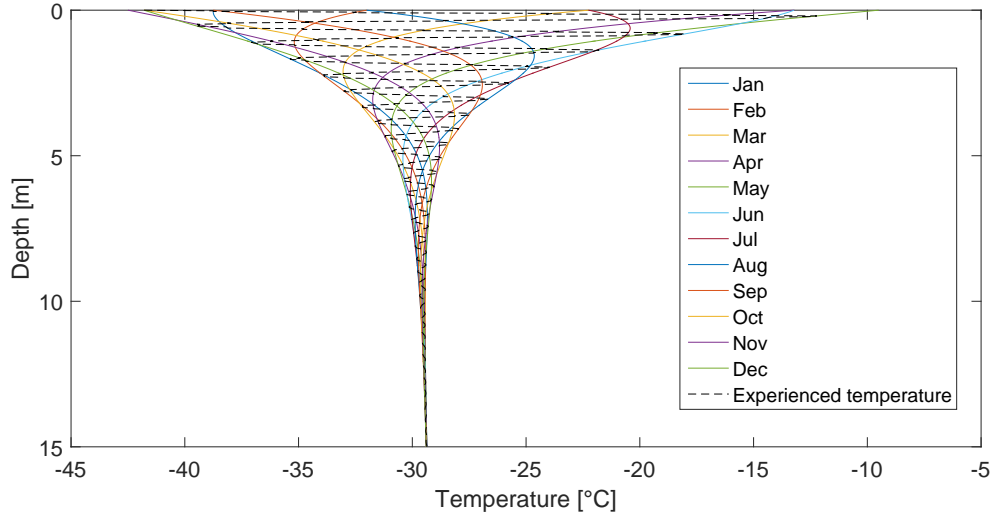


Figure A.1. Each solid colored line represent the temperature in one month of a year. The temperature a snow layer experiences as it moves down through the snow is represented by the black dashed line. The temperature is constant around 10-12 m. $T_{\text{mean}} = -29^{\circ}\text{C}$, $A = 0.22 \text{ myr}^{-1}$ ice.eq.

The surface temperature is parameterized as fluctuations around the mean annual temperature (T_{mean}) as in Simonsen et al., 2011:

$$T_{\text{surf}}(t) = T_{\text{mean}} + A \cos(bt) + B \cos(2bt), \quad (83)$$

where $A = 16.5$, $B = 3.0$ and $b = 0.5236$ are constants controlling the temperature amplitude and narrowness of the summer peak.

Figure A.1 shows the temperature variation a snow package experiences as it moves downwards. The seasonal temperature variation penetrates down to a depth of 10 – 12 m. The heat equation is solved numerically by using a Crank-Nicolson scheme (Durrant, 2010).

A.3 ICE DIFFUSIVITY

The solid ice diffusivity parametrization we use in this study is based on Ramseier, 1967 as it is consistent with previous studies. In this section we provide the reader with parametrizations from other studies. We assume an Arrhenius type relationship for the ice diffusivity of the form:

$$D_{\text{ice}} = D_o \exp\left(-\frac{X}{T}\right) [\text{m}^2\text{s}^{-1}]. \quad (84)$$

Table A.1. Four experimental studies with their estimated activation energies (Q), the pre-exponential factors (D_0), the activation energies (X), and the corresponding ice diffusivities for the temperature of $T = 245$ K (D_{245}).

	D_0 [m^2s^{-1}]	Q [kcalmol^{-1}]	X [K^{-1}]	D_{245} [m^2s^{-1}]
Ramseier, 1967	$9.2 \cdot 10^{-4}$	14.28	7186.5	$1.68 \cdot 10^{-16}$
Itagaki, 1964	0.014	14.97	7534.2	$6.18 \cdot 10^{-16}$
Blicks et al., 1966	$2.5 \cdot 10^{-3}$	14.51	7302.4	$2.85 \cdot 10^{-16}$
Delibaltas et al., 1966	$2.6 \cdot 10^{-3}$	15.66	7881.9	$2.83 \cdot 10^{-16}$

In Eq. 84, D_0 is the pre-exponential factor in m^2s^{-1} and X is the Arrhenius coefficient where $X = Q/R$ with Q being the activation energy in kcalmol^{-1} and R the universal gas constant ($8.314 \text{ JK}^{-1}\text{mol}^{-1}$).

Results from four experimental studies are summarized in Table A.1. Together with the pre-exponential factors and the activation energies, we also evaluate the four different expressions of ice diffusivities for the temperature of $T = 245\text{K}$.

When D_{ice} is known, a σ_{ice} calculation can be obtained by solving the differential equation describing the evolution of σ^2 with time (Johnsen, 1977):

$$\frac{d\sigma_{\text{ice}}^2}{dt} - 2\dot{\varepsilon}_z(t)\sigma_{\text{ice}}^2 = 2D_{\text{ice}}(t) \quad . \quad (85)$$

Using the integrating factor $F = \exp(\int -2\dot{\varepsilon}_z(t) dt)$ we get:

$$\frac{d}{dt} \left(\sigma_{\text{ice}}^2 e^{\int -2\dot{\varepsilon}_z(t) dt} \right) = 2D_{\text{ice}}(t) e^{\int -2\dot{\varepsilon}_z(t) dt} \quad (86)$$

This finally yields the ice diffusion length for a layer with age t' that has undergone ice flow thinning $S(t')$:

$$\sigma_{\text{ice}}^2(t') = S(t')^2 \int_0^{t'} 2D_{\text{ice}}(t) S(t)^{-2} dt \quad (87)$$

A.4 GENERATING SYNTHETIC DATA

The time series are generated using an AR-1 process with coefficient r_1 and variance ε

$$\delta_n - r_1 \delta_{n-1} = \varepsilon_n. \quad (88)$$

For the AR-1 process we use $r_1 = 0.3$ and $\varepsilon = 120\text{‰}^2$ for case A and 200‰^2 for case B. Each data section is 20m long and has an initial spacing of 10^{-3} m. The δD and $\delta^{17}\text{O}$ series are then generated assuming a d_{xs} signal of 10‰ and an $^{17}\text{O}_{\text{excess}}$ signal of 0 per meg:

$$\delta D = 8 \cdot \delta^{18}\text{O} + 10\text{‰} \quad (89)$$

$$^{17}\text{O}_{\text{excess}} = \ln(\delta^{17}\text{O} + 1) - 0.528 \ln(\delta^{18}\text{O} + 1) \quad (90)$$

The time series are then forward-diffused by means of numerical convolution with a Gaussian filter of variance σ_{input}^2 equal to the diffusion length for every case (Table 3.2 in Chapter 3). This input diffusion length is calculated as:

$$\sigma_{\text{input}}^2 = \sigma^2 \cdot \mathcal{S}^2 + \sigma_{\text{ice}}^2, \quad (91)$$

where σ^2 is the firn diffusion. For both case A and B, the ice diffusion is $\sigma_{\text{ice}} = 10^{-3}$ m with a thinning of $\mathcal{S} = 0.80$. Sampling with a discrete scheme of $\Delta = 0.025$ m and addition of white measurement noise completes the process of the time series generation. We use a noise level of 0.05‰ , 0.07‰ and 0.5‰ for $\delta^{17}\text{O}$, $\delta^{18}\text{O}$ and δD respectively, with the numbers being representative of measurement noise we have been observing over years of ice core measurements in our laboratory.

For a case B scenario, the sampled outputs of the synthetic data before and after diffusion is shown in Fig. A.2. Applying the forward-diffusion smoothens the large amplitudes of the high frequencies. This effect is further illustrated in Fig. A.3 which shows the PSD of the signal before and after diffusion.

A.5 DISCRETE SAMPLING DIFFUSION

The sample diffusion length σ_{dis} is estimated by setting the transfer function of a Gaussian filter equal to a rectangular filter with width of the sample size Δ . The transfer function for the Gaussian filter in Eq. 12 (in Chapter 3) is found by its Fourier transform:

$$\mathfrak{F}[\mathcal{G}] = \hat{\mathcal{G}} = e^{-\frac{k^2 \sigma_{\text{dis}}^2}{2}}. \quad (92)$$

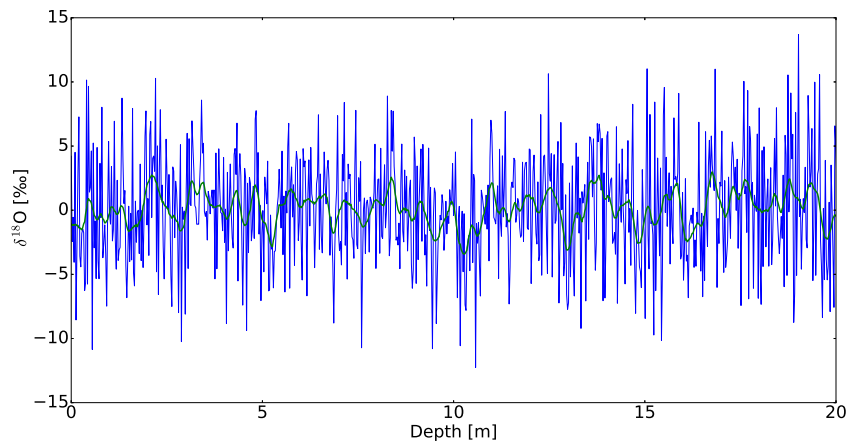


Figure A.2. Synthetic generated $\delta^{18}\text{O}$ series (case B) which both have been sampled. Blue curve represents the data before diffusion, and the green curve represents the data after diffusion. $\sigma = 8.4$ cm.

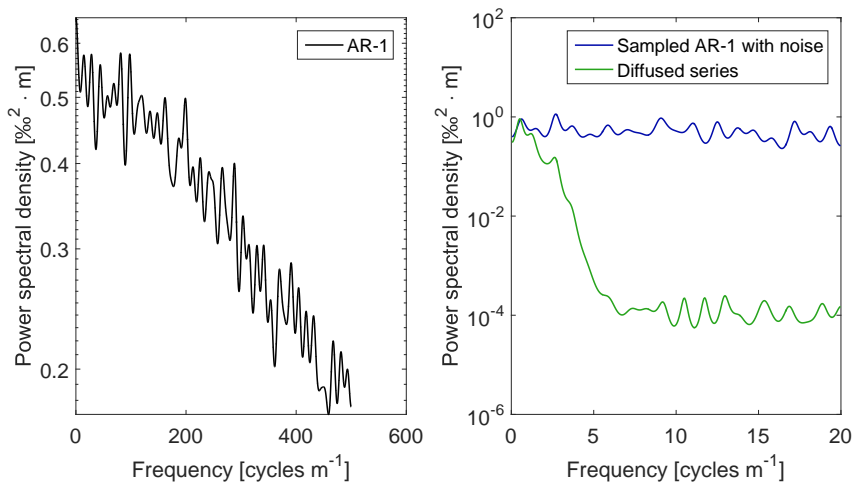


Figure A.3. Left: PSD of the raw AR-1 time series (case B $\delta^{18}\text{O}$ series). Right: PSD of the $\delta^{18}\text{O}$ series (from Fig. A.2). Blue curve represents the PSD of the sampled time series before diffusion, and the green curve represents the PSD of the sampled time series after diffusion. The y-scales are different in the two figures.

A regular rectangle function is defined as:

$$\text{rect}(t) = \begin{cases} 1 & \text{for } -\frac{1}{2} < t < \frac{1}{2} \\ \frac{1}{2} & \text{for } t = \pm\frac{1}{2} \\ 0 & \text{for } t > \frac{1}{2} \end{cases} \quad (93)$$

This can be transformed into a rectangular function ($\Pi(t)$) with width Δ and amplitude A :

$$\Pi(t) = A \cdot \text{rect}(t \cdot \Delta), \quad \text{for } -\frac{\Delta}{2} < t < \frac{\Delta}{2}. \quad (94)$$

Normalization yields an amplitude of $A = 1/\Delta$. The Fourier transformation of the rectangular pulse is written as:

$$\hat{\Pi}(f) = \int_{-\infty}^{\infty} \Pi(t) e^{-2\pi i f t} dt = \int_{-\Delta/2}^{\Delta/2} \frac{1}{\Delta} e^{-2\pi i f_{\text{Nq}} t} dt, \quad (95)$$

where $f_{\text{Nq}} = 1/(2\Delta)$ is the Nyquist frequency. Setting equations 92 and 95 equal to each other:

$$e^{-\frac{k^2 \sigma_{\text{dis}}^2}{2}} = \int_{-\Delta/2}^{\Delta/2} \frac{1}{\Delta} e^{-2\pi i f_{\text{Nq}} t} dt, \quad (96)$$

where $k = 2\pi f_{\text{Nq}}$. This results in the following solution for the discrete sampling diffusion length:

$$\sigma_{\text{dis}}^2 = \frac{2\Delta^2}{\pi^2} \ln\left(\frac{\pi}{2}\right). \quad (97)$$

A.6 FIGURES

Here we provide figures that show the performance of each diffusion technique. For each data section we have the estimated uncorrected diffusion lengths in a table.

A.6.1 *NEEM - late Holocene*

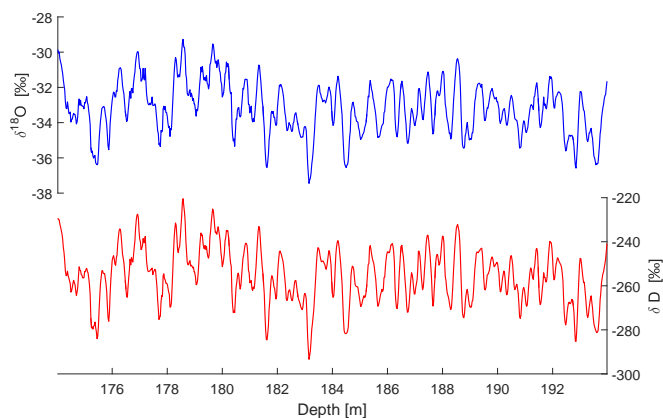


Figure A.4. NEEM. Late Holocene $\delta^{18}\text{O}$ (top) and δD (below) profiles with depth.

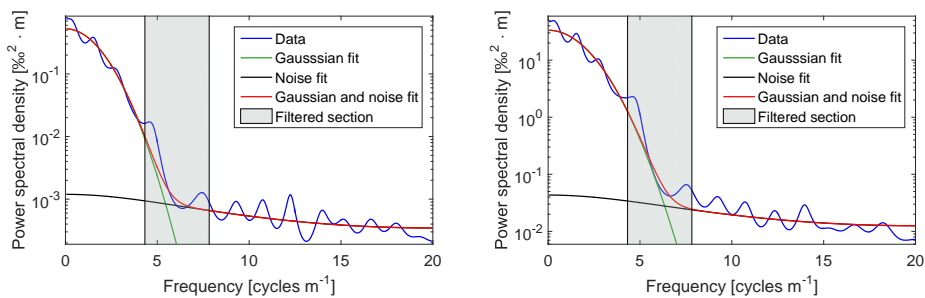


Figure A.5. NEEM. Late Holocene power spectra of $\delta^{18}\text{O}$ (left) and δD (right).

Table A.2. Estimated diffusion values for the NEEM late Holocene data. The values have not been corrected for sampling diffusion, ice diffusion and thinning.

σ_{18} [cm]	σ_D [cm]	$\Delta\sigma^2$ I [cm ²]	$\Delta\sigma^2$ [cm ²] II	$\Delta\sigma^2$ III [cm ²]
7.41	6.68	10.3	9.0	4.7

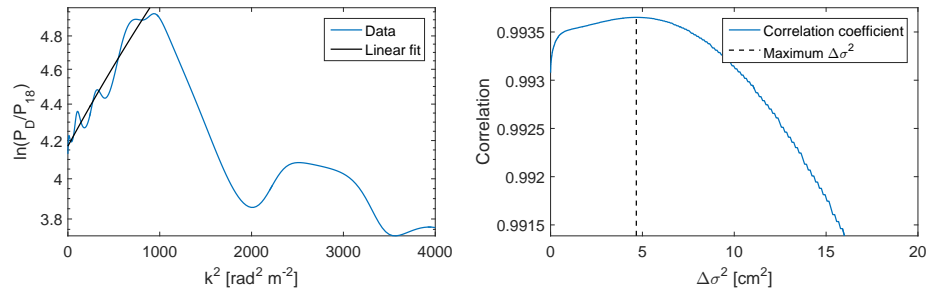


Figure A.6. Differential diffusion techniques applied on NEEM late Holocene data. Left: linear fit of the logarithmic PSD ratio ($^{18}\Delta\sigma^2$ II). Right: Correlation between $\delta^{18}\text{O}$ and artificially diffused δD ($^{18}\Delta\sigma^2$ III).

A.6.2 NEEM - CFA data section

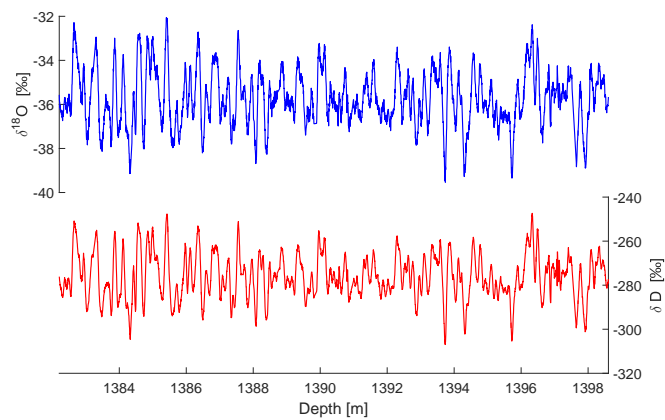


Figure A.7. NEEM - CFA data. Early Holocene $\delta^{18}\text{O}$ (top) and δD (below) profiles with depth.

Table A.3. Estimated values for NEEM early Holocene CFA data. The values have not been corrected for sampling diffusion, ice diffusion and thinning.

σ_{18} [cm]	σ_D [cm]	$\Delta\sigma^2$ I [cm ²]	$\Delta\sigma^2$ [cm ²] II	$\Delta\sigma^2$ III [cm ²]
3.12	2.78	2.0	1.1	1.0

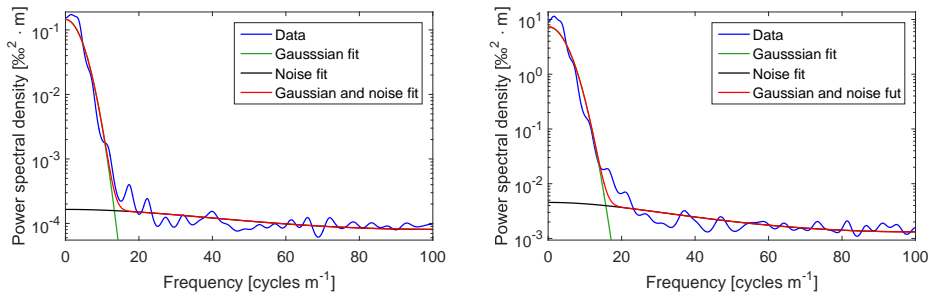


Figure A.8. NEEM - CFA data. Early Holocene power spectra of $\delta^{18}\text{O}$ (left) and δD (right)

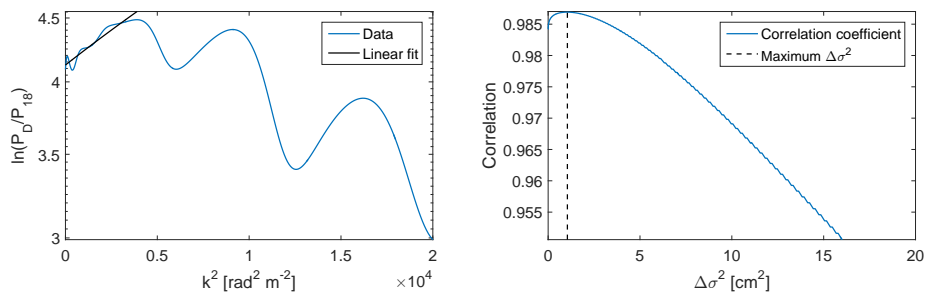


Figure A.9. Differential diffusion techniques applied on NEEM early Holocene CFA data. Left: linear fit of the logarithmic PSD ratio ($^{18}\Delta\sigma^2$ II). Right: Correlation between $\delta^{18}\text{O}$ and artificially diffused δD ($^{18}\Delta\sigma^2$ III).

A.6.3 NEEM - discrete data section

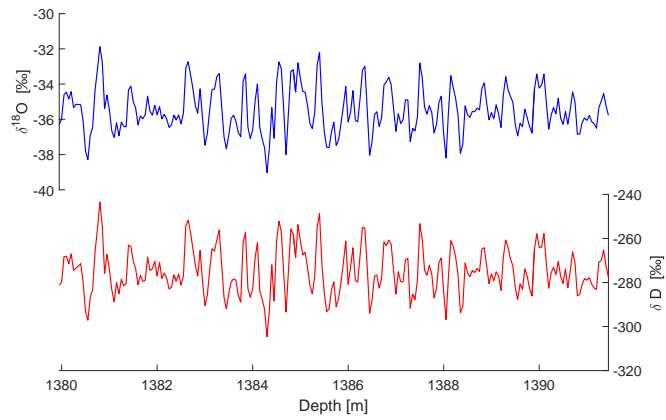


Figure A.10. NEEM - discrete data. Early Holocene $\delta^{18}\text{O}$ (top) and δD (below) profiles with depth.

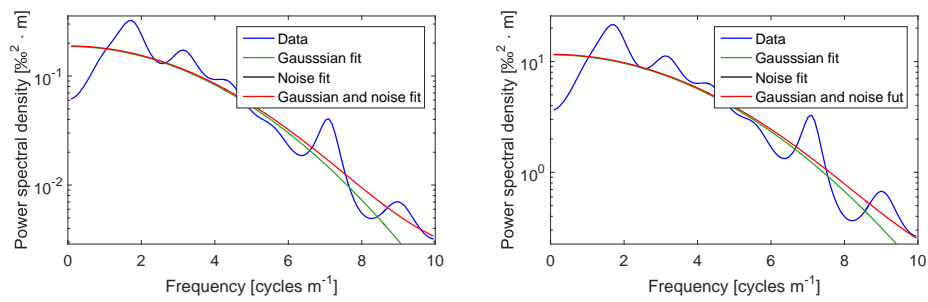


Figure A.11. NEEM - discrete data. Early Holocene power spectra of $\delta^{18}\text{O}$ (left) and δD (right)

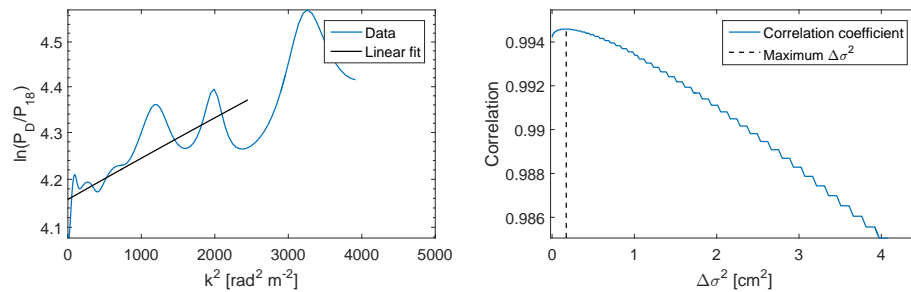


Figure A.12. Differential diffusion techniques applied on NEEM early Holocene discrete data. Left: linear fit of the logarithmic PSD ratio ($^{18}\Delta\sigma^2$ II). Right: Correlation between $\delta^{18}\text{O}$ and artificially diffused δD ($^{18}\Delta\sigma^2$ III).

Table A.4. Estimated values for NEEM early Holocene discrete data. The values have not been corrected for sampling diffusion, ice diffusion and thinning.

σ_{18} [cm]	σ_D [cm]	$\Delta\sigma^2$ I [cm ²]	$\Delta\sigma^2$ [cm ²] II	$\Delta\sigma^2$ III [cm ²]
3.58	3.35	1.6	0.9	0.2

Table A.5. Estimated value for NGRIP late Holocene data. The value has not been corrected for sampling diffusion, ice diffusion and thinning.

σ_{18} [cm]	σ_D [cm]	$\Delta\sigma^2$ I [cm ²]	$\Delta\sigma^2$ [cm ²] II	$\Delta\sigma^2$ III [cm ²]
8.39	-	-	-	-

A.6.4 *NGRIP - late Holocene*

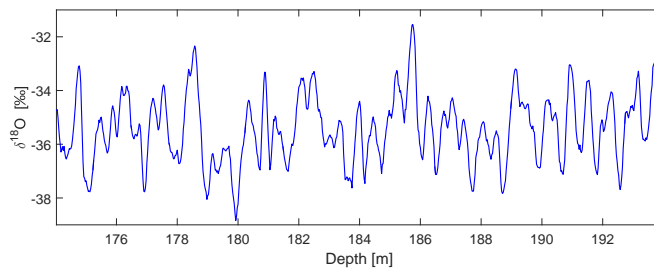


Figure A.13. NGRIP late Holocene $\delta^{18}\text{O}$ (top) and δD (below) profiles with depth.

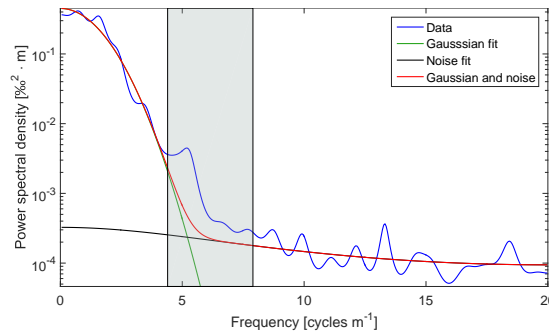


Figure A.14. NGRIP late Holocene power spectrum of $\delta^{18}\text{O}$.

Table A.6. Estimated value for NGRIP early Holocene core 1 data. The value has not been corrected for sampling diffusion, ice diffusion and thinning.

σ_{18} [cm]	σ_D [cm]	$\Delta\sigma^2$ I [cm ²]	$\Delta\sigma^2$ [cm ²] II	$\Delta\sigma^2$ III [cm ²]
5.53	-	-	-	-

A.6.5 NGRIP - early Holocene core 1

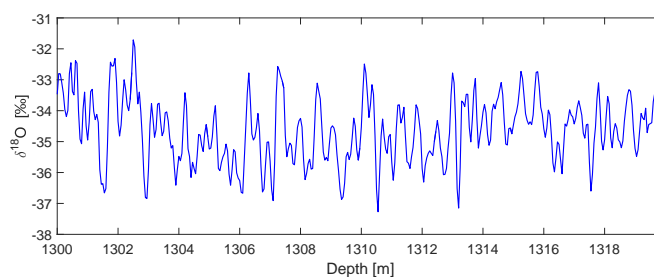


Figure A.15. NGRIP early Holocene core 1. $\delta^{18}\text{O}$ (top) and δD (below) profiles with depth.

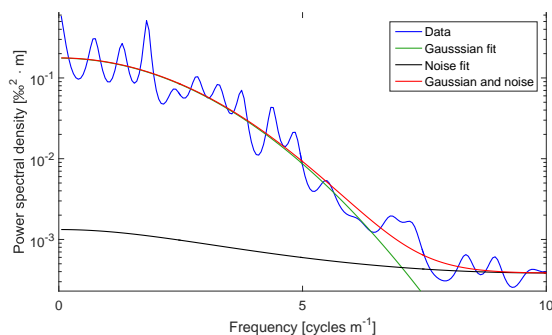


Figure A.16. NGRIP early Holocene core 1. Power spectrum of $\delta^{18}\text{O}$.

Table A.7. Estimated value for NGRIP early Holocene core 2 data. The value has not been corrected for sampling diffusion, ice diffusion and thinning.

σ_{18} [cm]	σ_D [cm]	$\Delta\sigma^2$ I [cm ²]	$\Delta\sigma^2$ [cm ²] II	$\Delta\sigma^2$ III [cm ²]
5.70	-	-	-	-

A.6.6 NGRIP - early Holocene core 2

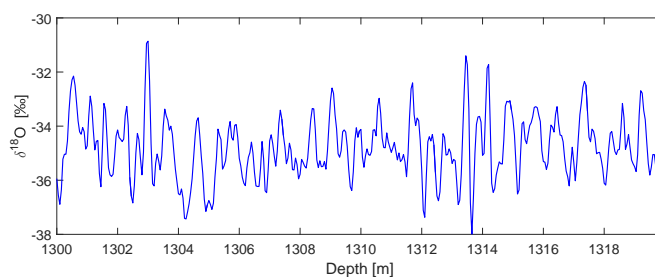


Figure A.17. NGRIP early Holocene core 2. $\delta^{18}\text{O}$ (top) and δD (below) profiles with depth.

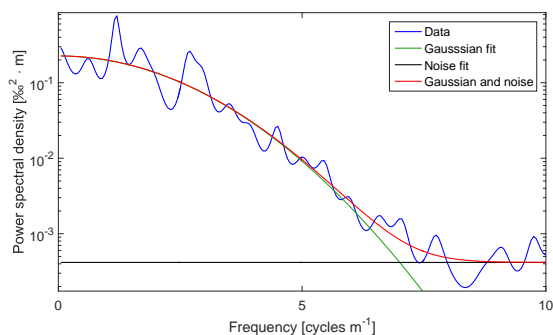


Figure A.18. NGRIP early Holocene core 2. Power spectrum of $\delta^{18}\text{O}$.

A.6.7 GRIP - late Holocene

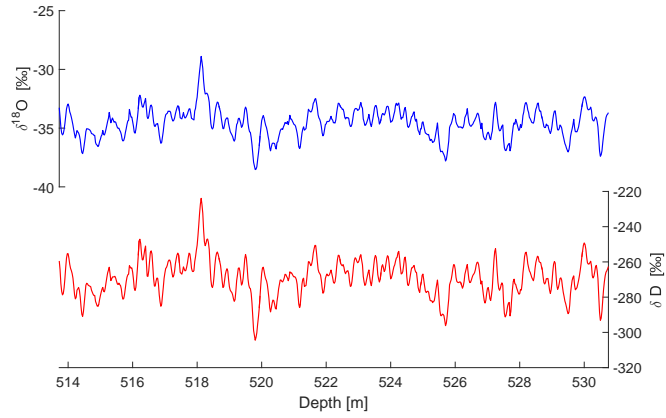


Figure A.19. GRIP. Late Holocene $\delta^{18}\text{O}$ (top) and δD (below) profiles with depth.

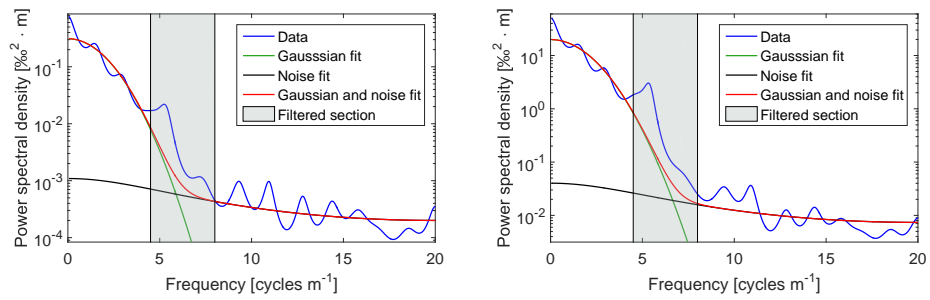


Figure A.20. GRIP. Late Holocene power spectra of $\delta^{18}\text{O}$ (left) and δD (right).

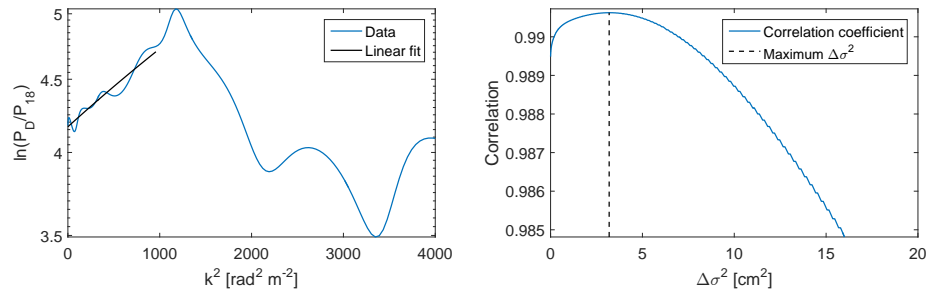


Figure A.21. Differential diffusion techniques applied on GRIP late Holocene data. Left: linear fit of the logarithmic PSD ratio ($^{18}\Delta\sigma^2$ II). Right: Correlation between $\delta^{18}\text{O}$ and artificially diffused δD ($^{18}\Delta\sigma^2$ III).

Table A.8. Estimated diffusion values for the GRIP late Holocene data. The values have not been corrected for sampling diffusion, ice diffusion and thinning.

σ_{18} [cm]	σ_D [cm]	$\Delta\sigma^2$ I [cm ²]	$\Delta\sigma^2$ [cm ²] II	$\Delta\sigma^2$ III [cm ²]
6.78	6.31	6.2	5.6	3.2

A.6.8 GRIP - mid Holocene

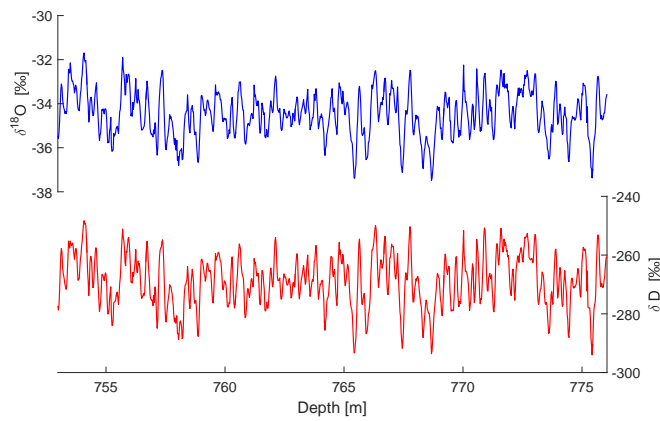


Figure A.22. GRIP. Mid Holocene $\delta^{18}\text{O}$ (top) and δD (below) profiles with depth.

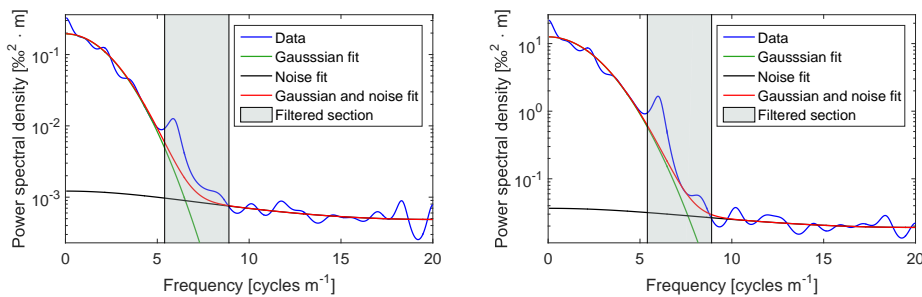


Figure A.23. GRIP. Mid Holocene power spectra of $\delta^{18}\text{O}$ (left) and δD (right).

Table A.9. Estimated diffusion values for the GRIP mid Holocene data. The values have not been corrected for sampling diffusion, ice diffusion and thinning.

σ_{18} [cm]	σ_D [cm]	$\Delta\sigma^2$ I [cm ²]	$\Delta\sigma^2$ [cm ²] II	$\Delta\sigma^2$ III [cm ²]
5.66	5.16	5.3	5.2	0.2

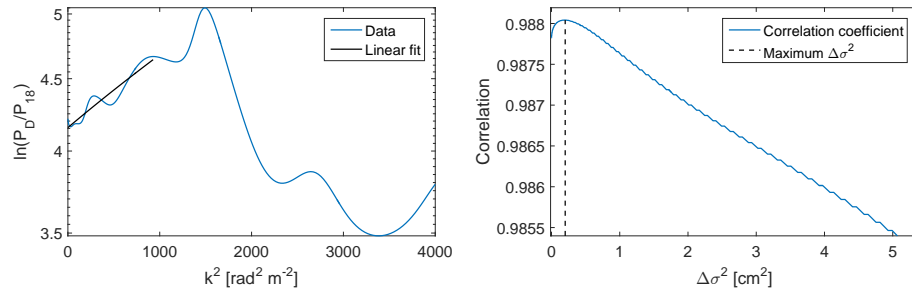


Figure A.24. Differential diffusion techniques applied on GRIP mid Holocene data. Left: linear fit of the logarithmic PSD ratio ($^{18}\Delta\sigma^2$ II). Right: Correlation between $\delta^{18}\text{O}$ and artificially diffused δD ($^{18}\Delta\sigma^2$ III).

A.6.9 GRIP - early Holocene

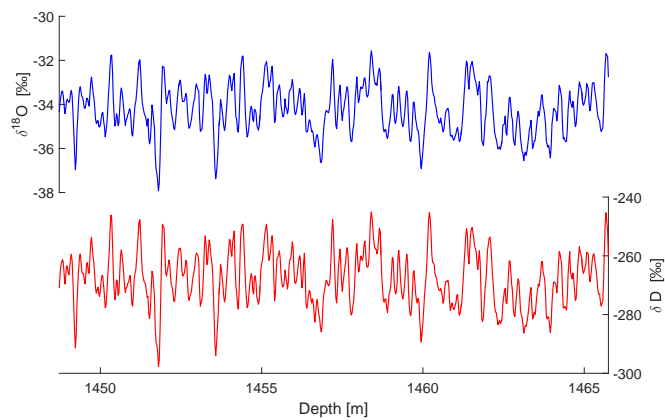


Figure A.25. GRIP. Early Holocene $\delta^{18}\text{O}$ (top) and δD (below) profiles with depth.

Table A.10. Estimated diffusion values for the GRIP early Holocene data. The values have not been corrected for sampling diffusion, ice diffusion and thinning.

σ_{18} [cm]	σ_D [cm]	$\Delta\sigma^2$ I [cm ²]	$\Delta\sigma^2$ [cm ²] II	$\Delta\sigma^2$ III [cm ²]
4.07	3.61	3.5	1.6	0.9

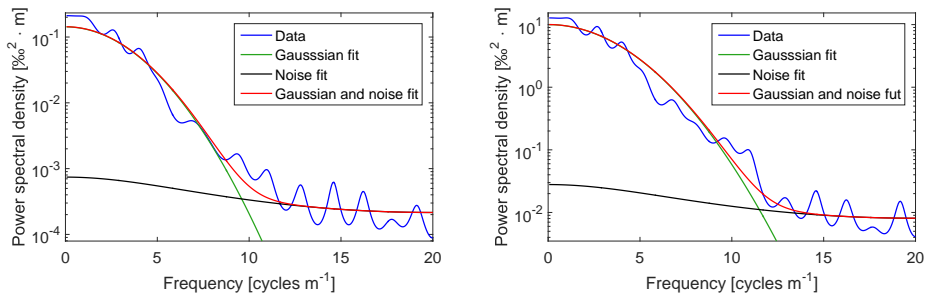


Figure A.26. GRIP. Early Holocene power spectra of $\delta^{18}\text{O}$ (left) and δD (right).

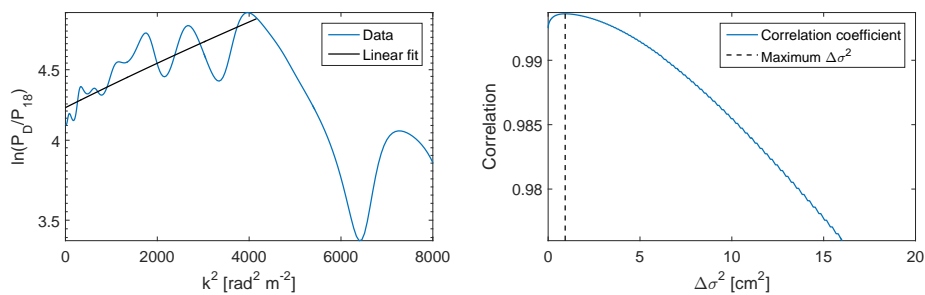


Figure A.27. Differential diffusion techniques applied on GRIP early Holocene data. Left: linear fit of the logarithmic PSD ratio ($^{18}\Delta\sigma^2$ II). Right: Correlation between $\delta^{18}\text{O}$ and artificially diffused δD ($^{18}\Delta\sigma^2$ III).

A.6.10 EDML

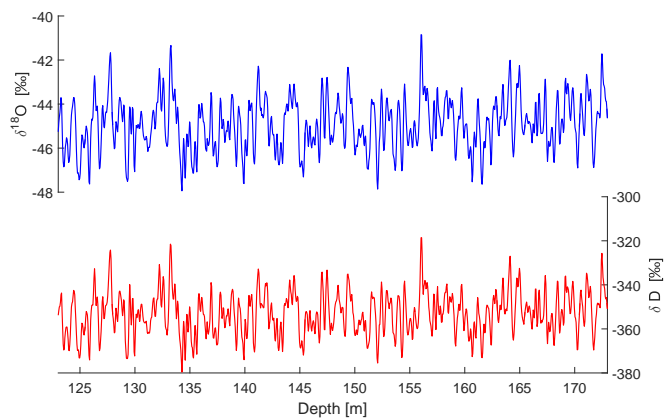


Figure A.28. EDML. $\delta^{18}\text{O}$ (top) and δD (below) profiles with depth.

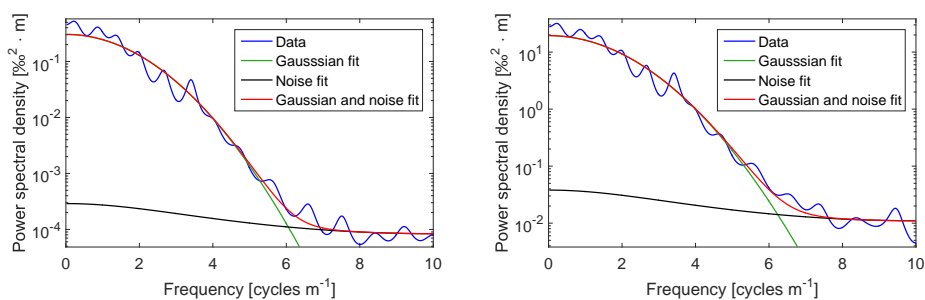


Figure A.29. EDML. Power spectra of $\delta^{18}\text{O}$ (left) and δD (right).

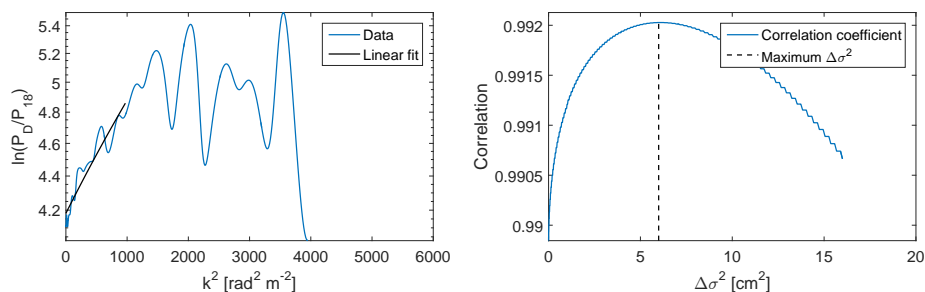


Figure A.30. Differential diffusion techniques applied on EDML Holocene data. Left: linear fit of the logarithmic PSD ratio ($^{18}\Delta\sigma^2$ II). Right: Correlation between $\delta^{18}\text{O}$ and artificially diffused δD ($^{18}\Delta\sigma^2$ III).

Table A.11. Estimated diffusion values for the EDML data. The values have not been corrected for sampling diffusion, ice diffusion and thinning.

σ_{18} [cm]	σ_D [cm]	$\Delta\sigma^2$ I [cm ²]	$\Delta\sigma^2$ [cm ²] II	$\Delta\sigma^2$ III [cm ²]
7.40	6.86	7.7	7.0	6.0

A.6.11 Dome C

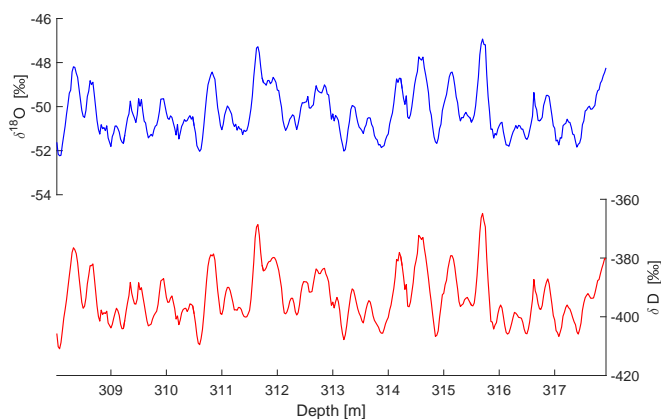


Figure A.31. Dome C. $\delta^{18}\text{O}$ (top) and δD (below) profiles with depth.

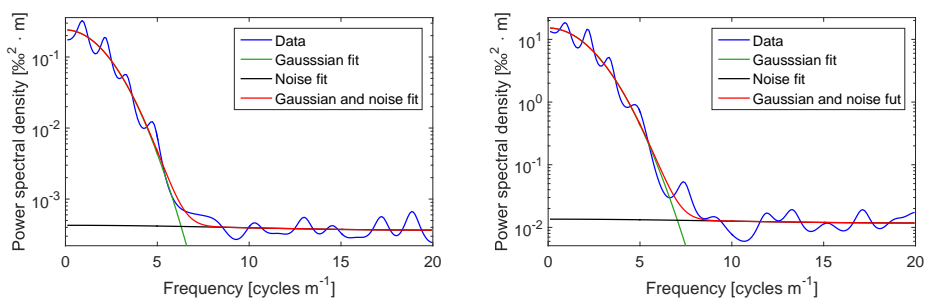


Figure A.32. Dome C. Power spectra of $\delta^{18}\text{O}$ (left) and δD (right).

Table A.12. Estimated diffusion values for the Dome C data. The values have not been corrected for sampling diffusion, ice diffusion and thinning.

σ_{18} [cm]	σ_D [cm]	$\Delta\sigma^2$ I [cm ²]	$\Delta\sigma^2$ [cm ²] II	$\Delta\sigma^2$ III [cm ²]
6.38	6.01	4.6	7.1	0.2

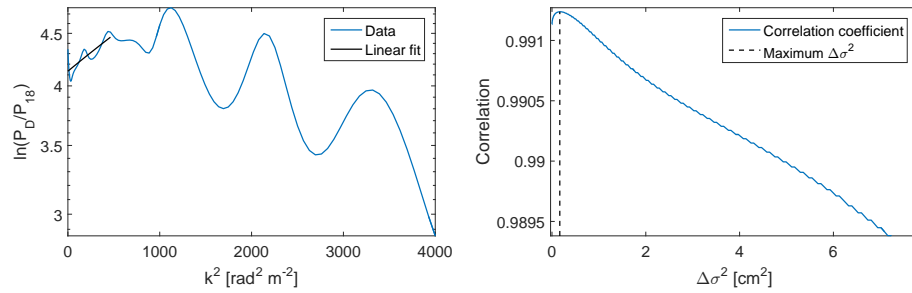


Figure A.33. Differential diffusion techniques applied on Dome C Holocene data. Left: linear fit of the logarithmic PSD ratio ($^{18}\Delta\sigma^2$ II). Right: Correlation between $\delta^{18}\text{O}$ and artificially diffused δD ($^{18}\Delta\sigma^2$ III).

A.6.12 Dome Fuji

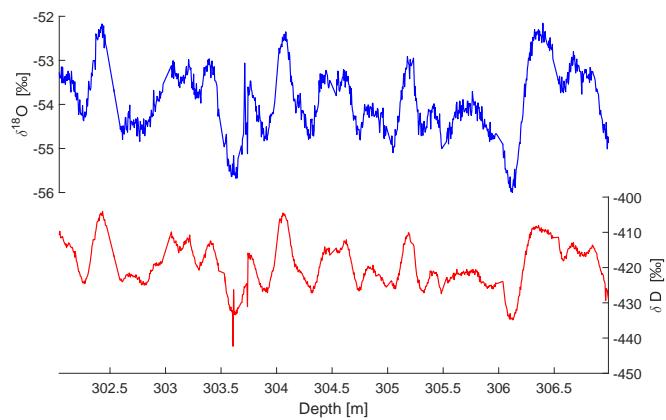


Figure A.34. Dome F. $\delta^{18}\text{O}$ (top) and δD (below) profiles with depth.

σ_{18} [cm]	σ_D [cm]	$\Delta\sigma^2$ I [cm ²]	$\Delta\sigma^2$ [cm ²] II	$\Delta\sigma^2$ III [cm ²]
5.70	4.30	14.0	5.2	6.1

Table A.13. Estimated diffusion values for the Dome F data. The values have not been corrected for sampling diffusion, ice diffusion and thinning.

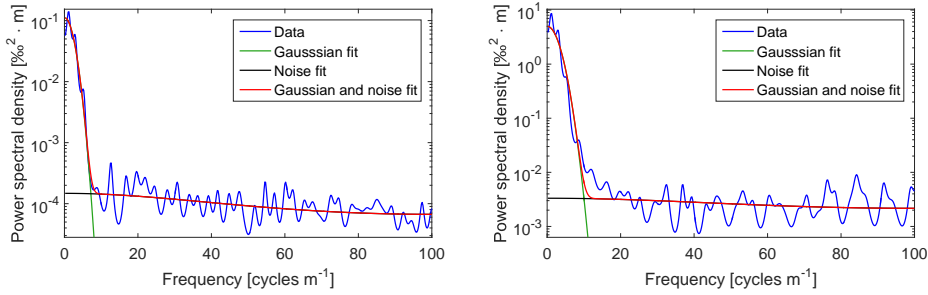


Figure A.35. Dome F. Power spectra of $\delta^{18}\text{O}$ (left) and δD (right).

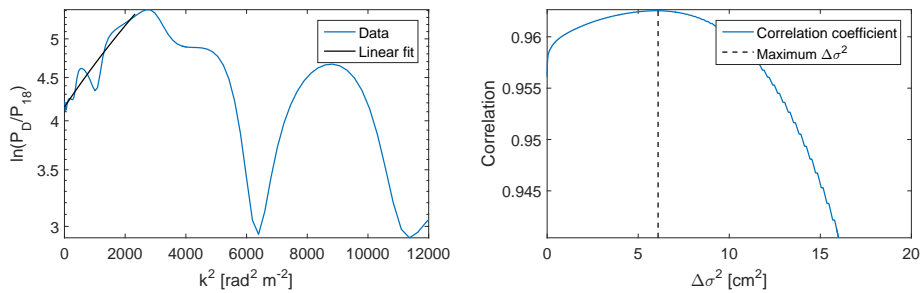


Figure A.36. Differential diffusion techniques applied on Dome F Holocene data. Left: linear fit of the logarithmic PSD ratio ($^{18}\Delta\sigma^2$ II). Right: Correlation between $\delta^{18}\text{O}$ and artificially diffused δD ($^{18}\Delta\sigma^2$ III).

A.6.13 WAIS Divide

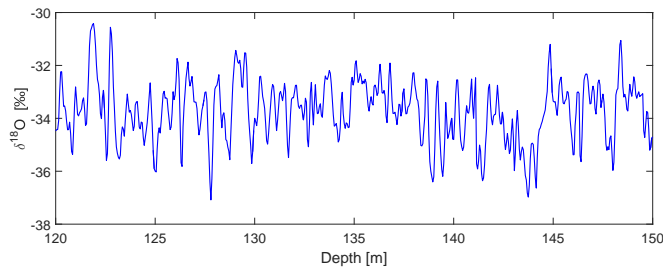


Figure A.37. WAIS D. $\delta^{18}\text{O}$ (top) and δD (below) profiles with depth.

σ_{18} [cm]	σ_D [cm]	$\Delta\sigma^2$ I [cm ²]	$\Delta\sigma^2$ [cm ²] II	$\Delta\sigma^2$ III [cm ²]
7.23	-	-	-	-

Table A.14. Estimated value for WAIS D Holocene data. The value has not been corrected for sampling diffusion, ice diffusion and thinning.

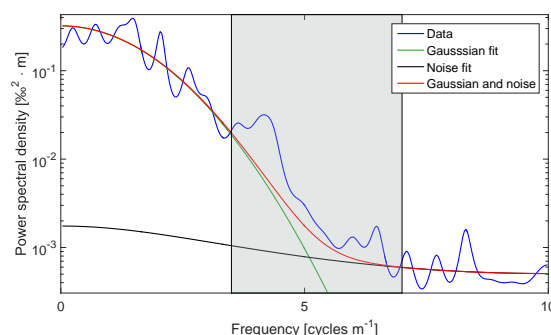


Figure A.38. WAIS D. Holocene power spectra of $\delta^{18}\text{O}$.

REFERENCES

- Adolph, A. C. and M. R. Albert (2014). “Gas diffusivity and permeability through the firn column at Summit, Greenland: measurements and comparison to microstructural properties”. In: *The Cryosphere* 8, pp. 319–328.
- Barkan, E. and B. Luz (2007). “Diffusivity fractionations of (H₂O)-O-16/(H₂O)-O-17 and (H₂O)-O-16/(H₂O)-O-18 in air and their implications for isotope hydrology”. In: *Rapid Communications In Mass Spectrometry* 21.18, pp. 2999–3005.
- Barkan, E. and B. Luz (2005). “High precision measurements of O-17/O-16 and O-18/O-16 ratios in (H₂O)”. In: *Rapid Communications In Mass Spectrometry* 19.24, pp. 3737–3742.
- Blicks, H., O. Dengel, and N. Riehl (1966). “Diffusion Von Protonen (tritonen) In Reinen Und Dotierten Eis-einkristallen”. In: *Physik Der Kondensierten Materie* 4.5, pp. 375–381.
- Cuffey, K. M. and W. S. B. Paterson (2010). *The physics of glaciers*. 4th. Elsevier, p. 400.
- Delibaltas, P., O. Dengel, D. Helmreich, N. Riehl, and H. Simon (1966). “Diffusion Von ¹⁸O In Eis-einkristallen”. In: *Physik Der Kondensierten Materie* 5.3, pp. 166–170.
- Durran, D. R. (2010). *Numerical Methods for Fluid Dynamics*. Springer, 2nd. Edition.
- Freitag, J., U. Dorbrindt, and S. Kipfstuhl (2002). “A new method for predicting transport properties of polar firn with respect to gases on the pore space scale”. In: *Ann. Glacio.* 35, pp. 538–544.

- Hall, W. D. and H. R. Pruppacher (1976). “The Survival of Ice Particles Falling from Cirrus Clouds in Subsaturated Air”. In: *Journal of the Atmospheric Sciences* 33.10, pp. 1995–2006.
- Holme, C., V. Gkinis, and B. M. Vinther (2018a). “Molecular diffusion of stable water isotopes in polar firn as a proxy for past temperatures”. In: *Geochimica et Cosmochimica Acta* 225, pp. 128–145.
- Itagaki, Kazuhiko (1964). “Self-Diffusion in Single Crystals of Ice”. In: *J. Phys. Soc. Jpn.* 19.6, pp. 1081–1081.
- Johnsen, S. J. (1977). “Stable Isotope Homogenization of Polar Firn and Ice”. In: *Isotopes and Impurities in Snow and Ice*, pp. 210–219.
- Johnsen, S. J., H. B. Clausen, K. M. Cuffey, G. Hoffmann, J. Schwander, and T. Creyts (2000). “Diffusion of stable isotopes in polar firn and ice: the isotope effect in firn diffusion”. In: *Physics of Ice Core Records*, pp. 121–140.
- Majoube, M. (1970). “Fractionation factor of ^{18}O between water vapour and ice”. In: *Nature* 226.1242.
- Merlivat, L. and J. Jouzel (1979). “Global Climatic Interpretation of the Deuterium-Oxygen 18 Relationship for Precipitation”. In: *Journal of Geophysical Research* 84.8.
- Merlivat, L. and G. Nief (1967). “Fractionnement Isotopique Lors Des Changements Etat Solide-Vapeur Et Liquide-Vapeur De Leau A Des Temperatures Inferieures A 0 Degrees C”. In: *Tellus* 19.1, pp. 122–127.
- Murphy, D. M. and T. Koop (2006). “Review of the vapour pressures of ice and supercooled water for atmospheric applications”. In: *Q.J.R. Meteorol. Soc.* 131, pp. 1539–1565.
- Ramseier, R. O. (1967). “Self-Diffusion Of Tritium In Natural And Synthetic Ice Monocrystals”. In: *Journal Of Applied Physics* 38.6, pp. 2553–2556.
- Schwander, J., T. Sowers, J.-M. Barnola, T. Blunier, A. Fuchs, and B. Malaizé (1997). “Age scale of the air in the summit ice: Implications for glacial-interglacial temperature change”. In: *Journal of Geophysical Research* 102.D16, 19, 483–19, 493b.
- Schwander, J., B. Stauffer, and A. Sigg (1988). “Air mixing in firn and the age of the air at pore close-off”. In: *Annals of Glaciology*, pp. 141–145.
- Simonsen, S. B., S. J. Johnsen, T. J. Popp, B. M. Vinther, V. Gkinis, and H. C. Steen-Larsen (2011). “Past surface temperatures at the NorthGRIP drill site from the difference in firn diffusion of water isotopes”. In: *Climate of the Past* 7.

B

VARYING REGIONAL $\delta^{18}\text{O}$ -TEMPERATURE RELATIONSHIP IN HIGH RESOLUTION STABLE WATER ISOTOPES FROM EAST GREENLAND

This is the appendix to Chapter 5 (Holme et al., 2018b, in review) and it has been included in its full length even though Appendix B.1 overlaps with Appendix A.1.

B.1 FIRN DIFFUSIVITY

This study uses the firn diffusivity parameterization of Johnsen et al., 2000:

$$D(\rho) = \frac{m p D_{ai}}{R T \alpha_i \tau} \left(\frac{1}{\rho} - \frac{1}{\rho_{ice}} \right) \quad (98)$$

which depends on the molar weight of water (m), the saturation vapor pressure (p), diffusivity of water vapor (D_{ai}), the molar gas constant (R), the site temperature (T), the ice–vapor fractionation factor (α_i) and the firn air tortuosity (τ). Similar to Johnsen et al., 2000 and subsequently used in Simonsen et al., 2011; Gkinis et al., 2014; Holme et al., 2018a, we used the following definitions which can be parameterized through annual mean surface temperature, annual accumulation rate, surface pressure and density (ρ):

- Saturation vapor pressure over ice (Pa) (Murphy and Koop, 2006):

$$p = \exp \left(9.5504 - \frac{5723.265}{T} + 3.530 \ln(T) - 0.0073 T \right) \quad (99)$$

- D_{ai} : diffusivity of water vapor (for isotopologue i) in air ($\text{m}^2 \text{s}^{-1}$). For the diffusivity of the abundant isotopologue water vapor D_a (Hall and Pruppacher, 1976):

$$D_a = 2.1 \cdot 10^{-5} \left(\frac{T}{T_o} \right)^{1.94} \left(\frac{P_o}{P} \right) \quad (100)$$

with $P_o = 1 \text{ Atm}$, $T_o = 273.15 \text{ K}$ and P , T the ambient pressure (Atm) and temperature (K). Additionally from Merlivat and Jouzel, 1979 $D_{a^{2\text{H}}} = 0.9755 D_a$ and $D_{a^{18\text{O}}} = 0.9723 D_a$

- R : molar gas constant $R = 8.3144 \text{ m}^3\text{PaK}^{-1}\text{mol}^{-1}$
- α_i : Ice – Vapor fractionation factor. we use the formulations by Majoube, 1970 and Merlivat and Nief, 1967 for $\alpha_{s/v}^{\delta\text{D}}$ and $\alpha_{s/v}^{\delta^{18}\text{O}}$ respectively.

$$\alpha_{\text{Ice/Vapor}}(^2\text{H}/^1\text{H}) = 0.9098 \exp(16288/T^2) \quad (101)$$

$$\alpha_{\text{Ice/Vapor}}(^{18}\text{O}/^{16}\text{O}) = 0.9722 \exp(11.839/T) \quad (102)$$

$$(103)$$

- τ : The firn tortuosity (Schwander et al., 1988):

$$\frac{1}{\tau} = 1 - b \cdot \left(\frac{\rho}{\rho_{\text{ice}}} \right)^2 \quad \rho \leq \frac{\rho_{\text{ice}}}{\sqrt{b}}, \quad b = 1.3 \quad (104)$$

Based on Eq. (104), $\tau \rightarrow \infty$ for $\rho > 804.3 \text{ kg m}^{-3}$

B.2 SIGNIFICANCE ANALYSIS

In this study, time series have often been smoothed with a 5 year moving mean before estimating their correlation. Potentially, this results in artificially improved correlation coefficients as a moving mean is a low-pass filter. It is therefore necessary to quantify the significance of the linear relationship (p -value) by running a Monte Carlo simulation. This study test said significance by examining what correlation coefficients we would estimate if we had random generated data instead of the $\delta^{18}\text{O}$ signal (following the procedure proposed by Macias-Fauria et al., 2011). For simplicity, this section refers to the correlation between $\delta^{18}\text{O}$ and temperature while it applies equally for all types of time series.

Synthetic data are created by generating time series with the same power spectrum as the $\delta^{18}\text{O}$ signal. This study uses a method outlined in Ebisuzaki, 1977 that is based on a random resampling of the $\delta^{18}\text{O}$ signal in the frequency domain. The synthetic time series is then found by taking the inverse fast Fourier transform of the shuffled signal. This procedure retains the same autocorrelation as the input time series hereby mimicking the influence of a 5 year moving mean applied on data.

This procedure is simulated 1000 times. For each iteration, the correlation coefficient between the synthetic $\delta^{18}\text{O}$ series and the temperature series is calculated. From this Monte Carlo routine, an empirical probability distribution function that describes the relation between synthetic generated data and the temperature series is obtained. From this distribution, it is possible to compute the p -value which describes how probable it is that the correlation between $\delta^{18}\text{O}$ and temperature is significantly different from that of the synthetic $\delta^{18}\text{O}$ and temperature. In this study, p -values below 0.05 are considered statistically significant.

B.3 FIGURES

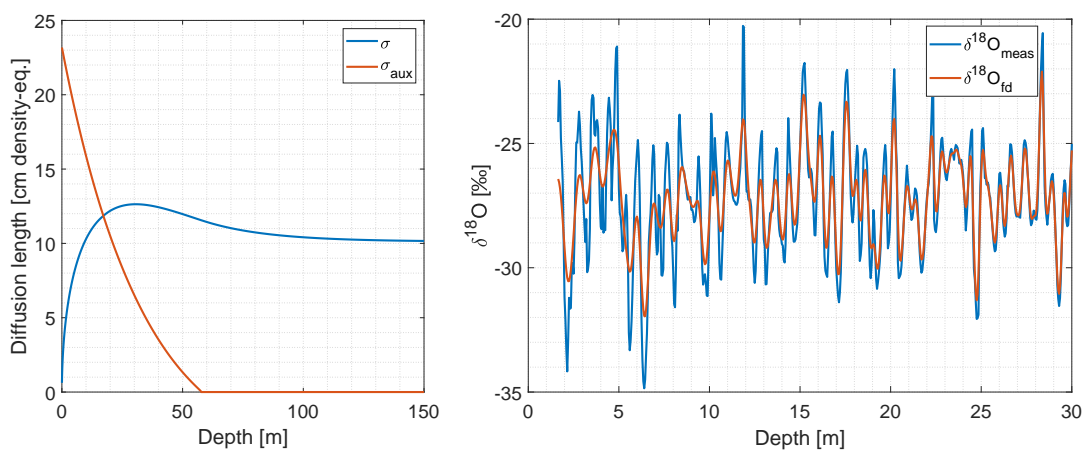


Figure B.1. Left: Modeled firn diffusion with depth (σ ; blue) and calculated auxiliary diffusion length that should be applied on the measured $\delta^{18}\text{O}$ data (σ_{aux} ; red). After the pore close-off ($\rho_{pc} = 804.3 \text{ kg m}^{-3}$), $\sigma_{aux} = 0$ as σ just changes due to the compaction of firn. Right: The measured $\delta^{18}\text{O}$ data (blue) and the forward-diffused $\delta^{18}\text{O}$ data (red) for the 1988 M core.

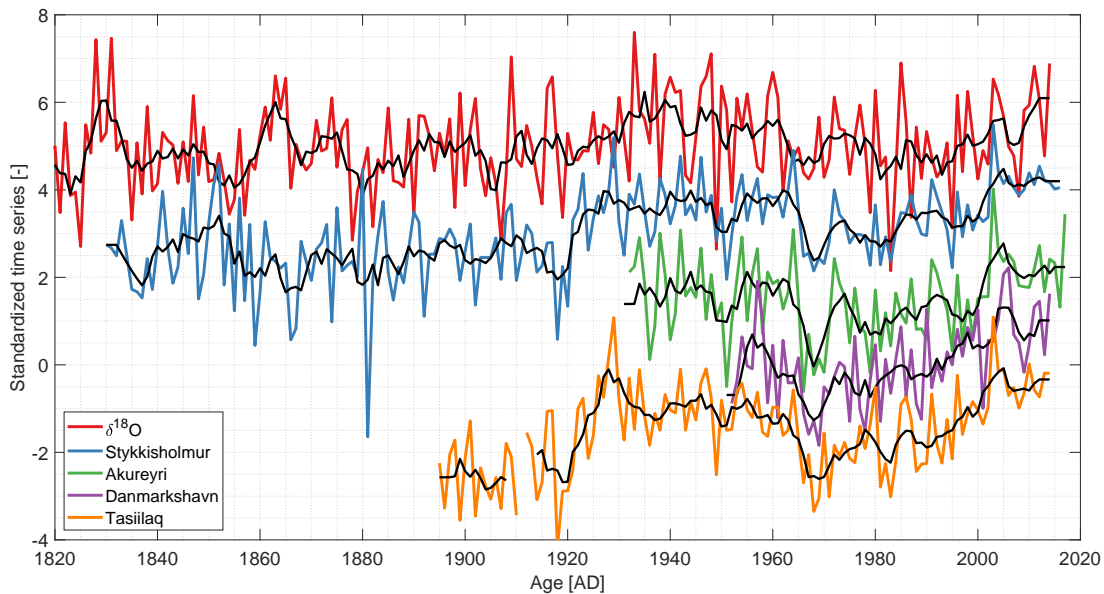


Figure B.2. Winter averaged $\delta^{18}\text{O}$ and temperature series. For visualization, the time series have been standardized and shifted vertically. The black curves represent a moving average of 5 years.

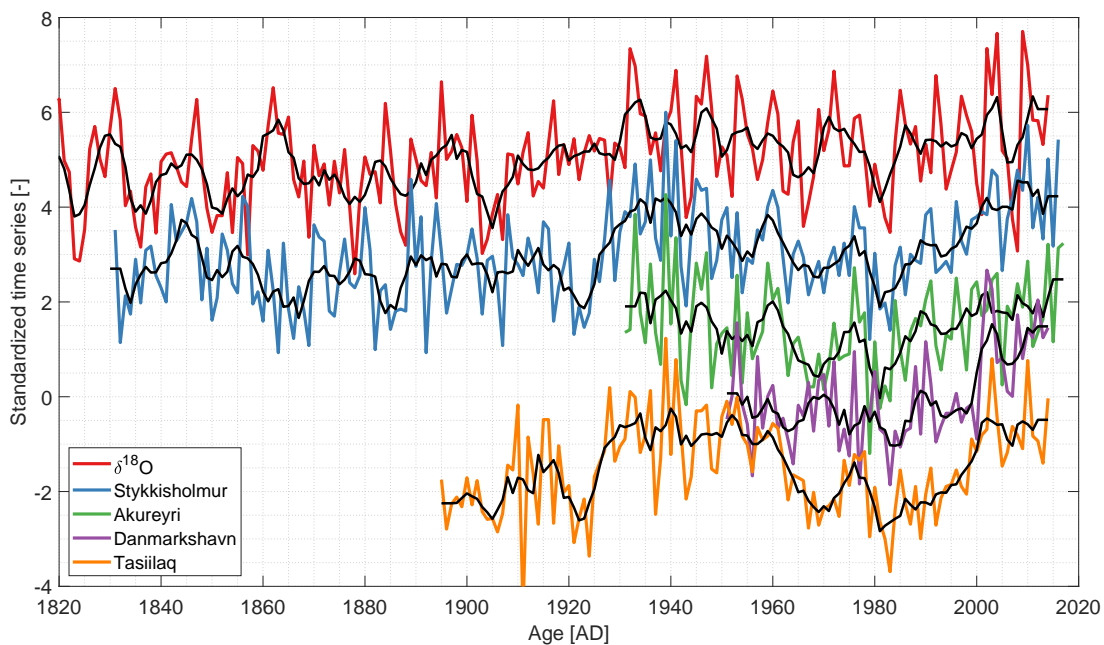


Figure B.3. Summer averaged $\delta^{18}\text{O}$ and temperature series. For visualization, the time series have been standardized and shifted vertically. The black curves represent a moving average of 5 years.

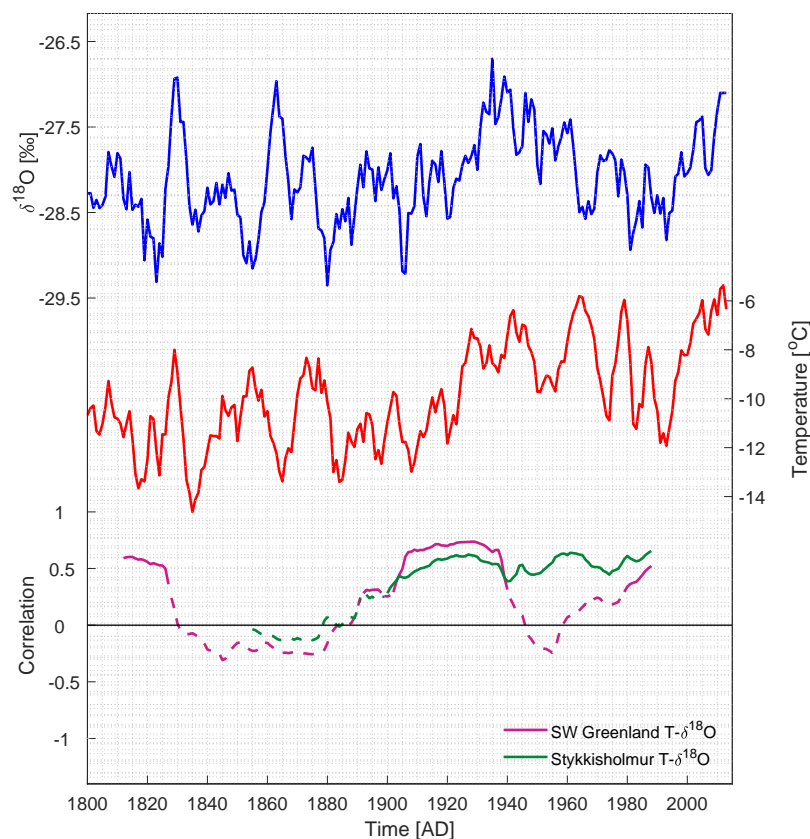


Figure B.4. Top: 5 year moving average of the winter averaged $\delta^{18}\text{O}$ stack. Mid: 5 year moving average of the December-January-February averaged Southwest Greenland temperatures from Vinther et al., 2006. Bottom: 50 year running correlations between $\delta^{18}\text{O}$ and Southwest Greenland (magenta) and $\delta^{18}\text{O}$ and Stykkisholmur (green). Each year represents the midpoint of the running window. Solid lines are significant correlations and dashed lines are insignificant ($p > 0.05$).

REFERENCES

- Ebisuzaki, W. (1977). "A method to estimate the statistical significance of a correlation when the data are serially correlated". In: *Journal of Climate* 10, pp. 2147–2153.
- Gkinis, V., S. B. Simonsen, S. L. Buchardt, J. W. C. White, and B. M. Vinther (2014). "Water isotope diffusion rates from the NorthGRIP ice core for the last 16,000 years - glaciological and paleoclimatic implications". In: *Earth and Planetary Science Letters* 405.
- Hall, W. D. and H. R. Pruppacher (1976). "The Survival of Ice Particles Falling from Cirrus Clouds in Subsaturated Air". In: *Journal of the Atmospheric Sciences* 33.10, pp. 1995–2006.

- Holme, C., V. Gkinis, M. Lanzky, V. Morris, M. Olesen, A. Thayer, B. H. Vaughn, and B. M. Vinther (2018b, in review). “Varying regional $\delta^{18}\text{O}$ –temperature relationship in high resolution stable water isotopes from East Greenland”. In: *review: Climate of the Past Discussions*. URL: <https://doi.org/10.5194/cp-2018-169>.
- Holme, C., V. Gkinis, and B. M. Vinther (2018a). “Molecular diffusion of stable water isotopes in polar firn as a proxy for past temperatures”. In: *Geochemica et Cosmochimica Acta* 225, pp. 128–145.
- Johnsen, S. J., H. B. Clausen, K. M. Cuffey, G. Hoffmann, J. Schwander, and T. Creyts (2000). “Diffusion of stable isotopes in polar firn and ice: the isotope effect in firn diffusion”. In: *Physics of Ice Core Records*, pp. 121–140.
- Macias-Fauria, M., A. Grinsted, S. Helama, and J. Holopainen (2011). “Persistence matters: Estimation of the statistical significance of paleoclimatic reconstruction statistics from auto-correlated time series”. In: *Dendrochronologia* 30 (2), pp. 179–187.
- Majoube, M. (1970). “Fractionation factor of ^{18}O between water vapour and ice”. In: *Nature* 226.1242.
- Merlivat, L. and J. Jouzel (1979). “Global Climatic Interpretation of the Deuterium-Oxygen 18 Relationship for Precipitation”. In: *Journal of Geophysical Research* 84.8.
- Merlivat, L. and G. Nief (1967). “Fractionnement Isotopique Lors Des Changements Etat Solide-Vapeur Et Liquide-Vapeur De Leau A Des Temperatures Inferieures A 0 Degrees C”. In: *Tellus* 19.1, pp. 122–127.
- Murphy, D. M. and T. Koop (2006). “Review of the vapour pressures of ice and supercooled water for atmospheric applications”. In: *Q.J.R. Meteorol. Soc.* 131, pp. 1539–1565.
- Schwander, J., B. Stauffer, and A. Sigg (1988). “Air mixing in firn and the age of the air at pore close-off”. In: *Annals of Glaciology*, pp. 141–145.
- Simonsen, S. B., S. J. Johnsen, T. J. Popp, B. M. Vinther, V. Gkinis, and H. C. Steen-Larsen (2011). “Past surface temperatures at the NorthGRIP drill site from the difference in firn diffusion of water isotopes”. In: *Climate of the Past* 7.
- Vinther, B. M. et al. (2006). “A synchronized dating of three Greenland ice cores throughout the Holocene”. In: *Journal Of Geophysical Research-Atmospheres* 111.D13102.